Development and Application of Gas-phase Raman Spectroscopy Techniques for Analysis of Carbon Nanotube Synthesis Processes

PhD Thesis

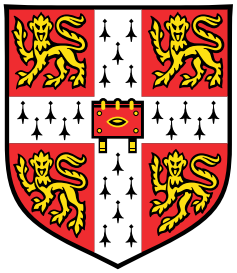

Maxim Kuvshinov

Department of Engineering
University of Cambridge

This dissertation is submitted for the degree of
Doctor of Philosophy

Hughes Hall

March 2021

Declaration

This thesis is the result of my own work and includes nothing which is the outcome of work done in collaboration except as declared in the Preface and specified in the text. I further state that no substantial part of my thesis has already been submitted, or, is being concurrently submitted for any such degree, diploma or other qualification at the University of Cambridge or any other University or similar institution except as declared in the Preface and specified in the text. It does not exceed the prescribed word limit for the relevant Degree Committee.

Maxim Kuvshinov
March 2021

Abstract

Development and Application of Gas-phase Raman Spectroscopy Techniques for Analysis of Carbon Nanotube Synthesis Processes

Maxim Kuvshinov

Carbon Nanotubes (CNTs) are structures with outstanding chemical and physical properties, making them an attractive candidate for multiple industrial applications. They can be produced via different techniques, with the floating catalyst chemical vapour deposition (FC-CVD) being one of the most attractive solutions for the mass production of CNTs. The current production rate of high-quality CNT material with tailored properties falls short of the rising industrial demand. One of the major limiting factors for high volume production is insufficient knowledge of underlying chemical processes that result in the CNTs growth via FC-CVD, making the rate-limiting factors of the system unknown. Another limiting factor in the manufacture of high quality CNTs is the lack of on-the-fly monitoring of synthesis parameters.

In this study, two Raman-based spectroscopic techniques were tested for the realisation of *in situ* measurements in a FC-CVD reactor.

Cavity-enhanced Raman spectroscopy (CERS) was found to be a powerful low-cost high-resolution tool for analysis of non-reacting gaseous mixtures. Based on experimental results, its application for analysis of reacting flows was deemed to be limited due to localised changes in refractive index in reacting flows. A comprehensive model was derived, which was able to calculate an expected amplification of Raman signal, compared to a more typical free space spontaneous Raman scattering setup. Quality of the model was confirmed by experimental measurements.

Pulsed Laser Raman spectroscopy setup was designed, constructed and implemented to perform *in situ* measurements of the CNT synthesis process via FC-CVD.

A bespoke cross-shaped reactor with a purging system was developed and applied to provide continuous optical access to the reaction volume of FC-CVD reactor.

Created Fluent-based computational fluid dynamics model was used to analyse fluid flow pattern and molar fraction distribution of chemicals inside the reactor in order to develop a suitable calibration procedure.

Constructed Raman spectroscopy setup was able to perform *in situ* quantitative analysis of thiophene thermal decomposition at small quantities in H_2 environment as a function of thiophene concentration and reactor temperature. Methane, H_2S, Si-H and Si-H_2 were detected as products of thiophene decomposition, followed by further decomposition of methane observed from quantitative measurements of H_2 molar fraction inside of the FC-CVD reactor.

The developed pulsed laser Raman setup successfully performed first of its kind *in situ* Raman measurements in a reaction volume of FC-CVD reactor during CNT synthesis at 1100 °C. The system was able to successfully provide key information of the reaction gas phase parameters which are vital for on-the-fly control synthesis process and quality of the CNT product.

The developed reactor and Raman system can be applied for in-depth analysis of not only CNT synthesis but other reacting flows.

Acknowledgements

First and foremost, I would like to thank my supervisor **Prof. Simone Hochgreb** for her continued support of my PhD research. She provided me helpful guidance on the direction of the project, encouragement and crucial advice during the period of thesis writing. Her open-minded approach to obstacles and rigorous attitude in academic research helped me to face and solve challenging problems.

I would like to thank **Dr. Adam Boies**, and **Dr. Michael de Volder** for their enlightening advice and support during my research.

I wish to thank **Dr. Brian Graves**, **Dr. Fiona Smail** and **Mr. Tyler Johnson** for their continued willingness to answer my queries, help with equipment and design of the reacting flow system.

I would like to thank **Filip Gökstorp** for providing me with valuable advice on the practices of CFD modeling.

I wish to extend my gratitude to the Division A workshop, in particular to **Mr. Roy Slater**, **Mr. Mark Garner**, and **Mr. Kenneth Griggs**, for providing enthusiastic continued technical support. The speed and quality of their work, coupled with their comprehensive understanding of the science behind the projects has been incredibly educational.

I would like to thank the **Hopkinson's** offices for great social environment at work.

I would like to extend a big thank you to the staff of **Hughes Hall** college, such as **porters**, and the **cohorts** of 2016-2019. I have met a staggering amount of fantastic people who made my years spent in Cambridge into best years of my life.

I would like to express my deepest appreciation for **Dr. Lee Weller**, who was there for the entirety of my PhD journey. His incredible patience, constant encouragement, knowledge of optical and spectroscopic processes allowed this project to achieve the goals that it did. Working with him side-by-side drastically improved my experimental skills, taught me how to deal with and anticipate problems and helped me to become the researcher I am today.

I would like to gratefully acknowledge the financial support of the EPSRC, without which this project would not be possible

Lastly, I would like to express eternal gratitude to **my family**. Their endless support, understanding, encouragement, teachings, lectures, and advice helped me to get to where I

am today. I would like to thank my grandparents for their excitement and investment in my progress, along with some scientific advice. But ultimately, I want to thank my parents, **Dr. Kuvshinov** and **Dr. Kuvshinova**, who helped me survive all of the work, all of the thesis writing and in the end, this PhD.

Associated publications

Journal Publications

- Weller, L., **Kuvshinov, M.** and Hochgreb, S. Gas-phase Raman spectroscopy of non-reacting flows: comparison between free-space and cavity-based spontaneous Raman emission. *Applied Optics*, 58(10):C92–C103, doi: 10.1364/AO.58.000C92.

Conference proceedings

- Weller, L., **Kuvshinov, M.**, and Hochgreb, S. Gas phase Raman spectroscopy : comparison of continuous wave and cavity based methods. *Imaging and Applied Optics 2018* (3D, AO, AIO, COSI, DH, IS, LACSEA, LSC, MATH, pcAOP), OSA Technical Digest (Optical Society of America, 2018), paper LW3C.2.

Table of contents

List of figures

List of tables

Nomenclature

Roman Symbols

A	Total losses of the optical cavity
b	Confocal beam parameter
c	Speed of light
c_0	Speed of light in vacuum
C_0	Purcell spontaneous emission enhancement factor
C_c	Effective Purcell factor in the cavity
d	Laser beam diameter at the lens
$d_{1/2}$	Distances of $w_{1/2}$ from mode-matching lens
f	Focal length of a lens
f_0	Characteristic length
H	Beam radius at the in-coupling mirror of the resonator
h	Planck's constant
I	Intensity of a Raman mode
k_b	Boltzmann's constant
l	Length of an optical resonator/cavity
N	Number of particles per unit volume
n	Refractive index

n_p Number of pump photons

n_s Number of scattered Stokes photons

P_{in} Pump laser power

q Imaginary beam parameter

$\dot{Q}$ Inlet volumetric flowrate

$R_{1,2}$ Reflectivity of an in-coupling/out-coupling mirror

$T_{1,2}$ Transmissivity of in- and out-coupling mirrors of a cavity.

$V_{\text{eff}}^{(c)}$ Effective volume of a cavity

$V_{\text{eff}}^{(f)}$ Effective volume in free space

w Beam waist

w_0 Beam waist of an optical cavity

X inlet molar fraction of gas

Greek Symbols

$\Delta\nu_p^{(c)}$ Cavity pump linewidth

$\Delta\nu_{FSR}$ Free spectral range

$\Delta\nu_p^{(f)}$ Free space pump linewidth

$\Delta\nu_S^{(c)}$ cavity Stokes linewidth

$\Delta\nu_S^{(f)}$ Free space Stokes linewidth

ε_0 Permitivity of free space

γ_c Rate of emission of Stokes photons from the cavity

γ_f Rate of emission of Stokes photons in free space

λ Wavelength of incident radiation

λ_p Pump photon wavelength

λ_s Stokes photon wavelength

ν_{AS} Wavenumber of anti-Stokes photon

ν_p Wavenumber of incident photon

ν_S Wavenumber of Stokes photon

ϕ Equivalence ratio

$\frac{d\sigma}{d\Omega}$ Differential Raman scattering cross-section

τ_0 Lifetime of the Stokes photons in free space

τ_c Lifetime of the Stokes photons in the cavity

Subscripts

p Pump photon

S Stokes photon

thio Thiophene

Other Symbols

$\mathcal{F}$ Finesse

$\mathcal{F}_R$ Theoretical finesse

$\mathcal{F}_I$ Curvature finesse

$\mathcal{F}_Q$ Surface quality finesse

$\mathcal{F}_p$ Cavity finesse for pump wavelength

$\mathcal{F}_S$ Cavity finesse for Stokes wavelength

$\mathcal{R}$ Radius of curvature of the mirror

Acronyms / Abbreviations

AR Antireflection

CARS Coherent anti-Stokes Raman spectroscopy

CFD Computational fluid dynamics

CERS Cavity enhanced Raman spectroscopy

CNT Carbon nanotube

CVD Chemical vapour deposition

CW Continuous wave laser

EM-CCD Electron multiplying charge-coupled device

EM Electromagnetic

FWHM Full width half maximum

HAB Height above burner

IR Infrared

LIF Laser-induced fluorescence

NA Numerical aperture of a lens

SEM Scanning electron microscopy

SNR Signal to noise ratio

$TEM_{m,n}$ Transverse electromagnetic mode with transverse mode numbers m, n

TEM Transmission electron microscopy

$TEM_{0,0}$ Primary Transverse Electromagnetic Mode

TGA Thermal gravity analysis

XDR X-ray diffraction

Chapter 1

Introduction

Carbon nanotubes (CNTs) are nanoscale structures which have been deemed as a material of the future since their discovery in 1991 by Iijima [4]. The CNT structure consists of one or more graphitic layers concentrically wrapped into a cylindrical geometry that typically does not exceed several nanometers in diameter but can reach up to hundreds of microns in length [5–8], resulting in aspect ratios of up to 10^5. Such a unique structure allows CNTs to achieve a fascinating range of mechanical, electrical and thermal properties, which shows their great potential in revolutionizing a vast multitude of research and industrial areas such as structural reinforcement, conductive plastics, automotive, medical, aerospace, and technical textiles. However, 30 years later, their wide adoption is yet to be seen. Nevertheless, the last few decades have seen a surge in the number of scientific publications related to CNT synthesis and manufacture, along with an ever more expanding number of companies worldwide incorporating CNTs in their products, as reported by de Volder et al. [9]. The review also highlights the fast increase in annual global CNT production capacity, which has increased ten-fold since 2006 [10]. However, the applications of CNTs are currently limited to high-end, luxury and niche products. Overall, the main hindrance to the widespread application of the CNT material remains its production cost and lack of on-the-fly monitoring of synthesis parameters, which heavily affect the product properties. Therefore, CNTs need to be grown by cost-effective, fast production synthesis processes that are able to produce CNTs of required morphologies in order to facilitate their widespread adoption and incorporation into our daily life products.

1.1 CNTs overview

Carbon nanotubes may be produced with different bulk structures. The simplest type of a CNT is called a single-walled carbon nanotube (SWCNT). It can be envisioned as a 2-D

graphene sheet that is wrapped flush onto itself forming a cylindrical hollow tube with a 1 atom-thick wall. SWCNTs have the smallest diameter of all CNTs, typically ranging between 1-2 nm [10, 11] with the smallest recorded diameter of 0.4 nm [12]. A more complex type of a CNT is called a double-walled carbon nanotube (DWCNT) which has a second sheet of carbon wrapped around a SWCNT. The complexity of the CNT structure increases with an increasing number of tube layers, with the resulting structure called multi-walled carbon nanotubes (MWCNT), the diameters of which typically range from 5 to 20 nm and can be larger [10]. The distance between the two layers of graphene, or the wall-to-wall distance, has been shown to be ≈ 0.4 nm [13]. Overall, the number of CNT walls present is proportional to its total diameter.

As carbon atoms of a CNT are arranged in a hexagonal lattice this gives rise to a property called chirality. It manifests itself as an angle between the axis of the CNT and the orientation of the lattice. It is possible to estimate the diameter of the CNT by knowing its chirality, as the C-C bond length in graphene was determined to be 1.42 $\mathring{A}$. Furthermore, the knowledge of chirality allows to determine whether the SWCNT is metallic or semiconducting in nature. Typically, during synthesis, both types of SWCNTs are produced simultaneously with some cases being able to shift nearly all of the product either towards metallic (>90%) [14] or semiconducting (>95%) [15] CNTs. Chirality is less important for MWCNTs as it is highly likely that they are metallic, as having just a single metallic CNT will make them so. They have been shown to demonstrate excellent electrical and thermal conductivities, competing with copper and aluminium, with the current density upper limit of 10^9 A cm^{-2} [16], where no structural deterioration was observed. Peculiarly, it was found that the electrical resistance of a CNT without any defects is approximately 12.9 kΩ, regardless of its length [17].

Both, SWCNTs and MWCNTs have displayed extremely high on-axis thermal conductivity, with the former reaching 3180 Wm^{-1} K^{-1} [18] and the latter exhibiting 3500 Wm^{-1} K^{-1} at room temperature [19]. This is nearly twice as much that of natural diamonds and nearly 9 times greater than copper. It has been theorised that SWCNTs may be able to reach thermal conductivity of up to 6000 Wm^{-1} K^{-1} [20]. However, compared to their excellent on-axis performance the off-axis thermal conductivity is very low and has been measured to be 1.52 Wm^{-1} K^{-1} [21].

Mechanically, CNTs have extraordinary properties, when compared to conventional construction materials. According to theoretical calculations, a pristine CNT would have a Young's modulus of 1 TPa and tensile strength of over 100 GPa [22–24]. However, in practice, the reported values are noticeably lower, as even a small number of defects can have a significant impact on strength and performance [25]. Experimental values for tensile strength and elastic modulus of a single SWCNT have been found to be 60 GPa [26] and

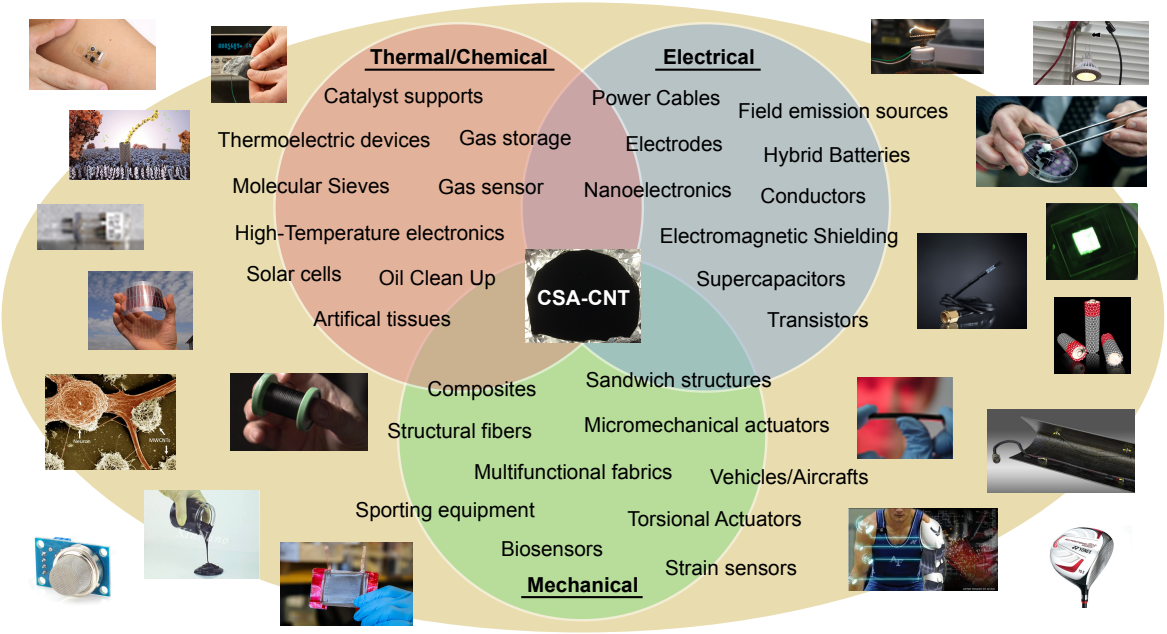

Fig. 1.1 Various applications of CNTs

915 GPa [27] respectively. The tensile strength of SWCNTs has shown dependence on their diameter and chirality with small diameter armchair CNTs displaying the highest amount. The tensile strength of MWCNTs has been measured to be between 11 to 63 GPa, which is nearly 100 times stronger than steel at fraction of the weight [28].

1.2 CNT applications

Due to their excellent performance across multiple metrics, CNTs find themselves applied in many research and industrial applications. Some of the major fields will now be briefly discussed, with the more detailed reviews provided in ref [29, 10]. One of the first large scale applications of MWCNTs was in the manufacturing of polymer composites. MWCNTs were added to function as an electrically conducting component. The high electrical conductivity of metallic CNTs, coupled with their low weight, allowed them to be used in electronics, electromagnetic shielding and the automotive sectors. With the help of their high thermal conductivity, their application would range from being used as small wires, capable of carrying high current loads without significant heating, to being incorporated into plastics to help and dissipate electrostatic charge [10]. Likewise, CNTs can be used as a conductive additive to composite materials, increasing their electrical conductivity with loadings as little as 0.01 wt%. This, along with CNTs mesoporous character and resilience has seen successful application of pure CNTs and their composites as an additive in the manufacture

of electrode components [30]. Conducting additives are often essential for electrodes as they drastically increase the cell's stability and longevity, particularly in high charge and discharge rate applications. In some cases, the presence of CNTs can double the cell's performance, by also acting as the electrode's binder [31]. Overall, the use of CNTs as an additive to battery active material has been successful enough to warrant their adoption in commercial devices [32, 33]. Additionally, CNTs have shown promise in capacitor applications. The capacitance of pure CNTs has been found to be average, ranging from 5 to 40 F/g [34], and it is strongly influenced by their microporosity. However, it can be drastically improved via mixing with either electrically conducting polymers such as polypyrrole (with capacitance up to 170 F/g) or with transition metal oxides such as MnO_2 (with capacitance up to 220 F/g) [30]. This makes them a competitive candidate for the manufacture of next-generation supercapacitors.

Due to their exceptional mechanical properties CNTs have been used as an addition to or a replacement for carbon fibre in next-generation structural composite materials. As they possess high strength and low mass they have been used in weight-sensitive fields such as space and aircraft, defence and automobile sectors. In addition, CNTs can be used as fillers that improve material damping without compromising the structural integrity and mechanical properties of composites [35]. Hence, such CNT enhanced materials have been used by sports equipment manufacturers in a variety of products, e.g., baseball bats, bicycle frames and tennis rackets [10]. During deformation CNT mats and fibres exhibit a significant amount of resistive forces from CNTs shearing past each other. This results in high toughness, allowing mats and fibres to be used in safety products such as body armour, crash barriers and vehicle crumple zones.

The large on-axis and small off-axis thermal conductivity CNT-based materials and be used as solid-state heat conductors. They can be implemented as a substitute for convective cooling, which traditionally uses liquid or gas, that otherwise would result in heavier or more complex systems. A simple heat pipe made out of CNT materials would make for a lightweight, effective cooling solution in electronics for components such as amplifiers and processors, that currently rely on heavier copper or vapour chamber solutions [10].

Additionally, CNTs may have unique applications which utilise the majority of their properties at once. For instance, CNTs can be incorporated into the electronics of a fighter pilot's helmet to improve conductivity while simultaneously providing structural integrity and weight reduction. Efforts have been made to manufacture CNT-based functional coatings and films that are electrically conductive and optically homogeneous [36]. These may be used in photovoltaics to create window solar panels, displays and touch-screen devices [10].

Overall, there is a plethora of applications and fields in which CNTs may be applied and provide a significant leap forward in technological advancement. With an increasing rate of their adoption, the demand for CNTs in varying forms and morphologies is likely to grow in the upcoming years. Therefore, it is important to develop CNT productions methods that would allow CNT synthesis in sufficiently high volume to meet the demand while providing a low cost and fine property/quality control in order to facilitate their wide adoption and application.

1.3 Existing methods of CNT Synthesis

Generally, there are three ingredients that are necessary for CNT growth: a carbon source, a catalyst and a high temperature environment. Catalysts can either be traditionally deposited on a substrate, resulting in a batch process or are suspended in a gas, resulting in floating catalyst chemical vapour deposition process (FC-CVD). Numerous techniques have been used to study the CNT growth during the batch process so the focus will be shifted towards the FC-CVD, as that is the process of interest for this thesis.

Currently, there are several well-developed processes of CNTs synthesis: pulsed laser vapourisation, arc discharge [37], flame synthesis and Chemical Vapour Deposition (CVD) [38], with their schematics shown in Fig.1.2. While the cost, complexity and the nature of the processes vary they share three common features: a high temperature environment, a carbon source and a catalyst precursor source. Catalysts typically consist of transition metals, with iron and nickel being highlighted as the most effective. Out of the two, nickel has been shown to be most effective of all, but iron is more commonly used since its precursor compounds are typically less toxic and are cheaper. CNTs can grow on the catalyst particles via two mechanisms: tangential or perpendicular growth. In tangential growth, the CNT walls begin tangent to the catalyst's surface, such that the CNT diameter matches the diameter of the catalyst particle. In contrast, perpendicular growth results in CNTs with a smaller diameter than the catalyst particle, such the alignment of the CNT walls to the comparatively broad catalyst particle surface becomes perpendicular.

1.3.1 Arc Discharge

The arc discharge was the first method by which CNTs were first discovered and produced by Iijima [4]. The apparatus consists of two pure graphite rods where one is used as anode and the other as a cathode, respectively. Electrodes are placed in a gas chamber, which is filled with a homogeneous gas at a target pressure prior to synthesis. A large amount of

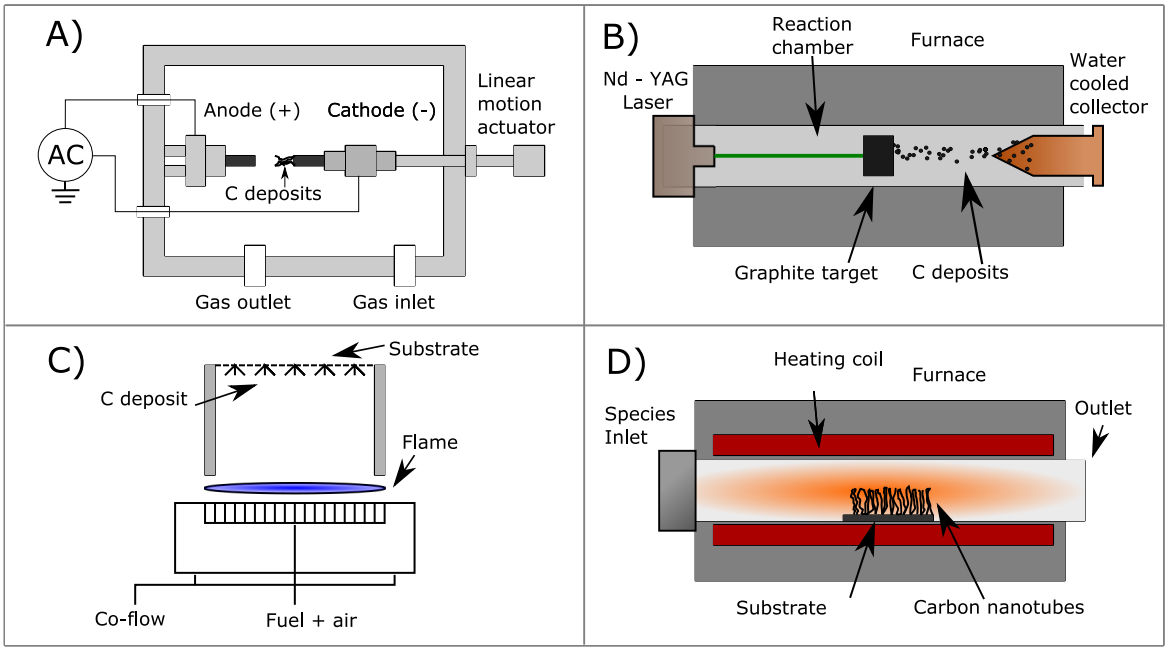

Fig. 1.2 Schematic of the mainstream methods of CNT synthesis a) arc discharge, b) pulsed laser vapourisation, c) flame synthesis, d) hot-wall chemical vapour decomposition

DC arc voltage is then applied to the electrodes, resulting in a discharge that evaporates carbon material from the anode. The resulted evaporated carbon consists mostly of fullerenes which permeate throughout the whole gas chamber. However, a small amount of CNTs gets deposited on the cathode. Doping the anode graphite rod with metal catalysts such as iron, nickel or cobalt, while keeping the cathode rod pure results in production of SWCNTs. It was found that gases containing hydrogen atoms, such as pure hydrogen [39, 40] or methane, led to more effective CNT production than the inert gases. The arc discharge method allows the production of highly crystalline CNTs with a low number of defects, but, their alignment is difficult to control [41]. Furthermore, mass production of CNTs is not feasible with this method and it has been limited to laboratory investigations.

1.3.2 Pulsed Laser Vapourisation

Pulsed laser vapourisation was initially developed by Smalley et al, for the synthesis of fullerenes, after which it was modified for production of SWCNTs [42] and MWCNTs [42]. In this method, the CNT synthesis occurs when a high power laser is used to vaporise carbon from a graphite target at high temperatures. In order to enable SCWNTs production, similar to arc discharge, the graphite target needs to be doped with metal catalyst particles. The properties of produced CNTs depend on multiple factors such as the amount and type of

catalysts [43], laser power and wavelength, environment temperature [44], pressure, type of inert gas and the fluid dynamics near the carbon target [45]. The vapourisation system consists of a quartz tube that is placed inside a furnace, that provides uniform temperature control. A graphite target is positioned in the centre of the tube with a laser source and a water-cooled collector being placed on opposite sides of the tube respectively. Typical laser sources are Nd:YAG or CO_2 lasers [41]. A flow system is connected to the quartz tube for the inert gas injection. The laser gets focused onto a carbon target, which typically consists of 1.2 % of metal catalyst with 98.8% of carbon composite under an argon atmosphere (of 500 Torr) brought to 1200°C [46]. Carbon material gets vapourised under intense localised heating from the laser and CNTs are self-assembled, which are then carried by the argon gas and condense onto the water-cooled collector. The major advantage of laser vapourisation over arc discharge is its ability to produce highly-crystalline SWCNTs with high purity (up to 90%) with a very narrow distribution of diameters (1.0-1.6 nm). The disadvantage of this method is once again limited productivity and costs associated with energy intensity, making it an unfavourable industrial production process for large scale CNT growth.

1.3.3 Flame synthesis

Flame synthesis has become a popular method for the production of nanomaterials which include such commercial products as carbon blacks, printing ink, fumed silica, titanium dioxide pigments and lithium-ion batteries cathode manufacture. The existence of MWCNTs was first discovered in flames by Howard, in which MWCTNs were formed along with soot particles during synthesis using premixed hydrocarbon flames in low-pressure chambers [47]. Since then, numerous flame configurations have been developed and employed for the synthesis of CNTs with different properties [48, 49]. Flame synthesis systems typically consist of a premixed or a diffusion flame burner with a gas supply system that delivers the reactants. Both types of burners have been used for CNT synthesis. Regardless of the burner choice, an appropriate carbon source must be provided to the system to generate gas-phase carbon species necessary for CNT growth. The stable heat source provided by the direct combustion of flammable mixtures results in catalytic precursor decomposition and the subsequent formation of the catalyst nanoparticles. The catalyst nanoparticles are then activated in the flame where the formation of the solid graphitic layers is initiated due to the high temperature environment [49]. This promotes CNT growth on the surface of the metal nanoparticles which are either supported by a metal alloy substrate [50] or are suspended in gas [51].

While flame synthesis has been successfully used to produce well-controlled nanostructured materials of high purity and narrow size distribution on a commercial scale [48] its

application towards CNT mass production has yet to be successful, as the mechanisms of CNT synthesis have not been fully understood. Difficulties arise from the presence of the flame medium, which facilitates in formation of abundance of intermediate radicals such as polycyclic aromatic hydrocarbons [52], which make the investigations of the synthesis challenging and decrease the quality of the final product. Furthermore, the collection of the CNTs relies on thermophoresis or filter capture, making material manufacture on a larger scale quite challenging.

1.3.4 Chemical Vapour deposition

It became clear that, in order to address and meet the growing demand for high-quality CNTs, additional methods for large scale CNT production needed to be developed. Chemical vapour deposition (CVD), has proven its capabilities of producing CNTs with controllable morphology and properties in large quantities [53, 10]. It is regarded as the most popular and probably the simplest way to grow CNTs in a laboratory and semi-pilot scales. The main components that determine the properties of the produced CNTs via CVD synthesis are: the content and size of the metal catalyst provided, the process temperature, the pressure inside the chamber and the nature of the gaseous hydrocarbon compound. Over decades, various variants of the CVD method have been developed, for instance, fixed bed [54], fluidized bed [55], floating catalyst [53] and even plasma-enhanced [56] CVD methods that address different aspects of CNT production such as synthesis of high-quality materials, manufacture of coating and films, and large scale, continuous production respectively.

The discussion will now focus on the two most popular types of CVD methods that are used for large scale CNT production.

Substrate Based Fixed-Bed reaction

Historically, CNTs have been grown on substrates placed within the reactor. Prior to reaction, the substrates are embedded with catalyst particles, typically consisting of Ni, Fe and Co, that are either pre-manufactured and then deposited onto the substrate [57] or are formed on the substrate itself [11]. A hydrocarbon source in the gas phase is fed into a reactor tube and is subjected to heat from an energy source such as plasma or a resistively heated coil, in order to transfer energy to the gaseous carbon molecules. Simple hydrocarbons such as methane, carbon monoxide and acetylene are commonly used as the carbon sources. The hydrocarbons are carried by a buffer gas into the reactor tube that has been heated to the target temperature at which the hydrogen-carbon bonds break, producing pure carbon molecules.

Carbon diffuses towards the heated substrate to which it binds. CNT growth then takes place, provided all of the other synthesis conditions are maintained.

Substrate growth is often referred to as carpet or forest growth as the produced CNTs are typically tightly-packed and are vertically-aligned resembling trees in a forest. This process has been thoroughly investigated and synthesis conditions can be finely controlled to tailor the CNT properties resulting in a very high quality, high purity product. CNTs synthesised via substrate growth are produced via the root growth mechanism where the catalyst particle remains fixed to the substrate and carbon mass is added to the CNT at its base. This makes the penetration of additional gaseous carbon through the dense 'forest' of CNTs difficult and can result in diffusion-limited growth that can restrict the maximum growth rate between 0.2 and 17 μm s^{-1}. Additionally, due to CNTs anchoring to the substrate there is an inherent difficulty in removal of CNTs from the fixed substrate, which could cause damage to the final product. Furthermore, substrate-based growth is a non-continuous process and, therefore, is not ideal for very large-scale CNT production. Instead, a better-suited process would consist of continuous synthesis that is not limited by low carbon diffusion and is able to increase the CNT production rate to the point of availability and cost that are suitable for their widespread application.

Floating Catalyst Chemical Vapour deposition Method

The floating catalyst chemical vapour deposition method (FC-CVD) overcomes many of the limitations associated with the substrate growth synthesis due to its continuous nature. It is the primary process by which mass production of CNTs is currently achieved. This method is controllable, cost-effective and has great industrial scalability [58] while permitting continuous CNT production with direct extraction from the reactor [53]. In the FC-CVD, the catalyst precursors are suspended in the carrier gas and travel through a reactor that is placed in a furnace or some heating medium, rather than being fixed to a substrate. A gaseous carbon source is simultaneously introduced into the reactor. As the gaseous mixture travels downstream of the reactor the catalysts precursor vapourize first, followed shortly by decomposition of the carbon source. As the result, catalyst particles are exposed to an abundant amount of gaseous carbon atmosphere where the diffusion is fast. As renucleation of the catalyst occurs, CNT growth takes place at rates of at least several μm s^{-1} and on some occasions has been estimated to exceed 100 μm s^{-1}. This results in continuous production of CNTs on a large scale, which can be increased by increasing the reactor dimensions or reactant flow rates. When compared to the corresponding substrate-based methods FC-CVD requires fewer reaction steps as CNTs are not anchored to anything apart from the host catalyst particle.

1.4 Aerogel formation

Depending on the version of FC-CVD process, multiple unique macroscopic structures can be created. The process of interest for this thesis is called the Windle process in which CNTs are grown in a hot-wall reactor at sufficient length and number concentration that they self-assemble into a continuous CNT network known as the 'aerogel'. The aerogel can be consistently extracted from the back end of the horizontal [59] or vertical reactor and be wound onto a motorised bobbin to produce fibres or mats. This results in bulk CNT materials that can be produced in a single-step process. The Windle process has the potential to be highly scalable as it has been shown to work with precursor input rates ranging in three orders of magnitude. The aerogel formation occurs in three stages: catalysts particle production, CNT growth, and agglomeration. For successful aerogel formation CNTs need to grow to the maximum possible length within the relatively short residence times of tens of seconds. To achieve that, the use of effective catalysts must be employed, with the most common being iron (that comes from ferrocene [60] or pentacarbonyl [61]), with the others being cobalt and nickel. Catalysts are introduced via sublimation of vapourisation of these metal-containing precursors. A small abundance of a promoter compound, which consists of elements from group 16 in the periodic table, is necessary for the success of direct-spun process. Sulphur is the most commonly used promoter, that gets introduced via precursors such as thiophene [62, 63, 59], whose role will be discussed shortly. Selenium and tellurium have also been used as substitutions for thiophene in the form of selenophene and tellurophene respectively. Both the catalyst and the promoter precursors may be delivered into the system by a carrier gas that can be a mixture of Ar, He, N_2 - H_2 along with pure H_2 [64], N_2 [65] and Ar [66].

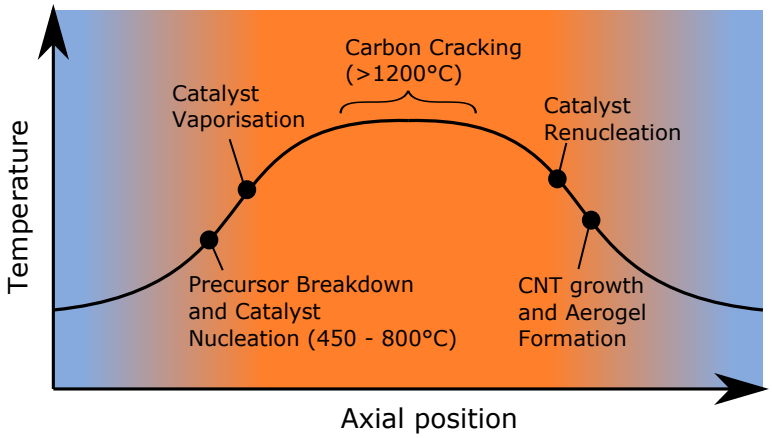

Fig. 1.3 Schematic of Windle process

The stages of the Windle process are shown in Fig. 1.3 which represent the evolution of the reactants in a hot-wall furnace with a typical temperature profile that is a function of the axial displacement along the reactor. Taking the most commonly used elements, the precursor materials enter the hot zone of the reactor and decompose, producing a vapour of iron and sulphur nanoparticles. As the vapour pressure reaches saturation, the nanoparticles begin to nucleate. A small amount of CNTs begins to grow on the particles, however as this molecular complex moves further into the hotter zone of the furnace the CNTs vapourise. As the reactant gases pass through the peak of the furnace's temperature profile they begin to cool and the particles begin to renucleate. This makes the Windle process independent of the initial input size distributions of the precursor and catalyst compounds as all the particles evaporate and renucleate. Instead, the only crucial parameter that governs the success of aerogel formation is the mass concentration of the catalyst material entering the reactor. Presence of sulphur in the catalyst chemistry increases the onset of renucleation, making the catalysts particles available earlier upstream and hence allowing for CNT growth to occur for longer and at a higher temperature. It is also believed that sulphur increases the surface carbon mobility on the catalysts by lowering the surface tension of iron.

The second stage of the process begins when carbon becomes available for CNT growth. This can either be induced by physically introducing carbon at this stage or through the pyrolysis of carbon-containing compounds that were injected along with catalyst material. Gaseous phase carbon atoms get absorbed by the catalyst particles. When the absorption saturation point is reached carbon atoms begin to precipitate and form CNTs on the surfaces of their host catalyst nanoparticles [67]. A wide plethora of carbon sources have been used in Windle process including, but not limited to, methane, toluene and xylene in addition to alcohols such, ethanol, propanol and other oxygen-containing compounds such as diethyl ether, ethylene glycol, and acetone.

In the Windle process, it is beneficial for the molecules to react catalytically on the surface of the particles instead of decomposing thermally. This poses a restriction on the reactor temperature such that it should be sufficient enough to maintain catalytic breakdown yet avoid thermal decomposition of the molecules. Typical peak furnace temperature range for the Windle process is between 1100 and 1450°C. Thermal decomposition leads to the production of amorphous carbon and soot. These materials make little contribution towards the properties of aerogel yet can substantially increase its mass. Despite the effectiveness of iron catalysts, CNT growth has been found to occur only on a small fraction of the generated catalyst particles. This leads to many of these unused catalyst particles being contained in the produced CNT fibres. Furthermore, the conversion rate of carbon ranges from 1 to 10 % (while the conversion rates for the industrial processes have been reported to be as high

as 60 to 80 %). In addition, there is a compromise between the increase of the carbon yield and decrease of the quality of produced CNT material, which manifests in higher amorphous carbon fraction. One of the key areas of CNT synthesis research, along with increasing the yield, is the increase of the reaction density, which would lead to the increase of the production rate while maintaining a high-quality end product.

The third stage of the process begins when the collision frequency of CNTs increases as they get longer and more numerous. A collision between two CNTs results in their reorientation and alignment due to van der Waals forces attempting to reduce the surface energy of the system. This reorientation process continues as additional CNTs collide, resulting in formation of CNT bundles. With each addition of a CNT the bundle becomes stiffer and more massive. Therefore, if two large bundles collide, they would not be able to reorient before an additional collision occurs, resulting in a network of bundles, which ultimately forms into aerogel. The aerogel typically forms at a specific radius within the reactor tube [68], however, currently, there is no consensus on the origin of this phenomenon. From that point, it can then be removed continuously from the exit of the reactor and wound directly onto a motorised bobbin to form a mat. Alternatively, the aerogel can be condensed by spraying volatile liquids such as acetone, which would evaporate and condense the CNTs into a fibre via capillary forces. Both methods of aerogel collection can be carried out immediately upon its exit from the reactor and the process can operate indefinitely. This makes Windle process appealing not only because it is continuous but it is able to produce a product that is directly self-assembled into a useful macroscopic structure, which is a particular advantage as some CNT applications may only be possible with pre-formed material. Performance of the aerogel material in metrics of interest such as thermal and electrical conductivities, elasticity, and tensile strength is either on par or surpasses the values of conventional materials, such as copper and aluminium, or the substrate-grown CNT mats and fibres. A detailed overview of aerogel performance is provided in the following article [69].

1.5 Characterisation of CNTs and synthesis methods

At present, a wide array of *ex situ* diagnostic techniques is necessary to characterise produced CNTs as no single method can provide the majority of the required information. Properties such as purity of the product (i.e the amount of non-carbonous materials present in the CNTs), the chirality of CNTs, presence of functional groups, bundle alignment in the fibres and mats, the crystallinity of CNT walls and their number are some of the typical metrics used to classify the synthesised product.

The most commonly occurring techniques in literature used for the analysis of solid-state samples are as follows. Scanning and Transmission Electron microscopy (SEM, TEM) is widely used to measure the lengths and diameters of CNT bundles along with determining the presence of SWCNT, double-wall CNTs (DWCNTs) and MWCNTs in the sample and their respective ratios. X-ray based techniques such as Small and Wide-angle elastic scattering can determine CNTs anisotropy and sample purity, while X-ray diffraction has been used to analyse the crystal structure [70]. Raman spectroscopy is frequently used to determine the crystalline quality and purity of the CNTs by examining the ratio of the distinctive Defect (D) and Graphitic (G) mode intensities. In addition, Raman is able to detect the existence and diameter of SWCNTs in the sample, identified by the presence of Radial breathing modes. Coupled with the use of Kataura plots the metallic or semiconducting nature of CNTs can be determined, along with their chirality. X-ray photoelectron spectroscopy has been employed to analyse the elemental surface composition of CNTs along with identifying the attached functional groups [71]. Lastly, thermogravimetric analysis (TGA) is frequently utilised to measure process yield and carbon conversion. The method is able to determine the masses of CNTs, amorphous carbon and other metal content present in the sample.

While there is a suite of sufficiently developed methods available for CNT product analysis there exists a severe lack of *in situ* techniques or attempts that have been aimed at the study of the direct-spinning process itself. More precisely, to the author's knowledge, there have been no publications demonstrating any *in situ*, non-invasive optical measurements of CNT synthesis via FC-CVD, leading to a lack of thorough chemical analysis of the process that is currently observed in the field. The difficulty of probe or optical access remains one of the main issues in the implementation of said techniques, as synthesis is carried out predominantly in cylindrical furnaces. Major modifications to the reactor tube or freezing the reaction could enable these measurements, however, this is associated with difficult engineering challenges. This places a great obstacle in the way of studying the species distribution and the formation mechanisms of CNTs in the tube reactor during FC-CVD. As consequence, the finer details of the synthesis process, such as underlying chemical reactions, nucleation and agglomeration mechanisms of CNT aerogel formation are still not well understood. The investigations currently proceed on a semi-empirical basis [72–74], by varying various synthesis parameters such as reactant stoichiometry, furnace temperature, residence time and reactor dimensions, and observing how that affects the final product characteristics, by performing *ex situ* diagnostics and analysis. In particular, quantitative results rely on manual collection and weighing of the CNT mats and fibres to determine the product yield. While some reactants are either in gaseous form, with their amount monitored by mass flow controllers, or are liquid and may be sprayed into the lines using pumps,

the most popular catalyst and precursor (ferrocene and thiophene) may be delivered into the system by gas sublimation. Therefore to determine precise amount delivered into the system their vessels need to be removed from the setup and weighed, which is a crude and time-consuming process. Some in-line dynamic precursor concentration measurements of the reactants have been performed using FTIR prior to their injection into the furnace [75], however, this technique is insensitive to simple diatomic molecules, making its application situational.

Having said that, a number of *in situ* invasive techniques have utilised to study the Windle process. The axial and radial temperature profiles are typically measured with the use of thermocouples. Hoecker et al. have used a probe to perform *in situ* axial measurement of catalyst particle size distributions along the centre-line of the reactor as a function of furnace set-temperature using a Scanning mobility particle sizer [59]. In addition, they have used a commercially available Fourier Transform Infrared spectrometer to analyse the exhaust gases and study the decomposition of thiophene and ferrocene as a function of furnace set-temperature. In later work, Hoecker et al. used alumina circular filters to perform axial measurements of aerogel formation as a function of hydrocarbon source by examining accumulated mass on the filters [76]. While these techniques are able to provide some information on the underlying processes of the aerogel synthesis, they fail to detect intermediate species and, due to their invasive nature, may have an effect on the chemistry. Furthermore, the inability of 'freezing' samples at their formation temperature may result in misleading conclusions.

1.6 Selection of technique for optical diagnostics of FC-CVD

Application of *in situ* optical diagnostics techniques for the study of reacting flows has been an active area of research for a number of decades. In particular, the diagnostics have been applied in a number of environments similar to the FC-CVD reactors such as turbines, combustors and substrate-based CVD systems [77–79]. A plethora of *in situ* optical diagnostic techniques have been applied to study properties and formation of CNTs produced by substrate-growth [80–82], accompanied by appropriate reactor modifications for their realisation. These include X-ray photoelectron spectroscopy [83], optical emission spectroscopy [84], pyrometry [85], laser absorption [86, 87], optical microscopy [88, 89] and Raman spectroscopy [90, 91]. The investigations focused on measurements of CNT properties, such as rate of growth, length and presence of functional groups. However,

all of the techniques were performed on a sample present in a solid phase, which provide high signal magnitudes in a low background environment, which is not representative of spectroscopic conditions encountered in a FC-CVD system.

In contrast, combustors and turbines typically include reactants in gaseous phase present in a high temperature environment. Thus, optical techniques which are commonly employed for their diagnostics should be applicable for the analysis of FC-CVD systems. The main focus for the FC-CVD investigation is the quantification of the reagent and product amounts, in particular hydrogen, ferrocene, thiophene and the hydrocarbon source, as the function of the reactor parameters. Therefore, only the techniques which are capable of performing multispecies analysis will be included in the discussion.

The three most common techniques which fit this criterion are IR absorption spectroscopy, laser induced fluorescence and Raman spectroscopy. Near and mid-IR spectroscopy produces the largest amount of signal per same laser energy, however, it is not sensitive to homonuclear molecules such as hydrogen, which are key chemical components in the CNT synthesis [92]. Laser induced fluorescence (LIF) provides broad spectra that do not contain detailed information about specific species and is typically used for mapping out distributions of OH radicals and polycyclic aromatic hydrocarbons [93]. Raman spectroscopy has been used to provide point-wise and line of sight, temporal and spacial molar fraction species distribution and temperature measurements [94–96]. However, Raman scattering suffers from poor efficiency which results in very low signal magnitude [97]. Therefore, high-power lasers are commonly used to overcome this difficulty, which can be quite expensive [98]. Alternatively, Coherent anti-Stokes Raman spectroscopy has been employed in predominantly combusting flows to further increase the signal to noise ratio of Raman emission [99–101]. This technique requires the use of three lasers at different wavelengths, which creates a severe entry barrier to its application. Furthermore, while the signal improvement is significant, the need in fine-tuning of the laser wavelengths to image a molecule of interest limits the number of species that the system can detect simultaneously. Moreover, the system possesses a large footprint and the configuration of beam crossing may result in difficulty of laser injection into a FC-CVD system.

However, compared to other reviewed techniques, Raman spectroscopy offers significantly more information per shot with the potential for a high acquisition rate. Therefore, Raman spectroscopy was selected as the base process for development and implementation for the investigation of CNT-aerogel synthesis process via FC-CVD.

1.7 Aims and objectives

The main goal of the presented research is the development and application of a Raman-based technique, capable of performing non-intrusive *in situ* on-the-fly diagnostics of CNT-aerogel synthesis process parameters in a FC-CVD reactor. In particular, the technique should be able to determine the chemical reactions and species formed at aerogel-spinning conditions within the reactor. Furthermore, the system should be able to determine and provide qualitative data of the evolution of reactants and products inside the reactor, as a function of synthesis parameters.

A bespoke FC-CVD reactor should be engineered, capable of providing constant optical access without affecting the key characteristics necessary for CNT formation, such as temperature and velocity profiles.

An appropriate data post-processing procedure should be developed to allow proper interpretation and implementation of the collected data in the growing number of models that aim to describe direct-spinning process.

1.8 Thesis Structure

Chapter 1 summarises the background of CNTs, their structure, properties, and current applications. Various commercial methods of CNT production are reviewed with an emphasis on the Floating catalyst chemical vapour deposition method for continuous CNT synthesis. Application of various diagnostic techniques of CNTs and CNT synthesis process have been discussed.

Chapters 2 describes the theory of spontaneous Raman scattering. Comparison is made between continuous wave (CW) and pulsed laser excited Raman emission. Lifetimes of various competitive spectroscopic processes in a reacting flow are discussed. A model for spontaneous Raman emission by continuous wave laser is introduced. Operating principles of Cavity Enhanced Raman spectroscopy (CERS) are discussed. A model for Cavity-enhanced Raman emission is developed.

Chapter 3 introduces technical aspects of the CW and CERS-based setups. Theoretical and experimental compassion of the two techniques is provided.

Chapter 4 discusses the requirements necessary for the successful implementation of Raman spectroscopy in a FC-CVD reactor. The development and optimisation of the emission and collection parts of the pulsed laser Raman spectroscopy setup are presented on a flat flame.

Chapter 5 introduces the bespoke design of the FC-CVD reactor capable of providing continuous optical access. Raman spectra of single molecules of interest are discussed.

Chapter 6 discusses the developed Ansys Fluent-based model and highlights the results of numerical investigations of the flow patterns and chemical species distributions within the reactor.

Chapter 7 demonstrates the calibration procedure of the developed pulsed laser Raman setup which serves as the basis for quantitative data analysis procedure. Methodologies for the *in situ* gas temperature measurements by Raman spectroscopy are presented. Raman-based quantitative measurements of thiophene decomposition in a hydrogen environment are demonstrated. Qualitative *in situ* investigation of ferrocene decomposition and CNT synthesis via FC-CVD process are shown.

Chapter 8 presents a summary of the thesis and lays out plans for the future fork on the further development of pulsed laser Raman setup and the reactor in application to CNT synthesis via FC-CVD.

Chapter 2

Theory of Spontaneous and CERS Raman scattering

This chapter introduces the theory of Spontaneous Raman scattering generated by both continuous wave and pulsed laser excitation radiation. Comparison of cross-sections and lifetimes of competing spectroscopic processes encountered in a reacting flow is provided. A comprehensive model is developed for the calculation of the expected number of Stokes photons from a continuous wave laser setup. Afterwards, the operating principles of cavity-enhanced Raman spectroscopy are discussed. Furthermore, a thorough procedure is outlined for the assembly of a linear optical resonator with high reflectively mirrors, a key component of CERS setup, aimed at the amplification of Raman emission. This is accompanied by the derivation of a model which predicts the expected number of Stokes photons from a CERS setup.

2.1 Introduction to Raman scattering

2.1.1 Basic principles

Raman spectroscopy, named after Sir C. V Raman who first observed the effect in 1928 [102], is able to provide information about molecular vibrational, rotational and other characteristic chemical bond modes in the system, that can be used for sample identification and quantification [103]. This effect involves a source of a monochromatic light, such as a laser, that is incident on of the species of interest. The electromagnetic radiation interacts with the molecule's polarisable electron orbitals and bonds, and scatters off the molecule. Most of the radiation (nearly 99%) is scattered elastically giving rise to Rayleigh scattering, yet a small

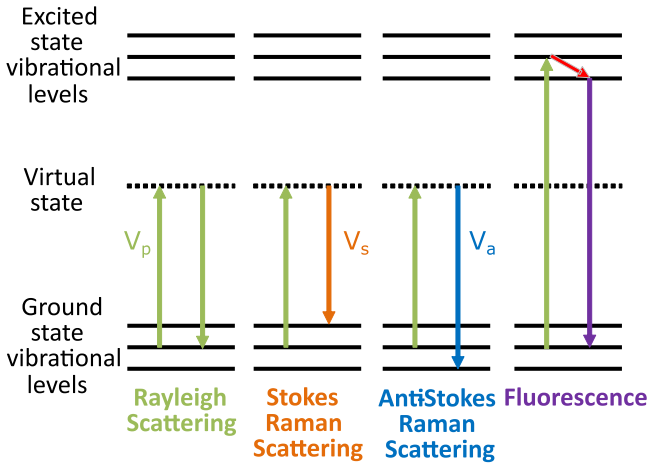

Fig. 2.1 Energy diagrams for Raman and Fluorescence processes.

fraction of the incident light is scattered inelastically, resulting in the shift in energy from the laser frequency due to the molecular interaction.

The incident photon excites the molecule in either the ground or the excited rovibronic state, which is a superposition of rotational and vibrational energy levels within an electronic state. The excitation places the molecule into a virtual energy state for a period of time on the order of femtoseconds, after which the photon scatters inelastically, as shown in Fig. 2.1. Following the photon interaction, the molecule rests in a different rotational or vibrational state. The difference in energy between the initial and final rovibronic states causes the scattered photon's wavelength to deviate from the incident wavelength. In order for the total energy of the system to remain constant, after a molecule has moved to a new rovibronic state, the scattered photon shifts to a different energy, where the energy difference is equal to the energy between the initial and final rovibronic states of the molecule. Depending on whether the final state is at higher or lower energy than the initial state, the shift in wavelength of the scattered photon is called Stokes or anti-Stokes Respectively. This shift in energy is known as the Raman shift, given by

$$E_{S/AS} = 10^2 hc(\nu_p - \nu_{S/AS}) \tag{2.1}$$

where h is Planck's constant, c is the speed of light, ν_p is the wavenumber of the incident radiation and $\nu_{S/AS}$ are Stokes and anti-Stokes emission wavenumbers respectively. At room temperature, the magnitude of a Stokes mode, which is of lower frequency and energy, is typically larger than the magnitude of an anti-Stokes mode as the molecular population of a species is predominantly located in the ground state. Therefore, transitions from higher to lower energy states are less likely.

The rovibronic modes are unique to each molecule, allowing the sensing of a molecular 'finger-print' that is dependent on the molecular geometry and chemical makeup, associated with the differential Raman scattering cross-section (area per unit collection solid angle) [104]

$$\left(\frac{d\sigma}{d\Omega}\right) = \frac{10^6 h(\nu_p - \nu_s)^4}{360\varepsilon_0^2 \nu_s \left(1 - \exp\left(-\frac{10^2 hc\nu_s}{k_b T}\right)\right)} g(45\alpha^2 + 7\gamma^2) \tag{2.2}$$

where k_b is Boltzman's constant, T is temperature of species' environment, ε_0 is permittivity of free space, $g(45\alpha^2 + 7\gamma^2)$ is the *scattering activity*, α^2 and γ^2 are the isotropic and anisotropic parts (in $C^2m^4V^{-2}$, in SI units) of the polarisability tensor and g is the degeneracy of Raman modes. Raman transitions depend on the molecular polarisability, not on its electric dipole moment. This allows homonuclear molecules like N_2 and H_2, which have zero dipole moments, to exhibit Raman emission, as their polarisability is non-zero [105].

The Raman cross-section for anti-Stokes emission has the same expression as Eq. 2.2 except with plus sign in front of the exponential inside the brackets of the fraction.

It can prove difficult to calculate precise differential scattering cross-section for each species of interest as the necessary values, such as scattering activity and polarisabilities, for each molecule may not be known or are difficult to obtain. The wavelength-dependent differential Raman scattering cross-section value, however, can be calculated by [1]

$$\frac{\mathrm{d}\sigma}{\mathrm{d}\Omega} = A\left(\frac{\nu_S^2}{\nu_i^2 - \nu_p^2}\right)^2 \tag{2.3}$$

where A and ν_i are fitting parameters. Equation 2.3 highlights the dependence of differential Raman scattering cross-section on excitation laser wavelength, $\propto \lambda^4$, where shorter lasing wavelengths result in higher cross-section values.

Table 2.1 shows differential Raman scattering cross-section values for some species of interest involved in CNT synthesis study, calculated by Eq. 2.3, including corresponding fitting parameters. The differential Raman scattering cross-section values of the listed species are within the same order of magnitude, therefore their major signatures would be observed simultaneously at the same excitation laser power.

Table 2.1 Raman scattering parameters and differential cross-sections of species of interest involved in CNT growth. Cross-section values calculated at 532 nm incident radiation and at room temperature (T = 293.15 K) and atmospheric pressure [1].

Molecule	ν_p-$\nu_{S/AS}$ (cm^{-1})	A($\times 10^{-28}$) (cm^2 sr^{-1})	$v_i(\times 10^4)$ (cm^{-1})	$d\sigma/d\Omega(\times 10^{-35})$ (m^2 sr^{-1})
N_2	2331	3.02	8.95	3.79
O_2	1555	0.459	5.69	4.88
CH_4	2986	10.4	7.23	27.36
H_2	4155	8,74	8.48	8.59

2.1.2 Comparison with competitive spectroscopic processes in reacting flows

A major downside of Raman spectroscopy is its low cross-sectional value when compared to other techniques, such as shown in Table 2.2. Moreover, Raman cross-sections for gaseous species are two orders of magnitude lower than cross-sections of solid phase samples.

Table 2.2 Approximate order of magnitude for cross-sections σ (per molecule) for various possible processes in spectroscopy [2].

Process	Cross-section	σ/cm^2
Absorption	Infrared	10^{-21}
Emission	Fluorescence	10^{-19}
Scattering	Raman scattering solid phase	10^{-29}
Scattering	Raman scattering gas phase	10^{-31}

Therefore, promising gas phase Raman detection schemes have been developed, based on the stimulated Raman methods such as coherent anti-Stokes Raman spectroscopy (CARS) [106] and photoacoustic stimulated Raman spectroscopy (PARS) [107], that increase signal magnitude with the introduction of setup complexity and cost.

Raman signal intensities I_r scale linearly with the incoming laser power I_e as follows [108]:

$$dI_r \propto I_e \, d\Omega \tag{2.4}$$

Alternatively, the problem of the intrinsically low sensitivity of spontaneous Raman spectroscopy can be overcome with the use of higher power lasers. The employed lasers must have a narrow linewidth, as that allows to concentrate the laser power in frequency space, resulting in a narrower Raman mode and, therefore, better signal to noise ratio (SNR).

A continuous-wave (CW) laser with high power would be a suitable fit, however, they are quite costly. An alternative approach is to place a Raman cell inside the laser resonator, together with the gain medium. Such configuration allows to utilise the effective high laser power, circulating within the laser resonator, to generate stronger Raman emission, effectively creating a intracavity laser Raman spectrometer [109]. This set-up, however, is challenging to construct.

Modified pulsed lasers, with longer pulse lengths, are also commonly implemented, as typical short-pulsed lasers with a pulse length of 5-10 ns suffer from broad linewidths. Furthermore, great care needs to be taken during their operation, to ensure that the laser irradiance is below the optical breakdown threshold of 34 $GWcm^{-1}$ [110], in order to avoid sample degradation and prevent the formation of localised plasma. This can be achieved with longer pulse lengths, on the order of hundreds of nanoseconds, that have an additional benefit of narrowing the lasing linewidth [97]. The pulse length of a short-pulsed laser can be increased by either using a pulse stretcher consisting of delay loops placed at the exit of the laser source [111] or with the use of a lengthened oscillator.

Reacting flow systems, the ones of interest to this project such as reactors or flames may produce strong background emissions which can make Raman detection challenging or even impossible in some spectral ranges [112, 113]. Consider a flame as an example of an optically challenging system. Prior to the introduction of laser excitation emission, the flame would give off spectroscopic signatures such as blackbody radiation due to heat and particulates [114], incandescence due to particles moving within the material and chemiluminescence, which arises from excited radicals such as OH* and CH*. All of the above emissions would produce a uniform background, the majority of which can be minimised by background spectra subtraction.

Consider a CW-based system, where a 10W Argon ion laser would result in a Raman scattered power of about 10^{-11} W/sr over a centimetre pathlength, from nitrogen present in a flame at atmospheric pressure and temperature of 2000 K [115]. The background luminosity from such an environment will exceed the spontaneous Raman signal produced by high power, CW laser by at least an order of magnitude [115], resulting in the requirement to use pulsed laser sources.

With the introduction of the pulsed laser, about 99 % of incoming laser power would produce Rayleigh scattering. As previously stated, spontaneous Raman scattering is a very weak process that results in a collected Raman to laser energy ratio of approximately 10^{-14} in high temperature reacting systems. However, Raman scattering has a lifetime of 10^{-12} s or less, making it essentially an instantaneously occurring process. The majority of the remaining energy will manifest as either fluorescence or phosphorescence, which have

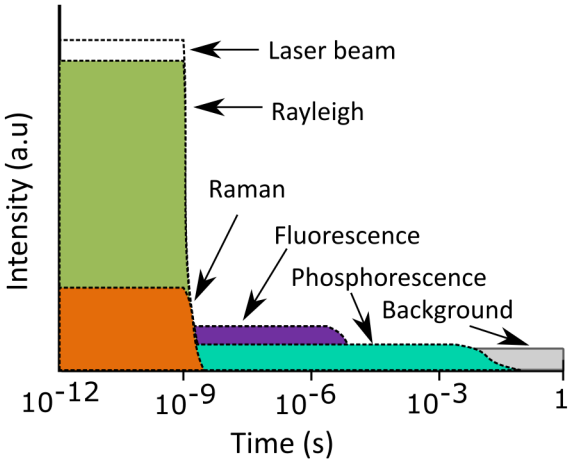

Fig. 2.2 Lifetimes of spectroscopic processes from pulsed excitation.

lifetimes of 10^{-10} to 10^{-5} and 10^{-4} seconds respectively. Figure 2.2 shows a schematic of lifetimes of spectroscopic processes present in the flame which occur as a result of excitation by a 300 ns laser. While fluorescence is a diagnostics technique of interest in combustion, as its species-specific, it can create a lot of interference with Raman signal as its cross-section is generally many orders of magnitudes larger [115], as shown in Table. 2.2. Therefore, fast temporal gating and shuttering have to be employed in order to increase the SNR of a collected Raman signal, remove interference and provide high quality quantitative data in a flame system [116].

The system of interest for this project consisted of an FC-CVD reactor. Even though it is a reacting flow system, it was anticipated to be a much less luminous environment when compared to a flame. The amount of carbon present in the gas phase and the CNT synthesis temperatures in a FC-CVD reactor are low enough to not induce incandescence. Furthermore, the correct choice of lasing wavelength, around 532 nm, provides an optimum compromise between sufficiently large Raman scattering cross-section in the visible range and limited generation of interferences from LIF of complex hydrocarbons such as polycyclic aromatics in fuel-rich flames [113, 117]. With the account of significant differences between a flame and a FC-CVD systems, a cost-effective, high resolution Raman spectroscopy method, based on CW emission called cavity-enhanced Raman spectroscopy, was first adopted for purposes of developing a setup capable of performing gas phase Raman Spectroscopy inside a FC-CVD reactor. The operating principles of CERS are discussed later in the chapter.

2.2 Spontaneous Raman Scattering Model

A model for spontaneous Raman spectroscopy due to CW laser emission was derived to allow evaluation of performance and enhancement of the Raman signal by CERS method. The model describes a system that consists of a CW laser-focused to a point in space, with Raman emission collected from laser focus at 90 degrees to the axis of beam propagation.

A detailed calculation of the rate of emission of Stokes photons can be found in [118, 119]. The rate of change of the scattered free space Stokes photons can be given as a balance of the pump and Stokes processes between the ground and virtual states

$$\frac{\mathrm{d}n_S}{\mathrm{d}t} = \frac{C_f}{\tau_0} n_p - \frac{1}{\tau_0} n_S \tag{2.5}$$

where n_S is the number of scattered Stokes photons, n_p is the number of pump photons, C_f is a multiplier constant for free space, and τ_0 is the lifetime of the free space Stokes photons. The latter is given by

$$\frac{1}{\tau_0} = \frac{8\pi c}{3} \frac{\lambda_S}{\lambda_p} N \frac{\mathrm{d}\sigma}{\mathrm{d}\Omega} \tag{2.6}$$

where c is the speed of light, N is the number of particles per unit volume, λ_p and λ_S are the pump and Stokes wavelengths, and $\mathrm{d}\sigma/\mathrm{d}\Omega$ is the differential Raman scattering cross-section (see Eq. 2.3). The free space factor, C_f, is given by

$$C_f = \frac{3}{8\pi^2} \left(\frac{\lambda_S}{n}\right)^3 \frac{1}{V_{\mathrm{eff}}^{(f)}} \frac{\nu_S}{\Delta\nu_S^{(f)}} \tag{2.7}$$

where n is the index of refraction and $\Delta\nu_S^{(f)}$ is the free space Stokes linewidth. The free space effective volume, $V_{\mathrm{eff}}^{(f)}$, which assumes a perfect overlap of the Gaussian beam waist with the collection solid angle that are perpendicular to each other, is given by [120]

$$V_{\mathrm{eff}}^{(f)} = \frac{128}{3\pi^2} \frac{f^3 \lambda_p^3}{d^3} \tag{2.8}$$

where d is the laser beam diameter at the lens and f is the lens' focal length. Substituting Eqs. 2.6, 2.7 and 2.8 into Eq. 2.5 gives the rate equation

$$\frac{\mathrm{d}n_s}{\mathrm{d}t} = \left(\frac{3\pi c}{128} \frac{Nd^3}{n^3 f^3} \frac{\nu_p^4}{\nu_S^3 \Delta\nu_S^{(f)}} \frac{\mathrm{d}\sigma}{\mathrm{d}\Omega}\right) n_p - \frac{n_S}{\tau_0} \tag{2.9}$$

Assuming a steady state solution ($\mathrm{d}n_s/\mathrm{d}t = 0$), the rate of emission of collected Stokes photons ($\gamma_f = n_S/\tau_0$) is equal to the rate of pumped photons

$$\gamma_f = \left(\frac{3\pi c}{128}\frac{Nd^3}{n^3 f^3}\frac{\nu_p^4}{\nu_S^3 \Delta\nu_S^{(f)}}\frac{\mathrm{d}\sigma}{\mathrm{d}\Omega}\right) n_p \tag{2.10}$$

One can now express the rate of Stokes photons emitted as a function of the pump power by assuming that the power is uniformly distributed over its line width, $n_p = 2P_{\mathrm{in}}\tau_p^{(f)}/h\nu_p$ where P_{in} is the pump input power and $\tau_p^{(f)} = 1/(2\pi\Delta\nu_p^{(f)})$, where $\Delta\nu_p^{(f)}$ is the free space pump linewidth. The expression for the rate of laser-induced Stokes photon emission from a CW laser becomes

$$\gamma_f = \frac{3c}{128}\frac{Nd^3 P_{\mathrm{in}}}{n^3 f^3 h}\frac{\mathrm{d}\sigma}{\mathrm{d}\Omega}\frac{\nu_p^3}{\nu_S^3}\frac{1}{\Delta\nu_S^{(f)}\Delta\nu_p^{(f)}} \tag{2.11}$$

which shows that the Raman signal is a strong function of the linewidths of the pump laser (which is governed by the type of laser) and the Stokes linewidth, which depends on the species of interest. Equation. 2.11 can be nondimensionalised to gain further insight into the parameters controlling the Stokes emission rate

$$\gamma_f = \left(\frac{3\mathrm{NA}^3}{16n^3}\right)\left(\frac{\nu_p}{\nu_S}\right)^3\left(\frac{P_{\mathrm{in}}}{h\Delta\nu_S^{(f)}\Delta\nu_p^{(f)}}\right)\left(Nc\frac{\mathrm{d}\sigma}{\mathrm{d}\Omega}\right) \tag{2.12}$$

Here NA is the numerical aperture of a lens (where $d/f = 2\mathrm{NA}$, typically $\mathrm{NA} = 0.002 \rightarrow 1$). For a Stokes emission frequency and wavenumber linewidth of $\nu_S = 4.9 \times 10^{14}$ Hz and $\Delta\tilde{\nu}_S = 10\ \mathrm{cm}^{-1}$ (encapsulating many linewidths from the individual Q-branches), respectively, the free space Stokes linewidth in frequency space can be expected to be $\Delta\nu_S^{(f)} = 3.0 \times 10^{11}$ Hz [121, 122]. For a pump frequency and linewidth of $\nu_p = 5.6 \times 10^{14}$ Hz and $\Delta\nu_p^{(f)} = 5.0 \times 10^9$ Hz [123], respectively, the following assumptions can also be applied $\nu_p/\nu_S \approx 1$, $\Delta\nu_S = \Delta\nu_S^{(f)} > \Delta\nu_p^{(f)}$ and $n = 1$, resulting in the following equation

$$\gamma_f = \left(\frac{3\mathrm{NA}^3}{16}\right)\left(\frac{P_{\mathrm{in}}}{h\Delta\nu_S^2}\right)\left(Nc\frac{\mathrm{d}\sigma}{\mathrm{d}\Omega}\right) \tag{2.13}$$

The simplified scaled rate of emission per molecule in free space is then given by

$$\frac{\gamma_f}{Nc\frac{\mathrm{d}\sigma}{\mathrm{d}\Omega}} = \left(\frac{3\mathrm{NA}^3}{16}\right)\left(\frac{P_{\mathrm{in}}}{h\Delta\nu_S^2}\right) \tag{2.14}$$

As an example, for an optical setup with NA $= 0.003$ ($d = 0.003$ m and $f = 0.5$ m) and a laser power of 200 mW, the scaled rate of emission per molecule in free space is on the order of 1500 photons s^{-1} (using Eq. 2.12). The maximum scaled rate of emission can be expected for a large diameter high power laser beam with a narrow linewidth focused with a short focal length lens. Note that a limit is reached for a diffraction-limited spot (NA $= 1$). However, the practical constraints on NA values in *in situ* measurements mean large values of NA are not attainable so that alternative solutions for Raman signal amplification must be found.

2.3 Cavity Enhanced Raman spectroscopy

The chosen approach in this work was to use the power build-up of laser radiation inside an external optical cavity. An optical cavity consists of two highly reflective mirrors positioned parallel to each other and perpendicular to the optical axis of propagation of the laser radiation. If the frequency of the laser is matched to the resonant frequency of the cavity, laser radiation can be effectively coupled into the cavity, resulting in a power build-up of the radiation by several orders of magnitude within it [124–127].

The power build-up inside the cavity can be utilised to enhance the magnitude of spontaneous Raman emission, resulting in a cavity-enhanced Raman spectroscopy technique (CERS) [128], [129].

2.3.1 Reference Cases

There have been numerous practical applications of CERS for the analysis of gaseous chemical species mixtures. Taylor et al. stabilised a 1 W, 532 laser to a short, linear cavity via an electronic feedback mechanism and managed to observe Raman signals from hydrogen in a 90 degree collection geometry [130]. A Raman cell was placed inside the optical cavity, however, the windows of the cell introduced significant optical losses, limiting the enhancement factor to 50.

Ohara et al. [131], used a method developed by King and Pitarro [128, 129] to couple an antireflection (AR) coated laser diode into a linear optical cavity, achieving an intracavity buildup of 800. They introduced a solid angle efficiency factor to quantify the collected Stokes photons for a 90° collection geometry from the middle of the cavity.

Li et al. demonstrated a different configuration, creating a multi-pass cell in a near confocal cavity [132]. This resulted in an excitation power build-up of 9 W from a 200 mW laser, as the beam was reflected 50 times inside the cavity. By using CERS, it was possible to carry out high-sensitivity detection of a mixture of eight gasses.

Salter et al. coupled a 635 nm laser diode into a linear optical external cavity, consisting of two highly reflective mirrors [92]. A build-up of the circulating power of 3 orders of magnitude was achieved using optical feedback stabilisation, with strong Raman signals collected in a forward scattering geometry. CERS spectra of air, CH_4, H_2 and benzene were recorded to demonstrate the capabilities of CERS for analytical applications and studies of fundamental molecules.

Thorstensen et al. constructed a low-cost CERS probe for multi-gas detection [133]. A 532 nm laser pointer was coupled into a Fabry-Perot cavity which allowed to increased the sensitivity of the gas probe by a factor of 50. The use of inexpensive components such as mirrors, laser source and the detector showed the possibility of CERS being used as a low-cost analysis tool.

Friss et al. also demonstrated the ability of CERS to acquire the Raman spectra of air [134]. A narrow-linewidth fibre laser at 1064 nm wavelength was locked to a high-finesse cavity containing the sample gas. They managed to generate an intracavity power build-up from 3.7 mW to 22 W, resulting in a 5900 build-up factor. Rotational Raman and Rayleigh scattering signals were collected for oxygen, nitrogen and carbon dioxide.

In the next sections, the theory of optical resonators is described so as to obtain an expression for the CERS signal, which would enable comparison with the free space unamplified Raman signals intensity, described in Eq. 2.12.

2.3.2 Theory of Optical Resonators

An optical cavity, resonating cavity or an optical resonator is an arrangement of two or more mirrors that allow the formation of standing waves of light/electromagnetic radiation inside the cavity.

The basic principle of operation of a resonator is to allow the coupled-in light to undergo multiple reflections, leading to the constructive interference of the electromagnetic radiation occurring when the length of the cavity is an integer multiple of half of the wavelength of the incident light. This results in the build-up of power of the radiation inside the cavity.

Before describing the more detailed working principles of the optical cavity, consider the geometry of propagation of the Gaussian beam. The derivations are readily available in multiple literature sources, so only the result is stated here [135–137]. In Cartesian coordinates, the relative field strength of an elliptical Gaussian beam profile is given by

$$u(x,y,z) = \frac{1}{q(z)} \exp\left(-ik\frac{x^2+y^2}{2R_b(z)} - \frac{x^2+y^2}{w^2(z)}\right) \tag{2.15}$$

where $R_b(z)$ is the radius of curvature of the beam, $w(z)$ is the beam radius and $q(z)$ is the complex beam parameter at a distance z along the optical axis (typically abbreviated as q), given by

$$\frac{1}{q(z)} = \frac{1}{R_b(z)} - \frac{i\lambda}{\pi w^2(z)} \tag{2.16}$$

where λ is the wavelength of the beam. In Eq. 2.15, the first term represents the spherical wave propagating along the z-axis with the real radius of curvature $R_b(z)$, and the second term represents the finite transverse Gaussian amplitude variation.

It is possible to calculate the whole path of propagation of the Gaussian beam by knowing its wavelength in the medium, λ, and beam waist w_0. The beam radius $w(z)$ and radius of curvature of the beam $R_b(z)$ are given by

$$w(z) = w_0\sqrt{1+\left(\frac{z}{z_R}\right)^2} \tag{2.17}$$

$$R_b(z) = z + \frac{z_R^2}{z} \tag{2.18}$$

where z_R is the Rayleigh length

$$z_R = \frac{\pi w_0^2}{\lambda_p} \tag{2.19}$$

2.3.3 Cavity Stability

One of the conditions for constructive interference to occur inside an optical resonator is for a wave to be able to fully retrace its ray paths after every round trip. Such a wave is called a cavity mode. The stability of the resonator defines its ability to allow the waves to manifest themselves as said modes. It is a function of the stability parameters of the mirrors used to construct the optical resonator and the distance between them [138]. The stability parameter of the mirror is given by

$$g = 1 - \frac{l}{\mathcal{R}} \tag{2.20}$$

where R is the radius of the curvature of the mirror and l is the length of the resonator, resulting in the following expression for the stability of the resonator constructed using two mirrors

$$0 < g_1 g_2 < 1 \tag{2.21}$$

where subscripts 1 and 2, denote in-coupling and out-coupling resonator mirrors, respectively. Stability of resonators with different mirror geometries can be observed graphically in Fig 2.3 in the shaded regions. An optical resonator will be referred to as a cavity from now on.

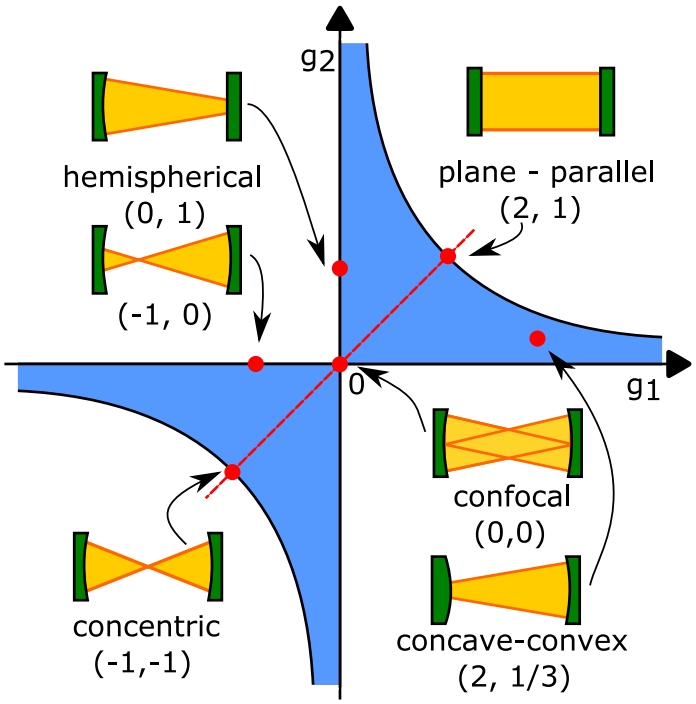

Fig. 2.3 Stability diagram of optical resonators. Stable resonators lie in the shaded region.

2.3.4 Longitudinal and Transverse Modes

Two different types of modes occur in an optical cavity, corresponding to longitudinal and transverse modes.

Given the general order of magnitude of wavelengths (hundreds of nm), multiple modes can exist in the cavity simultaneously. The number of modes present in the cavity depends on the cavity properties and the incident source of the EM radiation. The total number of theoretical modes that can simultaneously exist in the cavity is given by [135]

$$y = \frac{2l}{\lambda_p} \tag{2.22}$$

where y - number of modes in the cavity, l - distance between the mirrors (cavity length) and λ_p is the wavelength of the incident light. In the frequency domain, the spacing between the axial (longitudinal) resonant modes (also called the Free Spectral Range, $\Delta\nu_{\mathrm{FSR}}$) is given

by [135]

$$\Delta\nu_{FSR} = \frac{c_0}{2nl} \tag{2.23}$$

where c_0 is the speed of light, n is the refractive index of the medium in the cavity and l is the distance between the mirrors.

Transverse Electromagnetic Modes, TEM, represent the distribution of energy across the plane perpendicular to the direction of the beam propagation. The subscripts in the notation for describing a TEM mode, m and n refer to the respective axis of propagation [139]. The physical shape and mathematical treatment of transverse modes depend on the type of symmetry used to construct the cavity. The most commonly seen modes are Hermite-Gaussian [140] and Laguerre-Gaussian beams [141]. The former are generated in cavities where mirrors have rectangular symmetries whereas the latter are observed in cavities with circular/cylindrical end mirrors.

2.3.5 Mode-Matching

The best results from an optical cavity are obtained by correctly coupling the external light source into the cavity, so that all of the external radiation is converted into a $TEM_{0,0}$ mode. $TEM_{0,0}$ mode offers the lowest divergence, the ability to be focused to the smallest spot and having the best spatial coherence out of other possible modes. Additionally, it remains Gaussian when passing through other optical systems, making it easier to collect the transmitted electromagnetic (EM) signal into a spectrometer.

To efficiently couple the external light source into a cavity the light beam needs to be mode-matched to the principal Gaussian mode of the cavity. If a mode is represented as a wave beam travelling backwards and forwards between mirrors, its beam parameters do not change after completing one round trip. A beam that represents a mode travels in both directions between the mirrors and forms an axial standing-wave pattern, that takes an expected form of a resonator mode.

To further understand the mathematical representation of a cavity mode, we assume an optical resonator made with two mirrors, which have equal radii of curvature, $\mathcal{R}$. This system can be unfolded into a sequence of four lenses, representing the action taken on a travelling beam within the cavity as shown in Fig. 2.4 [140].

It is possible to define the complex beam parameter immediately to the right of a particular lens as q_1, permitting to calculate the beam parameter q_2 to the right of the next lens as follows

$$\frac{1}{q_2} = \frac{1}{q_1 + d} - \frac{1}{f} \tag{2.24}$$

where f is the focal length of the lens and d is the distance between the lenses.

The condition of self-consistency requires that $q_1 = q_2 = q$ which results in a quadratic equation for the beam parameter q at the lenses, or equivalently at the mirrors of the resonator.

$$\frac{1}{q^2} + \frac{1}{fq} + \frac{1}{fd} = 0 \tag{2.25}$$

The roots for Eq. 2.25 are given by

$$\frac{1}{q} = -\frac{1}{2f} \mp i\sqrt{\frac{1}{fd} - \frac{1}{4f^2}} \tag{2.26}$$

where only the roots that result in a real bandwidth are used. From Eq. 2.26 one can obtain a solution of the form

$$\frac{1}{q} = \frac{1}{R} - i\frac{\lambda}{\pi w^2} \tag{2.27}$$

which is the same as the Eq. 2.16, where R is the curvature of the wavefront. This means that the mirror surfaces coincide with the phase fronts of the resonator modes, allowing to equate R to $\mathcal{R}$. The width of the fundamental mode w inside the cavity, is given as

$$w^2 = \frac{\lambda\mathcal{R}}{\pi} / \sqrt{2\frac{\mathcal{R}}{d} - 1} \tag{2.28}$$

It is possible to calculate the radius of the beam w_0 in the centre of the resonator, where the shape of the phase front is a plane, resulting in $\mathcal{R} = 0$. Using $z = d/2$ (as cavity mirrors have equal $\mathcal{R}$) and

$$\frac{\lambda_p z}{\pi w_0^2} = \frac{\pi w^2}{\lambda_p \mathcal{R}} \tag{2.29}$$

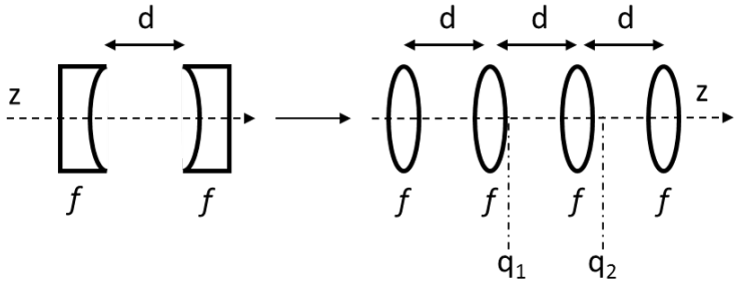

Fig. 2.4 Symmetrical laser resonator and the equivalent sequence of lenses with indicated q_1 and q_2 parameters

The beam waist is given by

$$w_0^2 = \frac{\lambda_p}{2\pi}\sqrt{d(2\mathcal{R}-d)} \tag{2.30}$$

After further mathematical derivations outlined by Kogelnik *et al.* [140] one eventually arrives to the equation for the beam waist width of the natural mode inside the cavity made of two mirrors with different radii of curvature.

$$w_0^4 = \left(\frac{\lambda_p}{\pi}\right)^2 \frac{d(\mathcal{R}_1-d)(\mathcal{R}_2-d)(\mathcal{R}_1+\mathcal{R}_2-d)}{(\mathcal{R}_1+\mathcal{R}_2-2d)^2} \tag{2.31}$$

The geometrical position of the beam waist inside the cavity can be found by equations

$$t_1 = \frac{d(\mathcal{R}_2-d)}{\mathcal{R}_1+\mathcal{R}_2-2d} \qquad t_2 = \frac{d(\mathcal{R}_1-d)}{\mathcal{R}_1+\mathcal{R}_2-2d} \tag{2.32}$$

The distances t_1 and t_2 can be more easily visualised by the sketch in Fig. 2.5a, which shows an optical resonator made from two mirrors with different radii of curvature, where $\mathcal{R}_1$ is greater than $\mathcal{R}_2$.

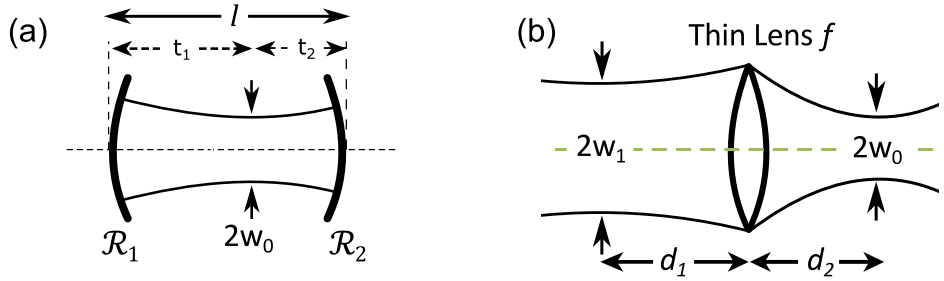

Fig. 2.5 a) Parameters of $TEM_{0,0}$ mode inside an optical cavity with mirrors of unequal radii of curvature, where $\mathcal{R}_1 > \mathcal{R}_2$. b) Matching two $TEM_{0,0}$ modes with the use of a thin lens.

The typical construction of a laser consists of a resonant cavity with pumping medium placed inside it. An excitation wavelength is injected into the cavity, where the power build-up occurs, and the EM radiation leaves the cavity through a mirror that has a lower reflectivity than its counterpart. Therefore, when carrying out mode-matching it is useful to understand that the light emission from the laser will have its own properties and parameters such as the beam waist and divergence.

For CERS, a light from a laser diode is typically injected into an external optical cavity. In order to ensure optimal light coupling into the cavity, the $TEM_{0,0}$ modes of the laser and the optical cavity have to be mode-matched, which is done with lenses. The problem of the beam-matching with a thin lens is typically set up as that of two beam waists that need

to be transformed into each other, where their origin distances with respect to the lens are known, as shown in Fig. 2.5b). In order to mode match those beams, one has to choose a lens that has a focal length larger than the characteristic length f_0, which is defined by the widths of the beams to be mode-matched and the wavelength of the incident radiation source. Characteristic length is given by [140]

$$f_0 = \pi w_1 w_2 / \lambda_p \tag{2.33}$$

Any lens with a focal length of $f > f_0$ can be used for mode matching. Assume two beam waists are located at distances d_1 and d_2 from the mode-matching lens. Once the lens with particular f has been established, the distances d_1 and d_2 have to be adjusted accordingly to satisfy the following mode matching equations [142].

$$d_1 = f \pm \frac{w_1}{w_2}\sqrt{f^2 - f_0^2} \qquad d_2 = f \pm \frac{w_2}{w_1}\sqrt{f^2 - f_0^2} \tag{2.34}$$

Confocal parameters b_1 and b_2 can be calculated and inserted into the matching formulas. They are defined by the beam waists of the beams of interest and their mutual wavelength.

$$b_1 = \frac{2\pi w_1^2}{\lambda} \qquad b_2 = \frac{2\pi w_2^2}{\lambda} \tag{2.35}$$

The expression for the characteristic length becomes

$$f_0^2 = \frac{1}{4} b_1 b_2 \tag{2.36}$$

And the mode matching equations are

$$d_1 = f \pm \frac{1}{2} b_1 \sqrt{\left(\frac{f^2}{f_0^2} - 1\right)} \qquad d_2 = f \pm \frac{1}{2} b_2 \sqrt{\left(\frac{f^2}{f_0^2} - 1\right)} \tag{2.37}$$

The confocal parameter for different cavity geometries, such as hemispherical or concave-convex, can be calculated using the formulas provided in the following review [140].

2.3.6 Finesse

An important property of the $TEM_{0,0}$ cavity mode is its Full Width at Half Maximum (FWHM), defined as the width of the peak at which the intensity of the peak has dropped to half of its value. If an optical resonator is treated as an optical filter, FWHM then serves as the frequency resolution of the resonator. The ratio of the $\Delta\nu_{FSR}$ to the FHWM of the

resonance peak of the cavity gives rise to a parameter called *finesse*, $\mathcal{F}$ [143]

$$\mathcal{F} = \Delta\nu_{\mathrm{FSR}}/\mathrm{FWHM} \tag{2.38}$$

The finesse represents the ratio of the power contained per unit mode of the cavity. It can be used to quantify the resolving power of the optical cavity, if such was to be treated as an interferometer or a transmission filter [143]. The resolving power of the cavity is largest when the reflectivities of the mirrors, for a particular wavelength, approach unity and there are very small internal losses inside the cavity. Finesse can be used to highlight the amount of losses in the resonator that arise from the surface quality of mirrors used, and estimate an interference factor based on the cavity geometry. In addition, finesse indicates the ratio of the circulating to incident laser power, which allows to calculate the maximum gain possible with the particular cavity geometry [144].

The theoretical finesse value for a monochromatic light, which provides an estimate to the expected power build-up within the cavity [145–147], is calculated as follows

$$\mathcal{F}_R = \frac{\pi(R_1R_2)^{1/4}}{1-\sqrt{R_1R_2}} \tag{2.39}$$

where R_1 and R_2 are reflectivity values for the wavelength of coupled light of the in-coupling and out-coupling mirrors, respectively. This expression is applicable for plane, parallel mirrors with perfect surface quality. For non-planar mirrors, a second factor, $\mathcal{F}_I$, needs to be considered to account for the radius of curvature. It is given by $\mathcal{F}_I = 16\lambda_{p/S}l^3/H^4$, where $\lambda_{p/S}$ is the wavelength of the pump/Stokes photon and H is the beam radius at the in-coupling mirror, defined as

$$\left(\frac{H}{w_0}\right)^2 = 1+\left(\frac{\lambda_p l}{2\pi w_0^2}\right)^2 = 1+\frac{1}{2\frac{\mathcal{R}}{l}-1} \tag{2.40}$$

Finally, the surface quality finesse, $\mathcal{F}_Q$, is a measure of the flatness of the mirror's surface, which is usually flat to within a fraction of the wavelength, λ/Q, where Q is the fringe-spacing integer, commonly used as a metric for the flatness of the optical surface. This means that no point on the ideal plane deviates by more than λ/Q, therefore it is assumed that $\mathcal{F}_Q = Q/\lambda$. For mirrors with high reflectivities (> 0.99) the $\mathcal{F}_Q$ value is typically very large and therefore can be ignored.

Combining all three factors gives a nondimensionalised equation for a total theoretical finesse of the cavity, $\mathcal{F}$, for a wavelength λ, [148]

$$\frac{1}{\mathcal{F}} = \sqrt{\left(\frac{1}{\mathcal{F}_R}\right)^2 + \left(\frac{1}{\mathcal{F}_Q}\right)^2 + \left(\frac{1}{\mathcal{F}_I}\right)^2} = \\ = \sqrt{\left(\frac{1-\sqrt{R_1R_2}}{\pi(R_1R_2)^{(1/4)}}\right)^2 + \left(\frac{\lambda}{Q}\right)^2 + \left(\left(\frac{H}{l}\right)^4 \frac{l}{16\lambda}\right)^2} \quad (2.41)$$

Table 2.3 Parameters inside an optical cavity of length l = 3 mm with mirrors of equal radii of curvature $\mathcal{R} = 1$ m and fringe-spacing integer $Q = 10$.

λ (nm)	R_1	R_2	T_1	T_2	w_0 (μm)	$\mathcal{F}_R$	$\mathcal{F}_{p/S}$
532	0.999	0.99993	0.001	0.00007	81	5870	4000
607	0.4	0.4	0.6	0.6	86	3.3	3.3

Using eq. 2.41 it is possible to calculate the total theoretical finesse values for both pump and Stokes emission wavelengths as a function of the nondimensional parameters $\mathcal{R}/l$ and λ/l, which are shown in Fig. 2.6. The figures illustrate that in the yellow region, $\mathcal{F}_R$ dominates (*i.e.* $\lambda/l << 1$) and the highest finesse values are dominated by the wavelength-specific reflectivity values of both mirrors. In the limit for small cavities, where $\mathcal{F}_I$ dominates (i.e. $\mathcal{R}/l \to \infty$) the finesse is at a minimum, and the value is determined by the length of the cavity. Table 2.3 gives the wavelength-dependent in and out-coupling mirror reflectivities, $R_{1/2}$ and transmissivities, $T_{1/2}$, along with the length of the cavity, l, radii of curvature, $\mathcal{R}$, and fringe-spacing integer, Q. The corresponding calculated (using Eq. 2.41) finesse values $\mathcal{F}_p$ and $\mathcal{F}_S$ for the pump and Stokes wavelengths, respectively, are also shown.

The measured finesse can be significantly lower than the theoretical values predicted by Eq. 2.38, such as when values of ideal reflectivity are used, especially for smaller cavities. If a measured experimental finesse value is 80% of the theoretical finesse value for the particular cavity configuration then this indicates good laser radiation-to-cavity coupling [149]. In summary, larger cavities can yield higher finesse *if* the mirrors can be appropriately positioned. However, it is often the case that in practice it is difficult to control the exact positioning of the mirrors, so that it is easier to obtain a power build-up in a cavity of smaller length, which offers a larger $\Delta\nu_{\mathrm{FSR}} = c/(2nl)$, in turn allowing easier stabilisation of a smaller number of modes, with limited control accuracy.

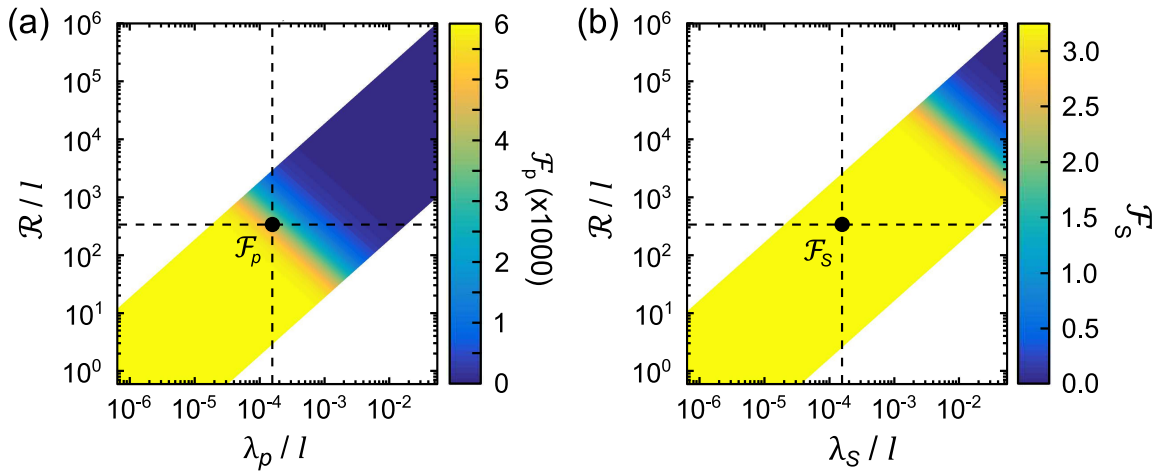

Fig. 2.6 Colour maps of the calculated a) pump and b) Stokes emission finesse (Eq. 2.41) as a function of nondimensional parameters of the cavity: $\mathcal{R}/l$ and $\lambda_{p/S}/l$, respectively. Dashed lines indicate the location of experimental values of nondimensional parameter ratios, discussed in Section 3.1.2. The white regions within the maps correspond to finesse values for unrealisable configurations.

2.3.7 Impedance Matching

Apart from mode-matching, a related condition must be obeyed to efficiently couple laser radiation into an optical cavity: the optical impedance of the incoming beam must be matched to the cavity, meaning that the mirror reflectivities and the spacing between them must be adjusted in order to maximise the energy transmission rate out of the cavity [149–151]. Failure to do so could lead to difficulties in injecting the pump beam into the cavity, as major losses could occur due to the initial back reflection from the in-coupling mirror. To achieve impedance matching, the energy transmission coefficient through the in-coupling mirror must equal all other losses in the resonator, plus the transmission through the out-coupling mirror. mathematically given by

$$T_1 = T_2 + A \tag{2.42}$$

where T_1 and T_2 are the transmission coefficients of the in- and out-coupling mirrors, respectively, and A represents the total losses of the cavity. Therefore, when the transmissivity of the in-coupling mirror is larger (smaller) than that of the addition of the transmissivity of the output mirror and the loss coefficient, the system is said to be over (under) coupled. In reality, it can be difficult to determine upfront the exact losses within the resonator for an arbitrary scatterer and it is difficult to dynamically adjust mirror reflectivities. For the cavity model discussed in Section 2.4 it is assumed that all of the light is getting into the cavity.

Therefore, the power in the cavity corresponds to the power measured before entering the in-coupling mirror.

2.3.8 Cavity Raman Enhancement

The purpose of constructing the optical cavity is to achieve the enhancement of the spontaneous Raman scattering, which occurs inside the cavity. The enhancement is carried out via three processes: resonant recirculation, Purcell effect and Double Resonance condition. A schematic of each process is shown in Fig. 2.7. In this section, only the discussion with regards to Stokes photons will be considered.

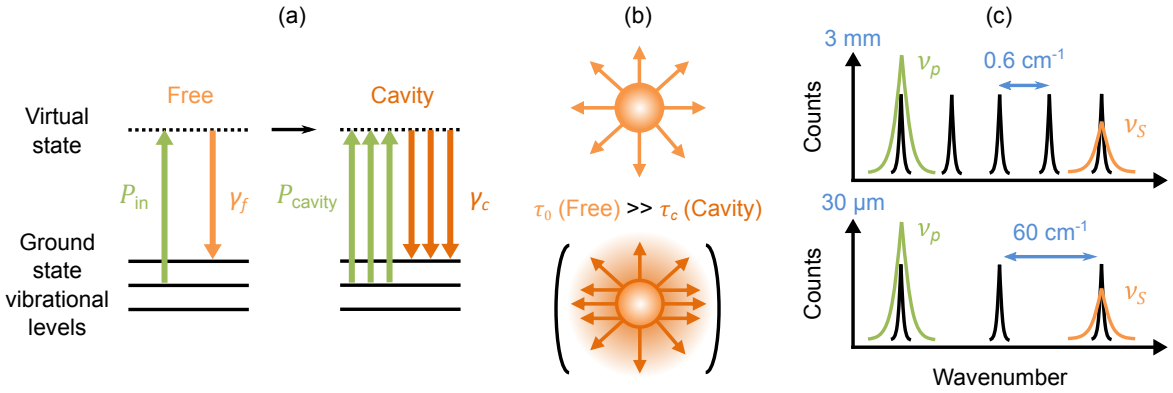

Fig. 2.7 Three main factors that contribute to the enhancement of spontaneous Raman scattering within a cavity: (a) Resonant recirculation, (b) Purcell effect and (c) Double resonance condition.

Resonant Recirculation

For light to be efficiently coupled into a cavity, resonant recirculation condition requires that the laser and the cavity frequencies are resonant with each other. The power build-up within the cavity is proportional to the finesse ($P_{\text{cavity}} \propto \mathcal{F}_p\, P_{\text{in}}$, see Eq. 2.38), as it represents the ratio of the power contained per unit mode of the cavity. For instance, for an incident laser with a power of 20 mW and a cavity with the finesse of value around 4000 one can expect recirculation powers on the order of tens of watts. Such enhanced powers create proportionally more Raman scattered photons that can be detected for the low cross-sections of gas molecules of interest, whilst demanding sufficient precision in rejecting modes away from the selected region.

Purcell Effect

Any two level system will undergo spontaneous decay by interaction with a vacuum continuum at a rate proportional to the spectral density of modes per unit volume evaluated at the transition frequency. However, within the cavity the density of modes is modified. From the view of the cavity modes, their maximal density occurs at the resonant frequencies of the cavity and can greatly exceed the corresponding free-space density. Purcell discovered this effect by noting that a single mode occupies a spectral bandwidth of $\delta v_c/Q$ within the cavity volume V, where Q_c is the quality factor of the cavity and δv_c is the resonant frequency [152]. Normalising the resultant cavity-enhanced mode density per unit volume of the mode density of free space results in the Purcell spontaneous emission enhancement factor, C_0 [153, 154]

$$C_0 = \frac{3}{4\pi^2}\left(\frac{\lambda}{n}\right)^3 \frac{Q_c}{V} \tag{2.43}$$

where n is the refractive index of the medium in the cavity.

In the regime where the resonance of the cavity is more narrow than a specific Raman feature, the effective Purcell factor becomes

$$C_c = \frac{3}{4\pi^2}\left(\frac{\lambda}{n}\right)^3 \frac{Q_{eff}}{V} \tag{2.44}$$

Eq. 2.44 account for the fact that the cavity enhances only a part of the Raman transition by introducing the effective quality factor $Q_{eff} = (Q_c^{-1} + Q_r^{-1})$, where Q_r^{-1} is the quality factor of the Raman feature [155]. Raman features of CNTs typically have $Q_r \approx 1,000 - 2,000$, so for a cavity with $Q_c = 10^5$ and $V = \lambda^3$ one can expect $C \approx 100$.

Double Resonance Condition

The double resonance condition states that when the cavity length is set such that the number of Free Spectral Ranges ($\Delta\nu_{\mathrm{FSR}}$) equals the shift of the Raman mode of interest, not only are the incident laser and cavity modes resonant but the scattered light exiting the cavity at the Stokes frequencies are as well. For a cavity of length 3 mm, with other cavity parameters given in Table. 2.3, $\Delta\nu_{\mathrm{FSR}} \approx 50$ GHz (0.6 cm^{-1}). For such a cavity, illuminated at $\lambda_p =$ 532 nm (5.64×10^5 GHz), the scattered modes are enhanced approximately every 0.02 nm, as shown in the upper half of Fig 2.7c. In the case of the N_2 vibrational mode emitting at a frequency 2331 cm^{-1}, there are nearly 3900 modes that can be enhanced between the excited frequency and this vibrationally scattered mode. The $\Delta\nu_{\mathrm{FSR}}$ for cavities of the order of tens of micrometers however, are of the order of 5000 GHz (60 cm^{-1}) making it very difficult

for the scattered Stokes photons to be enhanced, as each enhanced mode is separated by approximately 2 nm, as shown in the lower half of Fig. 2.7c. Therefore only 39 modes are enhanced for the example of N_2, reducing the likelihood of double resonance occurrence.

As a final note, manufacturing constraints in the high reflectivity of the cavity mirrors must also be taken into account when considering the double resonance condition, as one can normally expect decreasing oscillatory reflectivity behaviour for wavelengths further away from the pump wavelength. An ideal confocal Fabry-Perot cavity would need to be resonant with both the pump and Stokes frequencies in order to utilize all of the three simultaneously occurring Raman enhancement processes, to give an increased number of scattered Stokes photons at a faster rate of emission.

Mode locking

The final condition required for the efficient enhancement is that the cavity length must be an integer multiple of half of the wavelength of the pump emission. An electronic feedback loop is often used for maintaining the cavity resonance. Such feedback loops may either adjust the optical frequency of the laser to match the cavity frequency, or adjust the cavity length via a piezoelectric actuator. A number of different techniques have been used for locking the cavity into a resonance state [133, 156–158].

A Pound-Drever-Hall lock-in scheme is the more popular of the techniques, which locks the laser frequency to the resonance frequency of the cavity [158], based on a measurement of the phase offset. With proper implementation, it is able to reduce the laser linewidth and stabilize the frequency drifts to a particular cavity mode.

Salter et al. have used an alternative technique by building a low-cost lock-in amplifier, which adjusts the cavity length via a piezo-actuator [92].

In this work the low-cost lock-in device was used, which was able to achieve lock-in, but suffered from long time scale drift. This technique was chosen due to the cost and ease of use. Principles of its operation are discussed in Section 3.1.2.

In their most recent work, Smith et al. [156] have achieved lock-in using the optical transmission of the cavity and found that the laser can effectively self-lock without the need for additional electronic feedback. However, this requires a Fabry-Perot laser diode unlike the 532 nm DPSS laser diode used in this work, as discussed in Section 3.1.2.

2.4 Cavity Enhanced Raman Spectroscopy Model

The following model has been developed in-house to predict Stokes rate of emission from a CERS setup. The rate of change in photons emitted in a cavity is given by a balance between

the emission induced by the rate of pumping photons to the flux of photons emitted in the cavity [118, 119]

$$\frac{\mathrm{d}n_S}{\mathrm{d}t} = \frac{C_c}{\tau_0} n_p - \frac{1}{\tau_c} n_S \tag{2.45}$$

where τ_0 and τ_c are the lifetimes of the Stokes photons in free space and in the cavity, respectively. In the regime where the cavity mode is much narrower than the Stokes mode [159] the effective cavity Purcell factor, C_c, is given by

$$C_c = \frac{3}{4\pi^2} \left(\frac{\lambda_S}{n}\right)^3 \frac{1}{V_{\mathrm{eff}}^{(c)}} \frac{\nu_S}{\Delta\nu_S^{(f)} + \Delta\nu_S^{(c)}} \tag{2.46}$$

where $\Delta\nu_S^{(f)}$ and $\Delta\nu_S^{(c)}$ are the free space and cavity Stokes linewidths and $V_{\mathrm{eff}}^{(c)}$ is the effective mode volume of a cavity, given by [140, 118]

$$V_{\mathrm{eff}}^{(c)} = \frac{(\lambda_p + \lambda_S) l^2}{4 \tan^{-1}(1/\sqrt{2\mathcal{R}/l - 1})} \tag{2.47}$$

By assuming a steady state solution ($\mathrm{d}n_s/\mathrm{d}t = 0$) and solving for the rate of the emission of Stokes photons leaving the cavity ($\gamma_c = n_S/\tau_c$), Eq. 2.45 becomes

$$\gamma_c = \left(\frac{8Nc^3}{\pi l^2 n^3} \frac{\mathrm{d}\sigma}{\mathrm{d}\Omega} \frac{\nu_p^2}{\nu_S^2(\nu_p + \nu_S)} \frac{1}{\Delta\nu_S^{(f)} + \Delta\nu_S^{(c)}} \tan^{-1}\left(\frac{1}{\sqrt{2\mathcal{R}/l - 1}}\right) \right) n_p \tag{2.48}$$

Here it is assumed, as before, that the incoming laser power is distributed uniformly over the pump wavelength, $n_p = 2P_{\mathrm{in}}\tau_p^{(c)}/h\nu_p$ where P_{in} is the pump input power and $\tau_p^{(c)} = 1/(2\pi\Delta\nu_p^{(c)})$, where $\Delta\nu_p^{(c)}$ is the cavity pump linewidth. The values for $\Delta\nu_p^{(c)}$ and $\Delta\nu_S^{(c)}$ are expressed as a function of the free spectral range and finesse at their respective frequencies, given by Eq.2.38. The larger the finesse and length of the cavity, the smaller the respective linewidths will be. A factor of 1/2 is also introduced into the overall Eq. 2.48 to account for the fact that light is collected from only one side of the cavity. The final expression for the rate of emission from one side of the cavity is

$$\gamma_c = \frac{4\beta c^3 P_{\mathrm{in}} N}{h\pi^2 l^2 n^3} \frac{\mathrm{d}\sigma}{\mathrm{d}\Omega} \frac{\nu_p}{\nu_S^2(\nu_p + \nu_S)} \frac{1}{\frac{c}{2nl\mathcal{F}_p}\left(\Delta\nu_S^{(f)} + \frac{c}{2nl\mathcal{F}_S}\right)} \tag{2.49}$$

where $\beta = \tan^{-1}(1/\sqrt{2\mathcal{R}/l - 1})$, with $\mathcal{F}_p$ and $\mathcal{F}_S$ being the cavity finesse for the pump and Stokes wavelength, respectively. The equation can be regrouped to yield a similar expression

as the total photon emission in the free space emission case in Eq 2.12.

$$\gamma_c = \left(\frac{8\mathcal{F}_p\beta}{\pi^2 n^2}\right)\left(\frac{\nu_p}{\nu_S}\right)\left(\frac{P_{\text{in}}}{h\nu_S(\Delta\nu_S^{(f)} + \frac{c}{2nl\mathcal{F}_S})}\right)\left(\frac{c}{l(\nu_p+\nu_S)}\right)\left(Nc\frac{\mathrm{d}\sigma}{\mathrm{d}\Omega}\right) \tag{2.50}$$

It is possible to gain further insight into the relative contributions to the resonant cavity mode by considering the order of magnitude of the groupings for the current conditions. Stokes emission frequency and linewidth are $\nu_S = 4.9 \times 10^{14}$ Hz and $\Delta\nu_S^{(f)} = 3.0 \times 10^{11}$ Hz, respectively. The pump frequency and linewidth are $\nu_p = 5.6 \times 10^{14}$ Hz and $\Delta\nu_p^{(f)} = 5.0 \times 10^9$ Hz, respectively. In addition, $\mathcal{F}_p$ = 4000 and $\mathcal{F}_S$ = 3.3, as calculated in Table 2.3. To simplify this expression further we can now make the following assumptions: $\nu_p/\nu_S \approx 1$, $\Delta\nu_S = \Delta\nu_S^{(f)} >> c/2nl\mathcal{F}_S$ and $n = 1$ to give

$$\gamma_c = \left(\frac{4\mathcal{F}_p\beta}{\pi^2}\right)\left(\frac{P_{\text{in}}}{h\nu_S\Delta\nu_S}\right)\left(\frac{c}{l\nu_S}\right)\left(Nc\frac{\mathrm{d}\sigma}{\mathrm{d}\Omega}\right) \tag{2.51}$$

resulting in a simplified scaled rate of emission per molecule in a cavity, given by

$$\frac{\gamma_c}{Nc\frac{\mathrm{d}\sigma}{\mathrm{d}\Omega}} = \left(\frac{4\mathcal{F}_p\beta}{\pi^2}\right)\left(\frac{P_{\text{in}}}{h\nu_S\Delta\nu_S}\right)\left(\frac{c}{l\nu_S}\right) \tag{2.52}$$

For instance, with a cavity setup of l = 3 mm, $\mathcal{R}$ = 1 m, additional cavity parameters listed in Table 2.3 and a laser power of 200 mW, the scaled rate of emission per molecule in a cavity is on the order of 28000 photons s^{-1} (using Eq. 2.50). Note, this value is approximately 20 times larger than in the free space case calculated in Section 2.2, for the same pump power. Following the model predictions, the maximum scaled rate of emission can be expected for a high power laser beam with a narrow linewidth focused into a short cavity with a high finesse. The power build-up within the cavity scales linearly with input power. Narrow laser linewidth allows to concentrate power into the $TEM_{0,0}$, which results in a stronger Raman signal with narrow FWHM. Short cavities have the benefit or higher finesse values, as the distance over which losses can occur is minimised.

Chapter 3

Experimental Setups and Results of CW and CERS

This chapter introduces the experimental setups for Spontaneous Raman scattering and CERS used to perform Raman measurements of ambient air. A unifying model was developed for direct comparison of theoretical CW and CERS based emission magnitudes, predicted by their corresponding models outlined in Chapter 2 . Theoretical predictions were compared to the acquired experimental Raman measurements of ambient air. Major limitations of CERS for performing measurements of reacting flows in a FC-CVD reactor are discussed.

3.1 Experimental setups

3.1.1 Spontaneous Raman scattering using a CW laser

The schematic diagram of free space gas phase Raman setup is shown in Fig. 3.1 The pump radiation was provided by a green/blue argon-ion laser (Spectra Physics Stabilite 2017) primarily used for Phase Doppler anemometry. The laser beam output gives nine output wavelengths with two intense lines at 514.5 nm and 488.0 nm. The laser was configured to divert the majority of its power towards 514.5 nm emission. Dichroic filters separated out the blue and green lines before a 50 mm diameter lens (f = 0.5 m), **L1**, coated for the visible wavelengths, focused the 514.5 nm beam (d = 3 mm) to a spot with a diameter of approximately 110 μm, after which it defocused and hit a beam dump, **BD1**. The power output of 514.5 nm was measured to be 200 mW at the focus.

Both Rayleigh and Stokes scattered photons were collected by a configuration of lenses, perpendicular to the axis of beam propagation. Firstly, a 50 mm diameter lens with 100 mm focal length, **L2** collimated the photons, followed by a second 50 mm diameter lens with

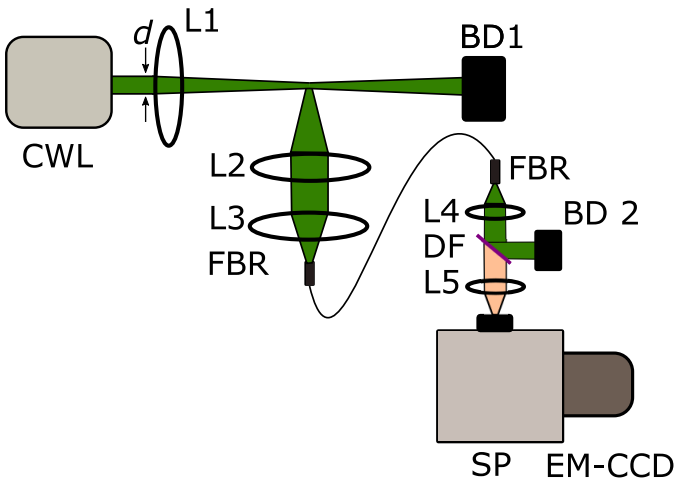

Fig. 3.1 Experimental setup for free space gas-phase Raman detection with a CW laser. Acronyms: CWL - CW laser, L - lens, BD - beam dump, FRB - fiber, DF - dichroic filter, SP-spectrograph, EM-CCD - Electron-multiplying charge-coupled device.

100 mm focal length, **L3**, which focused the light onto a 1000 μm fibre, Ocean Optics fibre, P1000-2-UV-VIS, **FBR**. The fibre output was collimated by a 25 mm diameter lens, **L4**, with a 100 mm focal length before passing through a long-pass 532 nm dichroic filter, **DF**, (LPD02-532RU-25). The filter reflected the Rayleigh photons acquired by the collection system at 90° which are captured by another beam dump, **BD2**. The Stokes photons transmitted through the filter are then focused down by a lens **L5** with 100 mm focal length onto the aperture of an Andor Shamrock SR-303i spectrograph, **SP**, with a slit size of 150 μm, which uses a 600 l/mm grating prism. The output of the spectrograph is monitored by an Andor Ixon Ultra-888 EM-CCD camera. The spectrograph and the EM-CCD are an integrated system, with electron-multiplying capabilities, which are used to amplify collected Stokes emission as the expected Raman signals are usually weak.

3.1.2 Cavity Enhanced Raman Spectroscopy

The schematic diagram of the CERS apparatus can be seen in Fig. 3.2. The excitation EM radiation for CERS was provided by a green Continuous Wave (CW) solid-state laser, Thorlabs DJ532-40, **LD**. The laser diode was mounted in a Thorlabs TCLDM9 Thermo-electrically cooled mount. Varying both the temperature and the current of the diode allows changing its output power and the lasing wavelength. The outlined parameters were controlled by Thorlabs LDC205C and TED200C controllers respectively. TED200c can vary the current from an external modulation source, allowing to sweep the wavelength of the laser.

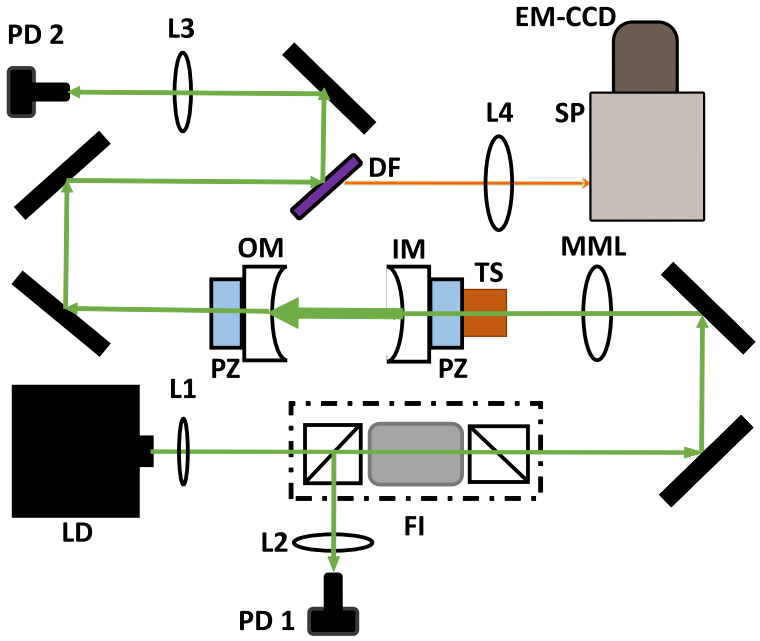

Fig. 3.2 Schematic of the CERS set-up. Acronyms: LD - CW laser diode, L - lens, PD - photodiode, FI- Faraday isolator, MML - mode matching lens, TS - translation stage, PZ - piezo-actuated mirror mount, IM - in-coupling mirror, OM, out-coupling mirror DF - dichroic filter, SP- spectrograph, EM-CCD - Electron-multiplying charge-coupled device.

Once the excitation light left the diode it was collimated by an aspheric lens **L1**, after which it passed through a Faraday isolator, **FI** which provided optical isolation against back reflections and prevented the diode from destabilising. A knife-edge technique, principles of which are outlined in appendix A, measured the beam waist radius w_1 of the collimated laser emission to be 500 μm. The collimation was checked by measuring the beam waist w_1 at various points along the beam over a distance of 1.5 m, which was found to be unchanged. A cavity distance of l = 3 mm was chosen for this setup along with mirrors of equal radii of curvature $\mathcal{R}$ = 1 m, to facilitate cavity's alignment and maximise the potential power amplification. This resulted in a calculated beam radius for the cavity (using Eq. 2.30) of w_0 = 81 μm at 532 nm.

The characteristic length of the system was f_0 = 240 mm (calculated using Eq. 2.33) using the values of w_1 = 500 μm and w_0 = 81 μm. This meant that a lens with f = 250 mm was suitable for mode matching. Since the laser beam was collimated, it was only necessary to calculate the distance d_0 (using Eq. 2.34) to establish the displacement of the lens from the in-coupling mirror, which was determined to be 262 mm. Therefore, after the Faraday isolator, beam guiding mirrors directed the laser light towards the mode matching lens, **MML** which coupled the laser light into a linear optical cavity consisting of two highly reflective

in-coupling **IM** [160] and out-coupling mirrors **OM** [161], with the reflectivity values for a corresponding wavelength listed in Table 2.3.

In order to achieve resonance in the cavity and observe signal output, its length needs to be a half-wavelength integer multiple of the lasing wavelength. In reality, this condition is difficult to achieve, so it is common to mount the mirrors into piezo actuated mounts, **PZ**, that possess a nanoscale precision, and to attach these mounts to a translational stage, **TS**, that has micron-scale positioning precision. The Kinematic Mirror mounts **PZ** used were Thorlabs Polaris - K1PZ with 3 piezo electric adjusters, coupled with piezo electric actuators (Polaris Thorlabs MDT693B), which possess three directional axes of control. The employed translational stage was Thorlabs DRV517 Feedback Piezo Element With Differential Micrometer, **TS**, controlled by Thorlabs KPZ101 K-Cube Piezo Controller, that provided single axis displacement to the in-coupling mirror. The resonance position of the out-coupling mirror was enforced by driving the piezo actuator using a periodic triangle function (with a frequency of 100 Hz) provided by a Wavetek model 142 analog signal generator [143].

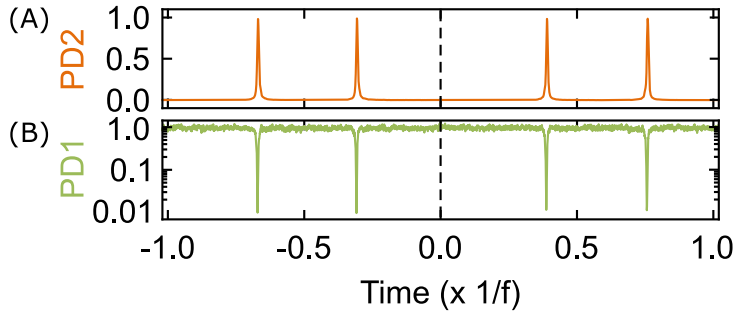

Fig. 3.3 Normalised voltage signals for a) modes transmitted through the cavity (collected by PD2) and b) Modes reflected from the in-coupling mirror (collected by PD1) as a function of the normalised modulation frequency.

During the continuous sweep of the out-coupling mirror position, at some point, the length of the cavity satisfied the resonance condition, where the cavity produced a series of light pulses out of the out-coupling mirror, **OM**, that are incident on a 532 nm long-pass dichroic mirror (LPD02-532RU-25), which allowed the Raman signal to pass through and reflect the pump laser radiation at 90 degrees. The reflected pump radiation was focused onto a Thorlabs photomultiplier PMM01 **PD2** via a 25 mm diameter, f = 50 mm lens, **L3**, allowing to monitor the intensity of the cavity's resonance peaks. The frequency of the mirror's position modulation function affected the intensity of the resonance peaks, which depends on the time the system has spent in resonance [149]. Increasing the amplitude of the

voltage of the modulation function dictated how many resonance peaks are observed in one sweep.

Additionally, during the periodic length modulation of the cavity, the light reflected from the in-coupling mirror, **IM**, was collected at the exit of the Faraday isolator and was focused down onto a Thorlabs photodiode DET10A, **PD1**, via a 25 mm diameter, f = 50 mm lens, **L2**. This signal provided information on the impedance matching of the optical cavity. Figure 3.3b shows the normalised reflected signal from the in-coupling mirror to highlight the fraction of light getting into the cavity on resonance. In order to estimate the absorption losses in the resonator, Eq. 2.42 was used with the reflectivity values of the cavity mirrors at 532 nm shown in Table 2.3. The absorption losses, A, were determined to be 9.3×10^{-4} (using Eq. 2.42) for an impedance-matched cavity. In reality, the cavity is likely to be over coupled as a result of the higher transmission coefficient of the in-coupling mirror. Therefore, the cavity benefits from larger recirculation power due to the increased transmission. Yet the cavity also suffers from lower excitation power transmitted due to the lower transmission coefficient of the out-coupling mirror [150].

The signal read by **PD2** was then used in a feedback circuit to minimize the magnitude of higher-order TEM modes via cavity alignment. Figure 3.3a shows the normalised **PD2** signal observed during the periodic displacement of the output mirror, with the experimental finesse being determined by the magnitude of the cavity line-widths and the calculated $\Delta\nu_{\mathrm{FSR}}$. A forward collection geometry was chosen instead of the 90° collection geometry from the centre of the cavity as this provided benefit from not only the increased effective volume but also from any small increases in signal due to the Purcell effect.

Once the cavity has been successfully aligned, the piezo modulation signal was changed to a rising DC offset until resonance was achieved and **PD2** detected a mode output. The **PD2** signal was fed into the lock-in amplifier that was sensitive to the voltage changes in the cavity signal. The out-coupling mirror position was corrected by the lock-in amplifier via a feedback DC voltage signal fed into the signal generator, which in turn altered its DC signal in order to bring the out-coupling mirror back to the resonance position, resulting in a cavity behaving as a high power CW laser.

The radiation that passes through the dichroic mirror, **DM**, consisted of Stokes Raman signal, as the anti-Stokes signals were below 532 nm and were reflected by the long-pass dichroic mirror (LPD02-532RU-25). Similarly to the free space CW setup, discussed in Section 3.1.1, the Stokes photons were focused down by a lens of 25 mm diameter, f = 100 mm, **L4**, onto the aperture of the Andor Shamrock SR-303i spectrograph with a slit size of 150 μm, which used a 600 l/mm grating prism. The output of the spectrograph is monitored by the Andor Ixon Ultra-888 EM-CCD camera. With the same acquisition settings

used as in free space CW case. Now that the models and the experimental procedures for free space and cavity based methods have been discussed, the calculated and experimental ratios of Raman signal from the two setups are now compared on ambient air.

3.2 Comparison of free-space and cavity-based methods

3.2.1 Model comparison

The ratio of theoretical counts of free-spaced vs Cavity based method is obtained by division of Eq. 2.50 by Eq. 2.12, as they both output rate of Stokes photons production, resulting in:

$$\frac{\gamma_c}{\gamma_f} = \left(\frac{128n}{3\pi^2}\frac{1}{\mathrm{NA}^3}\mathcal{F}_p\beta\right)\left(\frac{\nu_S}{\nu_p}\right)^2\left(\frac{\Delta\nu_S^{(f)}}{\Delta\nu_S^{(f)}+\frac{c}{2nl\mathcal{F}_S}}\right)\left(\frac{c\Delta\nu_p^{(f)}}{\nu_S l(\nu_p+\nu_S)}\right)\left(\frac{P_cN_c}{P_fN_f}\right). \tag{3.1}$$

where $P_{c/f}$ and $N_{c/f}$ are the input power and molecular number density for the free space and cavity-based methods, respectively. In order to find the main parameters governing the gain for a high power CW laser in free space compared to the same laser coupled with a high finesse cavity, it was assumed that the same laser power and gaseous sample conditions are used, such that $P_cN_c = P_fN_f$. Additionally, it is assumed that $\nu_S/\nu_p \approx 1$, and for cases with macroscopic cavities, $c/(2nl\mathcal{F}_S) < \Delta\nu_S^{(f)} = \Delta\nu_S$ and $n = 1$. It is also known that $\Delta\nu_p^{(f)} = c\Delta\lambda_p^{(f)}/\lambda_p^2$. An ε substitutes for the relative line width for the laser used, so that $\Delta\lambda_p^{(f)} = \Delta\lambda_p = \varepsilon\lambda_p$, with a value $\varepsilon \approx 1 \times 10^{-5}$ in this work. This results in the following simplified expression for the theoretical ratio of the Stokes emission between cavity and free space setups:

$$\frac{\gamma_c}{\gamma_f} = \left(\frac{64\varepsilon}{3\pi^2}\frac{1}{\mathrm{NA}^3}\,\mathcal{F}_p(\lambda_p/l,\mathcal{R}/l)\,\beta(\mathcal{R}/l)\right)\left(\frac{\lambda_p}{l}\right). \tag{3.2}$$

Equation 3.2 shows that the main factor controlling the Stokes signal amplification is the NA, as that represents the total effective volume of emission and collection in free space. The larger the volume illuminated with the same power, the larger the signal obtained in free space, and thus the smaller the relative amplification obtained by a cavity setup. Values for the ratio in Eq. 3.2 are plotted in Fig. 3.4 as a function of non-dimensional parameters $\mathcal{R}/l$ and λ_p/l, using a value of NA $= 0.003$, which is consistent with the **NA** value used in the present free space experiments. If **NA** value was not held constant, for realistic experimental values of NA $= 0.002 \rightarrow 1$, the maximum Stokes emission ratio magnitudes could range from 10^{-2} to 10^4.

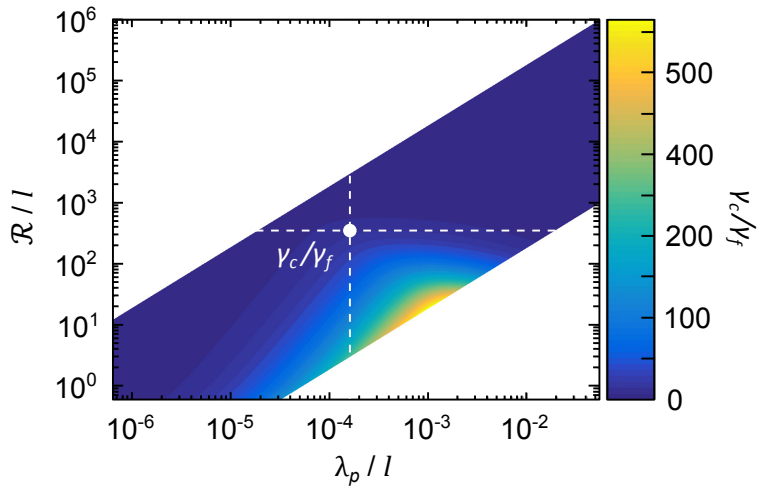

Fig. 3.4 Theoretical ratio of CERS vs. free space Stokes photon emission rate ratio for N_2 in air at ambient conditions, as a function of non-dimensional parameters: $\mathcal{R}/l$ and λ_p/l. The dashed white lines indicate experimental values of the non-dimensional parameter ratios. The Stokes photon emission ratio was calculated by Eq. 3.1 with an experimentally used NA value of 0.003.

Figure 3.4 shows that for a fixed pump wavelength, higher Stokes emission values using a CERS are obtained for either smaller cavities, or cavity built with mirrors of smaller radius of curvature. To achieve the highest γ_c/γ_f ratio for an excitation wavelength of 532 nm, Fig 3.4 indicates that the ideal cavity length and radius of curvature are $\approx$ 50 μm and $\approx$ 10 cm, respectively. Please note that, as discussed in Section 2.3.8, when the length of the cavity is reduced, the number of possible modes within the cavity also decreases. The resonant emission will occur every several nanometers (for a μm cavity) rather than a fraction of a nanometer (for a mm cavity), giving a greatly reduced emission spectrum (see Figure 2.7c) due to difficulty in meeting the double resonance condition.

The value for $\mathcal{F}_S$ (in Eq. 3.1) used in our experiments is limited to 3 due to the values of the mirror reflectivities at the Stokes wavelength for nitrogen, which is substantially smaller than the pump finesse, $\mathcal{F}_p$ that is closer to 4000. Therefore, $\mathcal{F}_p$, and the resonant recirculation process dominates the γ_c/γ_f ratio as shown in Eq. 3.2. It is possible to further increase the Stokes emission ratio value by ensuring that the correct optical elements for the species of interest are used in order to increase the value of $\mathcal{F}_S$. In general, this value is very much dependent on the mirrors reflectivities at Stokes wavelength.

For an increased reflectivity at the Stokes wavelength, the influence of the Purcell effect on the γ_c/γ_f ratio can be investigated. In this regime, the assumption that $c/2nl\mathcal{F}_S < \Delta\nu_S^{(f)}$ no longer holds true and $\mathcal{F}_S$ becomes important. Similarly to the $\mathcal{F}_p$, $\mathcal{F}_S$ also depends on the parameters $\mathcal{R}/l$ and λ_S/l. Therefore when the Purcell effect has a significant contribution the

expected γ_c/γ_f ratio has a more complex dependence. In order to distinguish and compare between the contributions from the recirculating power and Purcell effect, one would have to measure the flux of Stokes photons in the forward scattering geometry, along with the 90° scattering geometry from the middle of the cavity. Accounting for the differences in the effective volume, any measured increase in the flux of Stokes photons from 90° collection in contrast to the in-line collection would be due to the Purcell effect.

Figure 3.4 shows that the theoretical value of γ_c/γ_f for the present investigation should be around 18 for the same total input power, indicated by the white point. In order to compare the effectiveness of the CERS to free space technique, the expected power-dependent Stokes emission values were shown to be γ_f = 335 photons s^{-1} and γ_c = 611 photons s^{-1} by using Eq. 2.12 and Eq. 2.51, respectively, in conjunction with their complementary input parameters shown in Table 3.1.

To evaluate the accuracy of the model the two species (N_2 and O_2) of interest will now be discussed and the experimentally measured normalized signals will be compared to the model predicted values.

3.2.2 Experimental Comparison

Figure 3.5 shows the CW and CERS acquired Raman spectra for laboratory air, with the corresponding N_2 and O_2 peaks appearing at their respective 2331 cm^{-1} and 1555 cm^{-1} Raman shift values, acquired by the same spectrograph and EM-CCD with the same settings. To recall, the differential Raman scattering cross-section values for N_2 and O_2 are listed in Table 2.1 and the experimental parameters are outlined in Table 3.1. The laser power values outlined in Table 3.1 were the maximum powers achieved for the respective lasers after they passed through all of the respective optical elements in order to arrive at the sampling area of interest. As can be seen in Figure 3.5 (a) and Figure 3.5 (b) the measured count numbers

Table 3.1 Parameters used for acquisition of theoretical and experimental ratios for a N_2 molecule in CERS and CW techniques. EM gain = 200 and integration time = 60 s for both methods.

Experiment type	CERS	CW	Ratio
P_{in} (W)	0.02 (P_c)	0.2 (P_f)	0.1
NA	-	0.003	-
l (m)	0.003	-	-
$\mathcal{R}$ (m)	1	-	-
Theoretical (photons s^{-1})	611 (γ_c)	335 (γ_f)	1.8
Experimental signal ($\times$ 10^5 counts)	27	8.8	3.1

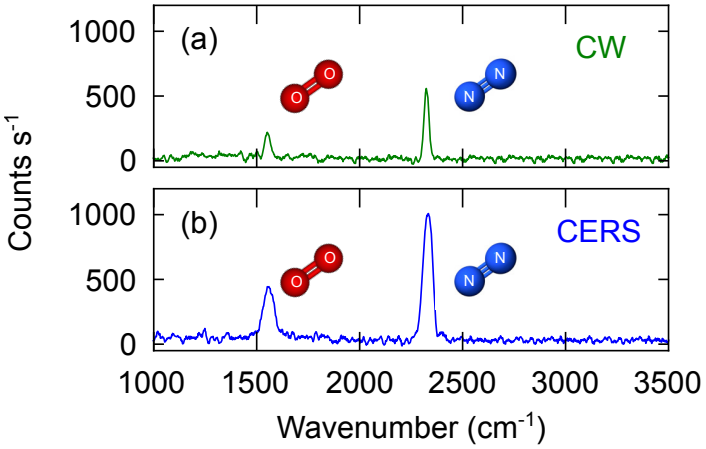

Fig. 3.5 Spectra of gas-phase Raman detection using (a) CW laser and (b) CERS of room air.

for N_2 integrated over the 2331 cm^{-1} peak areas are approximately 8.8×10^5 counts and 27×10^5 counts for an integration time of 60 s, for CW and CERS, respectively. As the measurements were carried out with an EM gain of 200, the normalized values for the CW and CERS techniques are 73 counts s^{-1} and 225 counts s^{-1} (assuming linear gain), respectively.

One could also compare the measured counts s^{-1} with the theoretically determined photons s^{-1} calculated in Section 3.2.1. The discrepancies between the theoretical and experimental values are shown in Table 3.1. For the free space CW case, these differences could be accredited to the imperfections in the size estimation and the overlap between the collection and illuminated volumes, which are assumed to be ideal in Eq. 2.9. Additionally, there are optical losses through the coupling optical fibre, resulting in not all of the generated Stokes photons being transmitted through the collection optics. Furthermore, the theoretical number was calculated for a pump wavelength of 532 nm, whereas the radiation source used was centred at 514.5 nm. This leads to one expecting a larger differential Raman cross-section for a lower wavelength, which would result in more photons. The decision to use the 532 nm pump wavelength for the theoretical calculations was made in order to facilitate the direct comparison between the two employed techniques.

For the CERS case, it can be observed in Figure 3.5 that the line-widths for CERS measurements are approximately twice as wide as the line-widths for the CW measurements. This could be due to multiple modes being excited within the cavity at once, leading to the broadening of the line-width. Furthermore, the stability of the locking technique used in this work was not ideal. It permitted drifts of cavity length over the duration of the experiment for longer exposure times, resulting in a fractional change in the amplified wavelength value, which once again, would lead to the increase of the cavity line-width. In addition, similar to

the CW case, it is possible that some of the radiation was lost due to going through additional optical elements before reaching the spectrograph.

In order to compare the theoretical γ_c/γ_f ratio and the experimental ratio, one assumes that the signal scales linearly with power [108] and number density, as stated in Eq. 3.1. For the free space and cavity-based methods, the measured power at the focal point was 0.2 W (see Section 3.1.1) and the measured power before entering the cavity was 0.02 W (see Section 3.1.2), respectively. In addition, for room air at atmospheric pressure, the number density of oxygen and nitrogen molecules is the same in both the cavity and free space setups. Therefore, hypothetically if the initial laser powers were the same in both experiments ($P_c = P_f$) the experimental gain ratio would then become 30 rather than 3 (shown in Table 3.1), which is closer to the model prediction of 18 (calculated by Eq. 3.1). In order to get a fairer comparison, one would need to directly measure the difference between a high power CW laser in free space versus the same laser coupled with a high finesse cavity.

Nevertheless, such power amplifications have highlighted CERS capabilities in amplification of Raman signal from gas phase species. However, it became clear that this technique was not applicable for *in situ* measurements of CNT synthesis in a FC-CVD reactor. The furnace, in which the reactor is placed, has a typical width of 300-500 mm, which is 2 orders of magnitude larger than the present cavity length. While an increase in cavity length results in higher mode density, it also introduces additional losses from molecules present in the volume. Most importantly, CERS operation relies on perfect beam alignment. CNT synthesis process occurs at temperatures around 1100-1400 °C, with temperature gradients present in the gas mixture, located in the reactor. This would give rise to localised fluctuations of the refractive index that would result in beam steering. Furthermore, the power amplification inside the cavity heavily relies on the reflectivity of the mirrors, which may become contaminated during the synthesis process. It was difficult to devise a solution that would maintain precise alignment of the mirrors during the furnace heating and cooling periods. Therefore, the project moved on to a different method of Raman spectroscopy, discussed in the following chapters.

3.3 Conclusions

This chapter provided a comparison for the use of spontaneous Raman scattering in gases, using either a high power CW laser or a lower power CW laser with an optical cavity formed out of two mirrors with high reflectivity for the wavelength of the pump laser. A model was developed, showing that the main design parameters governing the cavity gain relative to a free-space system are a) the cavity length relative to the mirror radius of

curvature, b) the cavity length relative to the wavelength and c) the numerical aperture used for the free-space system. The model is able to compute an amplification factor of Raman Stokes signals for CERS in comparison to free-space setups. The amplification factor has a strong dependence on the experimental parameters for both the free-space and cavity-based methods. Results show that amplification is not effective for unconfined light collection with the lowest numerical aperture. In reality, high numerical apertures are not feasible for *in situ* applications. This work showed that for low numerical apertures such as those in gas pipes or other remotely accessible devices, cavity-based methods can become attractive for multiplying the gas phase Raman signal emerging from the effective volume.

The expected Raman gain ratio between cavity-based and free-space signals using theoretical and experimental methods were compared. In the theoretical comparison, using the experimental parameters of free-space and CERS setups as input, resulted in the CERS gain factor of 18 per same laser pump power. CERS system was built out of inexpensive components forming a relatively small cavity. In the carried out experiments, CERS system used a laser with an order of magnitude lower power than the free-space system. The expected signal ratio (from the model) was 1.8 in favour of the cavity, and the experimentally measured value was 3.1. Inaccuracies in the estimation of the geometric and other parameters may have contributed to the observed difference.

Furthermore, the chapters provided an analysis of the potential and trade-offs for the measurement of gases in practical systems and outlined a comprehensive design process for selecting an appropriate pumping wavelength, cavity length, radius of curvature and reflectivities of the mirrors for significant signal amplification. This would allow investigators to understand the enhancement that can be practically obtained for a particular system and target species and plan their work accordingly.

While CERS showed great potential in amplification of Raman signal for gaseous species its application for analysis of a FC-CVD system looked challenging. CERS relies on the precision of beam overlap and mirrors' surface quality, which would be very difficult to maintain in a FC-CVD reactor due to temperature gradients and the formation of solid state species.

However, CERS has demonstrated great promise in studies of non-reactive flows or, potentially, reacting flows at room temperature, provided the mirrors can be kept free of surface contamination. Optimised CERS setups would be able to provide high-resolution continuous Raman spectra, at the fraction of the cost of powerful CW systems. Potential use for the system, due to its small footprint, is to be applied as an in-line gas sensor that can monitor the input and output molar and mass fractions of the reagents and products used for the CNT formation via FC-CVD in the reactor. Alternatively, CERS could allow

real-time, low-cost, small-footprint *in situ* measurements in a broad scope of scientific and industrial fields, ranging from the very small scale to planetary atmospheric detection including biological analysis [162], fermentation gases [163], food quality control [164], and deep-sea explorations [165].

Chapter 4

Development of Pulsed Laser Raman spectroscopy setup

4.1 Introduction

This chapter discusses the development of the excitation and Raman collection parts of the pulsed laser Raman system on a flat flame burner in preparation for *in situ* measurements inside a FC-CVD reactor. The discussion covers experimental techniques aimed at enhancement of Raman signal while minimising the influence of other competitive spectroscopic processes. Particular emphasis has been placed on the configuration of the laser beam and collection paths, spectral filtering of the acquired Raman signatures and maximisation of the spectroscopic resolution. The capabilities of the system were tested by performing temperature measurements and species identification in a flat flame.

4.2 Desired System Characteristics

Chapter 2 described the principles of spontaneous Raman scattering, in particular its dependence on the intensity of excitation radiation and emission lifetime of the Raman process. However, the application of Raman spectroscopy in high temperature reacting flows is quite challenging. Such environments contain high radiative backgrounds where multiple spectroscopic processes may be taking place, with their respective differential cross-sections higher than Raman's by few orders of magnitude. The emission lifetime of these processes is, however, significantly longer by few orders of magnitude. Therefore, Raman emission can break through the noise floor when excitation occurs with the use of high-intensity pulsed lasers. Fast temporal shutters are used in acquisition systems with gating windows

configured over the duration of the excitation pulse to prevent the detector from collecting additional thermal and radiative noise, in order to minimise their contributions to the acquired spectra [166].

A typical FC-CVD reactor used for CNT synthesis consists of a quartz tube enclosed by an electric furnace that maintains the carrier gas and reactants at high temperatures. The challenges for the application of optical diagnostics in such a reactor are associated not only with the background luminosity but particularly with problems of laser light injection and signal extraction in and out of the reactor. The solutions to this problem are discussed in Chapter 5.

The present chapter discusses (a) the equipment setup for the delivery of sufficiently high energies per pulse and image acquisition for obtaining pulsed Raman scattering intensities in high-temperature environments, (b) testing of the capabilities of the system using a flat flame.

4.3 Pulsed laser Raman setup for premixed flame diagnostics

The configuration schematic of the Raman signal delivery and collection system is shown in Fig. 4.1a. The excitation EM radiation was provided by a Litron LDY300 pulsed laser **(PL)**, Nd:YLF type with a dual cavity system and emission centred at 527 nm. The beam had an elliptical shape of 10 mm x 2 mm along the minor axis. The laser system is capable of high repetition rates (0.2 - 20 kHz continuously variable) with a pulse duration of 300 ns, which is a crucial characteristic as discussed in Section 2.2. Output energies at 70 % maximum current were measured as 19 mJ per pulse at 1.5 kHz, adding up to approximate total energy of 38 mJ when operated in dual pulse mode with beams temporally overlapped. This was the highest usable laser power that would not cause damage to the non-laser optical elements. The laser beam was guided by two highly reflective, high energy 532 nm mirrors, **M1** and **M2**, (with FWHM of 10 nm) onto a 50 mm diameter visible coated lens, **L1**, with a focal length of 100 mm. This lens focused the laser beam in the centre of the target sample, and onto a beam dump, **BD**.

The target consisted of the reactants and products of methane-air mixture pre and post-combustion, respectively, on top of a flat flame burner. The measurements were made at a starting distance of 2 mm above the surface of the burner (height above burner - HAB), well into the uniform product region of 11 mm. The equivalence ratio, ϕ, was varied from 0.76 to 1.15, with further details available in the results section 4.4.

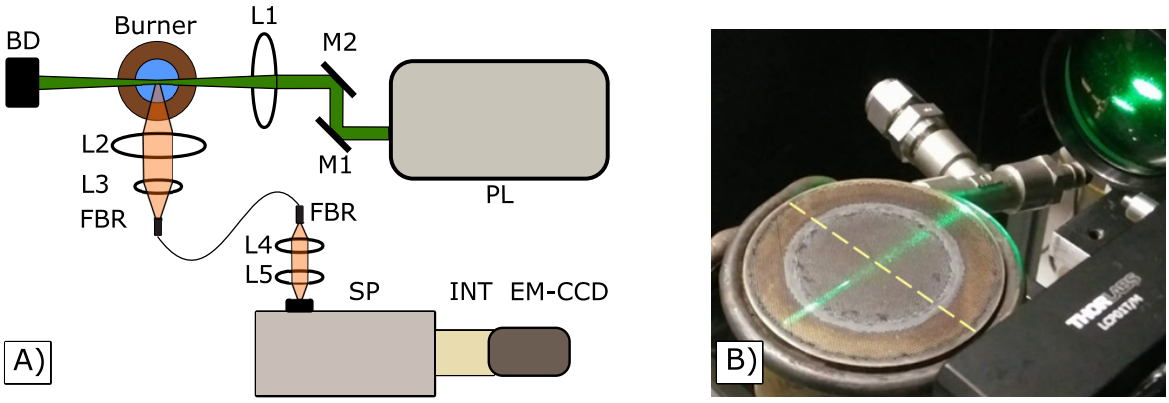

Fig. 4.1 a) schematic of pulsed laser fiber coupled Raman spectroscopy set-up Acronyms: PL - Pulsed laser diode, M - mirror, L - lens, BD - beam dump, FBR - fiber, SP - spectrograph, INT - intensifier, EM-CCD - Electron-multiplying charge-coupled device. b) the laser beam and collection configuration.

Scattered Raman signal was collected and collimated at 90 degrees from the beam direction and from the vertical, by a 50 mm diameter visible coated lens with the focal length of 100 mm, **L2**, as shown in Fig. 4.1b. The collected emission was then focused by a 25 mm diameter, f = 50 mm focal length lens, **L3**, which coupled the light through a 532 notch filter, **NF**, (with FWHM of 10 mm) onto a 1000 μm Ocean Optics fiber, P1000-2-UV-VIS, **FBR**. This fiber core size was chosen to maximise the amount of delivered light, at the cost of resolution. At the outlet of the fiber, the light was recollimated with the use of a 25 mm diameter, 100 mm focal length lens, **L4**, and focused down onto the input slit of a Shamrock-303i spectrograph, **SP**, using a 25 mm diameter lens, **L5**, with a focal length of 50 mm. The slit size was set to 1000 μm. The spectrograph has a 3 sided prism with grading ruled numbers of 300, 600 and 1200 ln/mm, allowing to focus on spectral regions of different sizes, at the cost of resolution. Additionally, it has two input ports, one perpendicular (side) and one along (front) the camera axis. The side port was used for light injection in order to prevent any stray laser emission, that might enter the spectrograph, from reaching the imaging apparatus. The Andor acquisition system consists of a spectrometer and Andor Ixon Ultra-888 EM-CCD, which has been factory calibrated. The camera is able to run in multiple acquisition settings, including fast speed acquisition for kinetic series with external triggering. However, the smallest possible exposure interval of the camera while it's in external triggering mode is 10 μs, which is too large in order to provide appropriate rejection of background luminosity and fluorescence. As a result, 'invisible Vision UVi' Camera intensifier (model 2550-10), **INT**, was used as an additional filtering device.

The usually connected spectrograph and EM-CCD were decoupled, in order to accommodate the intensifier, placed between the spectrograph and the camera. A coupling mount

was 3D printed in order to couple the output of the spectrograph to the input of the intensifier. It fully covered any gaps between the walls of the spectrometer and the intensifier input, preventing any stray light from entering into the spectrometer from the output port. Furthermore, it kept the aperture of the intensifier centred relative to the middle of the spectrometer's output. Particular care was taken to ensure that the focal planes of the spectrometer and the intensifier coincided, with the intensifier and the coupled EM-CCD being placed on single-axis mounting rails for fine adjustments.

The intensifier gating interval can be adjusted from 10 ns to 1 ms in increments of 5 ns, and the delay timings can be set between 30 ns and 10 ms in steps of 5 ns. No signal is transmitted when the intensifier gate is not on so that the device operates as an electronic shutter. However, the intensification process can add additional shot noise, owing to the processes of collision with the intensifier phosphors. The intensifier's operational wavelength range is from 200 nm to 900 nm. The intensifier trigger mode was set to positive edge throughout all of the experiments, being triggered by the laser sync output. The intensifier gain ranges up to 3×10^5.

The Andor Ixon camera was coupled to the intensifier by a Nikon F-mount lens. The camera was thermoelectrically cooled to -40 °C before the experiments were run. The camera was run in 'accumulation' acquisition mode, externally triggered by the 'laser sync' output. The camera exposure window was set to 10 μs, which is its lowest setting.The camera's chip array size was 1024 x 1024 pixels. The collected light was binned vertically over an area of 31 pixels in order to increase the strength of the observed Raman signal. These settings result in the acquisition rate of the camera, and therefore of the Raman system, of 139 Hz.

4.4 Raman spectra of a methane flame

The experiments were run using methane-air premixed mixtures. The equivalence ratio and the HAB were varied to test the sensitivity of the setup to changes in species molar fractions. The Raman spectra were acquired at HABs of 2, 3, 4, 5, 6 and 11 mm in order to provide a wide range of distances for temperature measurements. The burner was cooled with water in order to stabilise its temperature. The premixed fuel consisted of 10 SLPM of air mixed with varied methane flow ranging from 0.8 to 1.2 SLPM in increments of 0.1 SLPM, resulting in equivalence ratios of ϕ = 0.76, 0.86, 0.95, 1.05 and 1.15 respectively. The flowrates were controlled by Alicat MFCs, MC-20SLPM-D/5m.

The stoichiometric reaction equation for complete combustion of methane in air is:

$$CH_4 + 2(O_2 + 3.76N_2) = CO_2 + 2H_2O + 7.52N_2 \tag{4.1}$$

Incomplete combustion would result in the additional formation of CO. Fig.4.2 shows the side view of the flame at different equivalence ratios with the HAB lines at which Raman measurements were performed. The visible length of the primary combustion zone increases with an increase in equivalence ratio, as a result of higher visible emissions from excited products CO* and CO2*, resulting from the higher temperatures created in the product zones of richer flames.

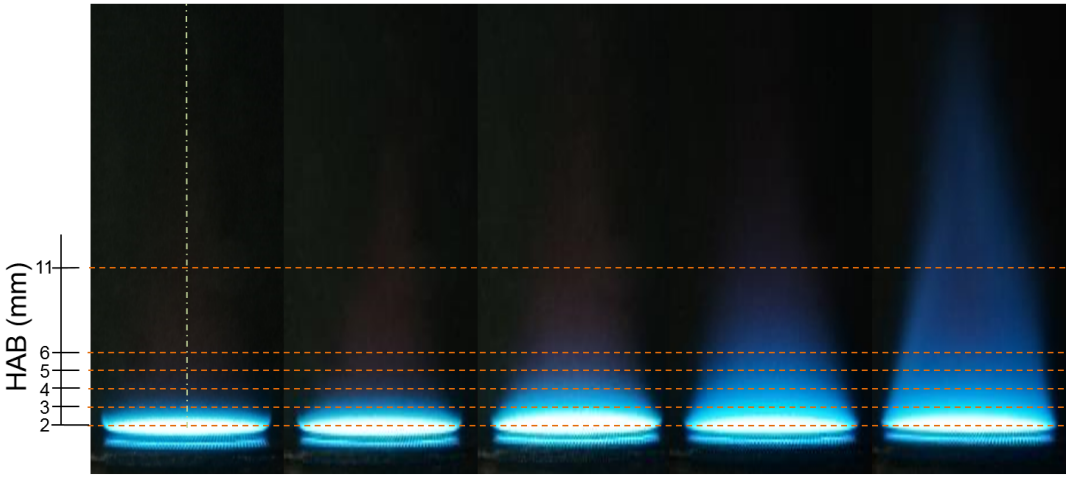

Fig. 4.2 Side view of the flame from a flat flame burner at equivalence ratios, ϕ of 0.76, 0.86, 0.95, 1.05 and 1.15.

The spectrometer grating was set to 300 ln/mm in order to capture Stokes emission of all of the molecules of interest in one acquisition, which were oxygen, nitrogen, methane, water and CO_2, with their respective Raman shifts given in Table 4.1. This covered the frequency range from 176.14 to 4118.30 cm^{-1}. Anti-Stokes Raman emission was captured as well by changing the position of the prism in the frequency space to a range of -5499.05 - 784.30 cm^{-1}. The laser power was set to 70% which resulted in 38 mJ per pulse. The number of shots per acquisition was set to 2000 in order to maintain a constant camera temperature of -40°C and to avoid bleaching. Five acquisitions were collected per each experimental condition, which were all averaged. Electric gain capabilities of the EM-CCD were not used as that resulted in data smearing on the edges of the CCD chip. Instead, the gain was provided by the intensifier that was set to 60%.

As the lifetime of Raman emission is very short, it was crucial to set the timing offset between the laser trigger, the intensifier gating window and the camera start as precisely as possible. The duration of the gating window and its delay with respect to the laser pulse was determined iteratively by maximising the amount of observed signal. This resulted in 4.38 μs trigger delay and 300 ns exposure window length for all conditions. The camera's exposure window start was triggered by a positive edge of the laser pulse.

4.4.1 Stokes flame emission

Figure 4.3a shows the Raman spectra for the premixed fuel mixture at HAB = 4 mm, and ϕ = 0.76, 0.96 and 1.15. The background subtraction was carried out by subtracting the spectra acquired in the absence of the laser pulse. The spectra are dominated by the Raman signatures corresponding to major v_1 symmetric vibrational modes of oxygen (O-O), nitrogen (N-N) and methane (C-H) that are clearly observed at 1562, 2346 and 2976 cm^{-1} respectively. The shoulder on the right side of the methane mode is due to the presence of modes that make up the higher-order pentad of methane. Resolution with the selected grating was quite coarse so that one could not distinguish the individual modes that make up the pentad's finer structure. Additionally, a smaller $2v_4$ methane Raman mode at 2594 cm^{-1} is observed, which could be interpreted as an acquisition anomaly. The magnitude of methane Raman mode increases while magnitudes of oxygen and nitrogen modes decrease with an increase in equivalence ratio, as expected.

The spectra of the flame at HAB = 4 mm and ϕ = 0.76, 0.95 and 1.15 are shown in Fig.4.3b. The magnitude of the N-N mode between the two conditions drops significantly as expected, due to a decrease in molecular number density as a function of higher temperature at the measurement point. The peaks of products are clearly distinguishable. The modes corresponding to the presence of methane are not present in Fig. 4.3b and instead the O-H (water) and two C-O (CO_2) modes, $2v_2$ and v_1 are observed at 3652 and 1285/1388 cm^{-1}, respectively. The magnitude of the O-H mode increases as the function of equivalence ratio while the magnitude of the N-N mode decreases. This is a result of the larger fraction of product molecules present relatively to nitrogen in the product gas. Additionally, on average the expected product temperature increases as the function of equivalence ratio, which would result in a reduction of number density and lead to a lower magnitude of the N-N mode.

The magnitude of CO_2 first increases with equivalence ratio, following a decrease at ϕ = 1.15 where another mode is observed at 2100 cm^{-1} which can be assigned to the C-O mode of carbon monoxide, which appears as a product of incomplete combustion. This could

Table 4.1 Raman shifts for molecules involved in methane combustion.

Molecule	v_p-v_s (cm−1)
O_2	1555
N_2	2331
CH_4	2986
CO_2	1285/1388
H_2O	3652
CO	2100

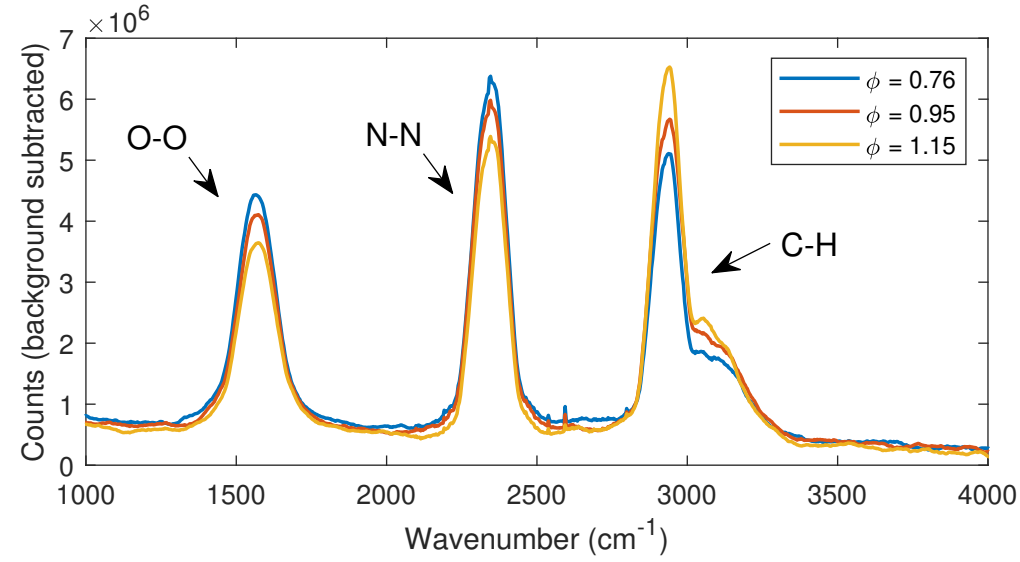

(a)

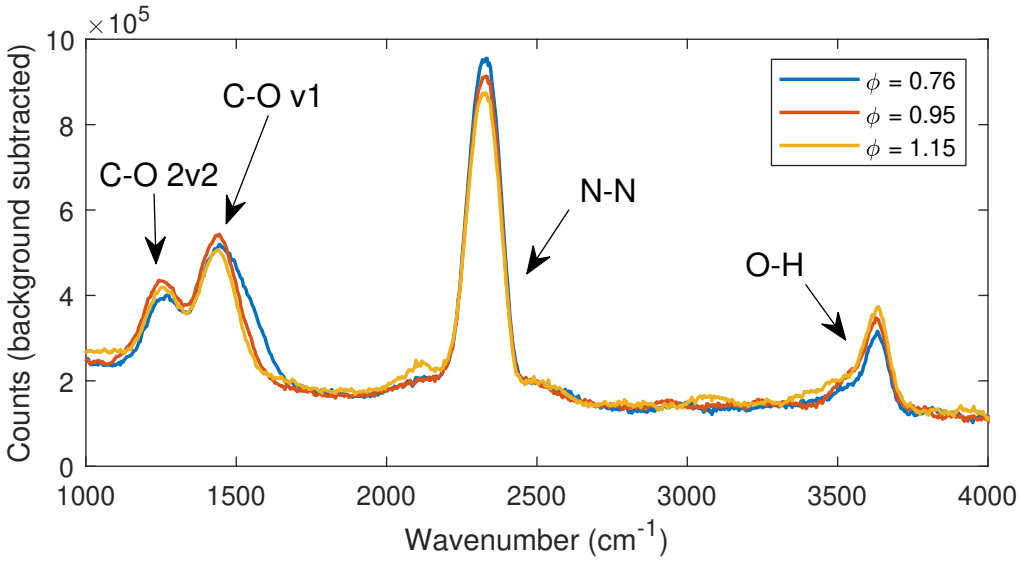

(b)

Fig. 4.3 Spectra of a) unreacted fuel-air mixture and b) methane flame products at HAB = 4 mm and ϕ = 0.76, 0.95, 1.15.

contribute to the reduction of the CO_2 modes as some carbon is used for CO formation. No overall background increase or Swan bands were observed in the ϕ = 1.15 spectra, making it difficult to state whether any carbon was formed as a product of incomplete combustion. No appearance of orange light was observed in the flame colour, as seen in Fig.4.2. At ϕ = 0.76 one would expect oxygen to be present at 6% molar fraction. It could be argued that the existence of the right shoulder on v_1 C-O mode is due to remaining oxygen, however, it is difficult to state that with certainty as C-O and O-O modes could overlap on account of the low resolution of the system.

4.4.2 Anti-Stokes flame emission

Anti-Stokes spectra of the methane flame were recorded in conjunction with the Stokes spectra seen earlier. They were not recorded for the non-reacting case as the molecular population at room temperature would predominantly be located in their ground energy states, resulting in very low anti-Stokes signal strengths. Figure 4.4 shows the Stokes and Anti-Stokes emission of the premixed methane flame at HAB = 4 mm and ϕ = 0.95. The spectra are dominated by Rayleigh emission of the laser, highlighting the difference between scattering cross-sections of different spectroscopic. The sharp cut-off on the right side of the Rayleigh mode is due to the notch filter incorporated in the system.

Figure 4.4 shows the full Raman spectra of the methane flame at HAB = 4 mm as a function of equivalence ratio. In addition to the Stokes modes observed earlier, their anti-Stokes counterparts are observed at their symmetrical locations with the O-H mode at -3631 cm^{-1}, the N-N mode at -2339 cm^{-1} and the two C-O $2v2$ and $v1$ modes at -1241 and -1421 cm^{-1} respectively. The acquisition setup introduced a lot of noise between -2000 and 650 cm^{-1} for all measurements, making a precise determination of mode locations and intensities challenging. The source of this error was the grating. The behaviour of both Stokes and anti-Stokes modes is similar as a function of the equivalence ratio. However, the anti-Stokes N-N mode reduced a lot less in magnitude compared to its Stokes counterpart. Furthermore, the intensity of the O-H anti-Stokes mode increased a lot more when compared to the Stokes mode. This is due to the molecular population redistribution from ground to higher energy levels as the result of higher environmental temperature, causing increased anti-Stokes emission.

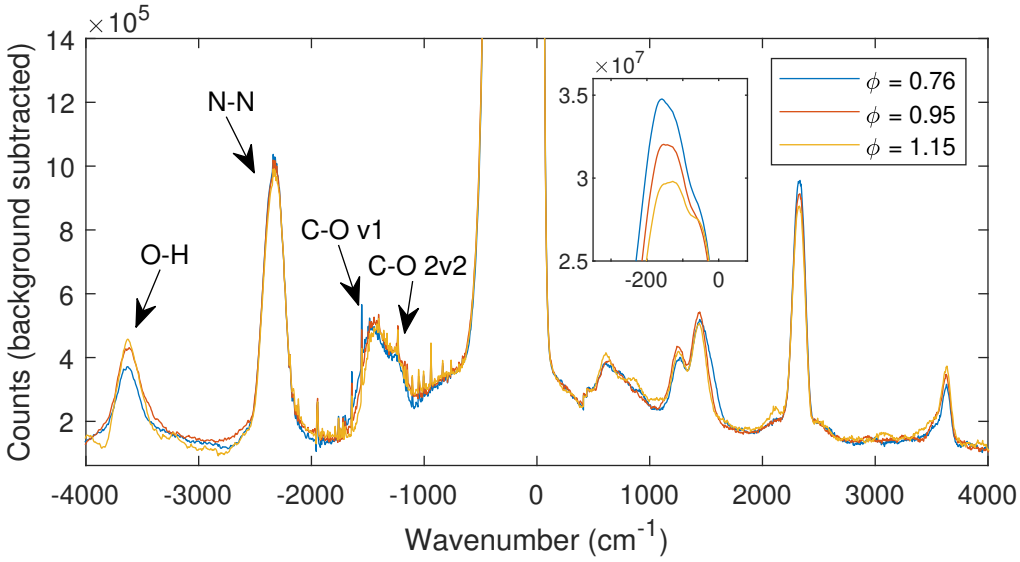

Fig. 4.4 Stokes and anti-Stokes emission of a premixed methane flame at HAB = 4 mm and ϕ = 0.76, 0.95 and 1.15.

4.4.3 Raman temperature measurements of a flat flame

Anti-Stokes/stokes mode ratio

Temperatures of a gaseous environment can be calculated with the use of Anti-Stokes/Stokes ratio [167, 168, 115], which is defined as:

$$\frac{I_a}{I_s} = \left(\frac{v_p + \Delta v}{v_p - \Delta v}\right) \times \exp\left(\frac{\hbar \Delta v}{k_b T}\right) \tag{4.2}$$

where I_a and I_s are anti-Stokes and stokes modes intensities respectively, v_p is laser excitation frequency, Δv is the Raman shift, $\hbar$ is the reduced Planck's constant, k_b is Boltzmann's constant and T is the temperature of the environment [169]. One of the major advantages of this formula is that, provided the acquisition methodology and setup for Stokes and anti-Stokes is the same, it disregards the need for knowledge of the polarization tensor, the degeneracy factor, the number density and the pulse energy. Another advantage of this method is its ability to use any species for temperature determination as long as the acquisition system is sensitive enough to detect anti-Stokes modes at low temperatures. However, particular care needs to be taken when using this method as the instrument response function of the Raman system needs to be known. The photons corresponding to the stokes and anti-Stokes modes are of different absolute wavelengths. So the wavelength-dependent sensitivity of the

instrument needs to be taken into account, otherwise, the measured intensities would not reflect the true signal strengths of the Raman modes pair.

Comparison of measured temperatures

Temperature measurements of the flat flame were performed at HAB = 4 and various equivalence ratios using the Stokes anti-Stokes ratio. Integrated N-N mode intensities were used as nitrogen was the only observed mode that did not participate in combustion reaction and had a good SNR. Figure 4.5 shows the extracted temperatures along with theoretical flat flame burner temperatures (calculated by Dr. James Massey) at the same equivalence ratios at HAB = 4 mm. It can be seen that while the measured temperatures do not exhibit the trend shown by the theoretical curve, their values are within 10%. Sources of error could be in imprecise HAB of the burner or the flame becoming more unstable at higher equivalence ratios.

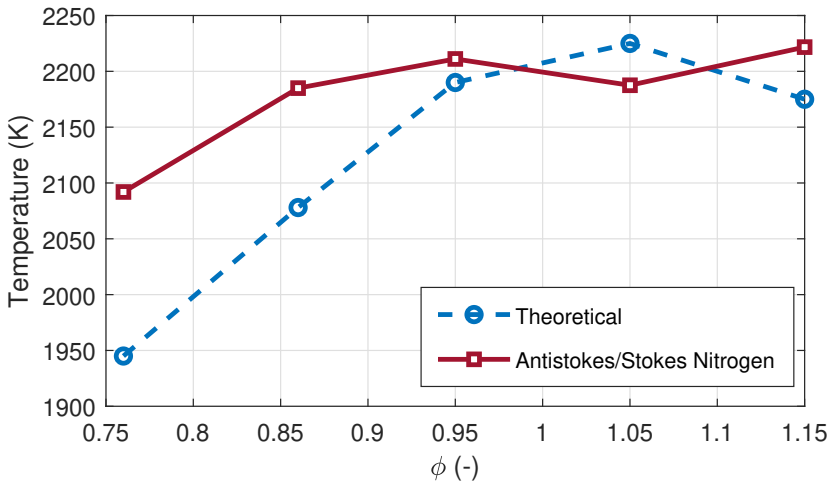

Fig. 4.5 Theoretical and measured temperatures of flat flame burner at HAB = 4 mm as a function of equivalence ratios.

Overall, it has been shown that the Raman system could perform qualitative measurements and be sensitive to molar fraction changes in a reacting flow as a result of different equivalence ratios of the fuel. It also has demonstrated temperature measuring capabilities. However, its two major shortcomings became apparent. The system's resolution was not sufficient to be able to distinguish overlapped modes, which could result in the loss of crucial information when investigating the synthesis process via FC-CVD. Furthermore, the implementation of a 90-degree signal collection inside the reactor would be quite challenging.

4.5 Further Optimisation of Pulsed laser Raman setup for premixed flame diagnostics

The delivery of the laser beam was modified by adding a long-pass dichroic filter, **DF** centred at 532 nm (10 nm FWHM) after the guiding mirror **M2**. Dichroic filter acted as a mirror in the direction of the laser beam propagation. It was positioned at such an angle that it reflected the laser beam at 90 degrees onto another high reflective, high energy broadband mirror, **BM**, which sent the beam through a 50 mm lens, **L1**, with a focal length of f = 400 mm. The focal length of **L1** lens has been increased in order to prepare the system for laser injection and Raman collection into and from the reactor, the centre of which was estimated to be located at that distance from the lens.

The Raman collection system was changed from perpendicular fiber collection to back-scattering, free-coupled, confocal configuration. Some of the Raman emission, isotropically generated at the focus of the laser beam, would retrace the laser beam path in the backwards direction, towards the laser focusing lens, which in turn would collimate it and impinge it onto the broadband mirror and then the long-pass dichroic filter, (LPD02-532RU-25). This allows for easier extraction of Raman emission as only one point of optical access is required. The wavelengths of the Stokes photons from the Raman emission are longer than the cutoff threshold of the dichroic filter, allowing them to transmit through the filter without being reflected. The Rayleigh scattered green laser light is reflected back towards the laser. The collimated Stokes emission passed through a notch filter, **NF**, (centred at 532 nm with FWHM of 10nm) and was then focused by a 25 mm diameter lens, **L2**, with the focal length of 50 mm, onto high energy 50 μm pinhole, **PH**, which prevented stray light from entering the collection path. The Raman emission that passed through the pinhole was then recollimated by a 25 mm diameter, f = 50 mm lens, **L3**, which was subsequently focused by a 25 mm diameter lens, **L4**, with f = 50 mm onto the input side port of the spectrometer with set slit size of 1000 μm. While free coupling the collected Raman emission into the spectrometer could be quite challenging it would result in higher resolution, compared to the fiber coupled emission delivery. Furthermore, this prevents losses that occur from light attenuation within the fibers, which would result in higher signal magnitudes.

The entire emission and collection parts of the Raman system were closed off by matte black shields and covered on top with matte black foil in order to prevent any stray light from hitting the collection optics and further reduce the background noise, as shown in Fig.4.6b. The section after the notch filter has been closed off with the use of shields and black tape, leaving a 20 mm diameter gap for the Stokes emission to pass through. Additionally, matte black foil has been placed underneath the stands of optical elements to reduce reflections

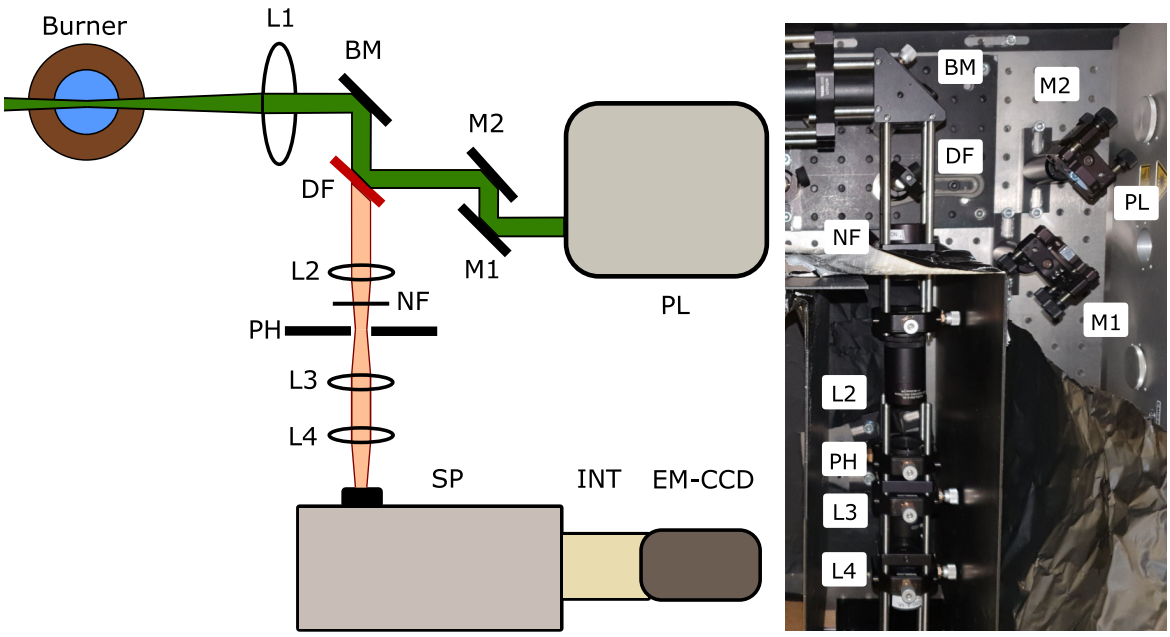

(a) (b)

Fig. 4.6 a) Schematic and b) picture of pulsed laser backwards scattering, free-coupled, confocal Raman spectroscopy setup. Acronyms: PL - Pulsed laser diode, M - mirror, L - lens, BM - broadband mirror, DF - dichroic filter, NF - notch filter, PH - pinhole, SP- spectrograph, INT - intensifier, EM-CCD - Electron-multiplying charge-coupled device.

from the silver metal surface of the optical bench. The spectrograph, the intensifier and the majority of the camera were covered with a box to prevent any stray light from getting inside their imaging parts. The rear end of the EM-CCD was left partially open in order to expose the air cooling vents.

The acquisition settings of the imaging system have been modified to further improve its resolving power. The prism grating of the spectrograph was changed from 300 ln/mm to 1200 ln/mm. As a consequence, it was impossible to image all areas of interest in one acquisition. The frequency space was separated into 9 sections, covering a range from 255 to 4260 cm^{-1}. The acquisition section regions were defined in such a way that each section had at least a 30% wavenumber overlap with the neighbouring sections. This was done to combat vignetting, which was observed on the edges of the acquired spectra. Such acquisition methodology ensured that every peak was at least double captured and therefore its magnitude was not underrepresented. The source of vignetting can be assigned to the performance of the intensifier's photocathode. Each acquisition consisted of 2000 shots with the vertical camera binning over 46 pixels and intensifier gain of 65% which resulted in a camera acquisition frequency of 136 Hz. Five acquisitions were taken at each frequency

Table 4.2 Showing the 9 acquisition regions in wavelength and frequency space.

Section #	Wavelength (nm)	Wavenumber (cm^{-1})
1	535.01 - 566.53	255.26 - 1295.22
2	549.00 - 580.34	731.47 - 1715.23
3	565.99 - 597.12	1278.51 - 2199.39
4	581.00 - 611.92	1734.73 - 2604.54
5	596.69 - 627.41	2187.56 - 3007.94
6	605.00 - 635.60	2417.64 - 3213.36
7	619.99 - 665.17	2817.33 - 3571.00
8	635.00 - 665.17	3198.44 - 3912.92
9	650.97 - 680.92	3584.86 - 4260.49

space section and were then averaged. The resultant section spectra were then stitched together to provide a single output spectrum.

The performance of the pulsed laser Raman system was tested on a compound of interest for the FC-CVD study with its appropriate amounts. Discussion in Chapter 1 identified thiophene, as one of the crucial species used in aerogel synthesis via FC-CVD, where it acts as the promoter. It is a heterocyclic compound consisting of a planar five-membered ring. It's an aromatic molecule, which is a colourless liquid with a benzene-like odour with a melting point of -38 °C. While some thiophene vibrational modes are IR inactive all of them are Raman active, making Raman a good technique for picking up trace amounts of thiophene in the reactor system [170].

Thiophene was delivered into the flow system with the use of a bubbler. In a bubbler system, the delivered thiophene amount depends on the vapour pressure difference between thiophene and carrier gas, which is a function of temperatures of the thiophene containing vessel and carrier gas flow. More detailed calculations of thiophene molar and mass rates in a gaseous environment are given in appendix B.

In this work, thiophene was placed in a thiophene bubbler that was held at 0 °C with an ice/water mixture in a pot. This was done to ensure that the mass rate would remain constant and independent of ambient conditions. The bubbler had switches on the inlet and outlet lines to prevent evaporation. Thiophene was delivered into the system by bubbling nitrogen through the bubbler. The amount of nitrogen delivered through the bubbler was set by an Alicat mass flow controller. The gas lines were modified such that the thiophene containing flow would mix with the methane-air mixture prior upstream of the burner outlet.

Figure 4.7 shows the Raman spectra of 0.5 SLPM of N_2 going through the thiophene pot (3% thiophene molar concentration in seeded flow) at HAB = 4 mm, mixed with $\phi = 0.95$ methane-air mixture (1.0 SLPM of methane, 10 SLPM of air) at ambient conditions. The

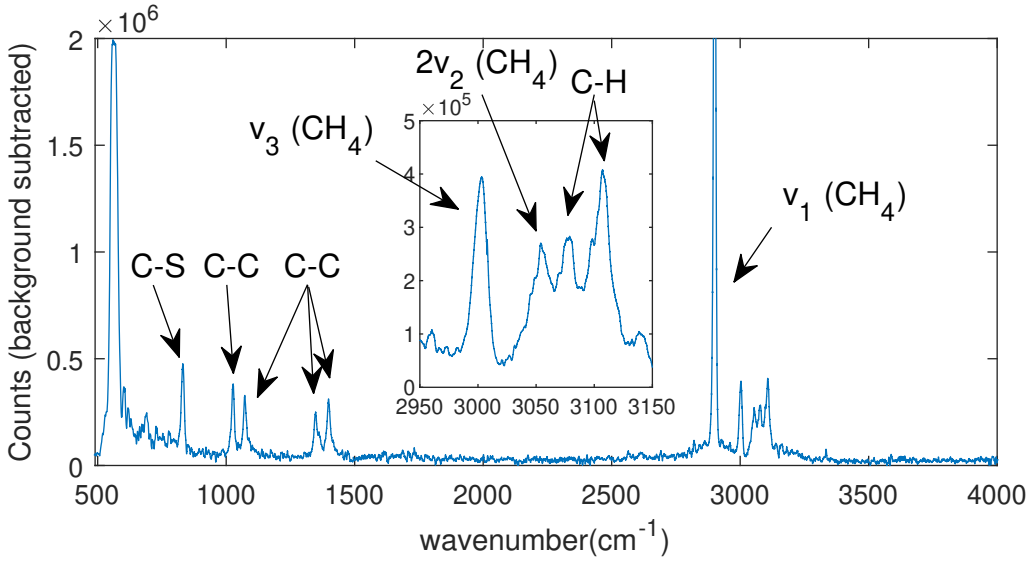

Fig. 4.7 Spectra of 0.03 thiophene molar fraction in 0.5 SLPM N_2 flow mixed with $\phi = 0.95$ methane-air mixture at HAB = 4 mm.

acquired spectra were background corrected by a spectrum of ambient air. Thiophene Raman signatures are clearly observed, with three modes located at 1084, 1364 and 1413 cm^{-1} that correspond to the C=C bond, a mode at 840 $^{-1}$ that is due to the C-S bond, a C-C bond mode at 1036 cm^{-1}, and two C-H modes at 3079 and 3107 cm^{-1}. A much finer structure of methane spectra is observed, in addition to the thiophene Raman modes. The different pentads are now clearly pronounced. In the 3100 cm^{-1} region, the thiophene and methane modes overlap, but they can still be individually resolved, as shown in the insert in the figure. A shoulder on the right side of the main v_1 C-H methane mode at 2900 cm^{-1} is no longer present when compared to spectra in Fig. 4.3a. Instead, the triply degenerate CH-stretch mode, v_3 centred at 3003 cm^{-1} and the $2v_2$ mode at 3053 cm^{-1} were detected.

4.6 Conclusion

A pulsed laser Raman system was developed and tested on a methane-air mixture pre and post ignition on flat flame burner. In a 90 degree Raman collection configuration the system demonstrated sensitivity to variations in molar fractions of flame as a result of different equivalence ratios of the fuel. It also has demonstrated temperature measuring capabilities.

In preparation for performing *in situ* measurements in a FC-CVD reactor the Raman collection part of the system was constructed in a back-scattering, free-coupled, confocal

configuration. Therefore only one location for optical access is required for both laser injection and signal collection in the reactor.

In the new configuration, the Raman system was able to detect thiophene signatures at 3% molar concentration in a N_2 seeded flow. Furthermore, the system was able to confidently resolve Raman modes with peak magnitudes located 30 cm^{-1} next to each other, showing suitable resolving power and overall satisfactory performance of the system.

Thus the discussion will now move on to the implementation of the pulsed laser Raman system with a FC-CVD reactor.

Chapter 5

Design and implementation in situ Raman scattering experiment

5.1 Introduction

This chapter focuses on the design and modifications of the reactor tube in order to enable *in situ* Raman measurements inside a FC-CVD reactor. The justifications of the reactor geometry and furnace alterations are provided. The need for a purging system is outlined, followed by its design and operation principles.

Raman spectra of single chemical species were then obtained to determine the location of key modes corresponding to chemical bonds in the system. Spectra were taken at 20 and 1100 °C to examine species evolution as a function of temperature, in absence of any other reagents.

5.2 Reactor tube design

The reactor tube used for the FC-CVD aerogel synthesis experiments underwent several design changes, shown in Fig. 5.1, which were necessary for maintaining the optical access. All reactor tubes were made from fused quartz and were manufactured by the Cambridge Glassblowing company. Fused quartz has a high-temperature resistance, annealing and softening points at 1215 and 1683 °C respectively, thermal shock resistance, chemical inertness and optical transparency in the 275-2000 nm range, which are key properties for the reactor tubes in this experiment.

The first tube, shown in Fig. 5.1a had a simple cylindrical geometry, with 23.2 mm inner radius, 2.2 mm wall thickness and a length of 600 mm. The reactor tube was placed inside an

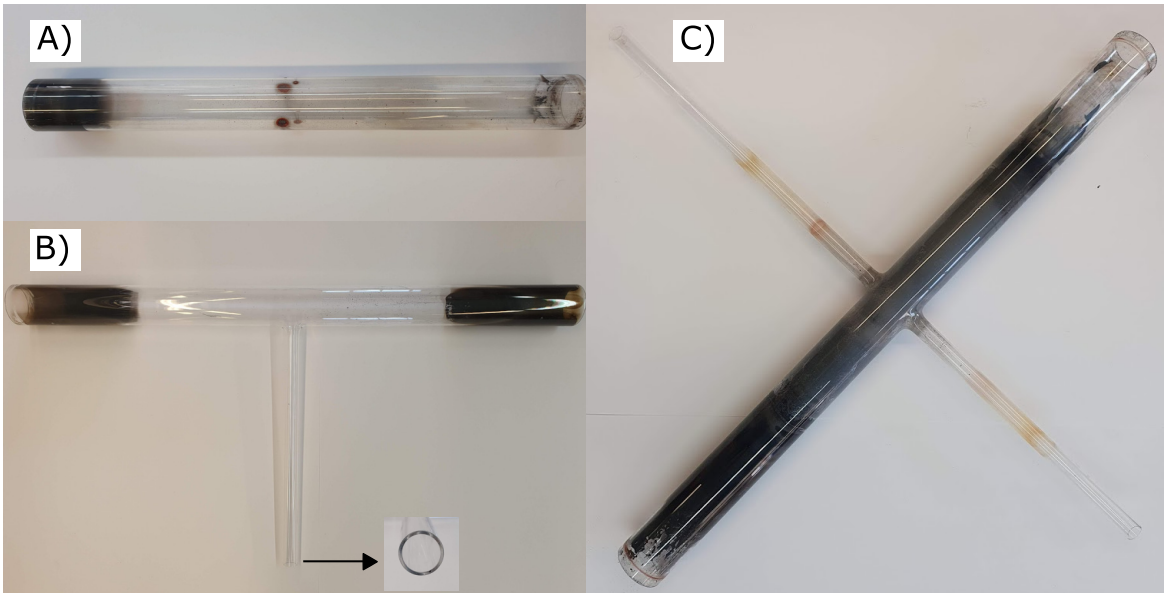

Fig. 5.1 Different reactor tubes a) cylindrical b) 'T-shape' c) cross.

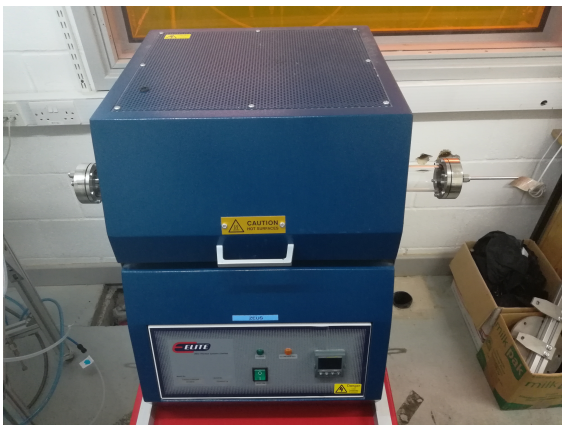

(a) Shows the closed furnace with visible tube ends and sandwich flanges.

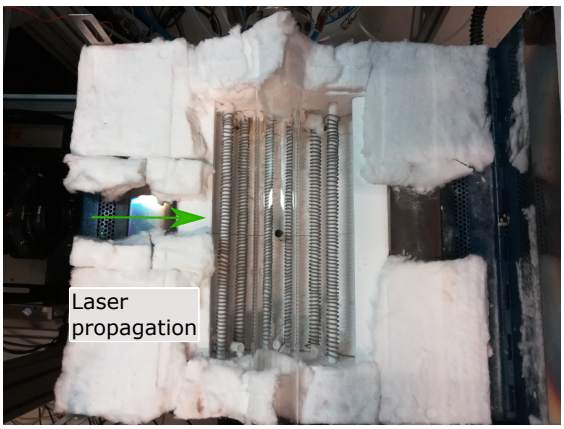

(b) Show top view of the tube positioned inside the furnace.

Fig. 5.2 Shows images of the tube inside the clam shell furnace

electrically heated furnace 'Elite Thermal systems limited' TSHH12/90/305/3216CC, which is horizontally split as shown in Fig.5.2a. It has a single heating zone with the maximum operating temperature of 1200°C. The heating volume has a length of 300 mm and a width of 150 mm. The furnace was placed on a trolley with adjustable height.

The ends of the tube were sealed off with the use of stainless steel sandwich flanges and Viton rings. This provided airtight seals, which was critical in order to prevent the influence of external gasses on the chemical process. CNT synthesis experiments run in a nearly 100% H_2 environment at high temperatures and use/produce harmful chemicals. While Viton has a maximum operating temperature of 230 °C, it was not expected for the flanges to reach that temperature as they are exposed to ambient air. The inlet and outlet flanges had one 6 mm Swagelok fittings welded into them, respectively, to provide airtight gas injection and extraction.

Fibreglass insulation was used to pad out with a thin layer (5 - 10 mm) the contact areas of two halves of the furnace, to improve the furnace's heat retention. Thicker layers of fibre insulation (> 10 mm after compression with the furnace lid) were placed at the laser entry side, to raise the lid such that the laser beam could propagate inside the furnace, as seen in Fig.5.2b. The furnace tube rests were also padded with insulation to raise the tube height such that the laser beam, aligned parallel to the floor level, would enter the tube normal to its wall.

As the laser beam passed through the tube it would impinge on the furnace hinge and the surrounding metal surfaces, burning off paint. This caused specular scatter and resulted in elevated background levels during measurements. A fibreglass layer was inserted before the point of laser impingement on the hinge, which drastically reduced the amount of background noise. High laser energies caused very slow burn-ins in the fibreglass and did not result in any unwanted Raman activity so it was deemed a suitable beam blocking solution.

Figure 5.3a shows Raman spectra of 3% molar concentration of thiophene in H_2 environment at furnace set-point temperatures of 20, 300, 600 and 900 °C. The thiophene molar fractions inside the reactor were achieved by bubbling 0.5 SLPM of pure H_2 through the thiophene pot maintained at 0 °C.

At 20 °C, two C=C modes of thiophene can be observed. The magnitude of the C=C modes decreased as a function of temperature until 900 °C where a broadband emission occurred, two orders of magnitude larger than previous background levels. The observed spectra were akin to blackbody radiation, accompanied by the formation of black-coloured deposition on the edges of the reactor tube. Subsequent Raman measurements performed at lower temperatures and 100% H_2 reactor-mixture composition demonstrated a decrease in broadband emission to the initial levels of background after 10 minutes.

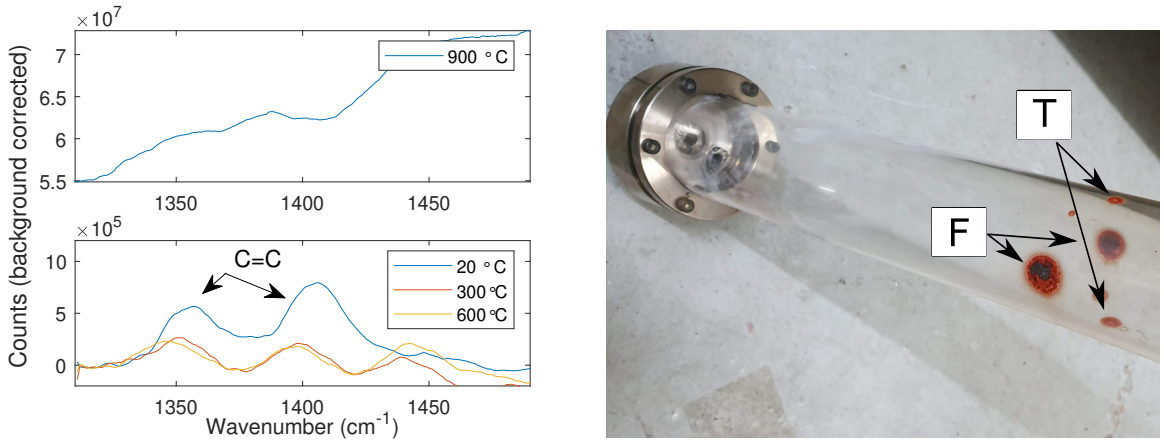

(a) (b)

Fig. 5.3 a) Raman spectra of the C=C mode region of 3% inlet thiophene molar concentration at 20, 300, 600 and 900 °C furnace set temperature in a cylindrical reactor, b) Solid state deposition on the tube wall at the laser impingement location from thiophene (T) and ferrocene (F).

After the reactor has been cooled down by continuous flushing of pure nitrogen, inspection revealed two black spots with hollow centres at the areas where the laser beam entered and exited the reactor tube, as shown in Fig. 5.3b marked as **T**. The rest of the tube no observed deposits. It is believed that at 900 °C thiophene decomposition took place, which formed solid-state carbon that was deposited onto the tube's walls via laser photolysis, as the areas right next to the spots were clean. However, at the centre of the beam, the energies were high enough to cause ablation of carbon solid deposits on the reactor wall, resulting in the higher intensity blackbody emission spectrum. At 900 °C the reactor system entered a cycle of carbon deposition and simultaneous ablation to and from the reactor wall, due to the presence of the laser beam. At lower reactor temperatures, no thiophene decomposition took place, allowing the laser energies to burn off the remaining carbon deposits, which resulted in the hollow centres of the observed spots at the location of laser impingement on the reactor wall, and subsequent lowering of the background levels.

Overall, the quality of the spectra was poor, with inconsistent background levels between measurements. This was attributed to the curved surface of the reactor tube, which caused specular reflections as the beam injection spot could vary with temperature along the curvature of the reactor, due to the reactor tube deformation.

Another pair of larger deposition spots in Fig. 5.3b was observed during the Raman measurements of ferrocene in a H_2 environment at 300 °C. Ferrocene (Acros Organics, 98%) was sublimed in a heated vessel at approximately 97°C and the vapour was carried into the furnace by passing 0.5 SLPM of H_2 through the vessel. The stainless steel gas lines leading

out of the vessel were heated to 150°C by resistive heaters to avoid ferrocene condensation. Temperature of the heaters was controlled by Omega CN740 PID controllers.

While no solid-state Raman analysis was performed on the samples from these spots. the red/orange colour indicated the presence of an iron-containing decomposition product, confirming that the occurrence of the spots was from ferrocene decomposition. The system response was similar to the one observed during thiophene measurements. However, the laser beam was unable to clear the observed deposition. This could be a result of the etching of the tube walls.

Thus, preventing decomposition products from forming deposits on the tube wall at the laser impingement location was crucial in order to obtain any species information past the temperature of decomposition.

A purging system was designed, to provide flow parallel to the propagation of the laser beam axis, which is perpendicular to the gas flow axis in the reactor tube. The reactor tube was modified such that it could provide a channel for the purging gas flow as shown in Fig. 5.1b, resembling a 'T' shape. The reactor tube consisted of two parts: the main tube and a smaller quartz tube (which is referred to as the 'purging channel' from now on). The length of the reactor tube was extended from 500 mm to 700 mm, to provide an option of performing spatial measurements along the furnace's temperature profile via the tube's axial displacement. The dimensions of the purging channel were 15.7 mm and 18.2 mm inner and outer diameters, respectively, with 300 mm length extending from the main tube wall, resulting in a total length of 323.2 mm from the centre of the reactor tube. The centre of the channel was located at the middle point of the reactor tube, 350 mm from its edge. Dimensions of the purging channel allowed a focusing laser beam to enter the reactor without touching the sides of the channel, with the furnace lid raised by a small amount in order to minimise heat loss.

The schematic of the purging flange is shown in Fig. 5.4 . It consists of three parts - two retaining plates and the main body. Two 1/8 inch NPT holes have been placed in the centre of the main body through which the purging gas enters the flange. One section of the body contains a 25 mm diameter quartz window, 3 mm thick with anti-reflective coating, which is sandwiched between two Viton o-rings, held in place by the retaining plate. This provides an airtight seal and a flat optical window for laser injection. This reduces the specular reflections from the injection surface and, coupled with the anti-reflective coating, results in an overall lowered background signal. The modular construction of the flange allows for the replacement of the quartz window in case of contamination by the decomposition products.

The second section of the flange couples the purging system to the reactor tube. A retaining plate and the O-ring are placed onto the outer surface of the channel, which is

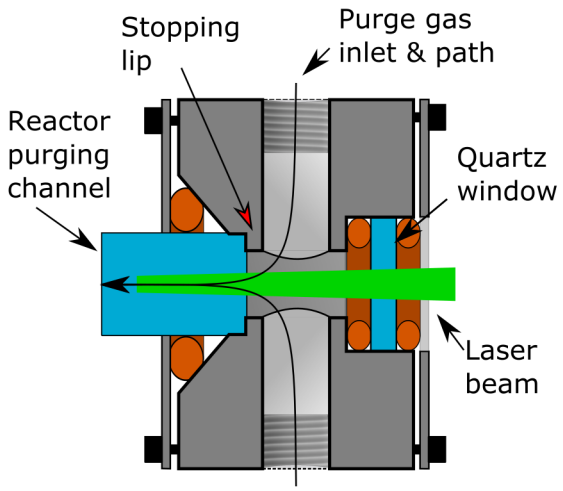

Fig. 5.4 The schematic of the purging flange.

then inserted into the flange up to the stopping lip, placing the o-ring into the angled section of the flange. The thickness of the channel O-ring was chosen such that it protruded past the flange's main body, resulting in an airtight seal when the retaining plate was tightened, locking the flange in place.

The 'T-shaped' tube was placed into the furnace with the purging channel facing the incoming laser radiation. The purging flange was mounted on the end of the purging channel. It was painted black to minimised stray reflections. Fibreglass insulation was placed underneath the reactor tube such that the purging channel level was parallel to the laser beam's axis of propagation. Raman measurements were performed on 3% inlet molar concentration of thiophene in a H_2 environment at the furnace set-point temperatures of 20 and 900 °C, with 0.5 SLPM centre flow and 0.1 SLPM H_2 flow in the purging channel. Moving forward, centre flow defines the volumetric flowrate through the inlet of the main reactor tube. The channel flow was controlled with an Alicat MFC, MC-20SLPM-D/5m.

The observed results were similar to ones measured in the cylindrical reactor and are shown in Fig. 5.5a. At 20 °C, the C=C modes were clearly visible along with the O-O oxygen. The background appeared more uniform, due to the minimisation of specular reflection inside the furnace as the laser entered through a flat surface, when compared to the spectra from the cylindrical reactor. At 900 °C, thiophene breakdown was once more observed in the form of broadband emission. The magnitude of the emission in the 'T'-reactor was smaller when compared to the spectra acquired in a cylindrical reactor, shown in Fig. 5.5a.

Visual inspection of the flange window revealed no deposits, showing that the purging system was working as intended. On the backside of the main tube, shown in Fig 5.5b, a black spot was observed, surrounded by a large amount of black deposit, which was matte on

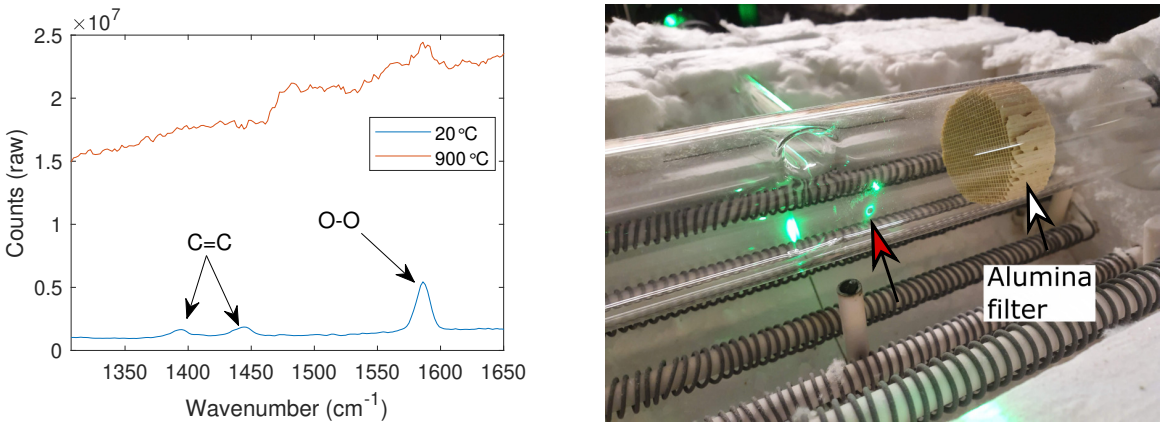

(a) (b)

Fig. 5.5 a) Raman spectra of the C=C mode region of 3% inlet thiophene molar concentration at 20 and 900 °C furnace set temperature in a 'T'-shaped reactor, b) The back wall of the 'T-shaped' reactor, with the etched spot marked by arrow

the inside of the reactor and glossy, with a grey hue on the side attached to the tube wall. The deposition easily peeled off like a film, after attempts were made to clean the tube. However, a faint spot of deposition remained akin to the ones observed in earlier experiments, as shown in Fig. 5.5b below the laser beam.

The experiments were repeated with varied purging flowrates, up to 0.2 SLPM, at a constant centre flow of 0.5 SLPM, which did not result in any significant change in the observed emission. Subsequent experiments were performed with the implementation of an alumina mesh filter, which absorbs up to 99 % of solid-state particles (such as carbon) present in the gas phase, placed at different positions in the reactor prior to the purging channel. However, no significant effect on the magnitude of the blackbody radiation was observed.

Therefore, the blackbody emission signal originated either from the carbon that was still present in the gas phase, after passing through the alumina filters, or from the solid-state deposition on the back wall of the reactor. To determine the exact source of the emission a final design of the reactor tube was made, shown in Fig. 5.1c. The design will be referred to as a 'cross reactor' from now on.

A second purging channel, with exactly the same inner and outer diameters as in the 'T' reactor, was placed coaxially with respect to the first channel, 350 mm from the edge of the main tube such that a straight optical path for the laser was created. The furnace hinge was modified to allow the second channel to protrude out of the clamshell furnace. The hinge was raised by two 25 mm thick, 200 mm in length and 50 mm in width stainless steel blocks positioned at each corner of the hinge. The blocks were made out of stainless steel to ensure that the metal would not melt during the furnace's maximum operating temperature

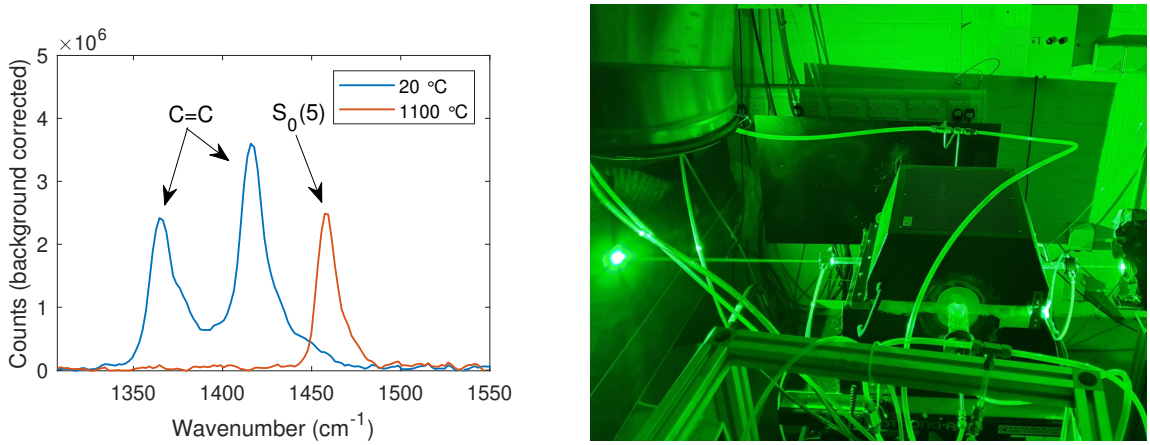

(a) (b)

Fig. 5.6 Raman spectra of C=C thiophene mode region at 3% inlet thiophene molar concentration in H_2 environment at 20 and 1100 °C furnace set temperature in a cross reactor, b) Laser beam passing through the reactor tube and the furnace.

of 1100 °C. Additional fibreglass insulation was placed around the steel blocks to improve heat retention.

The length of the second purging channel was increased to 350 mm from the main tube's back wall such that it could safely protrude past the raised hinge and the furnace body while not being touched by the furnace's lid when open. An identical purging flange was made for the second channel. Such reactor tube arrangement allowed the laser beam to cleanly pass through the furnace, as seen in Fig. 5.6b, which prevented unnecessary scatter from hitting the furnace's internal surfaces. This was physically observed, as the inside of the reactor tube under laser illumination was considerably dimmer.

The cross reactor design was tested by measuring Raman signatures of 3% inlet thiophene molar concentration at 20 and 1100 °C furnace set-point temperature, with the centre H_2 flow of 0.5 SLPM. The purging flow was set to 0.05 SLPM of H_2 in each channel. The acquired Raman spectra were background corrected by spectra of 0.5 SLPM and 0.05 SLPM in each channel of N_2, leading to a 100% nitrogen environment inside the reactor. The system's data acquisition settings were changed to 6000 shots per acquisition, with 2 horizontal and 61 vertical pixels binning. This improved signal to noise ratio and minimise acquisition time.

Acquired Raman background-corrected spectra are shown in Fig. 5.6a. At 20 °C, the two thiophene C=C modes are clearly present. The background levels of the spectra at 20 and 1100 °C are nearly equal, showing no presence of broadband background emission. The 1100 °C spectrum showed absence of C=C thiophene modes and a presence of the $S_0(5)$ rotational transition mode of hydrogen. This confirmed that the carbon deposits on reactor

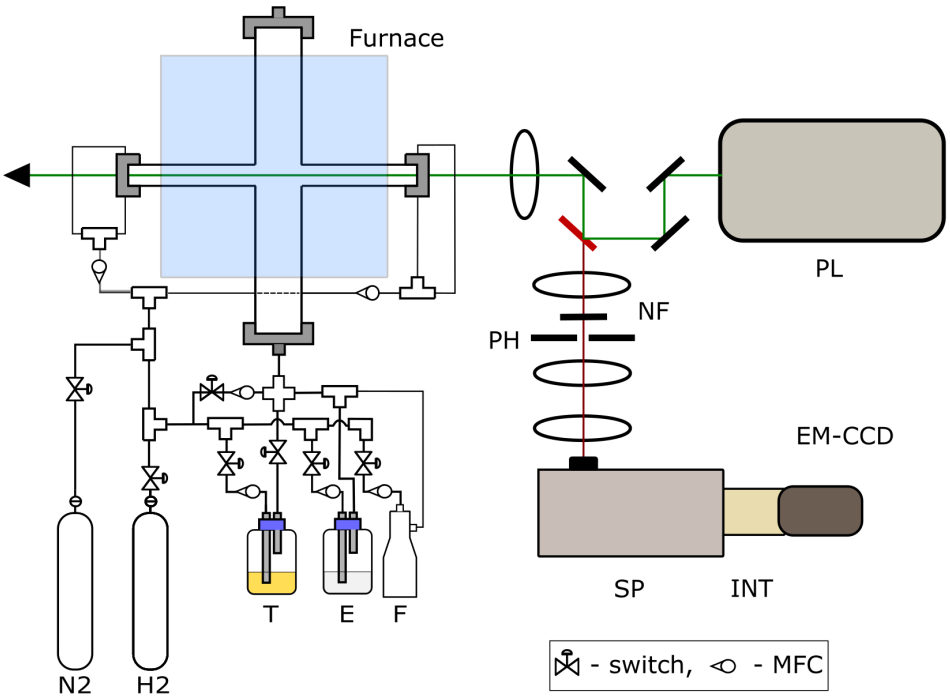

Fig. 5.7 Schematic of final configuration of pulsed laser Raman spectroscopy setup. Acronyms: PL - Pulsed laser diode, NF - notch filter, PH - pinhole, SP- spectrograph, INT - intensifier, EM-CCD - Electron-multiplying charge-coupled device, 'T' and 'E' - thiophene and ethanol bubblers, 'F' - ferrocene vessel.

tube walls were the source of the broadband blackbody radiation. The purging flanges were visually inspected after the reactor has cooled down, showing no signs of deposition on the quartz windows. The performance of the purging system was sufficient to acquire Raman signatures in a high temperature reacting flow. Figure. 5.7 shows the schematic of the final configuration of the pulsed laser Raman spectroscopy setup with a modified reactor, furnace and vessels for the reactant delivery.

5.3 Raman spectra of single molecules

Typically, multiple chemical species are introduced simultaneously into the FC-CVD reactor in order for the CNT synthesis process to take place. This can result in quite complex Raman spectra, which are difficult to interpret. Therefore, spectra of individual reagents were acquired, to identify the modes the constructed system is sensitive to, and their location. Some species were measured at 20 and 1100 °C, to provide an opportunity to verify the results observed by other studies.

Preliminary measurements have shown that the presence of purging flow at high temperature measurements is vital in the acquisition of Raman measurements of decomposing species. In order to perform a direct comparison between spectra taken at various temperatures, the purging flow was always present in the system, even at room temperature.

5.3.1 Modes of interest

Hoecker *et. al.* studied the decomposition of thiophene in a H_2 environment, as a function of furnace set-point temperature, by performing FT-IR on the exhaust gases coming out of the reactor. The FT-IR measurements detected a strong peak centred at 710 cm^{-1} which corresponded to the out-of-plane wagging motion (ω_{oop} of the C-H thiophene bond. It was used as an indicator for thiophene presence. An increase in furnace temperature from 750 to 1050 °C led to a decrease in the thiophene band intensity, while giving rise to a doublet mode that was assigned to an alkyne C triple bond stretch at 2150 cm^{-1}. It was concluded that the combination of the reduction of thiophene mode magnitude, coupled with the formation of the doublet, was indicative of the occurrence of the preliminary stage of pyrolysis. Methane was observed as an additional breakdown product, with two bands forming at 3020 cm^{-1} and 1300 cm^{-1} corresponding to the anti-symmetric stretch (ν_{as}) and asymmetric bending mode (δ_{as}) respectively. No thiophene modes were observed at 1050°C furnace set-temperature.

Methane gas is commonly used as a carbon source [69] in aerogel synthesis. Some investigations, however, have used ethanol in a liquid feedstock, which thermally decomposes into methane and water in a hydrogen environment [68]. Methane would then, consequently, react with the iron nanoparticles present in the gas phase, to form hydrogen and CNTs according to the following mechanism [63]:

$$CH_4(g) \longrightarrow C(s) + 2H_2(g) \tag{5.1}$$

where *g* and *s* subscripts indicate the physical state of the compound. It is generally accepted that the carbon that is formed due to the decomposition of CH_4 on the surface of an iron nanoparticle, provided by the decomposition of ferrocene, gets dissolved into the transition metal. The carbon then precipitates out, once the carbon saturation point has been reached, forming CNTs [67]. However, the addition of sulphur redirects the growth of CNTs from the bulk to surface diffusion. Sulphur forms a layer with negligible carbon mobility on the iron particle, which prevents carbon diffusion into the said particle. As consequence, this results in the formation of large double-walled nanotubes that grow through carbon surface diffusion.

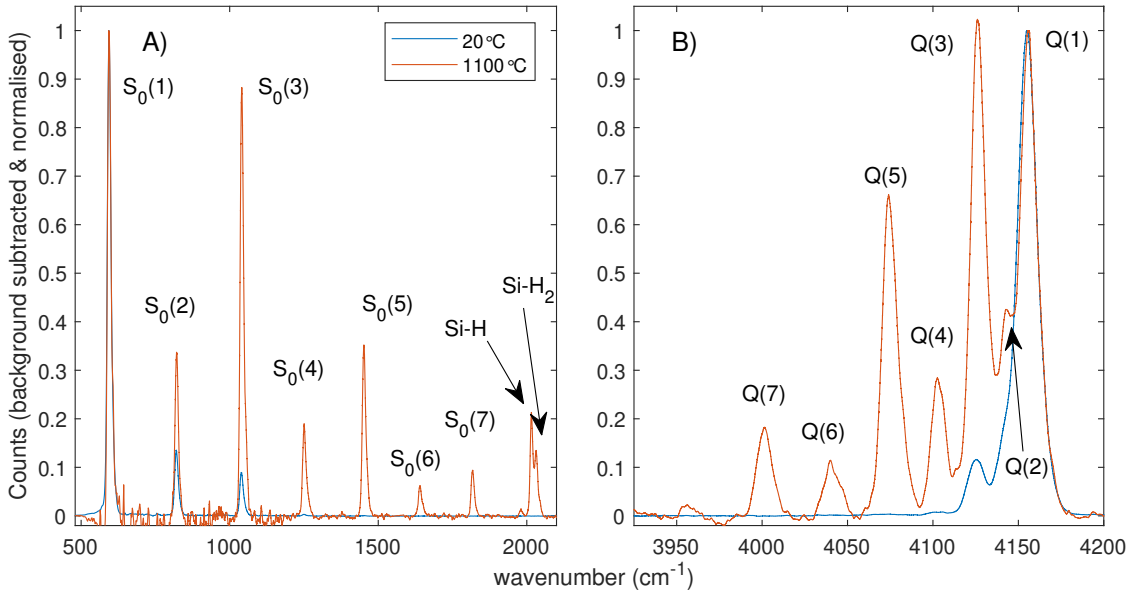

Fig. 5.8 a) rotational (S-branch) and b) rotational-vibrational (Q-branch) spectral regions of 0.5 SLPM H_2 in the main tube and 0.1 SLPM N_2 in the purging channels at 20 and 1100 °C

5.3.2 Hydrogen

Hydrogen (H_2) is a symmetric linear molecule that consists of two atoms linked by a covalent bond. H_2 is anisotropically polarisable due to its linear nature, hence it is able to give rise to both rotational (S-branch) and rotational-vibrational (Q-branch) transitions, referred to as vibrational transitions in shorthand.

Raman spectra of H_2 with inlet volumetric flowrates, $\dot{Q}$, of 0.5 SLPM through the reactor tube and 0.05 SLPM of N_2 through each purging channel were recorded at 20 and 1100°C furnace set-point temperature. Preliminary measurements have shown that the Raman system was sensitive to any gas species present in the beam path of the laser, with the majority of the observed signal originating from the laser focal point. Nitrogen was used as purging gas in order to keep H_2 confined to the main tube. Additionally, such gas arrangement minimised the effects of temperature gradients present in the purging channels on the observed H_2 spectra, as H_2 is confined to the centre of the reactor. Raman spectra for both temperatures were normalised by the S(1) and Q(1) modes for rotational and vibrational regions respectively, as they were the dominant modes at room temperature, as shown in Fig. 5.8.

Presence of the $S_0(1)$, $S_0(2)$ and $S_0(3)$ rotational modes were observed at 593, 821 and 1041 cm^{-1}, respectively, at room temperature. Additionally, the $S_0(4)$ and $S_0(5)$ modes were detected at 1250 and 1455 cm^{-1} but their magnitude was significantly lower, compared to the earlier modes. The intensity of the rotational modes is directly proportional to the population

of their initial rotational level, i.e J = 0 for S_0. The populations of the rotational levels are thermally driven and can be derived from Maxwell-Boltzmann statistics. As the temperature increases, the population of the rotational levels at higher energies increases, which leads to an increase in the magnitude of their corresponding transitions. However, as the result of the re-population and redistribution of mode intensities, coupled with the decrease in molecular density due to temperature increase, the signal-to-noise ratio of individual modes decrease. Thus, the Raman signals were normalised so that the spectra at 20 and 1100 °C could be compared simultaneously on the same figure.

Overall, the number of observed rotational modes increased from 5 to 8 as seen in the 1100 °C spectra of Fig.5.8a. The $S_0(6)$, and $S_0(7)$ modes were observed at 1641 and 1818 cm^{-1}, respectively. A group of modes was also detected in the 2000 wavenumber region. It was deduced that their magnitude was linked to the molar fraction of hydrogen in the system, increasing with the increasing H_2 molar fraction. A more detailed analysis of their intensity is shown in Chapter 7. The modes were assigned to the stretching of Si-H and Si-H_2 bonds[171, 172] as at high temperature, hydrogen starts to etch the walls of the quartz reactor tube, extracting silicon. This group of modes will be referred to as Si-H from now on.

The spectral region of rotational-vibrational transitions at room temperature is dominated by the Q(1) transition located at 4156 cm^{-1}, with the smaller Q(3) transition located at 4125 cm^{-1}. While hydrogen at room temperature consisted of 1:3 ratio of even to odd J number transitions, no Q(0) and Q(2) vibrational transitions were observed [92]. A very slight shoulder is present on the left of the Q(1) mode. However, the resolution of the setup is not fine enough to deconvolute the two transitions. A Q(4) transition was observed at 4103 cm^{-1}. At 1100 °C the number of observed Q(J) transitions increases from 3 to 7 with Q(2), Q(5), Q(6) and Q(7) observed at 4143, 4074, 4040 and 4001 cm^{-1} respectively. As with rotational modes, the increase in temperature leads to a molecular population redistribution towards higher energy levels, which in turn gives rise to the larger magnitude of higher energy vibrational transitions while lowering the magnitude of the lower energy modes. This allowed the Q(2) mode to break out of the shoulder of the Q(1) transition and be clearly observed. Additionally, the peak magnitude of Q(3) is larger than the magnitude of Q(1), which is in line with other observations at temperatures above 1000°C [173]. The magnitude of H_2 transitions will be used to in situ gas temperature measurements, discussed later in Section 7.3. It should be noted that no significant mode broadening was observed as the function of temperature which would allow to carry out quantitative analysis based on peak values of the modes.

5.3.3 Methane

Methane, CH_4 is a molecule with complex rovibrational spectra. Rotational vibration interactions complicate the simplicity of this highly symmetric molecule by lifting the degeneracy of rovibrational levels and strong anharmonic Fermi resonances couple CH-stretching and bending modes.

Figure 5.9 shows the Raman spectra of 0.5 SLPM of methane and 0.1 SLPM of total N_2 purging flow at 20 and 1000 °C, normalised to their highest respective count values.

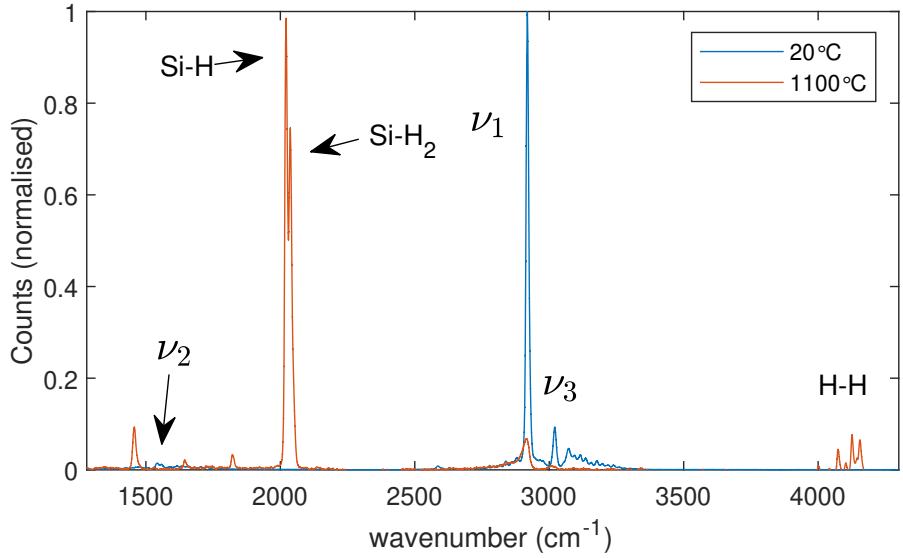

Fig. 5.9 Raman spectra of 0.5 SLPM of methane with 0.1 SLPM of N_2 purging flow at 20 (blue) and 1100 (orange) °C

At room temperature the vibrational levels are grouped into resonance polyads which are characterised by the polyad quantum number $N = v_1 + v_3 + 0.5 \times (v_2 + v_4)$, where v_1 and v_3 represent the stretching of the C-H bond with v_2 and v_4 being the C-H bending quanta. The two bending modes, v_2 and v_4 around 1500 cm^{-1} form a first polyad called dyad [174], shown in Fig.5.9. Only the v_2 mode was observed with a low magnitude. A second polyad, located in the region containing the C-H stretching fundamentals near 3000 cm^{-1}, consists of 5 interacting vibrational bands and is called a pentad. It consists of the C-H stretching fundamentals v_1 (2919 cm^{-1}) and v_3 (3019 cm^{-1}), the C-H bending overtones $2v_2$ and $2v_4$ and the combination band $v_2 + v_4$ [92]. The pentad's magnitude is much larger, as the energy of the stretching modes is at least twice that of the bending modes. As shown in Fig.5.9, the methane Raman spectrum is dominated by the Q-branch of the totally symmetric v_1 band at 2917 cm^{-1}. In addition, there are much weaker, rovibrational transitions which are components of v_3 observed near 3020 cm^{-1}.

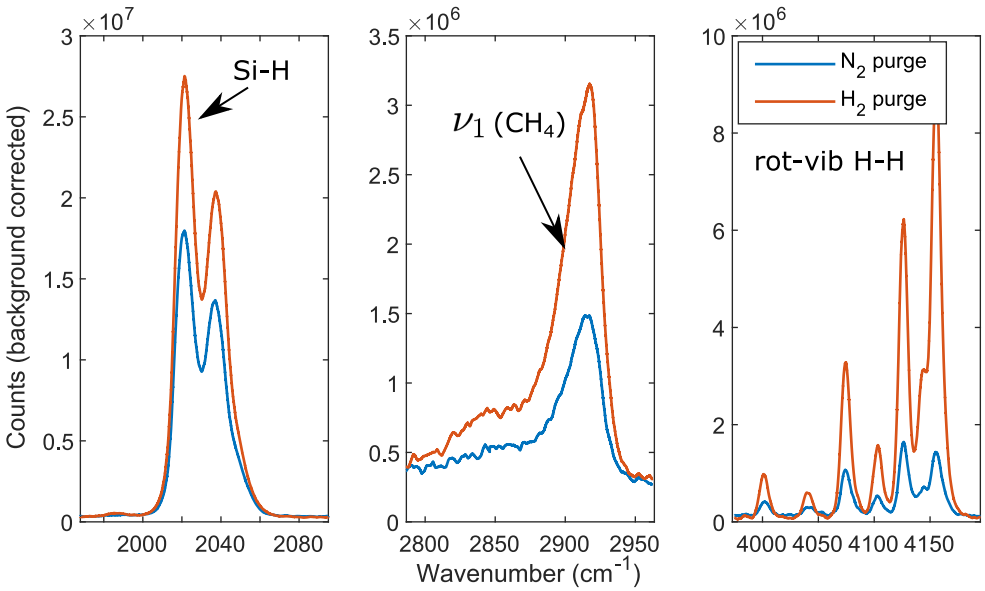

Fig. 5.10 Sections of Raman spectra of 0.5 SLPM of methane with 0.1 SLPM of N_2 (blue) or H_2 (orange) purging flow at 1100 °C

In the 1100°C spectra, the v_1 methane mode is still present, albeit with decreased signal magnitude. Lower magnitude methane modes present at room temperature were not detected with sufficient SNR. Furthermore, high temperature vibrational and rotational Raman modes of H_2 and, consequently, Si-H modes were observed at 1000-1800 cm^{-1}, 4100 cm^{-1} and 2000 cm^{-1} respectively, when no H_2 was input into the system. Such signatures indicate the occurrence of incomplete non-catalytic thermal cracking of methane.

Methane cracking and formation is a reversible process. As no hydrogen is initially present when N_2 is used as purging flow, methane thermally decomposes until an equilibrium condition is reached at 1100°C. Temperatures higher than 1200°C are required to obtain a reasonable rate of non-catalytic methane cracking [175].

As nitrogen is not typically present in the FC-CVD system during aerogel synthesis, a Raman spectrum of 0.5 SLPM of methane and 0.1 SLPM of H_2 purging flow at 1100° C was obtained and is shown in Fig. 5.10, along with spectra performed using N_2 purging flow. The v_1 methane mode and the Si-H modes appear to be larger when H_2 was used as the purging gas. While the increase of Si-H modes due to the presence of the larger amount of H_2 is not surprising, the higher methane mode magnitude suggests that N_2 purging flow facilitated in localised thermal cracking of methane at the measurement location. Therefore, purging gas indeed has an effect on localised chemistry. Unfortunately, it is necessary to utilise N_2 as purging gas in the current setup configuration in order to perform quantitative

measurements. For qualitative measurements, however, H_2 would be used as the purging gas to avoid altering the synthesis process at the measurement location.

5.3.4 Ethanol

Ethanol, CH_3CH_2OH, has been used as a hydrocarbon source in numerous aerogel studies [69]. Ethanol can be introduced into the system by atomising and spraying, or by bubbling through a carrier gas, akin to thiophene delivery. For these investigations, ethanol was delivered by bubbling H_2 through an ethanol-containing vessel placed at room temperature. Figure 5.11 shows the Raman spectra of 0.5 SLPM H_2 going through ethanol vessel with 0.1 SLPM total of H_2 purging gas, resulting in 7.2 % ethanol molar fraction, calculated by the Antoine equation, with coefficients listed in Appendix B.

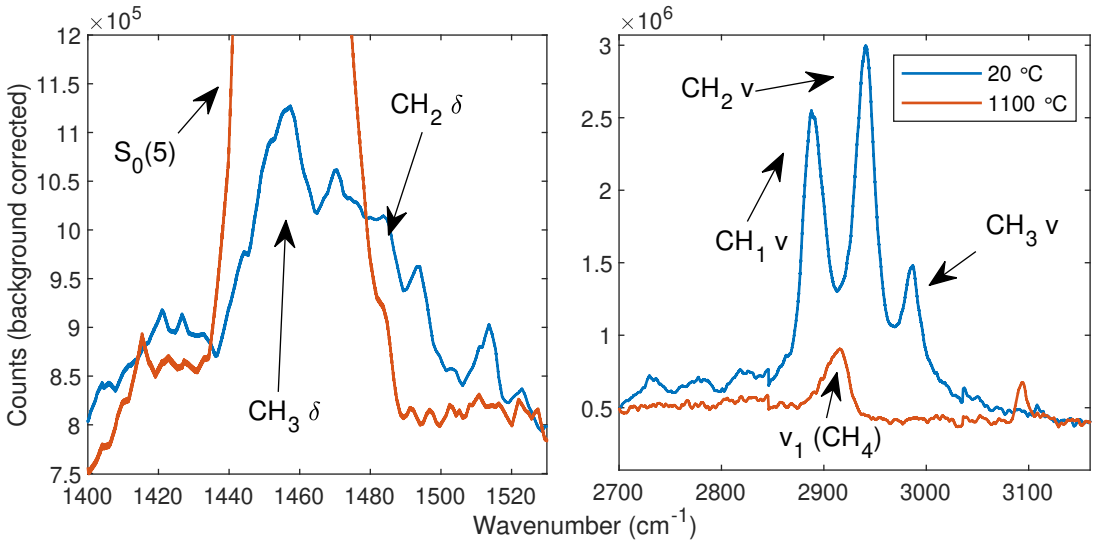

Fig. 5.11 Sections of Raman spectra of 7% Ethanol molar fraction in H_2 environment and H_2 purge gas at 20 and 1100°C furnace set-temperature.

The magnitude of ethanol modes was significantly lower than those of hydrogen, therefore, Fig. 5.11 focuses on sections of observed ethanol modes with y-axis limits optimised for observation of ethanol signatures. At room temperature, two bending vibration modes of CH_3 and CH_2 are observed at 1456 and 1486 respectively. Centred at 2900 cm^{-1} three distinct modes can be distinguished, which correspond to the symmetric stretching vibration of CH_2 at 2889, symmetric stretching vibration of CH_3 at 2941cm^{-1} and asymmetric stretching vibration of CH_3 at 2985cm^{-1} respectively [176].

No ethanol modes were present at 1100°C furnace set-point temperature. An $S_0(5)$ H_2 mode appears at 1450 cm^{-1}, as expected. In the 2900 cm^1 region a methane v_1 mode appears,

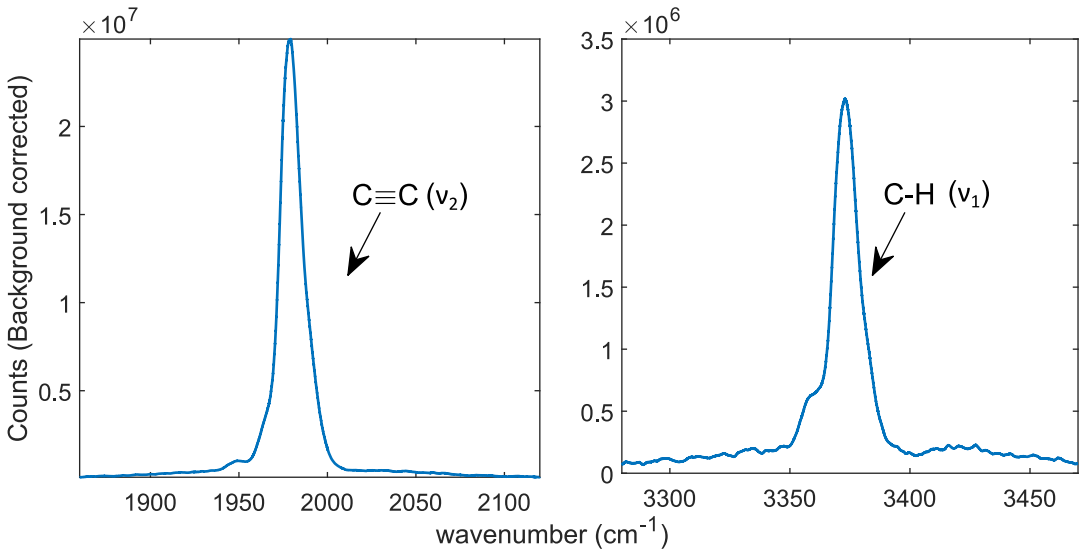

Fig. 5.12 Raman spectra of 100 % molar fraction of Acetylene (0.5 SLPM) with 0.1 SLPM N_2 purging flow

indicating that complete ethanol decomposition has taken place, in-line with the observations made by Conroy. *et al.* [68].

5.3.5 Acetylene

Hoecker *et al.* have detected the presence of alkynes in the exhaust gas. Therefore, Raman spectra of acetylene were captured to identify the location of C≡C modes for our system. Figure 5.12 shows spectra sections of 100%Acetylene within the reactor with N_2 purging gas at room temperature. Two Raman active modes were observed with the $C \equiv$C stretch ν_2 mode located at 1974 cm^{-1} and symmetric C-H stretch ν_1 mode at 3373 cm^{-1} [177].

5.4 Conclusion

Modifications to a FC-CVD system were performed to create a continuous optical axis for *in situ* measurements. The cylindrical reactor tube was modified with the addition of two purging channels which lied on-axis, perpendicular to the cylindrical reactor tube. Purging flanges of the modular structure were designed and constructed, which housed quartz windows with anti-Reflective coating. The windows allowed the laser beam to pass cleanly through the electrical furnace, following modifications to its hinge.

The modified system was used to perform Raman measurements on H_2, methane, and ethanol at 20 and 1100 °C, with measurements of acetylene performed at 20 °C. The system

produced Raman emission from every location along the beam path, therefore N_2 was used as the purging gas to confine the species of interest to the centre of the reactor, in the region of uniform temperature. However, thermal breakdown of methane was observed when N_2 was used for purging, contrary to no breakdown when H_2 was used instead. Therefore, the selection of the purging gas depends on the nature of the Raman measurement, *i.e* quantitative or qualitative. The observed thermal breakdown mechanisms of methane and ethanol were in-line with previously reported studies [68, 67].

The next chapter investigates the effect of purging channels on the recorded Raman spectra.

Chapter 6

CFD Simulations of heat and mass transfer in a Cross Reactors

6.1 Introduction

Previous chapter has highlighted the importance of introduction of purging flows in the system when performing Raman spectroscopy during species breakdown. Their inclusion prevents the formation of solid phase deposition on reactor walls and reduces the background interference. However, the choice of purging gas creates a dilemma. If hydrogen is used as the purge gas, quantitative assessment of hydrogen, such as its molar concentration and temperatures is made difficult, because of the contribution of the signal from the hydrogen present in the purging channels, excited by the incoming laser light.

When nitrogen is used in the purging channels, this problem is mitigated, but nitrogen can create a local disturbance to the mixture being probed. In order to investigate the effects of purging flow on the overall flow pattern in the reactor, computational fluid dynamics (CFD) simulations of the flow and heat transfer processes have been undertaken, and are discussed in the present chapter.

6.2 Model Governing equations

Numerical computational fluid dynamics investigations (CFD) were performed using Ansys® 'Fluent' 2020 R1. Fluent is a well recognised CFD solver that is used extensively in commercial and academic fields for the analysis of steady-state and transient systems. For all fluid flows, it solves conservation equations for mass and momentum. It uses a finite volume method to discretise the governing equations. If compressibility or heat transfer are involved,

an additional equation for energy conservation is solved. For more complex problems, that include species mixing or reactions, for instance, species conservation equations are solved, along with extra transport equations when the flow is turbulent.

The model used in the presented numerical studies included heat transfer, species mixing and buoyancy effects to achieve a more precise representation of the flow patterns and species distribution. The Reynolds number (*Re*) for the presented system was calculated to determine the nature of the flow. It represents the ratio of the inertial to viscous forces within a fluid which is subjected to relative internal movement due to different fluid velocities. Its expression has many forms, with the most common being:

$$Re = \frac{\rho u L}{\mu} \tag{6.1}$$

where ρ is the density of the fluid, u is the velocity of the fluid, μ is the dynamic viscosity of the fluid and L is the characteristic length of the system. The characteristic length L for a flow in a pipe is defined as hydraulic diameter d_h, which for the reactor of interest is its inner diameter of 46.4 mm. At room temperature and atmospheric pressure, the values for ρ, μ and u for hydrogen gas are 0.0827 km/m^3, 8.75 Ns/m^2 and 0.004928 m/s (assuming a total H_2 volumetric flow of 0.5 SLPM) respectively. This results in $Re = 2$, indicating that the flow is laminar.

Furthermore, as the system (the reactor) is stationary it can be represented by a non-accelerating reference frame. For such a system the equation for the conservation of mass, or the continuity equation solved by Fluent, can be written as follows:

$$\frac{\partial \rho}{\partial t} + \bigtriangledown \cdot (\rho \vec{v}) = S_m \tag{6.2}$$

where ρ is the density of the fluid, t is time, $\vec{v}$ is the flow velocity field and S_m is the mass added to the continuous phase from the dispersed second phase (e.g vaporisation of liquid droplets) or can represent any user-defined sources.

In a non-accelerating reference frame, the conservation of momentum is given by:

$$\frac{\partial}{\partial t}(\rho \vec{v} + \bigtriangledown \cdot (\rho \vec{v}\vec{v}) = - \bigtriangledown p + \bigtriangledown \cdot (\bar{\bar{\tau}}) + \rho \vec{g} + \vec{F} \tag{6.3}$$

where p is static pressure, $\bar{\bar{\tau}}$ is the stress tensor, and $\rho \vec{g}$ and $\vec{F}$ are external body forces respectively.

The problem of interest included hydrogen and nitrogen, two ideal gases of different densities. When conservation equations for a mixture of chemical species are solved, Fluent

predicts the local mass fraction of each species, Y_i, though the solution of a convection-diffusion equation for the ith species. The conservation equation is given as follows:

$$\frac{\partial}{\partial t}(\rho Y_i) + \nabla \cdot (\rho \vec{v} Y_i) = -\nabla \cdot \vec{J}_i + R_i + S_i \tag{6.4}$$

where R_i is the net rate of production of species i, and S_i is the rate of creation by addition from the dispersed phase, plus any user-defined sources. This equation is solved for $N-1$ species where N is the total number of fluid phase chemical species present in the system. As mass fraction of species must sum to unity, the Nth mass fraction is calculated as one minus the sum of the $N-1$ solved mass fractions. The diffusion flux, $\vec{J}_i$ of species i arises due to gradients of concentration and temperature. Fick's law was used to model mass diffusion due to concentration gradients, under which the diffusion flux for laminar flows can be written as:

$$\vec{J}_i = -\rho D_{i,m} \nabla Y_i \tag{6.5}$$

where $D_{i,m}$ is the mass diffusion coefficient for species i in the mixture.

Energy equation was incorporated into the model to account for the effects of heat transfer. Fluent solves the energy equation in the following form:

$$\frac{\partial}{\partial t}(\rho E) + \nabla \cdot (\vec{v}(\rho E + p)) = \nabla \cdot \left(k_{eff} \nabla T - \Sigma_j h_j \vec{J}_j + \tau_{eff} \cdot \vec{v} \right) + S_h \tag{6.6}$$

where k_{eff} is the effective conductivity. The first three terms in eq. 6.6 represent energy transfer due to conduction, species diffusion and viscous dissipation, respectively. S_h includes the heat of chemical reaction and any other defined volumetric heat sources. Furthermore, E in eq.6.6 is defined as:

$$E = h - \frac{p}{\rho} + \frac{v^2}{2} \tag{6.7}$$

where h is enthalpy for ideal gases as:

$$h = \Sigma_j Y_j h_j \tag{6.8}$$

In eq. 6.8, h_j is defined as:

$$h_f = \int_{T_{ref}}^{T} c_{p,j}\, dT \tag{6.9}$$

where $T_{ref} = 298.15$K. The flow considered in numerical investigations was pressure driven. When the pressure solver is used, the term for enthalpy transport due to species diffusion is

included in the governing energy equation 6.6 by default, and is given by:

$$\nabla \cdot \left(\Sigma_j h_j \vec{J}_j \right) \tag{6.10}$$

The viscous heating term was not included. The source of energy due to chemical reactions was set to zero as no reactions between nitrogen and hydrogen were anticipated.

6.3 Cross reactor model parameters

The rate of chemical reaction depends on multiple parameters. in particular temperature of the environment and the residence time of the species inside of the reactor. The residence time is a function of the gas velocity, reactor geometry and the flow pattern.

In a cross reactor, hydrogen acts as the carrier gas and nitrogen is used for purging, making them two major species of interest for the CFD studies. At 20 °C and atmospheric pressure, the densities of nitrogen and hydrogen are 1.165 and 0.0827 kg/m^3 respectively, which is a difference factor of 14.5. Such difference in densities would give rise to buoyancy forces inside of the reactor, which would affect the flow patterns and thus localised gas velocity. Therefore, unit volume residence time calculations may become difficult. However, gas velocity is dependent on the inlet volumetric flowrate into the reactor. Furthermore, the buoyancy forces can have a substantial effect on species distribution within the reactor. Therefore, the changes in the flow pattern and species distribution due to buoyancy were investigated as a function of inlet volumetric flowrate and reactor temperature.

6.3.1 Model geometry

A full-sized 3D geometry of the cross reactor was meshed, so as to properly represent heat transfer and buoyancy effects. The schematic of the cross reactor model is shown in Fig. 6.1.

The geometry consisted of 3 cylinders. The large cylinder represented the main reactor tube, with length L = 700 mm, and an inner diameter of 46.4 mm. Two cylinders, arranged perpendicularly to the reactor tube, represented the purging channels with lengths of 300 mm measured from the main tube's wall, and an inner diameter of 15.2 mm. The section where the purging channels join the reactor tube will be referred to as 'the junction'.

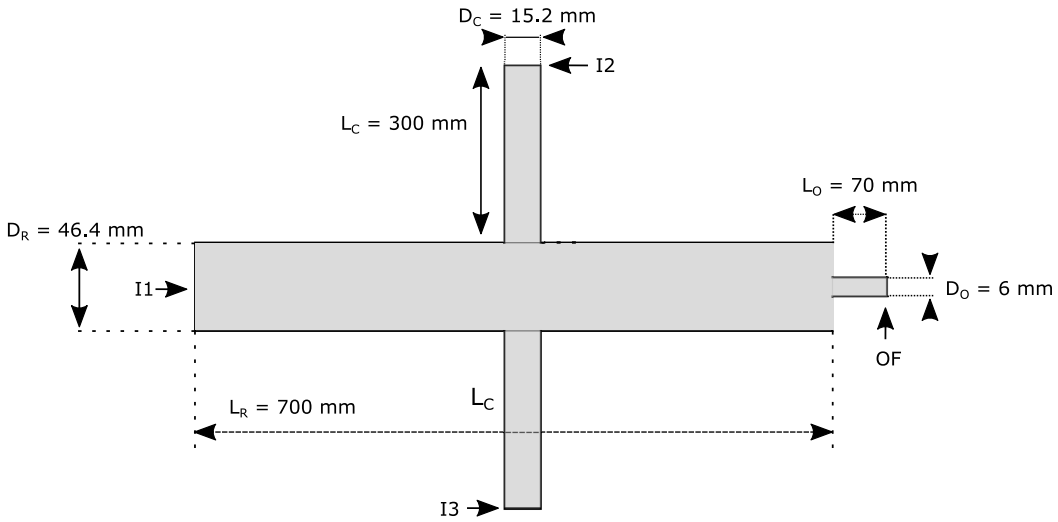

Fig. 6.1 2D, top-down view schematic of the reactor model.

6.3.2 Boundary conditions

Three gas inlets were defined for the model with **I1**, being the main reactor inlet, and **I2** and **I3** being the purging gas inlets, along with an outlet **OF**. The inlet boundary conditions were assigned to the circular faces of the cylinders.

The velocity specification method was set to 'Magnitude, normal to Boundary', with an 'Absolute' reference frame, which resulted in a uniform inflow. Such velocity inlet specification would permit comparison of the flow patterns to a plug flow. At the end of the reactor tube cylinder, a 70 mm tube with an inner diameter of 6 mm was placed, emulating the 6 mm Swagelok fitting welded into the out-coupling flange, therefore matching the geometry to the experimental setup. The outlet boundary condition was placed onto the 6 mm diameter

Table 6.1 Boundary properties for all simulations.

Boundary Condition	Type	Specification method
Inlet 1 (**I1**)	Velocity Inlet	Magnitude, Normal to the boundary; Initial gauge pressure = 0
Inlet 1 (**I1**)	Velocity Inlet	Magnitude, Normal to the boundary; Initial gauge pressure = 0
Inlet 1 (**I1**)	Velocity Inlet	Magnitude, Normal to the boundary; Initial gauge pressure = 0
Outlet (**OF**)	Outflow	Flowrate weighting = 1
Walls	Stationary	No slip

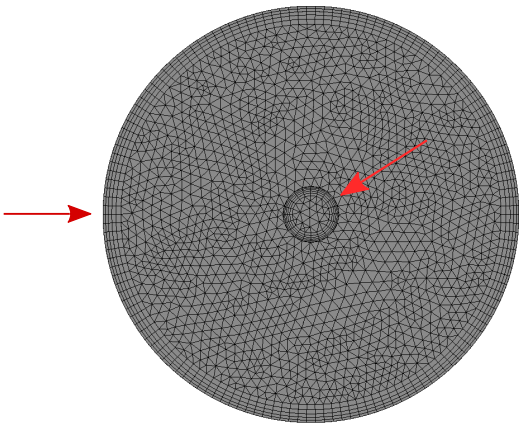

Fig. 6.2 Face mesh cells generated by inflation and wall boundaries.

face and was defined as an 'outflow', with the flowrate weighting of 1. Such boundary condition allows for flexibility in the outlet velocity and pressure values, which is crucial as the flow inside cross reactor involves flows of fluids of different densities passing through temperature gradients. The walls were set to 'no slip'. Summary of boundary properties for all of the simulations presented in this chapter are shown in Table. 6.1.

The solver calculated steady-state solution as it was assumed that Raman measurements inside of the reactor were performed at equilibrium conditions.

6.3.3 Mesh parameters

Mesh was constructed with CFD physics preference optimised for Fluent solver. The element order was set to linear with the element size of 1×10^{-3} m, resulting in 1260570 elements and 3860753 nodes. The sizing of the mesh, such as growth rate, max size and defeature size were set to default. Automatic inflation at the wall boundary was turned off. Instead, manual inflations were defined at both the reactor inlet, purging channels, and the outlet walls. Inflation options were set to total thickness, with 5 layers of growth rate 1.2 and a maximum thickness of 2×10^{-3} m. The schematic of inflations for the back-end of the reactor and outlet can be seen in Fig. 6.2, which can be observed as 5 concentric rings located at the wall edges. Such inflation would improve flow velocity and species concentration resolution at the boundary, which would aid with the visualisation of flow in the cross reactor.

6.4 Room temperature case

Initial numerical investigation of cross reactor focused on observing the difference in the purging flow behaviour in an environment at ambient conditions with and without implementation of gravity. The inlet boundary conditions for such study cases are shown in Table 6.2. Only two major species, hydrogen and nitrogen were considered in the model. It was assumed that concentrations of precursors, such as thiophene and ferrocene in bulk hydrogen flow, were low enough for them to be labelled as minor species. Thus, their chemical reactions and fluid properties would not have a significant effect on fluid dynamics. Properties of the hydrogen-nitrogen mixture, such as thermal conductivity, viscosity and molecular weight, were taken from the 'Fluent' built-in materials library database. Density of the resultant mixture was set to 'ideal gas' and specific heat C_p expressed as a piecewise polynomial with temperature dependence.

For all of the subsequently mentioned studies, inlet molar fraction in the reactor tube was set to $X_{H_2} = 1$ for **I1**, and $X_{H_2} = 0$ for **I2** and **I3**, resulting in 100% N_2 flow through the purging channels.

Table 6.2 Numerical studies cases at 25 °C with inlet boundary conditions such as velocity, corresponding volumetric flow $\dot{Q}$ at STP , H_2 molar fraction, and inclusion of gravity.

Case #	I1			I2/I3			Gravity
	u (ms^{-1})	$\dot{Q}$ (SLPM)	X_{H_2}	u (ms^{-1})	$\dot{Q}$ (SLPM)	X_{H_2}	
1	0.00493	0.5	1	0.00460	0.05	0	X
2	0.00493	0.5	1	0.00460	0.05	0	✓
3	0.00296	0.3	1	0.00276	0.03	0	✓
4	0.000985	0.1	1	0.000918	0.01	0	✓

The inlet velocities were based on the volumetric flowrates used in experimental measurements shown in Chapter 5. During the development of the purging system, volumetric flowrate through **I1** was set to 0.5 SLPM. Preliminary measurements indicated that the total purging volumetric flowrate of 0.1 SLPM provided the most amount of background reduction without significant dilution of species of interest. Therefore, the same volumetric flowrates were chosen for the initial numerical studies. The purging flow behaviour was investigated as a function of total volumetric flowrate through the reactor, in order to observe the effect of buoyancy forces on the flow pattern and species distribution as a function of gas velocity. The ratio of the inlet to total purge volumetric flowrates was kept at 5-to-1 for all cases to facilitate comparison between the conditions. Cases of this numerical study are outlined in Table 6.2.

For convention, inlet flow in the reactor tube travels along the $+z$ axis, purging flows travel perpendicular in direction of $-x$ and x, respectively, with gravity acting in the $-y$ axis.

6.4.1 Non-gravity case

Figures 6.3a shows the velocity contour along the topdown view plane xz for the non-gravity case # 1 in Table. 6.2. The H_2 enters the reactor through **I1** with a uniform flow front, which quickly becomes a plug flow with a parabolic velocity profile. The profile remains constant up to the junction, where the N_2 plug flows enter from the purging channels, perpendicular to the H_2 flow in the reactor tube. The N_2 flow gets carried downstream of the reactor tube by the momentum of the H_2 flow, where a uniform plug profile is formed with higher gas velocity.

The molar fraction contour of hydrogen as a function of axial displacement along the the top-down plane is shown in Fig. 6.3b. The N_2 molar fraction distribution mirrors the velocity profile, where N_2 enters the reactor tube, perpendicular to the H_2 flow and is then pushed along the reactor wall for a short distance by the momentum from the H_2 flow. As N_2 propagates further into the reactor, it quickly mixes with the H_2 flow, over a short distance, resulting in a uniformly distributed $X_{H_2} = 0.83$.

Figure 6.3c shows the molar fraction contour of H_2 in xy-plane located in the middle of purging channels for the non-gravity case # 1 in Table 6.2. This cross-section contour position will be further referred to as the 'purging plane'. The molar fraction of H_2 is symmetrically reduced at locations of nitrogen injection into the reactor tube at the junction, leading to a degree of dilution. The majority of H_2 is contained within the reactor tube, extending less than 10 mm into the purging channels.

6.4.2 Gravity-enabled case

Figure 6.4a shows the molar fraction contours of hydrogen as a function of axial displacement along the purging plane, for the gravity-enabled case # 2 in Table. 6.2. The molar fraction of H_2 is symmetrically distributed along the centre of the reactor tube, however, its distribution is notably different, compared to the no gravity case # 1. Presence of H_2 extends significantly into the purging channels, due to the influence of buoyancy forces.

Figure 6.4b shows the velocity vector field of the resulting flow pattern, under effects of gravity, in the purging plane which helps to explain presence of hydrogen in the purging channels, shown in Fig 6.4a. As nitrogen enters the purging channels at points **A**, it propagates towards the reactor in a uniformly distributed plug flow. However as N_2 is nearly 14.5 times

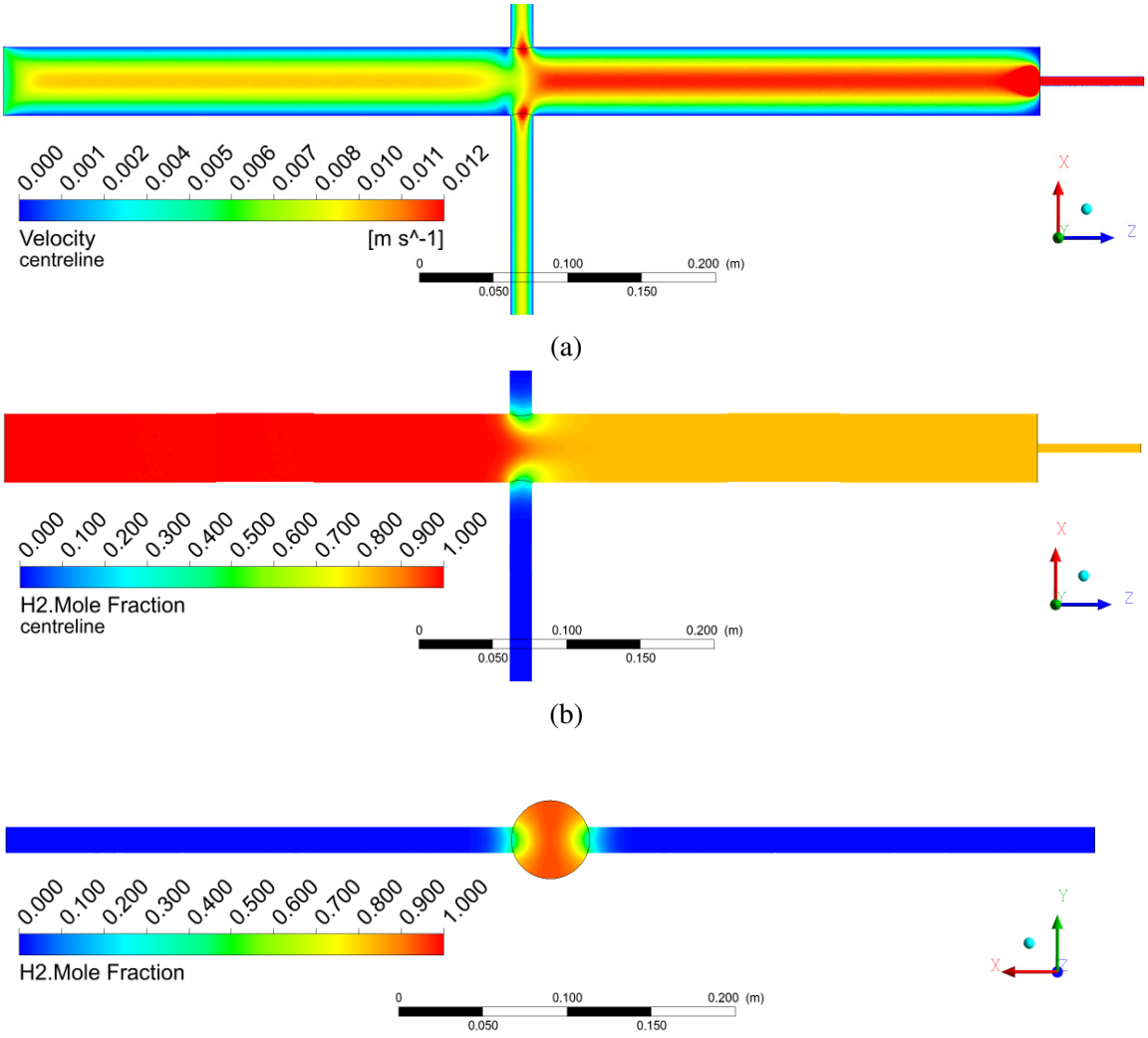

Fig. 6.3 a) Velocity magnitude and b) H_2 molar fraction contours along the topdown view *xz* - plane of the reactor tube and c) H_2 molar fraction contour along the purging plane *xy* for the non-gravity case #1 in Table 6.2

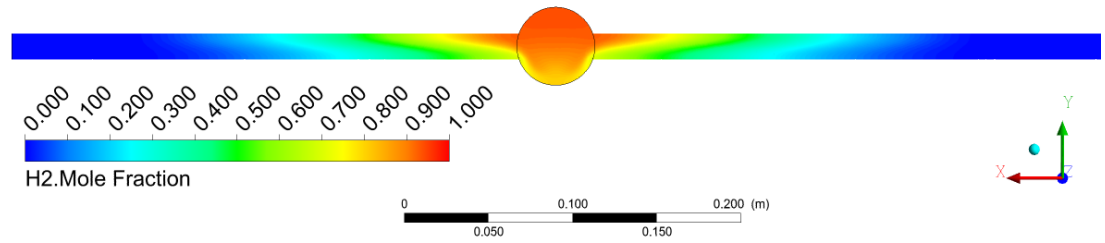

(a)

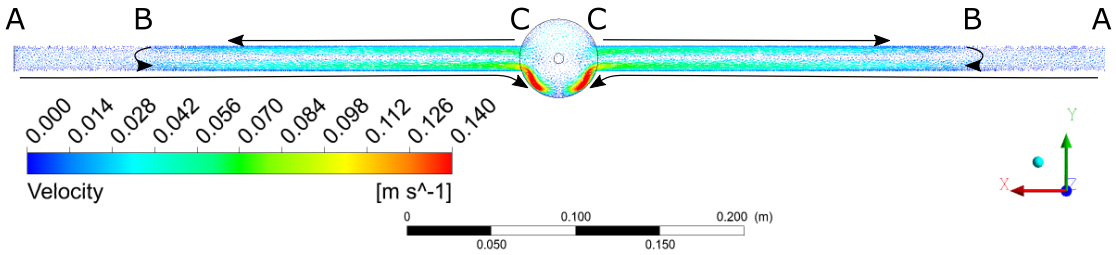

(b)

Fig. 6.4 a) H_2 molar fraction and b) velocity vector fields along the purging plane, for the gravity-enabled case # 2 in Table 6.2

denser than H_2 at standard temperature and pressure, with distance, N_2 begins to move towards the bottom of the purging channel as it encounters an H_2 counter-flow travelling upstream of the purging channel from the reactor tube, at point **B**. The H_2-containing flow mixes with the N_2 downstream-travelling flow as it moves upstream in the purging channel. Once the H_2 molar fraction drops to zero, closer to the purging channel inlet, the upstream flow recirculates into the downstream N_2 flow.

The 'effective channel cross-section' in which the N_2 flow travels towards the junction reduces as a function of axial distance due to an increase in volume of higher H_2 concentration. This leads to an increase in the velocity of N_2-rich flow along the bottom of the purging channel as it reaches the reactor tube, at point **C**. High concentration of H_2 inside of reactor tube facilitates in a rapid shift of N_2 towards the bottom wall of the reactor tube, effectively creating two symmetrical N_2 jets, as highlighted in Fig.6.5. When these two jets collide at the bottom of the reactor tube they create local flow disturbances, resulting in formation of rich N_2 flow upright, towards the middle of the reactor tube, as well as two flows travelling along the bottom wall of the reactor tube in opposite directions along the z axis, as shown at point **A** in Fig.6.6b.

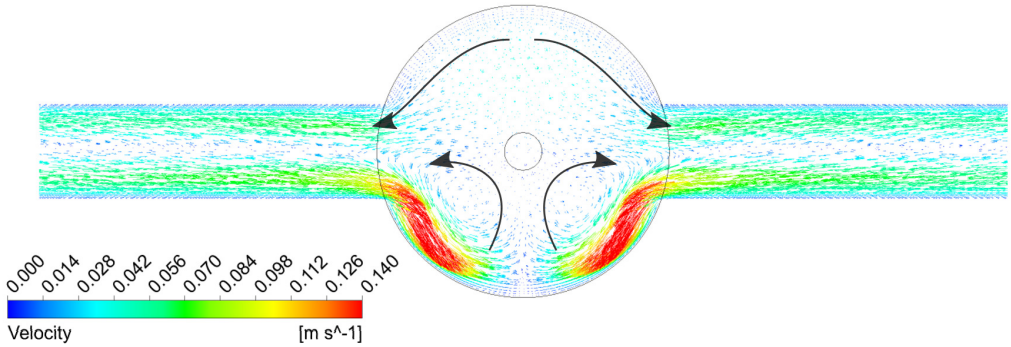

Fig. 6.5 Zoom of junction section in Fig.6.4b along the purging plane

Both flows start off at $X_{H_2} = 0.81$ and increase in value as they propagate further along their respective directions, mixing with the surrounding hydrogen, as shown in Fig. 6.6a. The flow travelling upstream in $-z$ direction does so on the bottom wall of the reactor tube, as it is denser than the hydrogen flow travelling downstream above it, as can be seen in Fig.6.6b. As the upstream-travelling flow reaches the inlet **I1**, it gets lifted by the incoming hydrogen flow, where the mixture of two gases starts travelling downstream, closer to the upper wall of the reactor. Past the point of purging flow injection at the junction, two flows, near the top and the bottom walls of the reactor travel downstream, where, via mixing, they merge into one flow, closer to the reactor outlet.

From hydrogen perspective, as H_2 enters the reactor it is displaced closer to the reactor's upper wall due to local density differences from the presence of nitrogen-containing counter-flow underneath. Upon reaching the middle of the reactor, a fraction of hydrogen is able to diffuse into the purging channels up to a certain distance where it becomes too diluted, so no further H_2 propagation takes place. The remaining amount of H_2 continues travelling downstream of the reactor where a region of constant X_{H_2} is formed.

6.4.3 Flow parametric study

One of the dimensions of interest for the Raman spectroscopy study was to investigate the effect of the residence time of the reagent mixture on the aerogel synthesis process. Residence time is a function of reactor dimensions, such as length and diameter, flow profile and gas velocity field, where the latter is dependent on total inlet volumetric flowrate and the reactor temperature profile. In plug flow reactors, calculation of residence time is quite trivial, as the flow possesses a parabolic velocity profile. However, as Fig. 6.6b has shown, the flow profile in cross reactor does not resemble a plug flow, making volume residence time calculations difficult. Nevertheless, the effect of buoyancy forces on hydrogen propagation

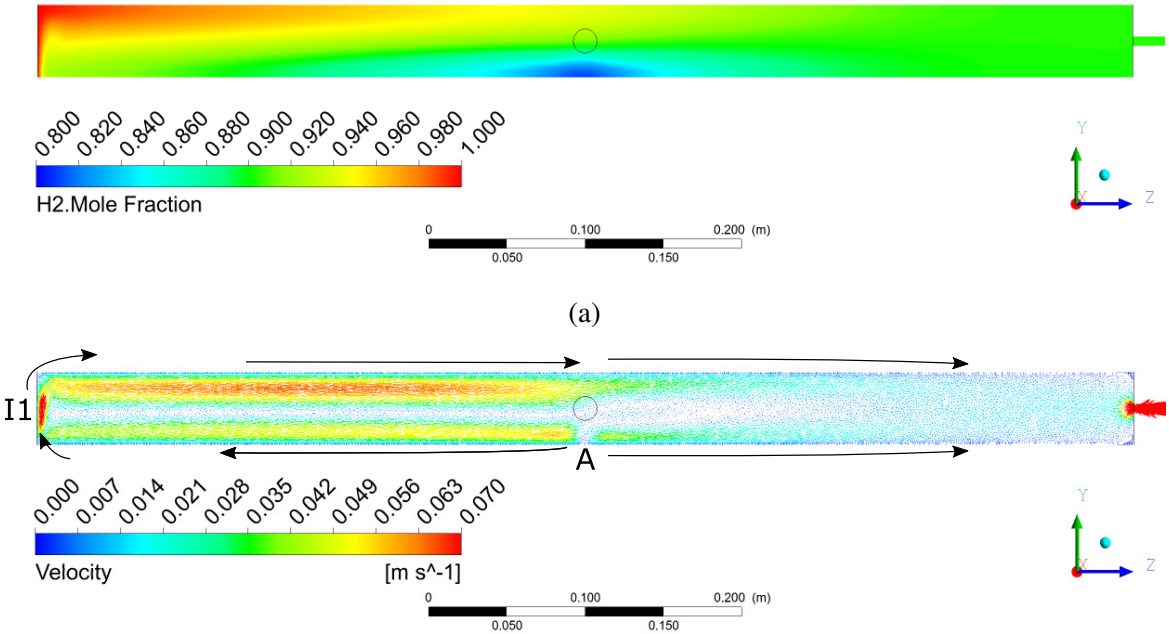

Fig. 6.6 a) H_2 molar fraction contour and b) velocity vector fields along the centerline plane *yz*, for the gravity-enabled case # 2 in Table 6.2.

into the purging channels at lower gas velocities and constant temperature was numerically investigated in gravity-enabled cases# 2-4, listed in Table 6.2, with the reactor tube inlet volumetric flowrate ranging from 0.1 $\rightarrow$ 0.5 SLPM.

Molar fractions of H_2 and N_2 have been extracted from each case outlined in Table 6.2, in the purging plane along the centreline going from the middle of the reactor to the purging channel inlet **I2**, emulating the laser beam path. Figure. 6.7 shows the gas molar fractions where solid lines represent X_{H_2} and dash-dotted lines represent X_{N_2} for the four evaluated cases, with a vertical line at 'axial displacement' of 23.2 mm representing the wall of the reactor tube where the purging channels are attached.

In absence of gravity, H_2 is efficiently contained within the reactor tube, with its molar fraction dropping rapidly to 0 in the purging channels, over a distance of 50 mm from the centre of the reactor tube. Hydrogen molar fraction does not equal to 1 in the middle of the reactor due to mixing with N_2 from the purging channel. The crossing point, an axial location at which hydrogen is no longer the dominant species, is located within the reactor tube.

Inclusion of gravity in cases # 2-4, in comparison to case # 1, results in a much different gas molar fraction distribution, which in particular is dependent on the total volumetric flow

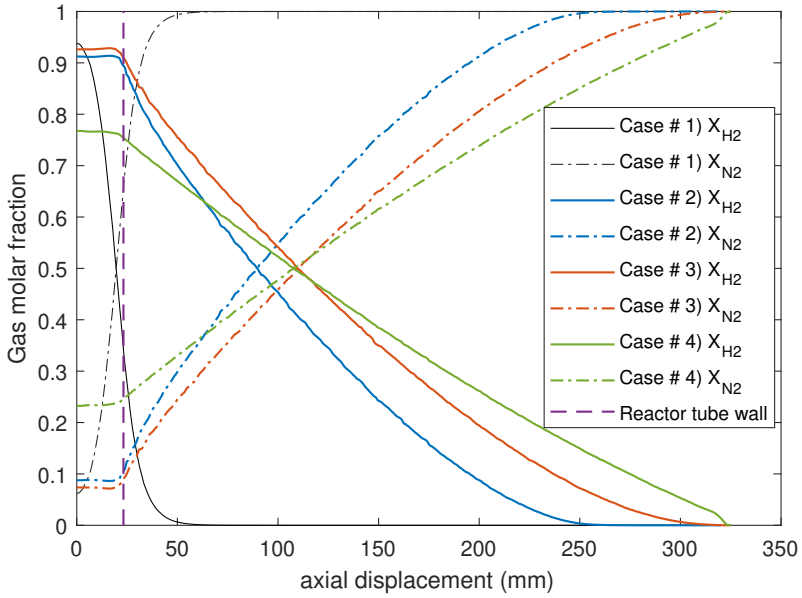

Fig. 6.7 Molar fractions of gases along the centre-line of the purging channel for cases outlined in Table 6.2.

within the reactor. At lower volumetric flowrates, the gas mixing occurs over much longer distances, which diminishes with an increase in volumetric flowrate. In all gravity-enabled cases, H_2 molar fraction remains nearly constant within the reactor tube, in contrast to the no gravity case, where gas mixing occurs within the tube. The X_{H_2} values inside of the reactor vary depending on the total volumetric flowrate, with 0.5 SLPM reactor inlet flowrate in case #2 resulting in the closest value to case #1, as the flowrates in both cases were the same. Lower volumetric flowrates result in lower gas velocities, which give more time for buoyancy forces to affect the molar fraction distributions. This is evident by the molar fraction from case # 4, with 0.1 SLPM reactor tube inlet flowrate, which results in the lowest X_{H_2} inside of the reactor.

The crossing point location varies between cases # 2 and # 3 (0.5 and 0.3 SLPM reactor tube inlet respectively), yet is very similar for cases # 3 and # 4. Changes in its location, coupled with variations in containment efficient of H_2 flow within the reactor tube as a function of total volumetric flow rate could lead to drastic differences in acquired Raman signal per same inlet gas concentrations at constant temperature, as the molar fraction variations inside the purging channels occur along the focusing section of the laser beam path.

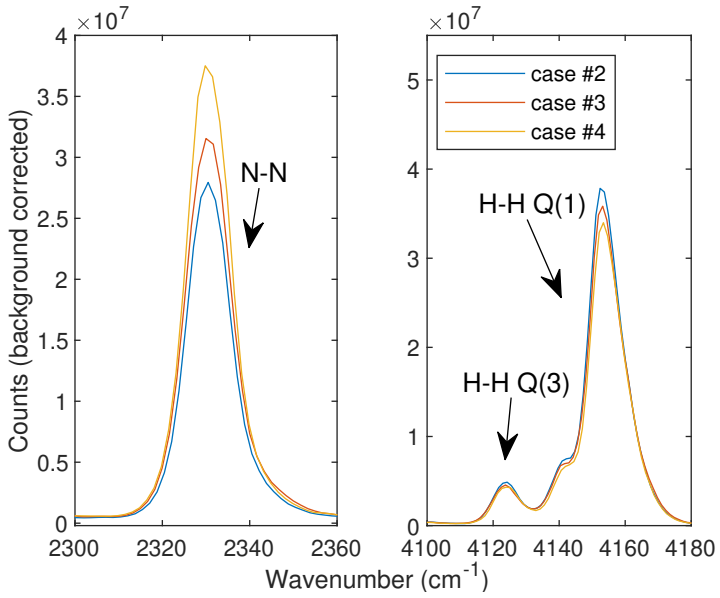

Fig. 6.8 Raman spectra of N_2 and vibrational modes of H_2 for cases # 2-4 in Table 6.2

6.4.4 Room temperature validation

Experimental Raman measurements were performed on cases # 2-4 from Table 6.2, in order to verify the effect of buoyancy forces on molar fraction distribution of gases as a function of volumetric flowrate in the reactor tube. Figure 6.8 presents the Raman modes of N_2 and H_2 as a function of total volumetric flowrate in the reactor. The magnitude of the N_2 mode increases with lower volumetric flowrate in the reactor. This indicates a higher presence of N_2 along the beam path, as it diffuses further towards the centre of the reactor, and hence, the laser focus. The magnitude of H_2 vibrational modes decreases with reduction in total volumetric flowrate. As hydrogen propagates further into the purging channels it moves further away from the focus, which, coupled with increasing dilution in the reactor tube, leads to lower Raman intensities. This highlights that the constructed pulsed laser Raman system is sensitive to the changes in gas mixing lengths in the reactor for gases at constant inlet concentrations at a constant temperature, which occur due to buoyancy forces.

6.5 Elevated temperature case

CNT synthesis occurs in the temperature range of 1100-1300 °C [69], therefore it is important to perform numerical investigations at such elevated temperatures. A gas mixture injected at ambient conditions into a high temperature zone would see an increase in gas velocity of approximately 4.6 times, at constant pressure and volume. In a plug flow reactor, this

would result in a simple gas velocity increase while the parabolic velocity profile shape is preserved. However, in a cross reactor, such velocity changes could lead to drastic differences in the flow pattern, when compared to room temperature. To address these changes, the model developed for flow parameters investigation has been modified with the addition of a heat transfer mechanism in order to investigate changes in the flow pattern and the effect of buoyancy forces on species distribution in a cross reactor at synthesis temperatures.

In order to effectively capture heat transfer in the numerical studies, multiple mechanisms such as conduction, convection and radiation need to be included. This requires precise knowledge of numerous parameters such as heat transfer coefficient of the reactor material, the emissivity of the furnace coils and the resulting radiation temperature, heat generation rate from the reactor wall and properties of shell conduction. Inclusion of all of the listed mechanisms results in computationally expensive models which may be difficult to solve. Instead, the model can be greatly simplified by simulating heat transfer between a gas and a wall boundary set at a fixed temperature. This resulted in an improvement of the stability of the model, as well as a reduction in computation time.

6.5.1 Heat transfer validation

When a fixed temperature boundary condition is used, the heat flux to a wall from a fluid-containing mesh cell is computed as:

$$q = h_f(T_w - T_f) \tag{6.11}$$

where h_f is the fluid-side local heat transfer coefficient, T_w is the wall surface temperature and T_f is the local fluid temperature. The fluid-side heat transfer coefficient is computed based on the local flow-field conditions such as temperature and velocity profiles. In laminar flows, the fluid-side heat transfer coefficient at the walls is computed using Fourier's law, applied at the walls. Fluent uses its discrete form:

$$h_f = k_f \left(\frac{\delta T}{\delta n} \right)_{\text{wall}} \tag{6.12}$$

where k_f is the thermal conductivity of the fluid and n is the local coordinate, normal to the wall.

A FC-CVD reactor is typically heated by an electrical furnace. Resistive coils inside the furnace heat up ambient air, where reactor is then heated by convection from hot air and radiation from the coils. If a reactor is not fully enclosed by the furnace, such as the case with the cross reactor, the gas inside of the reactor would be heated unevenly, giving rise

to gas temperature profiles, where temperatures range from ambient conditions to furnace set-point temperature.

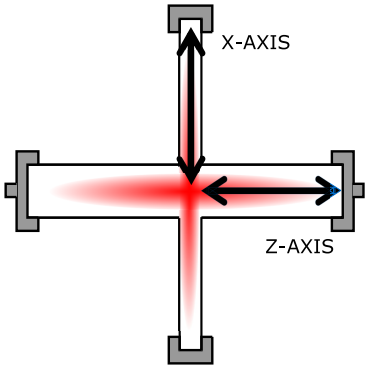

Fig. 6.9 Schematic of direction of axial thermocouple gas temperature measurements. Top view

Variations in gas temperature were investigated by performing traverse axial temperature profile measurements with type 'K' thermocouples at furnace set-point of 1100 °C. Gas temperatures were measured along the centrelines of the reactor tube and a purging channel from their respective starts, towards the centre of the reactor tube, as shown in Fig. 6.9. The measurements were carried at 10 mm intervals, with reactor tube inlet molar fraction set to X_{H_2} = 1 and volumetric flowrate of 0.5 SLPM, and purging channels inlet molar fraction X_{H_2} = 0, with volumetric flowrate of 0.05 SLPM . The measured experimental temperature profiles are shown in Fig. 6.10.

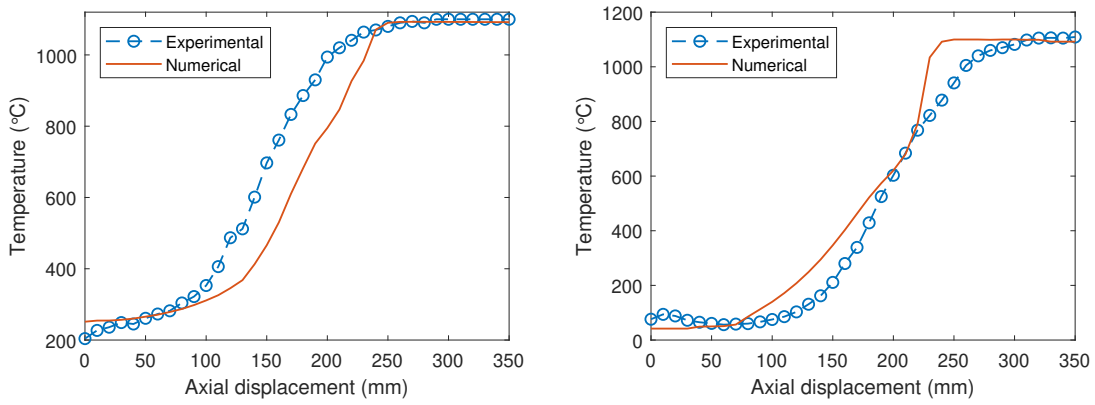

Fig. 6.10 Experimental and numerical temperature profiles along axis of a) the reactor tube (0.5 SLPM and X_{H_2} = 1) and b) a purging channel (0.05 SLPM and X_{N_2} = 1).

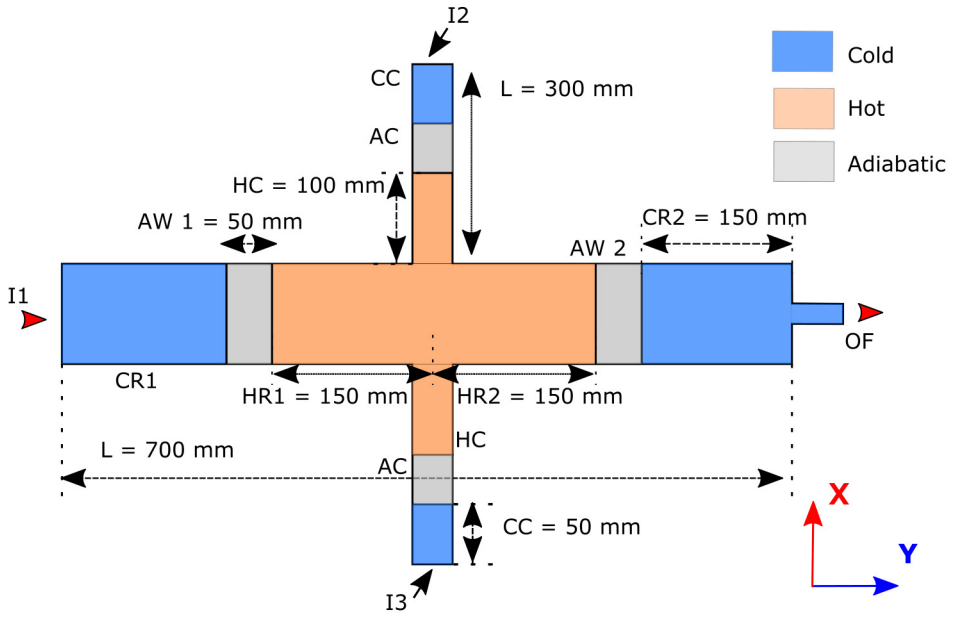

Fig. 6.11 Schematic of the cross reactor with different temperature wall boundary condition zones.

Measured gas temperatures at the reactor junction were within 5 degrees of the furnace set-point temperature. The temperature measured at the reactor tube's outlet (axial displacement = 0 mm in Fig.6.10a), where 100 mm of the reactor tube is located outside of the furnace, was 205 °C, 180 degrees higher than the ambient temperature of 25 °C. This was a consequence of a heat convection transfer by a gas mixture and solid phase heat transfer along the reactor's quartz wall. Temperature at the beginning of the purging channel was much lower in comparison, 75 °C, 50 °C above ambient temperature. This is due to the majority of the purging channel's length being located outside of the furnace's heating volume. Smaller diameter and hence, a smaller cross-section of the purging channel, resulted in a lower amount of heat conducted along the channel's walls.

In the performed numerical investigation, to reflect such temperature discrepancies, the wall boundary has been separated into different zones of constant temperatures, as shown in Fig. 6.11. The blue zones, labelled as 'Cold', represent sections of the reactor tube **CR1** & **2** and purging channels **CC** that are located outside of the electric furnace. Sections **CR1** & **2** and **CC** had different respective 'Cold' starting temperature, to be in-line with experimental measurements. The 'Hot' orange zones, **HR1** & **2** and **HC** represent reactor tube and purging channel walls, whose temperature was set to the furnace set-point temperature. Grey zones **AW 1** & **2** and **AC** indicate an adiabatic boundary wall condition.

Table 6.3 Numerical studies cases for $\dot{Q} = 0.5$ at STP of $X_{H_2} = 1$ through **I1** and 0.05 SLPM at STP of $X_{N_2} = 1$ through **I2** and **I3** respectively as a function of furnace set-point temperature T_h and cooling zones at temperatures T_{CR} and T_{CC}.

Case #	T_h (°C)	T_{CR} (°C)	T_{CC} (°C)
1	25	25	25
2	300	25	25
3	700	80	25
4	900	152	30
5	1100	205	75

The location and length of all of the different temperature boundary conditions have been determined iteratively by comparing centreline temperature profiles computed for case # 5 in Table. 6.3 against thermocouple temperature measurements, as shown in Fig. 6.10. The T_{CR} and T_{CC} temperature values, which represent temperatures of the wall for the cold sections of reactor, **CR1** & **2**, and purging channel, **CC**, respectively, were set to the thermocouple measurements temperature values at an axial displacement of 0 mm for the reactor and the purging channel respectively, shown in Fig. 6.10.

There are some differences between the experimental and numerical temperature profiles. In particular, the temperature drop at the end of the heating area is sharper for the numerical data, compared to a more gradual decrease in experimental values. Such discrepancies are due to the simplified treatment of heat transfer phenomena within the constructed model. However, the shapes of the numerical profiles are acceptably close to capture the major changes in temperature as a function of axial distance. Therefore, the lengths of temperature wall boundaries shown in Fig. 6.11, were used in subsequent numerical investigations for heat transfer modelling.

6.5.2 Gravity enabled case

Temperature, velocity and molar fraction distribution of species in a cross reactor are intertwined. Therefore, their behaviour will be examined on a plane-of-interest basis. The figures showcasing the parameters of interest employ a label system where they are split into the same regions as shown in Fig. 6.11, along with a further distinction referring to upper and lower halves of the reactor, **u** & **d**, respectively, suffixed to the zone label by a dash.

Figure. 6.12a shows gas temperature contour along the purging plane for case # 5 (1100°C furnace set-point temperature) in Table 6.3. As N_2 enters the purging channels its temperature remains constant along the cold wall boundary, **CC**. Once the adiabatic wall

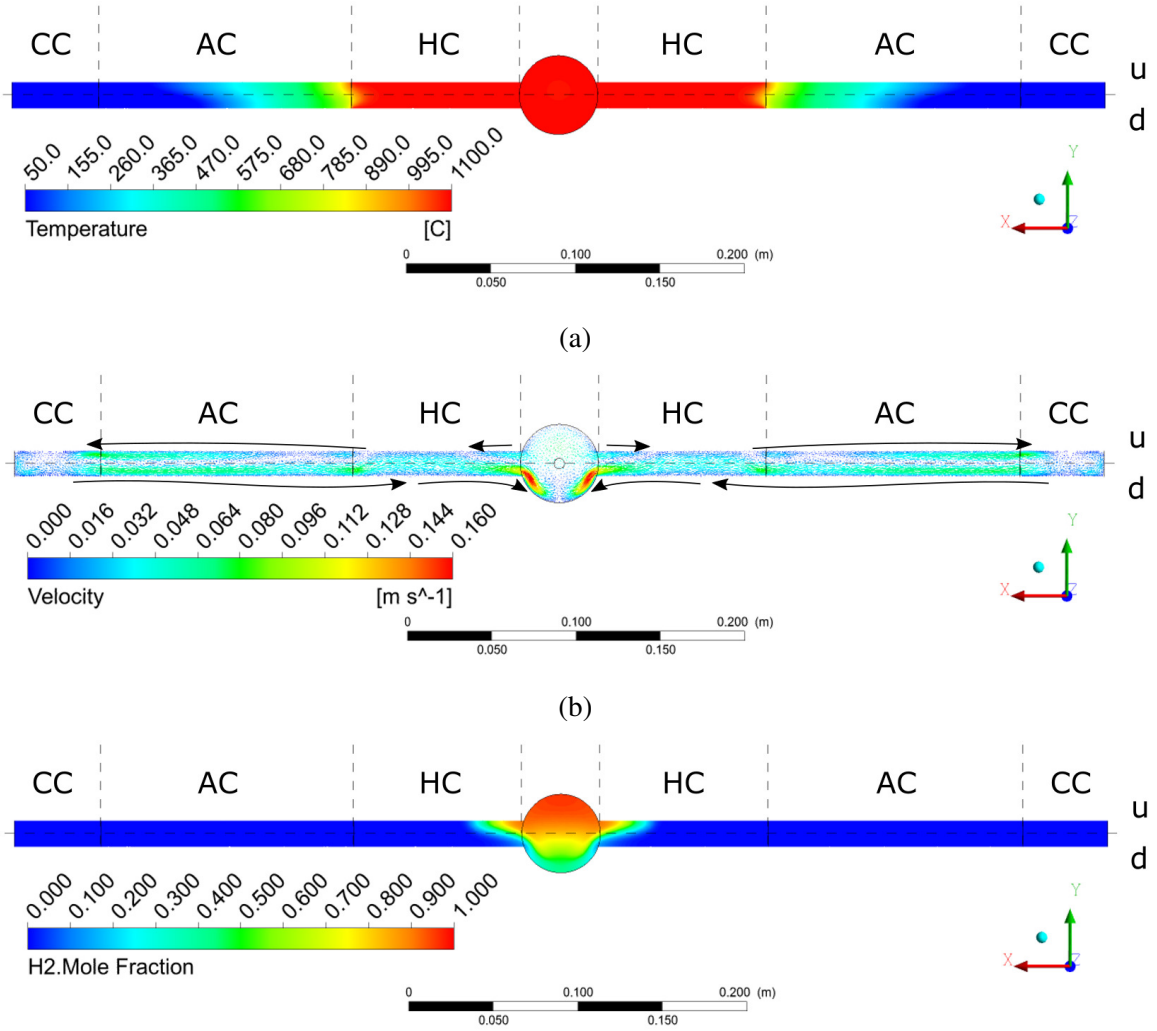

Fig. 6.12 a) Temperature, b) velocity and c) H_2 molar fraction contours along the purging plane for case # 5 in Table 6.3.

boundary (**AC**) starts, a temperature gradient is established along its length, with a constant gas temperature level reached at the start of the hot zone boundary of the purging channel, **HC**. Gas temperature remains constant throughout the hot zone. It should be noted that the temperature front has a curved profile at the start of the hot zone, **HC**, which is a consequence of the velocity vector field along the purging plane, shown in Fig. 6.12b.

At steady-state solution, at the beginning of the purging channel, injected cold N_2 flow moves downstream, towards the bottom of the purging channel, **CC-d** as heated recirculated N_2 flow travels upstream at the upper channel wall, **CC-u**, as seen in Fig 6.12b. Cold N_2 flow propagates towards the reactor junction through the adiabatic boundary, predominantly close to the bottom wall of the purging channel, **AC-d**. With further propagation downstream in **AC-d**, its temperature increases due to heat transfer from the hotter N_2 flow located above, which moves upstream from the start of the hot zone, **HC-u**. The temperature front inside of the purging channel flattens as it gets closer to the hot zone, **HC**, where gas temperature rapidly becomes uniform.

The downstream flow at the start of the hot zone, **HC-u**, adopts a parabolic velocity profile, which gets disrupted closer to the reactor junction due to changes in gas mixture composition, as the purging N_2 flow encounters a H_2 counterflow, travelling upstream from the reactor tube.

The 'effective cross-section' through which the purging N_2 flow travels in the channel decreases with the increase in flow's proximity to the reactor tube wall (boundary of **HC** and **RJ**), resulting in an increase of flow's gas velocity, as seen in fig 6.13b. This gives rise to the earlier mentioned H_2 counterflow, which travels upstream of the purging channel from the reactor tube in **HC-u**, close to its upper wall. Combination of such flow patterns results in the H_2 molar fraction distribution observed in Fig. 6.12c. The propagation length of the H_2 counterflow is much smaller at 1100 °C when compared to the same flowrates at room temperature, shown earlier in Fig. 6.4a. This leads to much more significant containment of the centre flow, as gas velocities are larger at the location where the purging and the reactor tube flows meet, diminishing the effect of buoyancy forces.

As the purging flows enter the reactor tube through a small cross-section, they form two jets that collide at the middle-bottom point of the reactor tube, forming local vortexes as observed earlier in the room temperature case, presented in Fig. 6.5. The vortexes create an N_2-containing jet in $+y$ direction which results in a localised reduction of X_{H_2} in the middle of the reactor tube cross-section.

In the reactor tube volume, similar to the room temperature case, N_2 jet collision in the cross area creates two N_2-containing flows travelling up and downstream along the axis of the reactor tube and its bottom wall, as shown in **HR1-d** & **HR2-d** zones of Fig. 6.13b. As

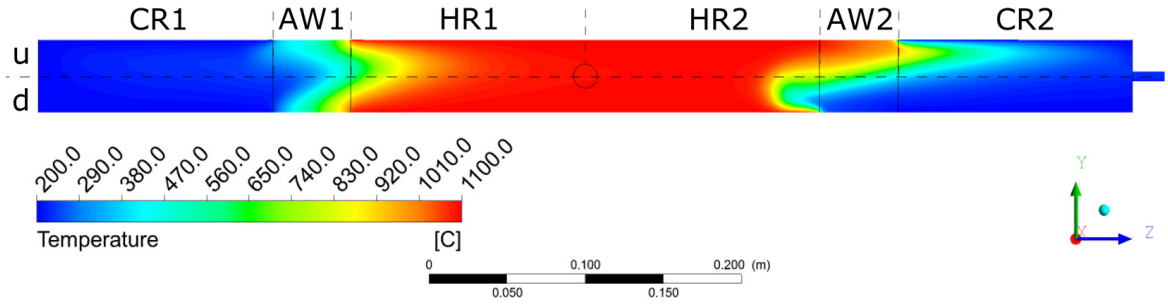

(a)

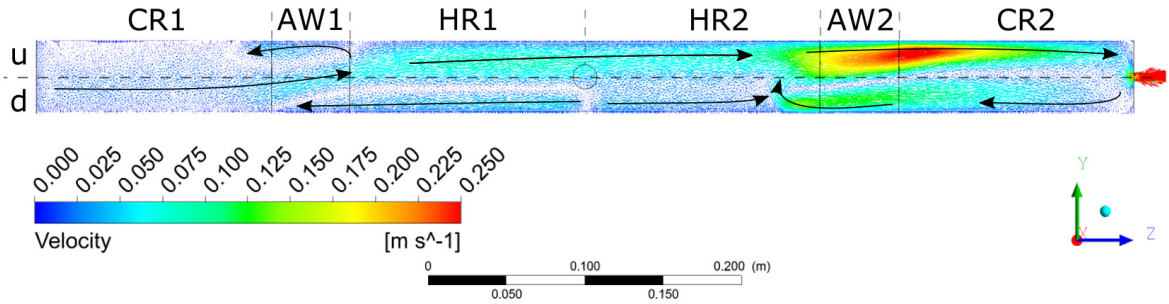

(b)

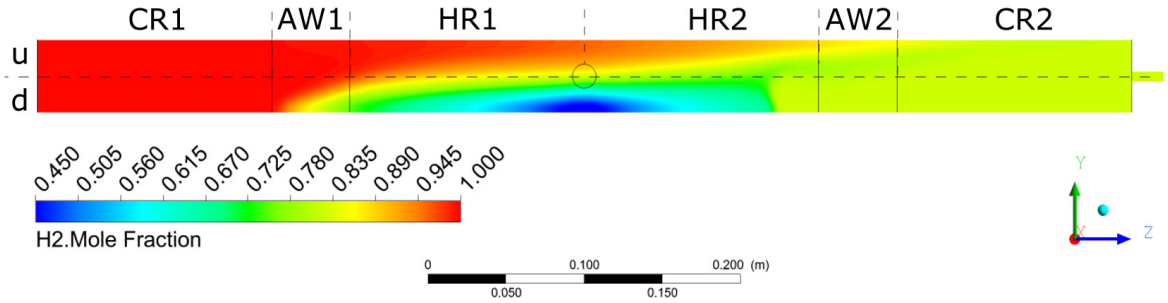

(c)

Fig. 6.13 a) Temperature, b) velocity and c) H_2 molar fraction contours along the centreline plane *yz* for case # 5 in Table 6.3.

N_2-containing flows travel in their respective directions in the reactor tube, they begin to mix with the H_2 flow travelling downstream through the reactor, as evident from the X_{H_2} contour located at the reactor tube centerline plane, shown in Fig. 6.13c. The upstream-travelling N_2-containing flow encounters a 100% hydrogen counterflow from inlet **I1**, at the start of the first adiabatic boundary **AW1-d**, counting from the reactor tube inlet. This H_2 flow moves radially upwards in **AW 1**, due to local gas density differences. Further downstream, a recirculation zone forms at the boundary of the adiabatic **AW1-u** and hot zone **HR1-u**, as a consequence of localised temperature differences. Such velocity profile, coupled with the heat delivered by N_2 upstream flow, gives rise to the non-uniform temperature front, observed in **AW1** in Fig. 6.13a.

The hydrogen-containing flow continues to travel downstream in the hot zone along the upper wall of the reactor, **HR1-u**, accompanied by N_2-containing counter-flow underneath, **HR1-d**. Hydrogen-containing flow's composition changes in presence of increasing N_2 concentration as it travels closer to the purging channel outlets located at the midpoint of the reactor tube.

After the reactor tube and purging channels junction in **HR2**, all of the present gases flow in the same direction downstream of the reactor tube. The overall flow can be separated into predominantly H_2 or N_2-containing streams located closer to the upper (**HR2-u**) or lower (**HR2-d**) reactor tube walls, respectively. The streams travel with different gas velocities. The flow pattern gets heavily disturbed by a temperature-driven recirculation zone formed from the end of the hot zone **HR2** and terminating at the reactor outlet. The velocity of the downstream-travelling H_2-rich flow increases at the start of the second adiabatic zone **AW2-u**, as the effective cross-section in which the flow propagates reduces due to presence of colder, and hence denser, counterflow, originating from the vortex formed at the end of the reactor tube, **CR2**.

High speed H_2-rich downstream flow reaches the end of the reactor tube where a fraction of the flow exits via the outlet. The remaining flow moves towards the bottom wall of the reactor as the result of the change in direction of propagation and further cooling, forming an upstream flow, at the end of **CR2-d**. The upstream flow propagates along the lower wall of the reactor due to its greater density, through the second adiabatic boundary **AW2-d**, after which its direction of propagation is reversed (at the end of **HR2-d**) by the incoming N_2-rich flow, formed as the result of purging jet collisions. The second recirculation zone establishes a region of uniform H_2 molar fraction is the second cooling zone, **CR2**.

The formation of the second recirculation zone in the employed reactor geometry may also be attributed to the small diameter of the outlet, which can introduce a restriction on the outflow, leading to the observed recirculation. It is hypothesised that if the outlet diameter

was to match the diameter of the reactor tube, the hotter gas flow travelling downstream of the reactor would exit in the **CR2-u** region, while a fraction of ambient gas would enter the reactor in an upstream direction, forming backflow at **CR2-d**.

Fig. 6.13c showcases the mitigating effect of the higher gas velocity on the gases mixing effect, particularly when compared to room case results shown in Fig. 6.6a. At high temperature, and hence higher gas velocities, one-quarter of the reactor tube, from its inlet, is filled with 100% hydrogen, contrary to the room temperature case. Nitrogen purging gas is much more contained in the middle of the reactor tube, resulting in higher molar fraction fluctuations as a function of reactor height.

6.5.3 Temperature parametric study

The changes in axial species distribution were investigated as a function of furnace set-point temperature at constant inlet volumetric flowrate in the reactor tube, as outlined in cases listed in Table 6.3. Thermocouple temperature measurements have shown that temperatures at the edge of the reactor tube and the purging channel are 180 and 50 °C higher, respectively, than ambient for furnace set-point temperature of 1100 °C. It is expected that at lower furnace set-point temperatures at the edge of the reactor tube and purging channels would be lower than at 1100 °C. The edge temperatures T_{CR} and T_{CC}, (temperatures of zones **CR1** & and **CC** as shown in Fig. 6.11) for numerical cases at lower furnace set-point temperatures were calculated by multiplying the T_{CR} and T_{CC} values at 1100°C with a correction factor $C_f = T_{set}/T_{ref}$, where T_{set} is the furnace set-point temperature of the case and T_{ref} is 1100 °C. If the corrected temperature was lower than 25 °C, it was set to 25 °C.

The gas molar fractions as a function of axial distance along the centre of the purging channel were extracted for the cases outlined in Table 6.3 and are shown in Fig. 6.14. There is a large difference between the crossing points and gas mixing lengths in the purging channel for the 25 °C and 300 °C furnace set-point temperature cases. With further increase in temperature, the difference in crossing point locations become less severe as they approach the location of the reactor tube wall.

The rate of change of the molar fractions becomes much sharper with an increase in temperature. Furthermore, the axial displacement location at which the molar fraction begins to change gets closer to the reactor as a function of temperature. This is a consequence of higher velocity of the purging gas, resulting in more efficient containment of the reactor tube flow. The two slopes observed in the molar fraction curves for case # 2 (furnace set-point of 300 °C), can be attributed to the start of the heating zone, **HC**, at 122 mm axial displacement from the centre of the reactor tube. The molar fraction variations in cases # 3-5 (set-point temperatures of 700-1100 °C) occur completely within the hot zone **HC**.

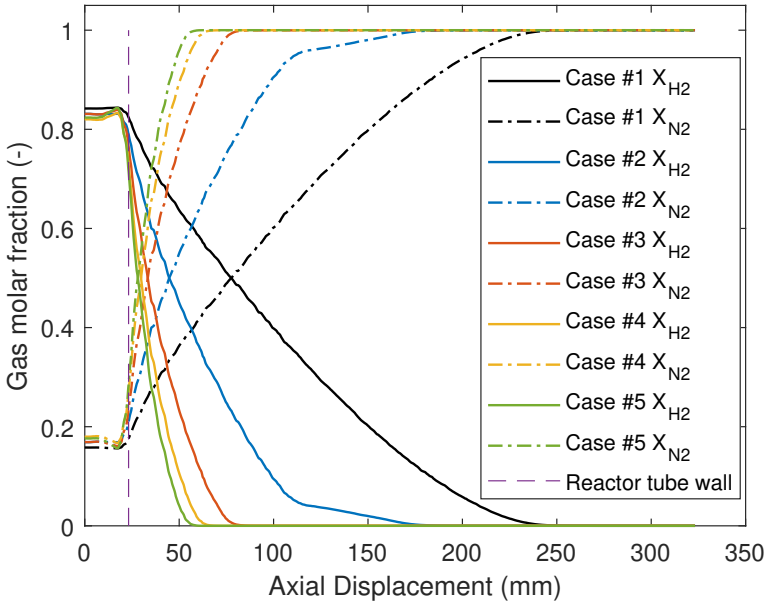

Fig. 6.14 Molar fractions of gases along the centre-line of the purging channel for numerical cases outlined in Table 6.3.

The molar fractions of H_2 inside of the reactor tube slightly diminish as a function of temperature, due to a higher presence of N_2 in the reactor tube. The slight increase of X_{H_2} from 0 to 23.2 mm can be attributed to the vortexes that occur when the N_2 jets collide and dilute H_2 present in the centre of the reactor from the bottom upwards. The strength of the vortexes increases as a function of temperature.

Overall, the containment of H_2 inside of the reactor tube becomes more efficient with an increase in temperature, as velocities of gases increase, diminishing the effect of buoyancy forces. The numerically calculated H_2 molar fraction inside of the reactor tube does not vary by a significant amount as a function of temperature, with much larger variations occurring in the purging channels. Containment of H_2 leads in its dilution by nearly 20%, which could prove detrimental when measuring trace amounts of chemicals.

6.5.4 Homogeneous flow composition case

The formation of the recirculation zones in Fig. 6.13b has been linked to the presence of density and temperature gradients within the reactor, which arose with the inclusion of gravity in the model.

Previous studies [59, 68], aimed at investigation of CNT synthesis process, have performed CFD calculations in cylindrical reactors with uniform inflow, known axial wall

temperature profile and atmospheric pressure, where effects of gravity, and therefore, buoyancy forces have been omitted. The resultant velocity and temperature profiles were those of plug flow reactors, where a homogeneous fluid composition is used.

The high temperature cross reactor model was applied to investigate the behaviour of the recirculation zones with and without gravity in a homogeneous H_2 flow, with case conditions outlined in Table. 6.4

Table 6.4 Numerical studies cases for $\dot{Q} = 0.5$ at STP of $X_{H_2} = 1$ through **I1** and 0.05 SLPM at STP of $X_{N_2} = 1$ through **I2** and **I3** respectively at 1100 °C furnace set-point temperature T_h and cooling zones at temperatures T_{CR} and T_{CC}.

Case #	T_h (°C)	T_{CR} (°C)	T_{CC} (°C)	Gravity
1	1100	205	75	X
2	1100	205	75	✓

Figure 6.15a shows the velocity vector field for the non-gravity case #1 in Table 6.4 with homogeneous flow composition. As the uniform flow enters the reactor tube a parabolic velocity profile is established, as expected. At the start of the adiabatic zone **AW1** the flow begins to accelerate as its temperature increases, resulting in the elongation of the velocity profile's parabolic shape. The shape of the temperature front, shown in Fig. 6.15b, at the start of the hot zone, **HR1**, reflects the velocity profile elongation, as higher velocity flow located in the radial centre of the reactor tube propagates faster with cooler temperature. The velocity magnitude of the flow remains constant up to the junction, where the extra flow is injected from the purging channels. The flow retains its plug flow nature after the junction, with velocity magnitude increasing due to the addition of the purging flows. At the end of the adiabatic zone **AW2**, the flow begins to cool down, leading to its velocity decrease.

Figure 6.15c shows the velocity vector field for the gravity-enabled case # 2 in Table 6.4 with homogeneous flow composition. The flow behaviour is significantly different in comparison to the non-gravity case, as the formation of two recirculation zones is observed close to the inlet and the outlet of the reactor tube, akin to the flow shown Fig. 6.13b.

At steady-state solution, cold flow incoming into the reactor moves to the bottom of **CR1-d** and travels along the lower wall, through **AW1-d** towards the centre of the reactor, with hotter, less dense flow travelling above it, in the upstream direction. Cold gas travelling downstream reaches the heating zone **HR1** and rises to the middle of the reactor, as its temperature reaches a constant value, as shown in Fig 6.15d. Some of the flow begins to travel upstream, starting the first recirculation zone, from the first half of **HR1-u**. The downstream-travelling flow resembles a plug flow, whose flow patterns are not disturbed after

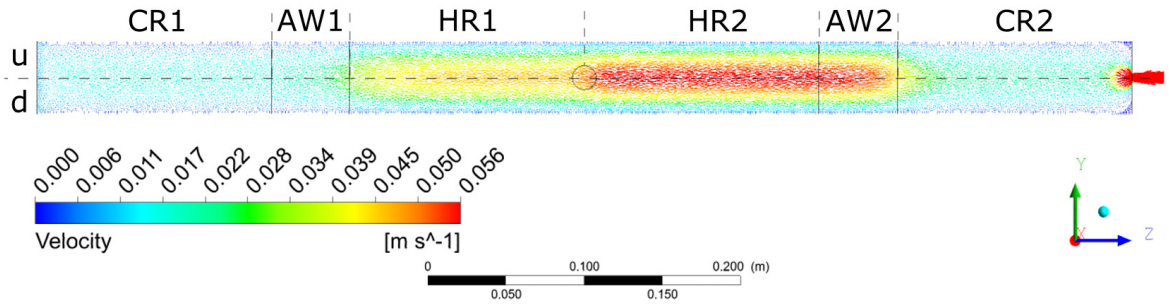

(a)

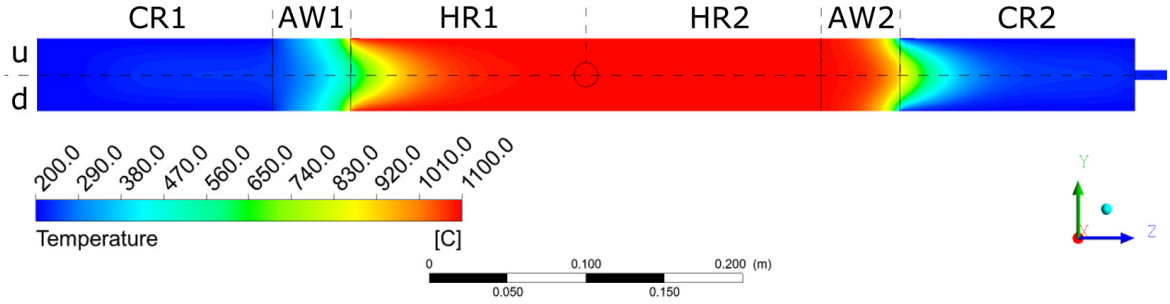

(b)

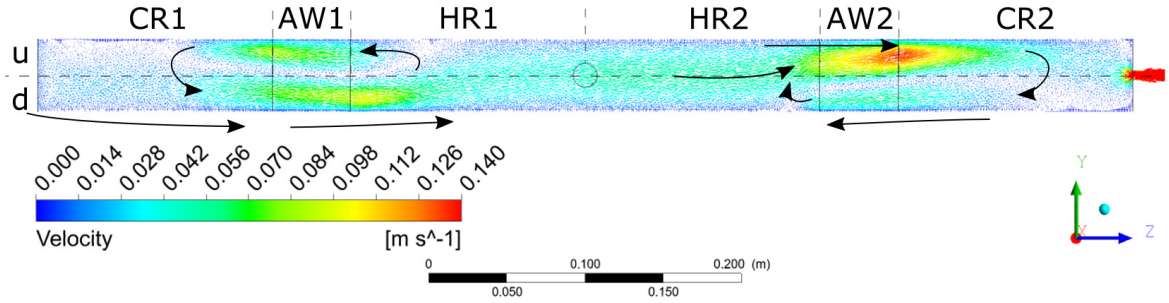

(c)

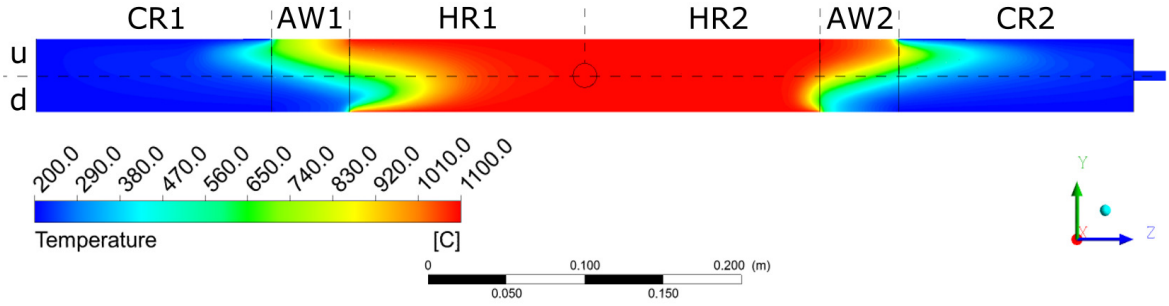

(d)

Fig. 6.15 a) Velocity vector field and b) temperature contour for the non-gravity case # 1 and c) velocity vector field and d) temperature contour for the gravity case # 2 in Table 6.4, along the centreline plane,.

crossing the reactor junction, as the incoming flow from the purging channels is of the same constant temperature. This makes the formation of the first recirculation zone independent of the presence of purging flow.

As the downstream-travelling flow reaches the second adiabatic wall boundary, **AW2**, it moves towards the upper reactor wall, with the colder flow travelling upstream from the second cooling region, **CR2-d**. The velocity of the downstream-moving flow in **AW2-u** increases due to a reduction in its 'effective cross section'. A fraction of the hotter flow leaves through the outlet, while the remaining flow cools down, and begins to travel upstream along the bottom wall of the reactor (in **CR2-d**) due to local density differences, completing the second recirculation zone.

Similarly to the case described in section 6.5.2, the formation of the second recirculation zone may be attributed to the restrictions of the outflow through the small diameter of the outlet with respect to the diameter of the reactor. It is once more hypothesised, that if the outlet diameter was made equal to the diameter of the reactor tube, the hot flow travelling downstream through **CR2-u** would fully exit the reactor, while a fraction of ambient gas would enter the reactor upstream through **CR2-d** region.

The shape of the temperature profile shown in Fig. 6.15d, is similar to the case with H_2 and N_2, shown in Fig. 6.13a. In the case of homogeneous H_2 flow composition, the temperature profile is more symmetric due to the presence of a larger, more uniform recirculation zone close to the start reactor tube.

It was shown that the shape and the length of the recirculation zones is both temperature and species dependent. Presence of recirculation zones has a significant effect on localised temperature values, which are not in agreement with the plug flow assumption. Therefore, if possible, gravity should be included in numerical studies that investigate the CNT-synthesis process, as such flow pattern fluctuations can have an effect on the underlying chemistry processes.

6.6 Conclusion

The numerical studies, performed in Fluent, have revealed complex dependence of H_2 and N_2 distribution within the reactor as a function of temperature and gas velocities. Multiple recirculation zones were formed as a result of the interaction of flows with different densities, temperatures and velocities. It was found that the propagation length of H_2 counterflow into purging channels varied heavily with the total volumetric flow within the reactor and temperature, with the former being experimentally confirmed by Raman measurements. This is crucial information for the acquisition of quantitative Raman measurements. These

results provide useful guidance on the development of the calibration and measurement procedure described in the next chapter. Furthermore, the numerical studies have highlighted the importance of inclusion of buoyancy forces in the models, as that may provide further insight into the kinematics and kinetics, and the formation of CNT-aerogel.

Chapter 7

Reacting Flow Raman measurements

7.1 Introduction

Chapter 5 has demonstrated acquisition of Raman signals for single species of interest with the constructed pulsed laser Raman setup *in situ* of the FC-CVD reactor at 20 and 1100 °C. The use of purging gas was crucial in obtaining Raman signal during species decomposition by preventing the formation of solid-state deposition on the optical access surfaces. Purging and reactor carrier gases had to consist of different species, such as nitrogen and hydrogen, in order to contain the carrier gas in the centre of the reactor tube, ensuring that Raman signal came from the region of constant temperature.

Numerical studies in Chapter 6, however, have shown that presence of the purging gas complicated interpretation of acquired Raman spectra. The containment efficiency of the reactor flow was dependent on the volumetric flows of carrier and purge gases, along with the furnace set-point temperature, which affected the gas velocities. The gas mixing distance increased with a decrease in total volumetric flowrate through the reactor at a constant temperature, due to buoyancy forces having more time to act on species distribution. This effect was most pronounced at room temperature as that's when the gas velocities were the lowest. At constant total volumetric flow input, the mixing length between the carrier and purging gases decreased with an increase in furnace set-point temperature.

As a consequence, the total volumetric flowrate was kept constant for all of the subsequent experiments mentioned in this chapter, in order to remove it as a variable that affects the mixing length of gases.

This chapter demonstrates the calibration procedure necessary for the acquisition of quantitative measurements from Raman spectra. Calibration is performed on non-reacting flows of H_2 carrier gas as a function of temperature and inlet molar fraction. *In situ* gas temperatures are obtained from the ro-vibrational transitions of H_2. Afterwards, the system is

used to study reacting flows, such as H_2-thiophene and H_2-ferrocene mixtures, as a function of temperature. The analysis is based on inspection of products of decomposition and quantification of H_2 molar fraction in the reactor. Finally, the system is used to perform *in situ* Raman measurements inside an FC-CVD reactor during CNT-aerogel synthesis.

7.2 Calibration of pulsed laser Raman system

One of the main goals for the project was to develop a system capable of providing *in situ* quantitative measurements from Raman spectra acquired inside of a FC-CVD reactor. A relationship between counts of observable modes of species of interest as a function of its input concentration had to be obtained, with sufficient precision to allow further use in the study of species decomposition.

The intensity I of a single Raman mode of a species of interest c_i, produced by the employed pulsed laser Raman system, is dependent on multiple instrumentation parameters and can be approximated by the following:

$$I_{c_i} \propto \frac{\Sigma\, n}{E} \propto G(\lambda) c_i(T) \frac{d\sigma_i}{d\Omega}(T) \tag{7.1}$$

where $\Sigma\, n$ is the intensity of the Raman mode, E is the laser pulse energy, $G(\lambda)$ is the system's wavelength-dependent electron multiplication factor, $c_i(T)$ is the molar concentration of species of interest at the observed temperature, and $\frac{d\sigma_i}{d\Omega}(T)$ is the temperature-dependent differential scattering Raman cross-section of the mode.

In an ideal scenario, provided all of the instrumentation parameters are known, one may acquire a calibration curve for the system, where the molar concentration of species of interest can be extracted from any observed Raman mode intensity, as their relationship is linear. There are, however, major limitations associated with this method. First, the acquisition system's wavelength gain response needs to be calibrated, which, depending on the wavelength range examined, may prove difficult and intensive. Second, the value of the differential Raman cross-section of the mode at a temperature of interest needs to be known, as that results in a non-linear dependence of the Raman mode magnitude on temperature. While such information is available for common species such as H_2 or N_2, it may be absent from literature for more complex chemicals, or is provided outside of the experimental temperature range of interest. Furthermore, the system's resolution needs to be sufficient enough to ensure that each mode is independently resolved, otherwise the mode's value may be overestimated due to its convolution with other neighbouring modes.

Table 7.1 Inlet volumetric flow rates and molar fractions of H_2 and N_2 inside of the reactor and purging channels, respectively. Experiments were repeated for temperatures of 20, 300, 500, 700, 800, 900, 1000 and 1100 °C.

Condition #	Q_{H_2/N_2} (rector) (SLPM)	X_{H_2} –	Q_{H_2/N_2} (channels) (SLPM)
1	0.0/0.5	0.0	0.00/0.01
2	0.1/0.4	0.2	0.00/0.01
3	0.2/0.3	0.4	0.00/0.01
4	0.3/0.2	0.6	0.00/0.01
5	0.4/0.1	0.8	0.00/0.01
6	0.5/0.0	1.0	0.00/0.01
7	0.5/0.0	1.0	0.01/0.00

The following calibration method was developed, which allowed extraction of the molar fractions of species, while circumventing the need for the knowledge of the instrumentation parameters, such as wavelength-dependent electron multiplication factor or the temperature-dependent differential Raman scattering cross-section. The employed calibration procedure is molecule specific, however, it can be applied to any molecule of interest provided it doesn't undergo thermal decomposition. The principles of its operation will now be described by looking at hydrogen.

Hydrogen molecule has between 6 to 14 Raman modes detectable by pulsed laser Raman setup in the wavenumber region of interest, depending on furnace set-point temperature. Raman mode magnitude had to have at least 2:1 SNR after background correction, for it to be used in calibration. Hydrogen's inlet molar fraction in the reactor tube, X_{H_2}, was varied from 0 to 1 in increments of 0.2 by dilution with pure nitrogen, as shown by the outlined experimental conditions in Table 7.1. Nitrogen was used as the purging gas to contain H_2 such that observed H_2 Raman signatures were coming from the centre of the reactor.

Calibration Raman spectra, for conditions shown in Table 7.1, were recorded at 8 different furnace set-point temperatures, to capture changes in molecular population distribution of H_2 and the diffusion length of gases as a function of temperature. Condition 1, which represented 100 % N_2 in the reactor, was used as background subtraction for conditions 2-6, after which the locations and peak heights of all of the observable H_2 modes were recorded.

As an example, Fig. 7.1a shows the evolution of Q(1) and Q(3) modes as a function of inlet H_2 molar fraction at 20 °C. The magnitude of hydrogen modes is zero at $X_{H_2} = 0.00$ and increases with the increase in X_{H_2}, as expected. The peak values of each individual H_2 Raman mode were plotted versus their corresponding inlet hydrogen molar fraction in the reactor, with Q(1) and Q(3) mode magnitudes shown as an example in Fig. 7.1b. The

relationship between mode magnitudes and inlet X_{H_2} is not linear, contrary to the expected observation from Eq. 7.1. Such discrepancy may appear due to considerable buoyancy effects at ambient conditions, as explained in Chapter 6. Introduction of N_2 for dilution of H_2 in the centre flow results in a further convolution of the system's response.

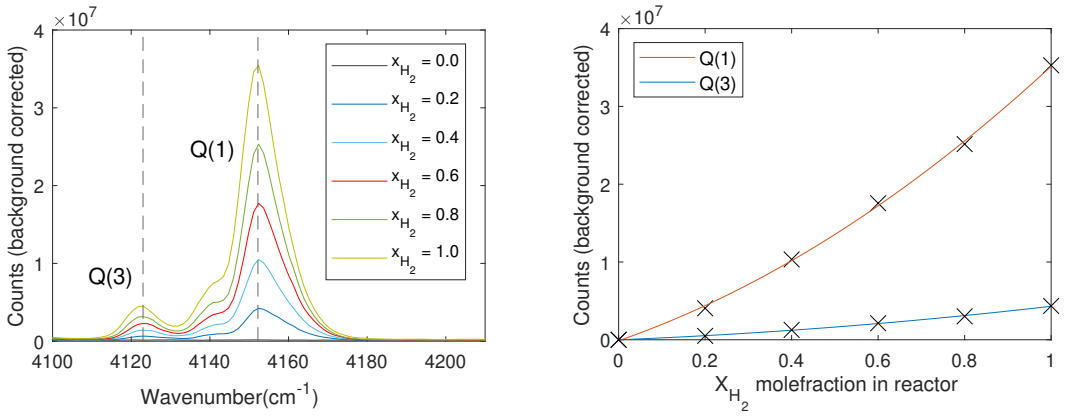

(a) (b)

Fig. 7.1 a) Vibrational modes of hydrogen as a function of inlet hydrogen molar fraction at room temperature, b) Peak magnitudes of Q(1) and Q(3) modes of hydrogen with second-degree fits as a function of hydrogen molar fraction at room temperature

The peak magnitudes of each mode were fitted with a second-degree polynomial. This resulted in an individual calibration curve for each observed Raman mode in the reactor at 20 °C, which allowed to bypass the need for calibration of the instrumentation gain response as a function of wavelength. The peak height fitting procedure was repeated at all other experimental temperatures listed in Table 7.1, in order to obtain corresponding calibration curves for the hydrogen modes at those furnace set-point temperatures. This allowed to incorporate temperature-dependent buoyancy effects into the calibration. With rise in temperature, the number of observed H_2 modes increases, thus, the calibration curves for the new modes were calculated per corresponding temperature basis.

The non-linear response of the mode magnitudes, observed at 20 °C, was investigated as a function of temperature. The peak values of every H_2 mode, recorded at the same temperature, were normalised by their corresponding inlet $X_{H_2} = 1.00$ condition peak value. As the temperature of the mixture at the measurement location did not vary significantly with different input molar fractions (shown in section 7.3), the magnitude of the H_2 modes would vary purely due to changes in X_{H_2}. Normalised mean peak counts for every X_{H_2} condition at the same temperature were calculated by averaging across the normalised peak values of every H_2 mode, as their peak heights now contributed equally to the mean.

Calibration curves were obtained for these normalised mean peak counts at each temperature with the use of second-degree polynomials, and are shown in Fig. 7.2a. The slope behaviour of the calibration curves changes with the furnace set-point temperature. The curves become more linear in nature with an increase in temperature. It is hypothesised that 'bowing' of the curves is due to non-linear changes in X_{H_2} inside the reactor tube due to buoyancy forces. At higher temperatures, gas velocities increase, which results in lesser impact of buoyancy forces, leading to more efficient containment of H_2 in the reactor tube and more linear changes in X_{H_2}, as discussed in Chapter 6.

To further visualise this effect, normalised mean H_2 counts at each temperature were calculated at $X_{H_2} = 0.5$ with the use of the calibration functions, along the dashed line shown in Fig. 7.2a. Ratios of those values vs known inlet molar fraction of $X_{H_2} = 0.5$ were calculated and are shown in Fig. 7.2b. The discrepancy between the measured and set molar fractions is largest at ambient conditions and is nearly equal to 20%. With increase in temperature, as the magnitude of buoyancy forces diminishes, the ratio approaches 1, where the experimental and set molar fraction values are within 5% error past 900 °C furnace set-point temperature.

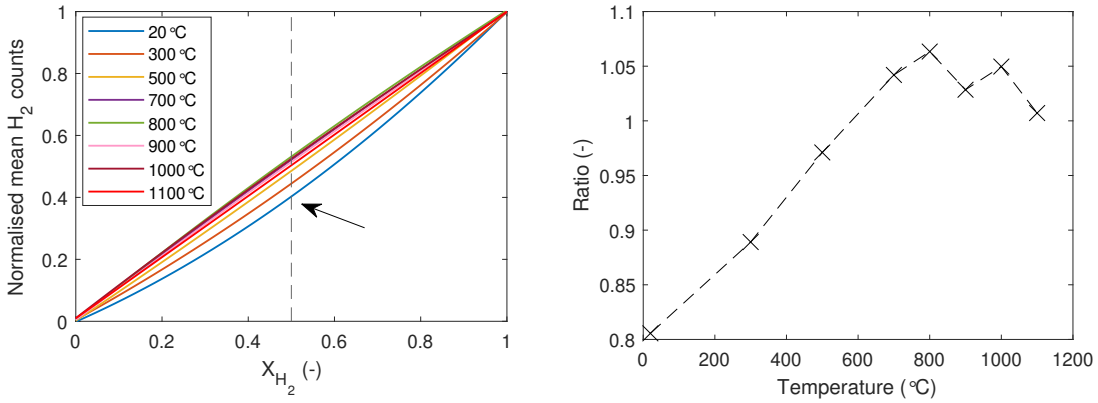

(a) (b)

Fig. 7.2 a) calibration curves for the normalised mean peak counts of hydrogen modes as function of hydrogen molar fraction in the temperature range of 20-1100 °C. b) Ratio of the normalised mean peak counts at $x_{H_2} = 0.5$ from (a) (indicated by an arrow) and 0.5 as a function of furnace set-temperature

The pulsed laser Raman system has been calibrated to variations of input H_2 molar fraction at specific experimental temperatures. The calibration procedure accounted for different magnitude of buoyancy forces at different temperatures, linked to both gas velocities and the mixture fraction of the flow. Furthermore, as each mode was compared to itself, the need for knowledge of the wavelength-dependent instrumentation gain function or temperature-dependent differential Raman scattering cross-section was removed. Thus,

investigations proceeded with quantitative analysis of reacting flows occurring during CNT-synthesis in FC-CVD reactor.

One of the major concerns during the reactor operation was potential leaks into and from the reactor of ambient air or hydrogen respectively. Not only would that affect the measured molar fractions but also result in health and safety concerns as oxygen would be in contact with heated hydrogen gas. The peak magnitudes of oxygen and water modes were monitored across all of the calibration conditions as they represented the species located outside of the reactor. Raman spectra of oxygen and water, along with their analysis, are shown in Appendix C. Results have shown that no leaks occurred into the reactor during the measurements.

7.3 In situ measurements of gas temperature by Fulcher-α hydrogen bands

The magnitude of Raman emission depends on the molecular number density, which in turn, is a function of gas temperature. The knowledge of temperature at which the Raman spectrum was recorded is crucial when performing quantitative measurements. Small fluctuations in gas temperature could result in large uncertainties when measuring the concentration of trace species between different spectra. Thermocouples provide precise temperature measurements and are commonly used in an *in situ*, invasive manner. However, they can not be used simultaneously with Raman spectroscopy at the measurement location as a high energy laser beam is present. Therefore, the following method has been adopted to extract temperature measurements from the acquired Raman spectra inside of the reactor.

This method is based on the analysis of population density distributions between various excited molecular states of H_2. It has been used for *in situ* temperature measurements of molecular plasmas [178–180] and gases, where it has been shown to be in good agreement with more convectional temperature measurement methods performed by Doppler broadening [181], CARS [182], and thermocouples. Furthermore, the method has the advantage of temperature extraction directly from the Raman spectra, without the need for comparison to theoretically modelled spectra [183–185]. A brief explanation of the method operation is given here, and a more thorough derivation is provided in [186].

The intensity of the spectral line I, due to the rovibronic transition $n,v,N \rightarrow n',v',N'$ can be written as:

$$I^{nvN}_{n'v'N'} = N_{n'v'N'} A^{nvN}_{n'v'N'} \tag{7.2}$$

where n is a set of quantum numbers describing an electronic state of the molecule, v is the vibrational and N is the rotational quantum number. $N_{n'v'N'}$ represents the population density (in cm^{-3}) of the initial rovibronic level and $A^{nvN}_{n'v'N'}$ corresponds to the transition probability of spontaneous emission (in s^{-1}). If the populations of the rotational levels in the excited n, v vibronic state are close to the Boltzmann's law then the rotational temperature $T_{rot}(n', v')$ for this state may be expressed as [187]:

$$N_{n,v,N} = c_{n,v} g_{a,s} (2N+1) \exp\left(\frac{-hcE_{nvN}}{k_b T_{rot}(n,v)}\right) \tag{7.3}$$

where $c_{n,v}$ is a normalising constant, $g_{a,s}$ is the degeneracy of the n v N level, connected with the nuclear spin, $E_{n',v',N'}$, h is Plank's constant, c is speed of light and k_b is Boltzmann's constant.

In order to work out the rotational temperature of the hydrogen gas, Eq. 7.3 can be simplified by adopting the following assumptions:

(1) the population distribution in the ground ($v' = 0$) vibronic state obeys Boltzmann's law, resulting in rotational temperature equal to gas temperature;

(2) the excited states are populated mainly via electron collisions from the ground ($v' = 0$) vibronic state;

(3) the transitions with a change in angular momentum $|\Delta N| \geq 2$ may be neglected and the rate coefficients are assumed to be independent of the rotational quantum number;

(4) the effective lifetime of the excited state does not depend on the rotational quantum number and is much shorter than the relaxation time of the rotational levels.

By making another assumption, that rovibronic transition probability is independent of the rotational quantum number, the population level of $v = 2$ can be related to the rotational temperature as follows:

$$\frac{N_{nvN}}{g_{a,s}} \propto \frac{I^{nvN}_{n'v'N'}}{(\nu^{nvN}_{n'v'N'})^3 \cdot g_{a,s} \cdot (2N+1)} \propto \exp\left(\frac{E_{X0N}}{T_{rot}}\right) \tag{7.4}$$

where I is the intensity of the rovibronic transition $n, v, N \rightarrow n', v', N'$, $\nu^{nvN}_{n'v'N'}$ is the wavenumber of the radiative transition (in cm^{-1}), N is the rotational quantum number, E_{X0N} is the rotational energy of the ground state (in K) and T_{rot} is the rotational temperature, that is equal to gas temperature (in K).

The transition parameters for the lines of (2-2)Q branch of the Fulcher-α band are listed in Table. 7.2 [188–190]. Figure 7.3a shows Raman spectra of hydrogen rovibrational transitions Q(x) (where $x = 1 \rightarrow 7$) as a function of temperature at $X_{H_2} = 1.0$ (condition 6 from Table. 7.1).

Table 7.2 Transition parameters for the first 7 lines of (2-2) Q branch of Fulcher-α band of hydrogen molecule [3].

Line	E_{X0N} (K)	v (cm^{-1})	N	$g_{a,s}$
Q(1)	170.5	4155.234	1	3
Q(2)	509.8	4143.447	2	1
Q(3)	1015.1	4125.855	3	3
Q(4)	1681.6	4102.565	4	1
Q(5)	2503.8	4074.000	5	3
Q(6)	3304.0	4039.478	6	1
Q(7)	4279.7	4000.044	7	3

Equation. 7.4 can be further simplified as:

$$\ln\left(\frac{I^{nvN}_{n'v'N'}}{(\nu^{nvN}_{n'v'N'})^3 \cdot g_{a,s} \cdot (2N+1)}\right) = \frac{E_{X0N}}{T_{rot}} + const. \tag{7.5}$$

where *const*. is a constant that combines all of the factors that are independent of the rotational quantum number.

Therefore, gas temperature can be determined by plotting the dependence of the logarithm of the reduced line intensity (left side of Eq. 7.5) on the molecular energy of the ground state E_{X0N}. The $I^{nvN}_{n'v'N'}$ term, in the logarithm, is the measured Raman peak value of the Q(x) transition, with the other parameter values provided in Table. 7.2. Examples of such fits are shown in Fig. 7.3b, for the logarithm of experimentally acquired reduced Raman mode intensities at inlet X_{H_2} = 1.0 and N_2 purging gas, and furnace set-point temperatures of 300 (red) and 1100 (blue) °C. The extracted gas temperature values from the Raman spectra are in good agreement with the furnace set-point temperatures.

Results of temperature measurements performed on the experimental conditions outlined in Table. 7.1, using the presently described technique within the reactor, are plotted against measurements made with a sheathed type-K thermocouple at the Raman measurement location, and are shown in Fig. 7.3c. The thermocouple measurements were not corrected for radiation. Raman temperature measurements at 20 °C were not deemed to be sufficiently accurate owing to only two transitions, Q(1) and Q(3) being visible, so instead they were set to 20 °C.

At X_{H_2} = 1 (condition 6 in Table. 7.1), the extracted temperatures are in good agreement with the thermocouple measurements up to 800 °C, with the discrepancy between two data sets increasing at higher temperatures. The intensities of the transition lines decrease with

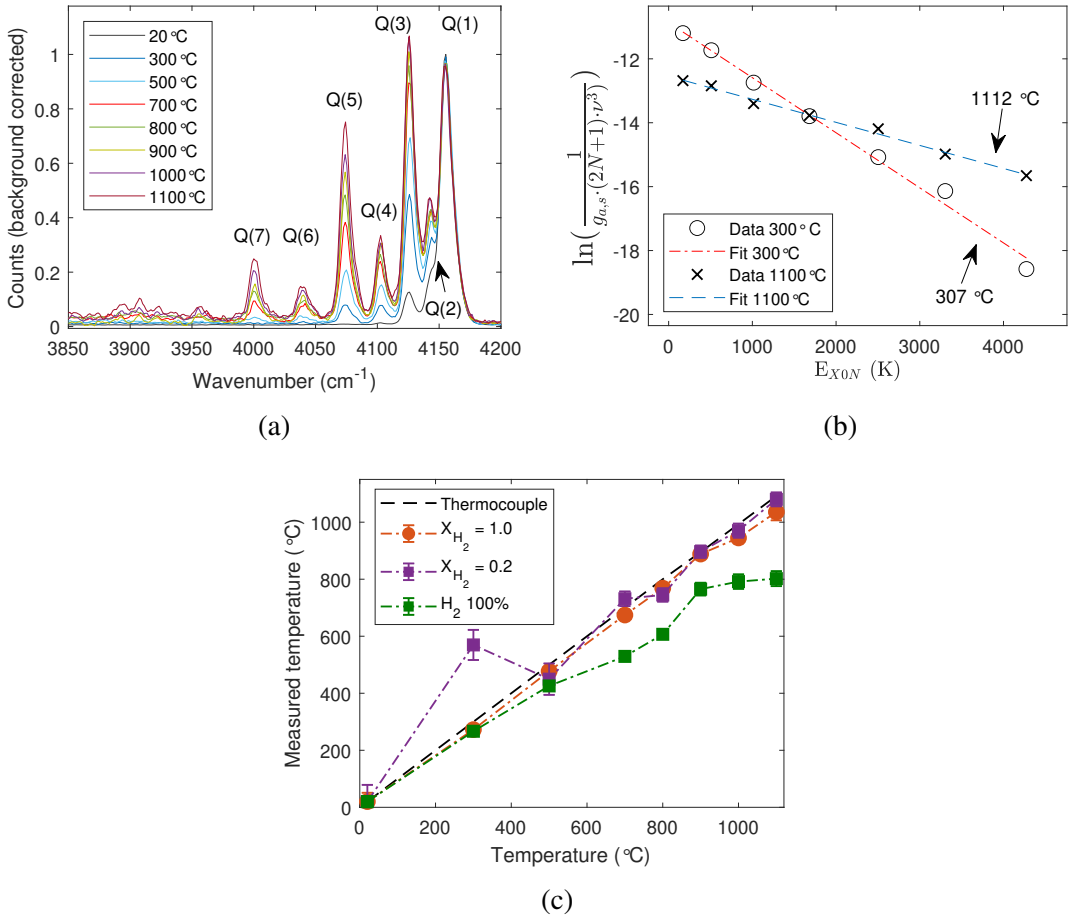

Fig. 7.3 a) the Q modes of hydrogen at $X_{H_2} = 1$ as a function of temperature, b) E_{XON} fits for Eq. 7.5 showcasing linearity of transition magnitudes, c) gas temperature at the laser measurement location measured by a thermocouple and H_2 Raman emission for $X_{H_2} = 1$ (orange), average across $X_{H_2} = 0$, 0.2, 0.4, 0.6, 0.8, and 1 conditions (purple), and $X_{H_2} = 1$ with H_2 purging flow (green).

the decreasing H_2 molar concentrations present at high temperatures which may lead to increased uncertainty in measurements.

The $X_{H_2} = 0.2$ (condition 2 in Table. 7.1) temperature set represents the lowest hydrogen concentration in the reactor measured during calibration. At 300 °C furnace set-point temperature, Raman based and thermocouple measurements are in a large disagreement. This arose due to low Raman mode magnitudes as consequence of small H_2 concentration within the reactor, coupled with only two transitions, Q(1) and Q(3), having a good SNR at that temperature. The agreement between the two datasets improves with increase in temperature, as more ro-vibrational transitions are observed. In fact, $X_{H_2} = 0.2$ temperature measurements are in better agreement with the thermocouple measurements than temperatures from X_{H_2}

= 1.0, in the furnace set-point temperature range of 900-1100 °C. Such behaviour may be due to the more efficient containment of H_2 within the reactor. Alternatively, the specific heat of N_2, C_p on average is 14 times lower than H_2, which may lead to the temperature of predominantly N_2 gas mixture be higher by a few degrees, compared to the H_2 mixture. Nevertheless, this demonstrates that the limiting factor in the application of Fulcher-α temperature measurement method is the number of detected transitions with sufficient SNR.

The $H_2 = 100\%$ data set in Fig.7.3c corresponds to condition 7 in Table. 7.1, where the centre and purging flows consist of X_{H_2} = 1.0. The disagreement between Raman and thermocouple measured temperatures increases as a function of furnace set-point temperature. This dataset clearly highlights the influence of the colder hydrogen gas located in the purging channels on the overall Raman spectra. The extracted temperatures are therefore a convolution of the central and purging channel signals.

Overall, this temperature measurement method has been proven to be an acceptable substitute for thermocouple gas temperature measurements. It is able to extract temperatures from *in situ* acquired spontaneous Raman spectra of a hydrogen-containing mixture inside of a FC-CVD reactor, without the need for comparison to any theoretical spectra. The method can be used from 300 °C, provided the X_{H_2} of the mixture inside of the reactor is close to one, resulting in good SNR of transition, or from higher temperatures where all 7 ro-vibrational transitions are observed at low quantities of H_2.

7.4 Thiophene decomposition study

7.4.1 Previous thiophene decomposition studies

Thiophene, a liquid at ambient conditions with a boiling point of 82 °C, is molecularly stable to temperatures of up 825°C [191, 192] in pure thiophene atmosphere. At prolonged heating times and high temperatures, main pyrolysis products of thiophene include benzene, hydrogen, methane and hydrogen sulphide, along with lower levels of dithiophenes. The nature of the thiophene decomposition products is dependent on multiple parameters, such as final pyrolysis temperature, carrier gas used and the reaction time.

Thiophene pyrolysis was previously performed in an electrical vertical furnace, with a hot zone of 29 cm in a fused silica reactor tube, 62 cm in length and 2 cm inner diameter [191]. The decomposition was studied at two temperatures, where a slight reduction of thiophene amount was observed at 800 °C, followed by an extensive deposition at 825 °C. Gas phase chromatography revealed a product consistency of 65% Hydrogen and 35% methane. No ethylene, acetylene or other hydrocarbon compounds were observed.

Pyrolysis of thiophene was also performed at temperatures of 900-1050 °C in a silica reactor, enclosed in an electrically controlled furnace [193]. Helium was used as a dilutant and carrier gas. Exhaust gases were analysed by gas chromatography. At 1050 °C no presence of thiophene was detected, with the products consisting mostly of benzene and methane. Ethylene and acetylene were present as intermediate species. Furthermore, at such temperature, benzene underwent some decomposition, leading to the formation of hydrogen sulphide in large quantities.

Thiophene vapour was put into a cylindrical Pyrex (length = 10 cm, diameter = 3.8) at pressures of a few hundred pascals (not specified by source), where it was pyrolysed by an IR laser, estimated to produce temperatures of 880 to 930 °C [194]. FTIR spectra were recorded directly using the cell, either from vapour of the liquid or solid deposits located on cell windows. Pyrolysis resulted in solid deposits of polythiophene, with acetylene being the major product present in the gas phase, along with trace quantities of methane and benzene observed after prolonged laser exposure.

A study of thiophene decomposition was performed in a shock tube experiment in an argon atmosphere, with pressures between 2.5 - 3.44 bar and a temperature range of 1598-2022 K [195]. At such high temperatures, H_2S and ethanethiol were detected as the main sulphur containing products, with lower levels of carbon disulphide becoming more prominent at higher temperatures. The main hydrocarbon species was acetylene, with lower levels, of methanol, ethene and propyne. The study was able to extract the reaction rate of thiophene decomposition.

Hoecker et al. studied the decomposition of thiophene in a H_2 environment, almost identical to the one present in this work, by performing FT-IR on the exhaust gases coming out of the reactor [59]. Thiophene decomposed over the 750-950°C temperature range, forming methane and an alkyne C triple bond stretch at 2150 cm^{-1}. No thiophene modes were observed at 1050°C furnace set-temperature.

7.4.2 Experimental Setup for the study of Thiophene thermal decomposition

The present experiments used the high-temperature electric furnace with the cross reactor for the study of thiophene thermal decomposition in a hydrogen environment. The two variables of interest in the decomposition study were the initial thiophene molar fraction and furnace set-point temperature. Thiophene was delivered into the reactor via hydrogen carrier gas, which bubbled through a thiophene-containing bubbler, akin to experiments described in Chapters 4 and 5. The thiophene molar concentration in the gas mixture can be determined

by two methods: a) measuring the change in mass of the thiophene-containing bubbler, or b) assuming equilibrium conditions and using the Antoine equation [69] (equation and thiophene specific coefficients are listed in Appendix. B).

The agreement of the two mass rate determination methods was investigated experimentally by the gravimetric analysis of the thiophene bubbler. The bubbler was filled with 60 ml of thiophene, such that the bottom of the inlet gas pipe was submerged in liquid. During all of the thiophene-containing experiments, the bubbler was placed in an ice bath where it was left for an hour and a half prior to running any experiments. This ensured that thiophene inside the bubbler would reach a constant temperature of 0°C.

For gravimetric analysis, the weight of the bubbler was measured before and after a flow of hydrogen, ranging from 0.1 to 0.5 SLPM in increments of 0.05 SLPM, has bubbled through the bubbler for one and a half hours. The bubbler was weighed by Sartorius LC1200 scales, which have 1 mg precision. Once the bubbler was removed from the ice bath, for the after measurement, it was placed briefly under some cold water in order to remove any ice that may have stuck to its walls. The bubbler was then dried, weighed, and put back into the ice bath for half an hour so that thiophene would reach 0°C, before proceeding with subsequent measurements.

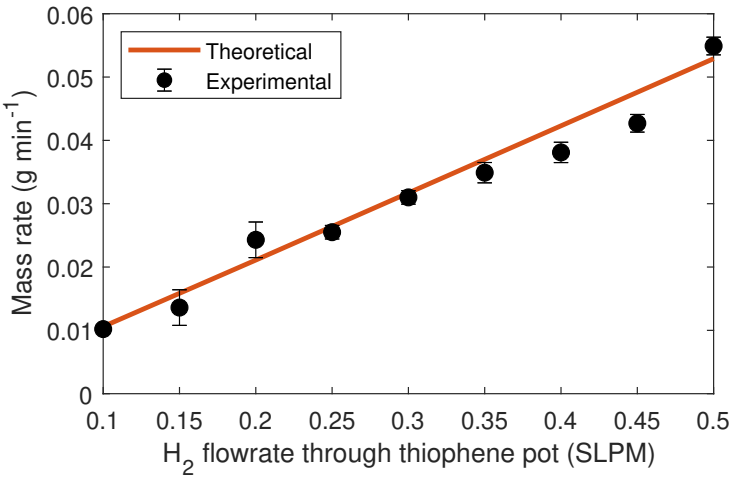

Fig. 7.4 Experimental and theoretically determined thiophene mass rates as a function of H_2 flow through the thiophene bubbler.

Figure. 7.4 shows the experimental and calculated thiophene mass rates using the Antoine equation. The experimental measurements are in good agreement with theoretical predictions up to 0.35 SLPM where the bubbler starts to provide less mass rate until over predicting at 0.5 SLPM. However, overall it was decided that the data sets were in good agreement and the molar fractions calculated from the Antoine equation would be used moving forward.

Table 7.3 Experimental conditions for thiophene thermal decomposition study. Listed: predicted hydrogen and thiophene mass and molar flow rates, concentration percentage inside the reactor from Antoine equation, partial pressures and $H_2(\dot{Q})$ volumetric flowrates sent through the bubbler and used for dilution. Thiophene bubbler kept at T = 0 °C, with the partial pressures for thiophene and hydrogen equal to 0.028 and 1, respectively. Experiments repeated at furnace set-point temperature of 20, 300, 500, 700, 800, 900, 1000 and 1100 °C. The molecular mass of thiophene and hydrogen are 84.14 g mol^{-1} and 2.02 g mol^{-1}, respectively.

Exp #	$\dot{Q}_{dilution/bubbler}$ (SLPM)	$\dot{n}_{H_2/C_4H_4S}$ $\times 10^{-4}$ mol m^{-1}	$\dot{m}_{H_2/C_4H_4S}$ $\times 10^{-2}$ g m^{-1}	Conc %
1	0.4 / 0.1	204.3 / 1.3	4.1 / 1.1	99.4 / 0.6
2	0.3 / 0.2	204.3 / 2.5	4.1 / 2.1	98.8 / 1.2
3	0.2 / 0.3	204.3 / 3.8	4.1 / 3.2	98.2 / 1.8
4	0.1 / 0.4	204.3 / 5.0	4.1 / 4.2	97.6 / 2.4
5	0.0 / 0.5	204.2 / 6.3	4.1 / 5.3	97.0 / 3.0

The outlined experimental conditions for the study of thiophene decomposition in a H_2 environment are listed in Table 7.3, with the schematic of the experimental setup shown in Fig. 5.7. The experiments were performed at the same furnace set-point temperatures as the hydrogen calibration work in section 7.2. At each temperature, five conditions with different input thiophene molar concentrations were established by varying the hydrogen flow through the thiophene bubbler and the hydrogen dilution flow, respectively, to the total volumetric flow inside the reactor of 0.5 SLPM. The two flows were mixed at a T-junction located 200 mm prior to injection location into the reactor, to ensure that they were mixed. Nitrogen gas was used for purging at 0.05 SLPM in each purging channel. The molar and mass rates per each condition are also shown in Table 7.3. The maximum thiophene molar concentration in the proposed experiments did not exceed 3%. Such limit was set to keep in line with the experimental conditions used in earlier studies of the CNT synthesis via FC-CVD [68, 196].

7.4.3 Equilibrium Calculations of Thiophene thermal decomposition

As discussed in Section 7.4.1, thiophene decomposition produces a vast array of hydrocarbon products. The abundance of a specific product seems to depend both on the decomposition temperature and the chemical composition of the environment.

Thermodynamic equilibrium calculations were performed in order to predict the expected products of thiophene decomposition for the presented system. These types of calculations have been used extensively to model chemically reactive flows such as flames or plug flows and even predict carbon deposition in fuel cells. A model has been developed by

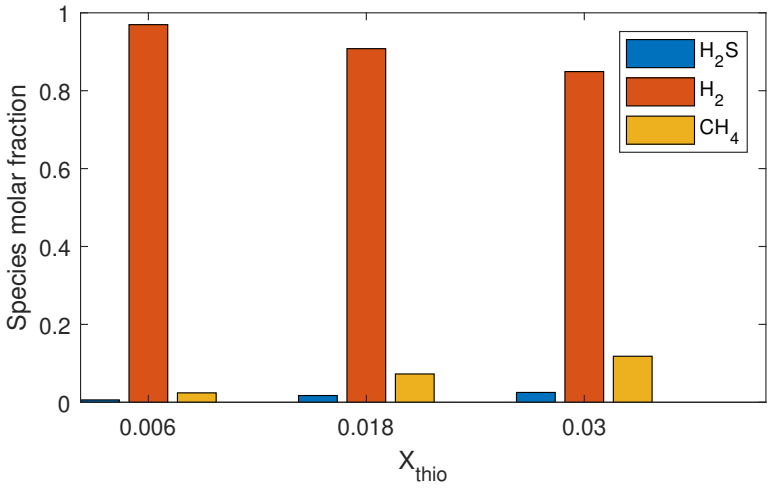

Fig. 7.5 Resultant equilibrium calculations molar fractions of major species of thiophene decomposition at 1100 °C mixture temperature and atmospheric pressure.

C. Zhang [197], capable of performing thermodynamic equilibrium studies for FC-CVD process using a software suite called Cantera [198]. The suite has been extensively used in chemistry and engineering research fields and has multiple object-oriented software tools for calculating problems of chemical kinetics and thermodynamics. Zhang has investigated the expected equilibrium products of the CNT synthesis in FC-CVD process over the range of temperatures and varied stoichiometry, with the inclusion of 125 species in three phases into his database. The results of the simulations and the list of species included in the database can be found in the following thesis [197]. While the present system of interest probably has not reached equilibrium at the Raman measurement location, it was deemed useful to perform the following equilibrium calculations for comparison with experimental data.

A gas-phase mixture was created with molar fractions of hydrogen and thiophene of experimental conditions 1,3 and 5 in Table. 7.3, at atmospheric pressure and 1100 °C. An equilibrium composition of the mixture was calculated, with resultant molar fractions of major species shown in Fig. 7.5.

The major species consist of hydrogen, methane and hydrogen sulphide (H_2S). With an increase of thiophene molar fraction in the initial gas mixture, the ratio of methane to H_2S has also increased. The minor product species, whose molar fraction was less than 0.01, were ethene, acetylene and carbon disulphide. While the presence of all of the listed products is in agreement with previously reported studies, their quantities differ drastically. As most of the measurements in the reported studies were performed ex-situ, the discrepancies are most likely due to the changes in the chemical composition during cooling of the product mixture on the way to the measuring apparatus.

7.4.4 Thiophene Raman spectra as a function of temperature

Figure 7.6 shows the Raman spectrum of 3% thiophene inlet molar concentration at room temperature (exp. 5 from Table 7.3), background-subtracted by 100% N_2 spectra. Table 7.4 lists the location and bond assignment of the 5 observed independent thiophene modes and 2 thiophene modes (marked with '*'), whose positions overlap with hydrogen Raman modes.

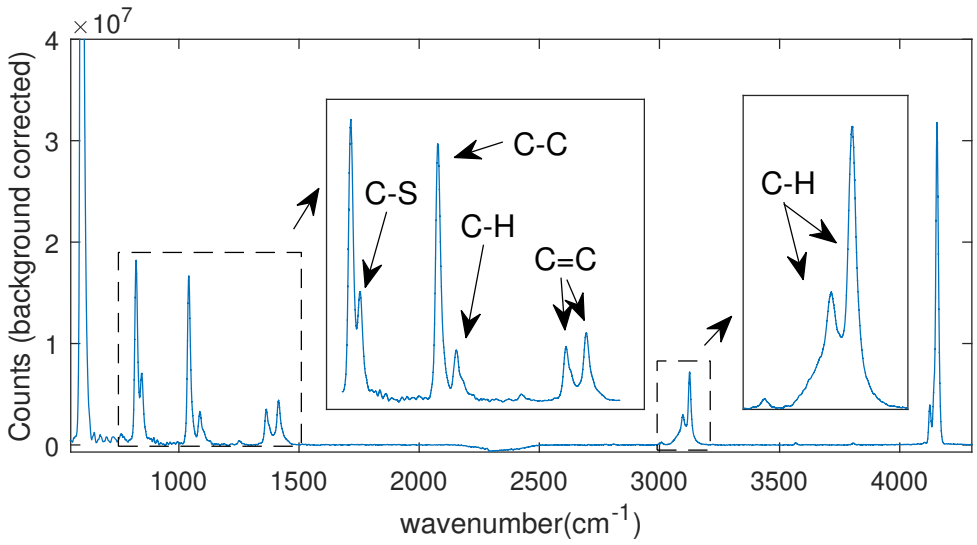

Fig. 7.6 Raman spectra of 3% mole fraction of thiophene in the reactor at room temperature.

The modes marked with an asterisk ' in Table 7.4 were used as markers for monitoring thiophene's presence in the reactor, as modes 1 and 3 are in the region of increased uncertainty from background subtraction due to the fluorescence emitted by the dichroic filter, which resulted in visual uncertainty during background subtraction.

Table 7.4 List of observed thiophene modes at room temperature. Position of modes marked by * overlap with position of H_2 Raman modes. Modes marked by ' are used for mode intensity analysis.

Mode #	Exp. freq (cm^{-1})	Assignment
1	846	C-S (ν)
2*	1040	C-C (ν)
3	1088	C-H (δ) C=C (ν)
4'	1365	C=C (ν)
5'	1415	C=C (ν)
6*	3098	C-H (ν)
7'	3126	C-H (ν)

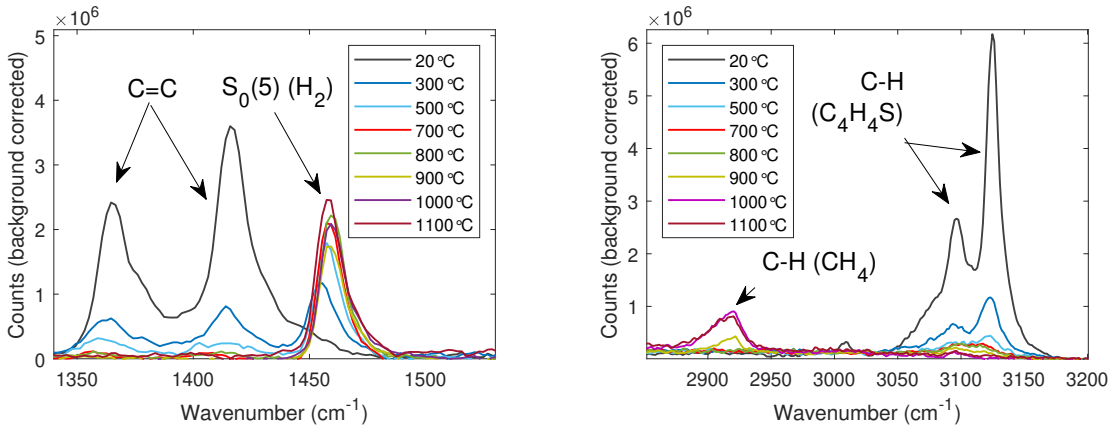

(a) (b)

Fig. 7.7 Thiophene Raman modes as function of temperature for input condition $X_{thio} = 0.03$.

Figure. 7.7 shows how the Raman spectra of the thiophene-H_2 mixture change as a function of temperature, for an inlet thiophene molar fraction of 0.03. Thiophene Raman modes decrease in intensity up to 800 °C, beyond which, the modes are indistinguishable from the noise floor. The wavelength location of the thiophene modes changes. Figure 7.8a shows the blue shift in wavelength experienced by the C-H bond at 3126 cm^{-1}, as a consequence of the thiophene molecule gaining more kinetic energy at higher temperatures and leading to a higher degree of molecular vibration.

At 900°C, a new mode appears at 2920 cm^{-1} which has been assigned to the v_1, C-H mode of methane. It reaches a maximum value at 1000 °C, followed by a slight decrease at 1100°C. Such mode magnitude decrease could be attributed to the lower gas number density at 1100 °C, in comparison to 1000 °C, resulting in a weaker Raman signal. Alternatively, the use of nitrogen as the purging gas could be facilitating the thermal breakdown of methane, as discussed in Section 5.3.3. Another mode is observed centred at 2600 cm^{-1}, as seen in Fig. 7.8b, that corresponds to the symmetric v_1 stretching vibrations of H-S bond of hydrogen sulphide [199]. The mode first appears at 900°C and reaches its highest magnitude at 1100°C. This would confirm the hypothesis that methane magnitude decreased at 1100°C due to thermal breakdown facilitated by the presence of nitrogen.

The magnitude of the observed H-S mode is quite low, especially at lower inlet thiophene concentrations where it becomes nearly indistinguishable from the noise. In order to confidently confirm its presence, the overall inlet volumetric flowrate in the reactor was dropped to 0.1 SLPM, which was all routed through the thiophene bubbler, resulting in $X_{thio} = 0.03$, with the total purging flow reduced accordingly by a ratio of 1/5 to 0.02 SLPM. The resultant spectrum is labelled by a star (*) in Fig.7.8b. The magnitude of the H-S mode is much

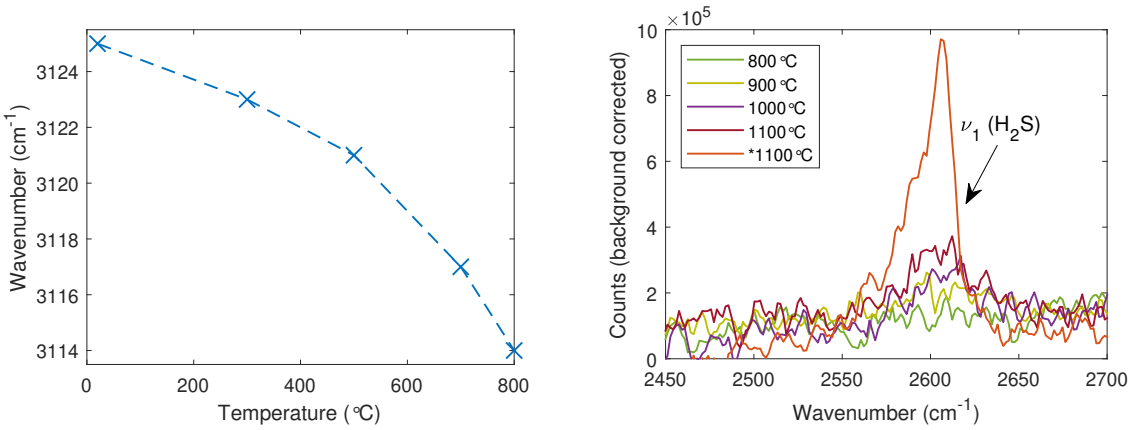

(a) (b)

Fig. 7.8 a) Blue shift of a thiophene C-H mode at 3126 cm^{-1} as function of temperature b) H_2S Raman mode as a function of temperature at $X_{thio} = 0.03$, 0.5 SLPM total reactor flow, 0.1 SLPM N_2 purging flow with *condition performed at $X_{thio} = 0.03$, 0.1 SLPM total reactor flow and 0.02 SLPM N_2 purging flow.

larger in condition (*), suggesting that central flow gas has diffused more into the purging channels due to the reduction in liner gas velocity. The signal to noise is such that it allows to confidently confirm the presence of H_2S as the product of thiophene decomposition.

Figure 7.9 shows the magnitude of CH_4 ($\nu 1$) and H_2S ($\nu 1$) Raman modes as a function of inlet thiophene molar concentration at 1100 °C. The mode magnitudes of both species are proportional to the inlet thiophene molar concentration, indicating that the amount of the products formed as the result of thiophene decomposition is directly related to inlet thiophene molar fraction.

While it was not possible to perform quantitative molar fraction measurements of methane and H_2, the observed products are in agreement with the thiophene thermal decomposition products predicted by Cantera simulations. Presence of the methane is in agreement with the products observed by Hoecker et al. However, no other major peaks were detected in the 2000-2100 cm^{-1} region with the presence of thiophene in the reactor, indicating that no acetylene or any other C≡C containing compounds were formed, contrary to their observations. The observed breakdown temperature range of thiophene in a hydrogen environment (800-900°C) is in agreement with the breakdown temperature observed in pure thiophene vapour atmosphere [191] and hydrogen environment [59].

In addition to H_2S and methane, Si-H Raman modes start to appear at 900 °C, centred at 2030 cm^{-1}, as observed earlier in Section 5.3.2. Figures 7.10a and 7.10b show the magnitudes of Si-H peaks as a function of temperature for inlet molar fractions of $X_{H_2} = 1.00$ and $X_{thio} = 0.03$ respectively. While in both conditions the magnitude of Si-H modes

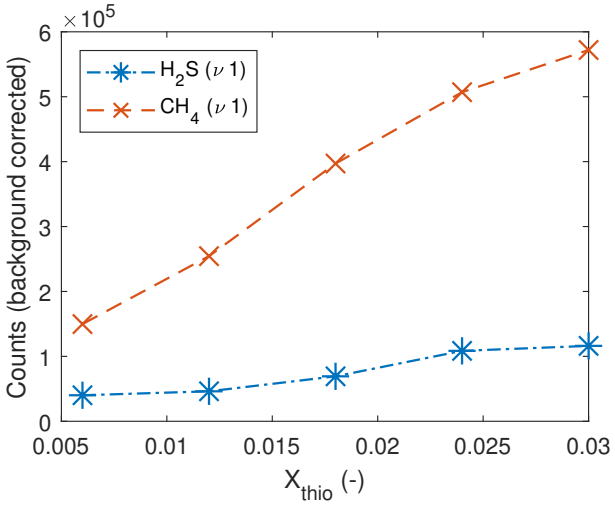

Fig. 7.9 Magnitudes of CH_4 ($\nu 1$) and H_2S ($\nu 1$) Raman modes as a function of inlet thiophene molar fraction at 1100 °C

increases with temperature, presence of thiophene seems to encourage higher Si-H production. Figures 7.11a and b show the variations of Si-H mode magnitudes as a function of inlet X_{H_2} and X_{thio}, respectively, at 1100 °C furnace set-point temperature. Both hydrogen and thiophene have a direct impact on the magnitude of the observed Si-H modes. By tracking the magnitude of the left mode Si-H (marked in Fig.7.11), the linear dependence of Si-H mode magnitude on the amount of thiophene and hydrogen is revealed, as shown in Fig.7.12.

An increase in thiophene inlet molar fraction leads to the formation of larger quantities of thiophene decomposition products, which in turn reduce the molar concentration of hydrogen in the reactor at 1100 °C. However, the reduction in X_{H_2} due to an increase in the amount of decomposition product formation is assumed to be negligible in comparison to the variation of $X_{H_2} = 0 \rightarrow 1$, shown in Fig. 7.11a. Therefore, it is possible to conclude that both, variations in inlet molar fractions of thiophene and hydrogen have a linear effect on Si-H production. However, the presence of thiophene decomposition products in the reactor results in a larger production of Si-H, as the intensity of its Raman emission is nearly one magnitude larger than in a pure hydrogen environment.

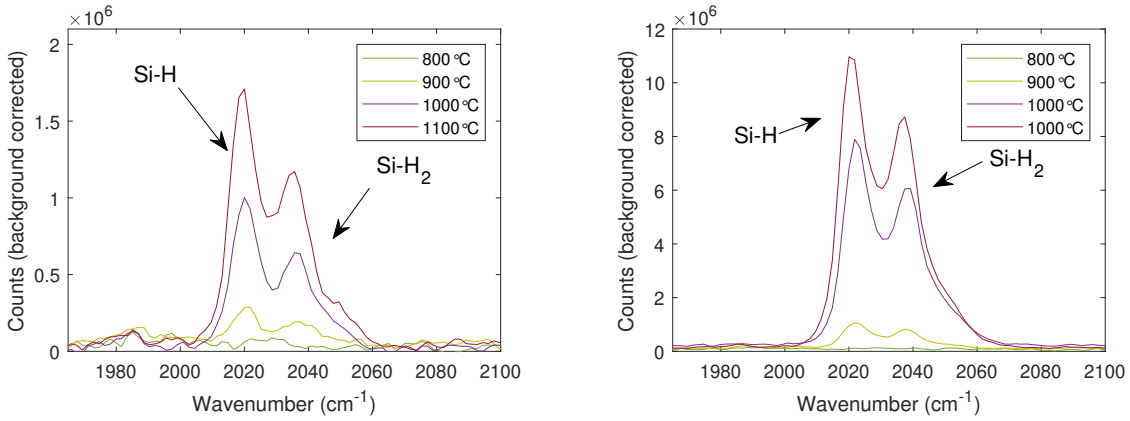

Fig. 7.10 Raman modes of Si-H and Si-H_2 modes as function of furnace set-temperature at a) $X_{H_2} = 1.00$ and b) $X_{thio} = 0.03$

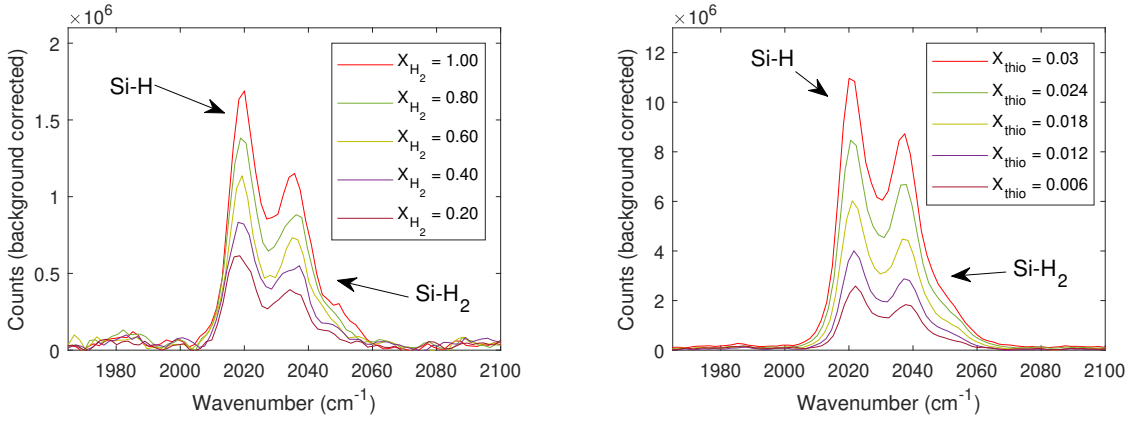

Fig. 7.11 Si-H modes as function of a) X_{H_2} and b) X_{thio} at 1100°C furnace set-temperature

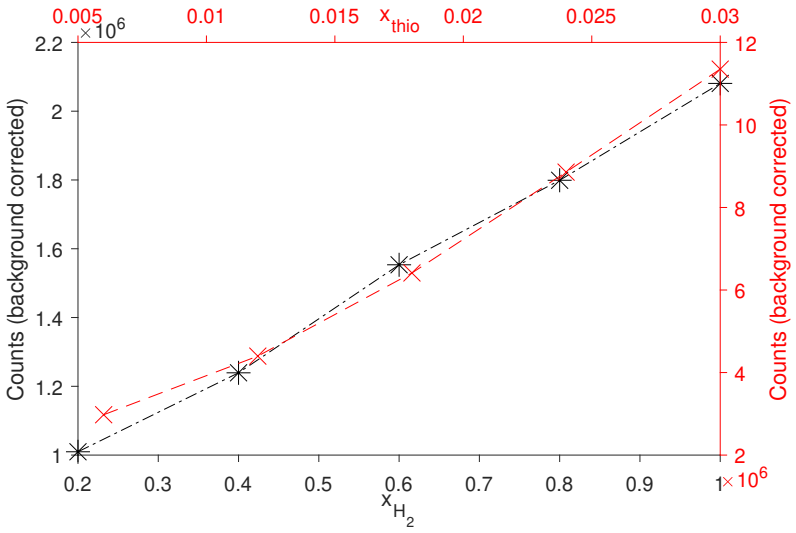

Fig. 7.12 The magnitude of the Si-H Raman mode as a function of X_{H_2} (black) and X_{thio} (red) at 1100°C furnace set-temperature.

7.4.5 Evolution of Thiophene Raman signatures as a function of temperature

Earlier in the chapter, Section 7.2 discussed how the population redistribution of the internal energy modes of a molecule as a function of temperature can introduce complications in the acquisition of quantitative measurements from Raman spectra. The Raman response if further convoluted by the temperature dependence of the differential Raman scattering cross-section, with its value, typically, increasing as a function of temperature [200]. While the applied calibration procedure circumvented these difficulties for non-reacting species, its application is not valid for Raman measurements of the reacting chemicals, as their mode magnitude is affected not just by its input molar fraction but by the furnace set-point temperature as well.

Nevertheless, the magnitudes of thiophene Raman modes were tracked as a function of temperature to gain further information about the thiophene decomposition in the cross reactor. Fuest *et.al* have demonstrated that the Raman response of N_2, CO and acetylene does not increase by more than 20 %, due to temperature dependence of differential cross-section, as a function of increasing temperature from 20 to 1100 °C [200]. For the following analysis, it was assumed that the differential cross-section value of thiophene remained constant across all temperatures.

Room temperature Raman spectra of a thiophene-H_2 mixture (exp.# 1-5 in Table 7.3) were background corrected by the spectrum of 100% concentration of N_2 in the reactor at room temperature. A mean of thiophene Raman modes' peak values (peak # 4, 5 and 7 in

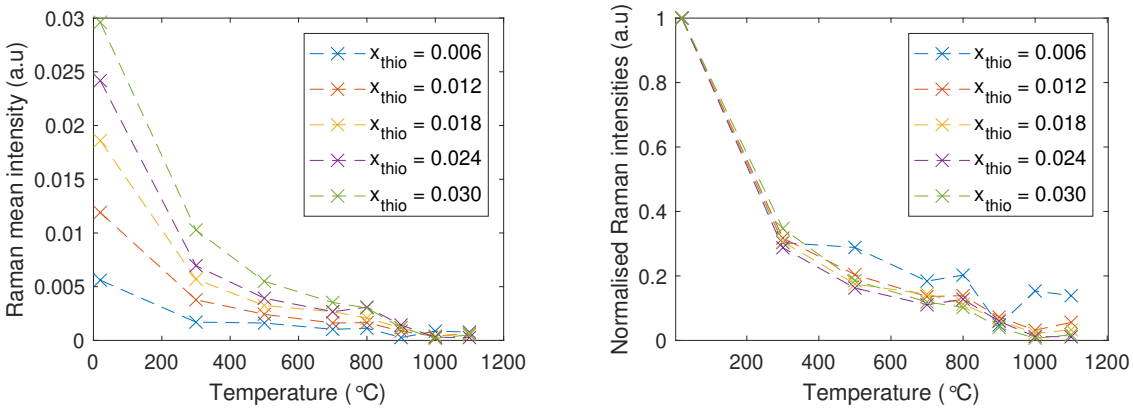

(a) (b)

Fig. 7.13 a) Mean and b) normalised mean magnitudes of thiophene modes as a function of temperature for various thiophene input molar fractions.

Table 7.4) was calculated per inlet thiophene molar fraction, as the mode intensities were within one order of magnitude.

The thiophene modes from the remaining experimental temperature conditions listed in Table 7.3 were background corrected by the 100% N_2 spectrum from the corresponding temperature, after which the mean peak values of the thiophene modes for the corresponding thiophene inlet molar fraction were calculated. These mean peak values were corrected with the temperature factor $f_t = T_{(\text{thio})}/T_{ref}$ to compensate for the decrease in the molecular number density due to an increase in temperature, where f_t is the temperature factor, $T_{(\text{thio})}$ is the temperature extracted by the Fulcher-α method from thiophene-containing experimental conditions and T_{ref} is 20 °C.

The resultant temperature corrected mean peak and normalised mean peak magnitudes of thiophene modes were grouped according to their input thiophene molar fraction and plotted vs temperature in Figs. 7.13a and 7.13b respectively. Figure. 7.13a shows, that while the thiophene mean mode magnitudes differ, depending on the thiophene inlet molar fraction, their behaviour exhibit a similar trend, further highlighted in Fig. 7.13b. The data sets are in close agreement, apart from the data corresponding to the smallest set inlet molar fraction $X_{\text{thio}} = 0.006$. The discrepancy for the $X_{\text{thio}} = 0.006$ condition arises from the peak magnitudes being nearly in the noise floor, as their magnitude decreases with the reduced molecular number density at higher temperatures.

The normalised intensity of thiophene modes decreases non-linearly with temperature for all inlet molar fractions. In particular, a decrease of nearly 70% is observed in all data sets from 20 to 300°C, with diminishing changes in magnitude as a function of temperature. While for reactive species, that could be indicative of its decomposition, the spectra shown

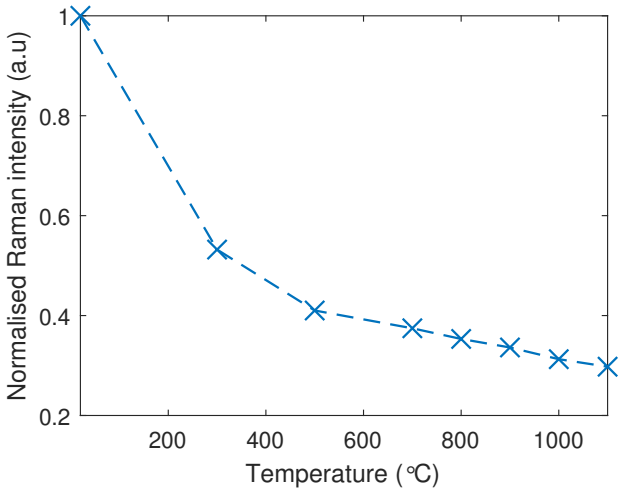

Fig. 7.14 Temperature corrected normalised Raman mode magnitude of H_2 Q(1) transition for X_{thio} = 0.03 as a function of temperature.

earlier indicated that thiophene decomposition began in the range of 800-900°C, which is also confirmed by the sudden drop in the thiophene mode intensities in Fig.7.13a, beyond 800 °C.

Thus, the signal decay, prior to 800 °C, was attributed to the reduction of the thiophene-H_2 mixture-containing volume inside of the reactor, purging channels in particular, as a function of temperature, as the effect of buoyancy forces on the flow became less pronounced, leading to more efficient containment of the central flow. As shown by the CFD studies in chapter 6, the mixing length of gases drastically reduced between 20 and 300 °C, with subsequent lesser changes observed at the higher temperatures.

Figure 7.14 shows temperature corrected normalised H_2 Raman mode magnitude of Q(1) transition for inlet X_{thio} = 0.03 as a function of temperature. The mode magnitude exhibits similar behaviour to thiophene normalised magnitudes, with a great reduction in intensity in the range of 20-500 °C. This further supports the hypothesis that the decrease of thiophene mode magnitudes is due to the reduction of thiophene-H_2 mixture-containing volume inside the reactor as a function of furnace set-point temperature. The normalised magnitude of the Q(1) transition does not drop by the same amount as thiophene magnitudes. This can be attributed to the population redistribution of internal energy modes of H_2, coupled with a different response of the temperature-dependent differential Raman scattering cross-section.

At present, it is not possible to use hydrogen to calculate a volume correction factor due to the strong influence of population redistribution on its Raman spectra. Instead, for future work, in order to be able to extract quantitative information from thiophene signatures directly, the change in the mixture-containing volume needs to be calibrated. This can be

done with the use of a non-reactive gas with simple Raman spectra that is injected into the reactor at trace quantities.

7.4.6 Quantitative measurement of H_2 molar fractions.

It is possible to gain further, quantitative insight into thiophene thermal decomposition by inspecting the evolution of the hydrogen molar fraction in thiophene-containing spectra as a function of temperature. It has been assumed that thiophene is perfectly intermixed with the H_2 carrier gas within the reactor, such that both species occupy the same volume, and do not dissociate as the mixture travels downstream.

Peak magnitudes of hydrogen modes were extracted from each experimental condition outlined in Table 7.3 and were grouped according to their inlet thiophene molar fraction and furnace set-point temperature. Temperature specific, per-peak hydrogen calibration curves of each mode were used to calculate X_{H_2} value per H_2 mode in thiophene-containing data. Averages of these X_{H_2} values were then computed per corresponding input thiophene molar fraction and are shown in Fig. 7.15, as a function of temperature. The error bars were calculated by the standard error propagation of the extracted molar fractions from each peak.

At 20°C, it is assumed that measured 1-X_{H_2} values result in thiophene molar fraction in the reactor. By inspection, the extracted X_{H_2} values are within error of their corresponding inlet thiophene fraction. Furthermore, the values of X_{H_2} are smaller for larger input thiophene molar fraction, as expected. The error on the X_{H_2} values diminishes up to 700 °C, at which larger disagreement between values is observed. The influence of background subtraction becomes more significant at higher temperatures as magnitudes of hydrogen modes become lower, due to a reduction in molecular number density at the measurement location, which leads to larger uncertainties.

Thermal decomposition of thiophene starts between 800-900 °C, which gives rise to the simultaneous occurrence of H_2S, methane and Si-H modes. Formation of decomposition products reduces the measured X_{H_2}, as new species occupy the observed volume and utilise H_2 in their formation. The X_{H_2} steadily decreases up to 1000 °C, after which it rapidly increases at 1100 °C, where extra hydrogen is released into the reactor due to non-catalytic thermal decomposition of methane.

The main source of uncertainty is believed to be the precision of calibration curves. It has been shown in Section 7.2, that their behaviour is not linear. Furthermore, with a maximum thiophene input molar fraction of 3%, it was not expected for X_{H_2} molar fraction in the reactor to vary by a significant amount. The hydrogen calibration functions performed over the range of $X_{H_2} = 0.0 \rightarrow 1.0$ incorporate the buoyancy forces effects that may not be present over a narrower variation range of X_{H_2}. Thus the calibration curves may be unnecessarily

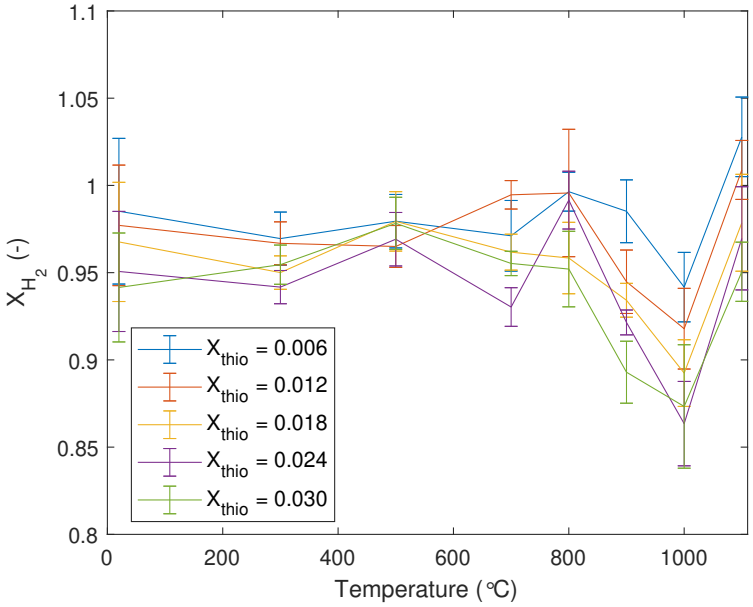

Fig. 7.15 Extracted H_2 molar fractions for thiophene-containing spectra, listed in Table 7.3 as a function of temperature.

skewed. Furthermore, calibration was performed in steps of $\Delta X_{H_2} = 0.2$, making them quite coarse. Additional calibration measurements must be performed in the $X_{H_2} = 0.85 \rightarrow 1.0$ region to improve their precision for the molar fraction range of interest.

Additionally, it was noticed that the quartz reactor warped slightly with an increase in temperature, resulting in the purging channels not lying on the same axis. This lead to changes in the location of the laser beam injection on the purging flange window at each temperature. As seen in chapter 6, due to buoyancy effects, the measured molar fractions of gases may change as a function of laser beam height, resulting in further added uncertainty.

Figure 7.16 shows the Raman spectra of $X_{thio} = 0.03$ at 1000 and 1100 °C. While no new product modes are observed, there is a slight broadband background increase in the region of 500 to 3800 cm^{-1} at 1100°C, compared to 1000 °C. Such an increase could be attributed to the broadband emission from carbon present in the gas phase as a product of methane decomposition, which would be in line with the carbon production process outlined by Li et al. [63].

7.4.7 Summary

Overall, the pulsed laser Raman system was able to perform Raman spectroscopy measurements of thiophene decomposition at low inlet molar fractions as a function of temperature in

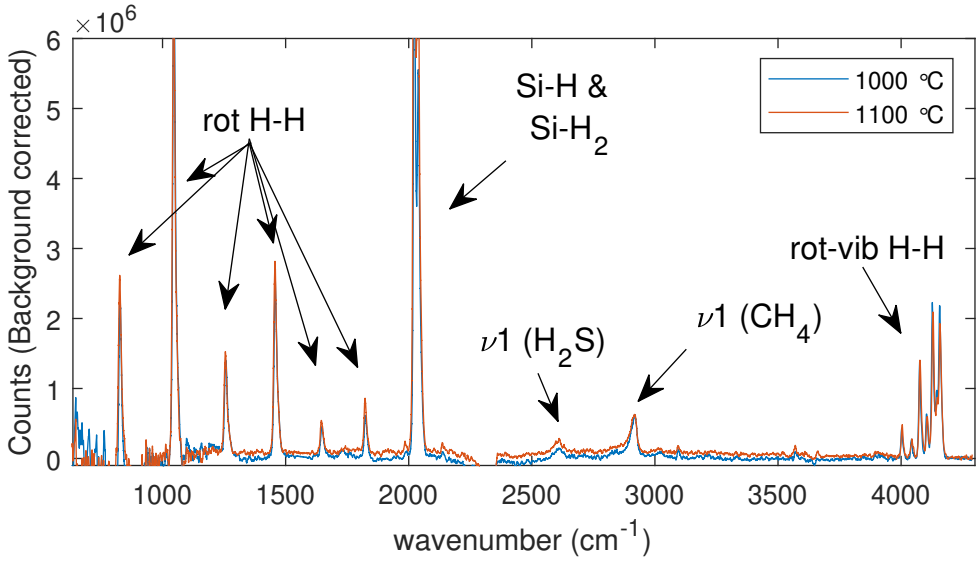

Fig. 7.16 shows Raman spectra of X_{thio} = 0.03 in H_2 environment at 1000 and 1100 °C furnace set-point temperature.

the range of 20 to 1100 °C. The system was confidently able to track thiophene Raman mode magnitudes up to the point of its decomposition. Calibration of change in the thiophene- H_2 mixture-containing volume as a function of temperature would allow the system to measure X_{thio} directly from thiophene Raman signatures. Methane and H_2S have been identified as two major products of thiophene decomposition, which are first observed at 900 °C, with their magnitudes increasing as a function of temperature. The use of N_2 as purging gas facilitated in the non-catalytic thermal decomposition of methane, which resulted in the formation of carbon at 1100 °C, identified by the presence of a broadband emission in the spectrum. The presence of thiophene decomposition products resulted in accelerated production of Si-H modes when compared to a pure hydrogen environment.

These deductions have been made possible by investigating the change of the X_{H_2} inside of the reactor as a function of temperature and initial X_{thio}. While quantitative changes have been extracted, they are subject to numerous sources of error. Nevertheless, the system was able to provide quantitative information about thiophene decomposition which, with further post-processing can be used in model validations and further understanding of the CNT synthesis process.

7.5 Analysis of the CNT-aerogel formation process.

Earlier in the chapter, the system's capabilities have been shown for the analysis of thiophene thermal decomposition. The discussion will now focus on the application of the pulsed laser Raman system for *in situ* analysis of the reacting flow mixture used for the formation of CNTs in an FC-CVD reactor.

7.5.1 Ferrocene

Prior to proceeding with investigations of the full mixture used for CNT synthesis in FC-CVD, Raman measurements of a Ferrocene-H_2 mixture were performed, in order to identify the location of Ferrocene's Raman modes and their evolution as a function of temperature. Ferrocene was a much more challenging molecule to analyse, compared to thiophene, as it comes in powder form and has a much lower molecular stability temperature.

Ferrocene (Acros Organics, 90%) was delivered into the reactor by sublimation in a metal vessel. A thermocouple was inserted through the top of the vessel, submerged into the ferrocene powder, in order to monitor its temperature. The vessel was wrapped in resistive heaters and was then covered in foam insulation. The resistive heaters were controlled by an 'Omega' CN740 PID controller, whose reference temperature input came from the thermocouple inside the vessel. To prevent ferrocene condensation while travelling in gas lines, stainless steel pipes downstream from the vessel were wrapped with the resistive heaters controlled by the same PID controller, which were then covered by the foam insulation. Additional resistive heaters, set to a temperature higher than the ferrocene pot, were wrapped around the reactor's inlet flange and around the exposed sections of the quartz reactor tube between the flange and the furnace, to eliminate potential cold spots. That area was also wrapped in insulating foam. A thermocouple was placed next to the 'T' junction, where ferrocene flow would mix with bulk reactor flow 200 mm upstream from the in-coupling flange, plugged into a second PID controller, which set the temperature of the gas lines.

For all of the following experiments, the purging flow has been switched to H_2, in order to mitigate any effects N_2 might have on the chemistry at the measurement location. Typically, during CNT synthesis, the ferrocene pot is set to 92 °C, which corresponds to a molar fraction of 0.6 % when being flushed with 0.2 SLPM of H_2 [59], as given by Antoine equation in appendix B. No ferrocene Raman modes were observed at such inlet ferrocene molar fraction. The vessel temperature was increased to 150 °C, which resulted in the ferrocene molar fraction of 3 % when flushed with 0.5 SLPM of H_2. The temperature of the gas line heaters was set to 260°C. The furnace temperature was set to 300°C in order to begin ferrocene

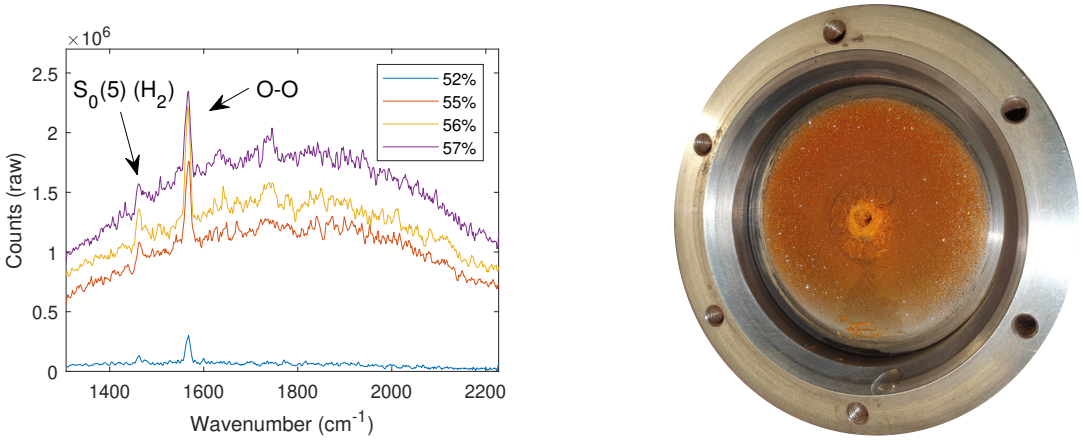

(a) (b)

Fig. 7.17 a) Background magnitude during ferrocene measurements as a function of laser power, b) out-coupling reactor flange after a ferrocene measurement

vaporisation but aim to prevent its breakdown before the measurement location, while also avoiding its condensation within the tube.

Initial Raman measurements, performed with the laser energy of 38 mJ per pulse (70% laser power), resulted in an overwhelming amount of broadband emission. However, it was observed that with the reduction of laser power the background magnitude would drastically decrease, as shown in Fig 7.17a. This has been attributed to the fact that at 300 °C, ferrocene has not yet fully been vapourised. Therefore, high laser powers were creating localised ablation of solid ferrocene particles present in the gas phase, resulting in large background emission. The presence of solid-state particles was observed on out-coupling flange, which had large deposits of orange crystal-like structure, hence iron-containing powder, as seen in Fig. 7.17b. Experimentally it was found that the laser power of 20 mJ per pulse provided sufficient Raman signal without causing localised ablation. To compensate for the lower magnitude of the observed Raman signal due to the reduced laser power, the number of shots per acquisition was increased from 6000 to 15000 and laser power was set to 20 mJ per pulse for all subsequently discussed experiments.

The Raman spectrum of 3% molar fraction of ferrocene in a hydrogen environment at 300 °C is shown in Fig. 7.18. Only two ferrocene Raman modes were detected - a symmetric ring breathing mode (ν_3) at 1113 cm^{-1} and the symmetric stretch of C-H bond in the ring (ν_1) at 3119 cm^{-1} [201].

The region of the C-H (ν_1) mode was investigated as a function of furnace set-point temperature, while keeping all other experimental conditions constant, with resultant spectra shown in Fig. 7.19b. Some studies have suggested that ferrocene begins to thermally

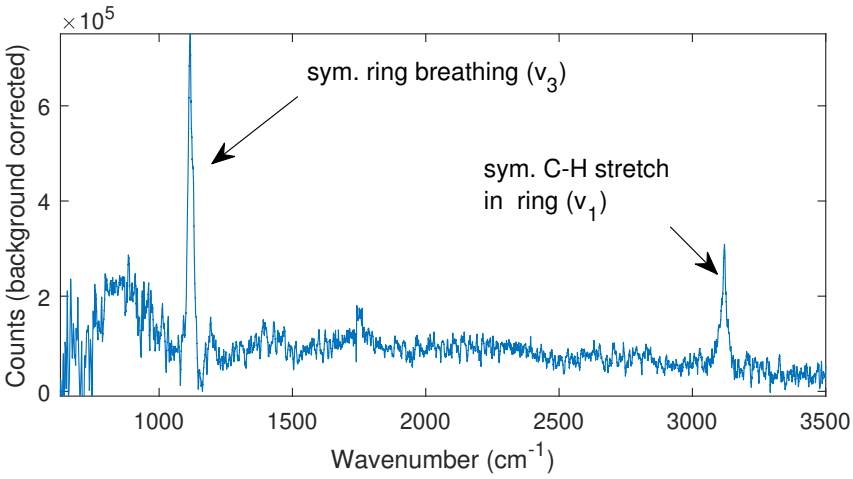

Fig. 7.18 a) Raman spectra of 3% inlet ferrocene molar fraction (0.5 SLPM through the vessel) at 300 °C, 0.1 SLPM H_2 purging gas.

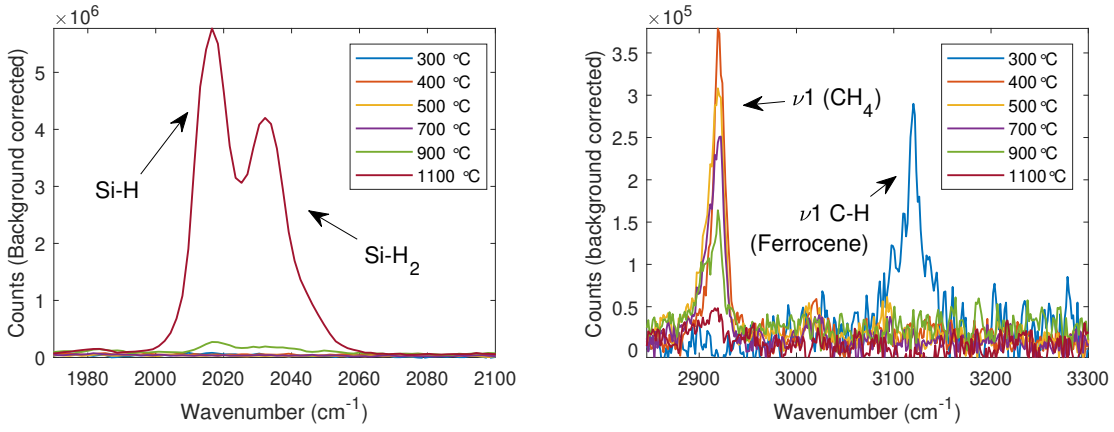

Fig. 7.19 Raman spectra of a) Si-H and b) ferrocene sections at 3% inlet ferrocene molar fraction (0.5 SLPM H_2) as a function of temperature, 0.1 SLPM H_2 purging gas.

decompose at around 500°C [202, 203]. At 400 °C, the C-H (v_1) mode of ferrocene disappears and instead a C-H (v_1) mode of methane is observed, which has formed due to the thermal decomposition of ferrocene. The magnitude of the methane mode decreases with temperature, suggesting that ferrocene has fully broken down by 400 °C. It is expected that iron catalyst nanoparticles would renucleate further downstream of the measurement location which would result in catalytic methane breakdown.

7.5.2 CNT-Aerogel Spin conditions

The pulsed laser Raman system was employed to perform measurements on species mixture used in CNT-aerogel synthesis. The main criterion of the mixture in this investigation was for its volumetric flowrate through the reactor not to deviate much from the previously used volumetric flows of 0.5 SLPM. The mixture composition was based on previously reported studies [68, 196]. Ethanol was used as the hydrocarbon source due to its overwhelming popularity in other CNT-aerogel synthesis studies [69], as larger alkyl alcohols tend to generate more amorphous carbon. Methanol was reported to produce no carbon [69].

Four experimental conditions were outlined, which are shown in Table. 7.5. Condition a) represents the CNT-aerogel synthesis mixture, with ferrocene, thiophene and ethanol molar concentration percentages based on Li et al. [63], and Hoecker et al. [76] respectively. Thiophene bubbler temperature was kept at 0 °C, with ethanol bubbler kept at room temperature. Ferrocene vessel temperature was set to 92 °C, with the gas lines heated to 150°C. Conditions b) and c) aimed to provide spectra either without a hydrocarbon source or without precursors, respectively, with condition d) used as a background of 100 % H_2. A new cross reactor tube was used to ensure that wall depositions, which have accumulated during thiophene and ferrocene thermal decompositions in the last reactor, would not influence the measurements.

Conditions were carried out in reverse order, to the one outlined in Table. 7.5. Reactor was flushed with condition d) for half an hour between each condition, to make sure no breakdown products would influence the measurements. Each condition was flown into the reactor for twenty minutes before measurements, to ensure that steady-state condition is reached. Two alumina mesh filters were positioned into the tube, 10 and 100 mm upstream from the measurement point in order to capture any produced amorphous carbon, which may introduce interference in the Raman signal.

Figure 7.20 shows the Raman spectra for conditions listed in Table 7.5 at 1100°C furnace set-point temperature. The data sets have been background corrected by 100% N_2 Raman spectrum inside of the reactor at 1100 °C.

The differences between spectra manifest as changes in background magnitude and intensities of the C-H (v_1) mode of methane at 2900 cm^{-1}, the Si-H modes centred at 2050

Table 7.5 Molar flow rate $\dot{n}$, and concentration percentage of ferrocene, thiophene, ethanol and H_2 in 4 conditions. Ferrocene vessel set to T = 92°C with partial pressure of 0.0020. Thiophene bubbler temperature set at T = 0°C, with the partial pressures of 0.028. Ethanol bubbler temperature set at 25 °C with partial pressure of 0.077. $\dot{Q}_{H_2}$ is the volumetric flowrate of H_2 through species containing vessels. Carrier Gas flow is added H_2 for dilution. The furnace set-point temperature was 1100 °C.

Vessel content	Values	Conditions (a)	(b)	(c)	(d)
Ferrocene	$\dot{Q}_{H_2}$ (SLPM)	0.2	0.2	-	-
	$\dot{n}_{Ferro}$(mol/min)	1.25×10^{-5}	1.25×10^{-5}	-	-
	Ferrocene Conc.(%)	0.05	0.05	-	-
Thiophene	$\dot{Q}_{H_2}$ (SLPM)	0.1	0.1	-	-
	$\dot{n}_{Thio}$ (mol/min)	1.26×10^{-4}	1.26×10^{-4}	-	-
	Thiophene Conc. (%)	0.51	0.51	-	-
Ethanol	$\dot{Q}_{H_2}$ (SLPM)	0.3	-	0.3	-
	$\dot{n}$(mol/min)	9.49×10^{-4}	-	9.49×10^{-4}	-
	Ethanol Conc. (%)	3.71	-	3.71	-
Carrier Gas Flow (H_2)	$\dot{Q}_{H_2}$ (SLPM)	-	0.3	0.3	0.6
Total H_2 content in the mixture	H_2 (mol/min)	2.45×10^{-2}	2.45×10^{-2}	2.45×10^{-2}	2.45×10^{-2}
	H_2 Conc. (%)	96.27	99.44	96.27	100

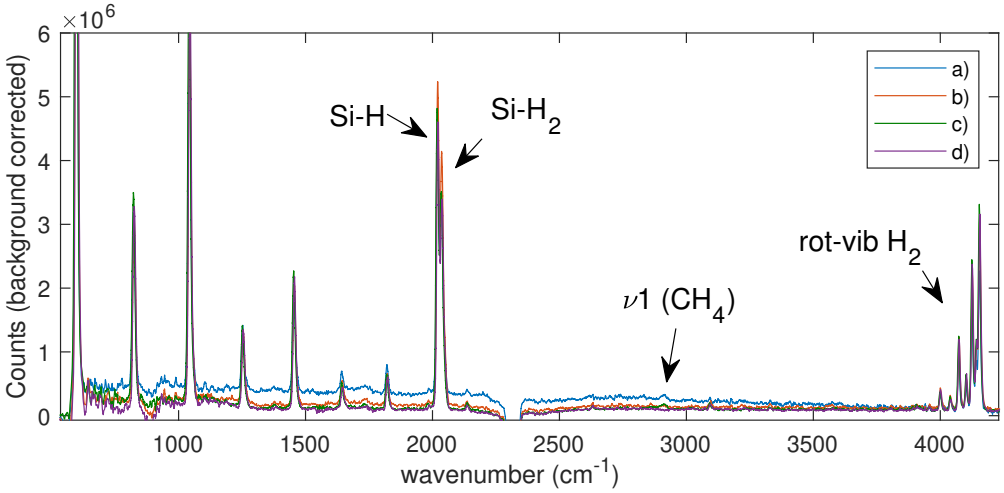

Fig. 7.20 Raman spectra of experimental conditions outlined in Table. 7.5.

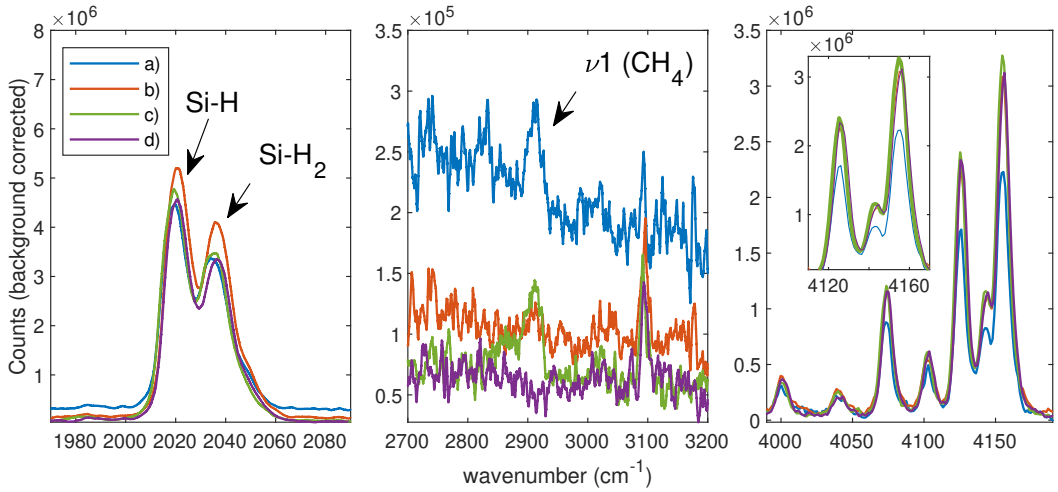

Fig. 7.21 Sections of Raman spectra for experimental conditions outlined in Table. 7.5

cm^{-1} and hydrogen modes. Figure 7.21 shows sections of Raman spectra at Si-H, methane and rovibrational transitions of hydrogen modes locations. Methane mode is confidently observed only in ethanol (hydrocarbon source)-containing conditions, a) and c). It could be argued that there is a methane mode in precursor-containing condition b), however, its SNR is too low in order to confidently confirm its presence. This is an interesting result, as methane mode was observed at inlet X_{thio} = 0.006 and 1100°C condition, which is an inlet molar fraction value close to the thiophene inlet molar concentration in condition b). The peak magnitude of methane mode in the condition a) is 20% larger when compared to the mode magnitude in condition c), once both spectra have been reduced to the background level of zero. While methane in condition c) occurs as a product of ethanol breakdown, additional methane in condition a) could originate from the breakdown of thiophene and ferrocene.

There are distinct differences in background levels between investigated conditions. Conditions c) and d), which consist of the ethanol-hydrogen mixture and pure hydrogen respectively, have relatively flat backgrounds with indistinguishable differences in magnitude between them. The precursor-hydrogen mixture in condition b) produced a broadband background emission, slightly elevated from the conditions c) and d). Such background emission can be attributed to the presence of iron in the gas phase, which has appeared as the result of thermal breakdown of ferrocene. The CNT-aerogel spin condition a) exhibits an average of 5 times increase in broadband background emission, compared to pure hydrogen condition d) and a 3 times increase compared to condition b). The background increase has been linked to the presence of carbon in the gas phase, which resulted in observed broadband

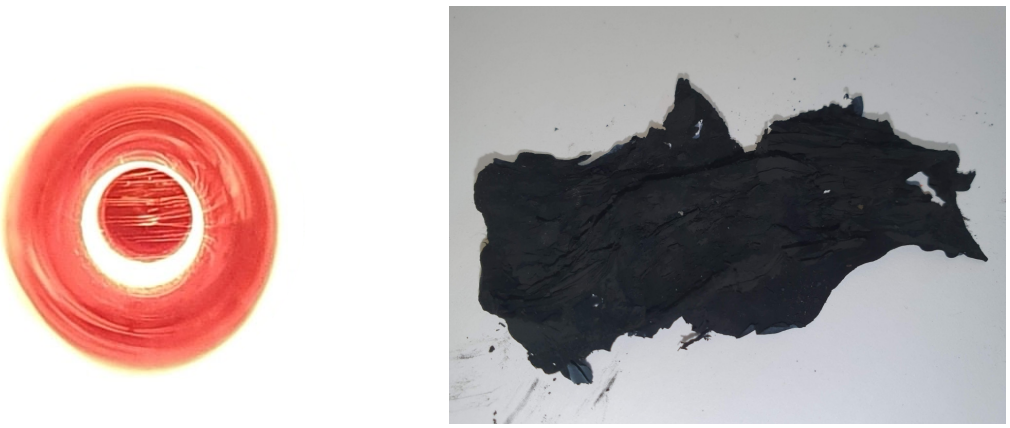

(a) (b)

Fig. 7.22 a) Fibrous material attached to the alumina filter, b) Collected mat-like material from the inner surface of the reactor out-coupling flange

emission. Presence of carbon in the gas phase was confirmed visually with the observation of soot floating inside of the reactor.

The existence of carbon in the condition a) would reduce the molar concentrations of other species in the mixture, which resulted in a substantial decrease in the magnitude of rovibrational hydrogen modes and a decrease in Si-H modes, as seen in Fig 7.21. The hydrogen modes in ethanol-hydrogen mixture condition c) are higher in magnitude compared to pure hydrogen condition d) as a consequence of hydrogen being released into the system due to thermal breakdown of ethanol. This is accompanied by the higher Si-H modes magnitudes in conditions c) compared to a) due to a larger presence of hydrogen in the system. Precursor-containing condition b) has the highest Si-H mode magnitudes out of all datasets, as the presence of thiophene results in larger Si-H production, compared to an increase in hydrogen as shown in Fig. 7.12. This, in turn, reduces the molar concentrations of other species in the product mixture, as demonstrated by the lower hydrogen rovibrational mode magnitudes in condition b) compared to d).

The reactor was visually inspected before, during, and after each of the experimental conditions by looking at the protruding sections of the main reactor tube and looking down the purging channels for signs of depositions on quartz windows. After the measurements of condition a) some fibre-like structures were observed, anchored to the alumina filter positioned just to the right of the measurement location, as seen in Fig. 7.22a by looking down the purging channel. The fibres swayed with the movement of the fluid flow. Once the reactor has been cooled down, during which it was continuously flushed with nitrogen gas, the alumina filter was extracted and inspected. No fibre-like structures were observed,

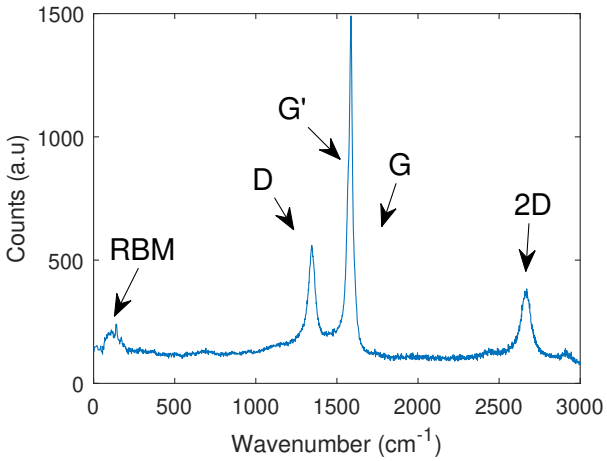

Fig. 7.23 Solid state Raman spectra of mat-like material.

suggesting they had burned off in the nitrogen atmosphere. The fibres could have consisted of soot particles that have agglomerated due to van der Waal's forces.

A large mat-like material, shown in Fig. 7.22b was found attached to the inner surface of the reactor out-coupling flange. It was easily peeled off with tweezers and was also quite sticky, akin to CNT-containing materials.

Solid-state Raman analysis of the sample was performed by Horiba Explora Plus using a 532 nm laser, with the resultant spectrum shown in Fig. 7.23. The distinct D and G bands of graphitic structures can be observed at 1345 cm^{-1} and 1587 cm^{-1} respectively. The G band is a characteristic feature of the graphitic layers and corresponds to the tangential vibration of carbon atoms. The D band is typically used to quantify the defects of the graphitic structure manifested by the dispersive disorder. A 2D peak was observed at 2633 cm−1. Some potential radial breathing modes can be observed, centred at 140 cm^{-1}, however, they are not very pronounced and are not in a correct position to help identify the nature of the CNTs. A very weak presence of a G' band (the second-order Raman scattering from D-band variation) was observed at 1571cm^{-1} on the shoulder of the G band. The I_G/I_D, which is a well-known indicator of graphitic crystallinity in single-wall nanotubes, for this sample equals 2.66, indicating good crystallinity and presence of a graphitic structure.

7.6 Conclusion

The constructed pulsed laser Raman system has demonstrated its capability in performing *in situ* quantitative and qualitative Raman measurements of reacting flows inside a FCCVD reactor. The system was able to track Raman signatures of thiophene, ranging from $0.6-3\%$

molar concentrations as a function of temperature and to detect products of thiophene decomposition, which were methane, H_2S and carbon. Furthermore, it was able to provide quantitative measurements of variations of X_{H_2} in the reactor as a function of inlet thiophene molar fraction and reactor temperature, describing the chemical evolution of the system.

Buoyancy forces have been determined as the main governing factor in the variation of the thiophene-H_2 mixture-containing volume inside of the reactor. This has a direct influence on the magnitude of the Raman signal and, correspondingly, on the acquisition of quantitative information of thiophene decomposition directly from its spectra. These effects, however, can be minimised with the reconfiguration of the setup or additional calibration, discussed in the next chapter.

The constructed Raman system was also applied to the investigation of thermal breakdown of ferrocene as a function of temperature. It was found that ferrocene broke down in the region of 300-400 °C with methane formation observed as a product.

To the author's knowledge, first of its kind Raman measurements were performed *in situ* during CNT synthesis via FC-CVD. The system was sensitive to the product species formed and different broadband emission levels as a function of synthesis-mixture composition. The measurements have shown great potential for further, more in-depth *in situ* studies of CNT synthesis via FC-CVD.

Chapter 8

Conclusions and future work

8.1 Conclusions

The aims of the presented project were to develop a Raman-based spectroscopy setup capable of performing quantitative and qualitative *in situ* analysis of CNT synthesis process inside a FC-CVD reactor

Two different Raman-based techniques were selected, on the basis of the literature review, and tested for their applicability to the outlined research goal. The first introduced technique, Cavity-enhanced Raman scattering, used a highly reflective linear optical cavity to amplify the power of a CW laser in order to generate a high magnitude signal from gaseous phase species, as their Raman signatures are typically low in reacting flow environments. To the author's knowledge, for the first time, a thorough procedure was outlined for the construction and operation of CERS setup. A comprehensive model was developed, which compared the spontaneous rate of Stokes Raman emission induced by free-space CW and CERS methods. Numerical results of the model were compared with CW and CERS Raman experiment performed on ambient air. The experimental CERS Raman signal was 3 orders of magnitude larger than spontaneous Raman emission per same excitation laser power. The model and the experimental results were in close agreement.

It was shown that CERS could not be used for the analysis of reacting flows, such as those occurring in FC-CVD as CERS operation requires precise beam alignment within the cavity. Temperature gradients in a FC-CVD system would cause localised fluctuations in the refractive index of the flow, which would lead to beam steering, severely reducing CERS effectiveness. Moreover, CERS relies on surface quality and reflectively of cavity mirrors, which would get drastically reduced by contamination. Nevertheless, in this research CERS was shown to be a cost-effective solution for high resolution gas phase Raman spectroscopy, which could be used for the analysis of gaseous mixtures at a constant temperature.

Another technique, based on pulsed laser spontaneous Raman scattering, was employed for *in situ* analysis of CNT synthesis in a FC-CVD. Cylindrical reactor, commonly used for CNT-aerogel synthesis, was not suitable for Raman spectroscopy due to the formation of solid state deposition on the reactor wall at the location of laser beam impingement, during decomposition of species such as thiophene and ferrocene. Cylindrical reactor was modified into a cross shape reactor with the introduction of two co-axial purging channels, arranged perpendicular to the reactor tube. A custom modular purging flange was developed, equipped with anti-reflective quartz windows, which provided anti-reflective flat surfaces for laser beam injection into the reactor, significantly reducing background noise. Combination of such reactor design and purging system provided continuous optical access with the use of purging gas flows.

Numerical studies were performed to investigate the effects of buoyancy forces, flow rate, inlet gas composition on flow patterns and species distributions inside of the cross reactor. Inclusion of gravity resulted in complex distribution of species, which arose as consequence of density differences between carrier and purge gases and temperature gradients within the reactor. This has been experimentally confirmed by Raman measurements. It was shown that inlet volumetric flowrates and the reactor temperatures had a direct impact on the formation of multiple recirculation zones, which in turn, governed the species distribution profile. These findings were used to devise a calibration procedure, which enabled quantitative measurements of hydrogen molar fraction inside of the reactor by Raman spectroscopy. The numerical studies have highlighted the importance of the inclusion of gravity when modelling CNT-synthesis by FC-CVD, as the flow pattern did not resemble plug flow, which was assumed in other published studies.

The constructed pulsed laser Raman setup has successfully detected H_2, methane, Si-H, and Si-H_2 as products of thiophene decomposition in the hydrogen atmosphere. Intensities of their Raman signatures increased as a function of temperature. Thiophene decomposition occurred within the range of 800-900 °C, which is in agreement with published data. No presence of alkynes was found, in contrast to the hypothesis of some other research groups.

The constructed pulsed laser Raman system was able to confidently track thiophene Raman modes up to the point of its decomposition, with thiophene inlet molar fractions ranging from 0.006 to 0.03.

It was shown that the presence of thiophene decomposition products resulted in a significant formation of Si-H, and Si-H_2. Si-H, and Si-H_2 signatures were also detected in pure hydrogen atmosphere in lesser quantities. The thiophene decomposition was quantitatively analysed by extracting values of H_2 molar fraction in the reactor from Raman spectra. Quantitative measurements at room temperature were in agreement with set inlet molar fractions

of the gas mixture. Quantitative data confirmed the occurrence of thiophene breakdown from 800 °C, and non-catalytic breakdown of formed methane between 1000-1100 °C in presence of N_2 purging flow.

The Raman system was also applied to investigate ferrocene breakdown in a hydrogen environment. Breakdown was found to occur between 300-400 °C, forming methane as product.

To the author's knowledge, the pulsed laser Raman system has demonstrated first of its kind *in situ* on-the-fly gas phase composition measurements in the volume of the FC-CVD reactor during CNT-aerogel synthesis at 1100 °C. The CNT-synthesis mixture consisted of ferrocene and thiophene as precursors, and ethanol as the hydrocarbon source in a H_2 atmosphere. Strong methane Raman signal was detected in hydrocarbon-containing flows. Elevated broadband emission was detected due to the presence of iron in gas phase for the precursor-hydrogen mixture. Significant broadband emission was observed in the reaction mixture, attributed to presence of gaseous carbon. This was accompanied by a reduction of molar fractions of H_2, Si-H and Si-H_2. Thus, the developed pulsed laser Raman system was able to successfully provide key information of the reaction gas phase parameters which are vital for on-the-fly control synthesis process and quality of the CNT product.

Implementation of the cross reactor and the purging system did not cause any significant effect on the formation of CNTs. A CNT mat-like material formed on the out-coupling flange of the reactor during the Raman analysis of the CNT synthesis mixture. Its graphitic structure was confirmed with solid state Raman, where the characteristic D and G bands were observed. Therefore, for the first time to the authors knowledge, Raman *in situ* diagnostics were performed during successful CNT synthesis in a FC-CVD reactor.

8.2 Future Work

Based on the results and findings outlined above further research should focus on the following:

Raman measurements could be performed at various axial locations along the reactor via reactor displacement or the introduction of additional points of optical access. Such configuration may allow simultaneous multipoint *in situ* data acquisition for the formulation of particle kinematics and kinetics as well as temperature profile along the axis of the reactor.

The pulsed laser Raman system can be applied for *in situ* analysis in the regions of precursor decomposition and product formation. Raman system could be used to locate precise axial and radial point of CNT-aerogel formation. Raman spectroscopy could be performed on

the forming CNT-aerogel itself, which could provide *in situ* on-the-fly information about the nature and quality of the forming CNTs, such as the number of walls of their metallic nature.

With an increase in inner diameter of the purging channel, Raman measurements can be performed as a function of reactor height.

Additional optical techniques could be applied in the developed reactor for *in situ* analysis. For instance, as the laser beam cleanly exits the reactor, laser extinction can be performed to measure carbon particle concentration. Laser induced incandescence can be used to provide *in situ* particle measurements, such as the size of the catalysts nanoparticles.

The reactor heating system needs to be modified. The employed electric furnace could not reach temperatures higher than 1100°C, which limited reactions such as non-catalytic cracking of methane. The furnace size was too wide, which resulted in long purging channel lengths. As consequence, this increased the laser beam path, which in turn resulted in the convolution of the observed Raman signal.

Beam delivery and Raman collection need to be optimised, with beam and collection overlap volume made minimised as much as possible. Raman signal collection was sensitive to species all the way along the beam path.

The purging channel geometry could be redesigned with larger inner diameters such that the laser beam and the collection volume could enter the reactor at different heights, with their foci crossing in the middle of the reactor. Alternatively, additional purging channels could be introduced at a normal to the cross reactor plane, resulting in a 90 degree signal collection. The heating system would have to be modified appropriately to accommodate the proposed reactor design. Furthermore, such reactor design allows the use of camera-based techniques, such a particle image velocimetry.

The use of a long-pass dichroic filter in the Raman collection system introduced a significant amount of fluorescence at lower wavelength regions, which led to loss of information. The dichroic filter can be changed to short-pass, such as the system would be able to pick up anti-Stokes emission, filtering any fluorescence emission.

Both Stokes and anti-Stokes photons could be collected from both sides of the reactor, as the beam cleanly passes through. This would allow temperature measurements from any species present in the reactor. Such modifications to the setup however can be quite expensive as it would require two sets of imaging apparatus. Lasers with higher powers could be used to provide single-shot measurements or faster rates of acquisition.

References

[1] W. K Bischel and G. Black. Wavelength dependence of Raman Scattering cross sections from 200-600 nm. *American Institute of Physics*, 100:181, 1983.

[2] Ricardo Acora. *Surface-Enhanced Vibrational Spectroscopy*, page 31. John Wiley & Sons, Ltd, 2006.

[3] Zanda Gavare, Gita Revalde, and Atis Skudra. Plasma Temperature Determination of Hydrogen Containing High-Frequency Electrodeless Lamps by Intensity Distribution Measurements of Hydrogen Molecular Band. *International Journal of Spectroscopy*, 2010:1–8, 2010. ISSN 1687-9449. doi: 10.1155/2010/804506.

[4] S. Iijima. Helical microtubules of graphitic carbon. *Nature*, 354:56–58, 1991.

[5] Naoyuki Matsumoto, Azusa Oshima, Sachiko Ishizawa, Guohai Chen, Kenji Hata, and Don N. Futaba. One millimeter per minute growth rates for single wall carbon nanotube forests enabled by porous metal substrates. *RSC Advances*, 8(14):7810–7817, 2018. ISSN 20462069. doi: 10.1039/c7ra13093g.

[6] A. A. Puretzky, D. B. Geohegan, S. Jesse, I. N. Ivanov, and G. Eres. In situ measurements and modeling of carbon nanotube array growth kinetics during chemical vapor deposition. *Applied Physics A: Materials Science and Processing*, 81(2):223–240, 2005. ISSN 09478396. doi: 10.1007/s00339-005-3256-7.

[7] L. X. Zheng, M. J. O'Connell, S. K. Doorn, X. Z. Liao, Y. H. Zhao, E. A. Akhadov, M. A. Hoffbauer, B. J. Roop, Q. X. Jia, R. C. Dye, D. E. Peterson, S. M. Huang, J. Liu, and Y. T. Zhu. Ultralong single-wall carbon nanotubes. *Nature Materials*, 3 (10):673–676, 2004. ISSN 14761122. doi: 10.1038/nmat1216.

[8] Guohai Chen, Robert C. Davis, Hiroe Kimura, Shunsuke Sakurai, Motoo Yumura, Don N. Futaba, and Kenji Hata. The relationship between the growth rate and the lifetime in carbon nanotube synthesis. *Nanoscale*, 7(19):8873–8878, 2015. ISSN 20403372. doi: 10.1039/c5nr01125f.

[9] M.F.L. De Volder, S.H. Tawfick, R.H. Baughman, and A.J. Hart. Carbon nanotubes: present and future commercial applications. *Science*, 339:535–539, 2013.

[10] Michael F.L. De Volder, Sameh H. Tawfick, Ray H. Baughman, and A. John Hart. Carbon nanotubes: Present and future commercial applications. *Science*, 339(6119): 535–539, 2013. ISSN 10959203. doi: 10.1126/science.1222453.

[11] Shuchen Zhang, Lixing Kang, Xiao Wang, Lianming Tong, Liangwei Yang, Zequn Wang, Kuo Qi, Shibin Deng, Qingwen Li, Xuedong Bai, Feng Ding, and Jin Zhang. Arrays of horizontal carbon nanotubes of controlled chirality grown using designed catalysts. *Nature*, 543(7644):234–238, 2017. ISSN 14764687. doi: 10.1038/nature21051.

[12] Lu-Chang Qin, Xinluo Zhao, Kaori Hirahara, Yoshiyuki Miyamoto, Yoshinori Ando, and Sumio Iijima. The smallest carbon nanotube. *Nature*, 408(6808):50–50, 2000. ISSN 0028-0836. doi: 10.1038/35040699.

[13] S. Bandow, F. Kokai, K. Takahashi, M. Yudasaka, L. C. Qin, and S. Iijima. Interlayer spacing anomaly of single-wall carbon nanohorn aggregate. *Chemical Physics Letters*, 321(5-6):514–519, 2000. ISSN 00092614. doi: 10.1016/S0009-2614(00)00353-5.

[14] Avetik R Harutyunyan, Gugang Chen, Tereza M Paronyan, Elena M Pigos, Oleg A Kuznetsov, Kapila Hewaparakrama, Seung Min Kim, Dmitri Zakharov, Eric A Stach, and Gamini U Sumanasekera. Preferential Growth of Single-Walled Carbon Nanotubes with Metallic Conductivity. *Science*, 326(5949):116–120, 2009. ISSN 0036-8075. doi: 10.1126/science.1177599. URL https://science.sciencemag.org/content/326/5949/116.

[15] Lei Ding, Alexander Tselev, Jinyong Wang, Dongning Yuan, Haibin Chu, Thomas P. McNicholas, Yan Li, and Jie Liu. Selective Growth of Well-Aligned Semiconducting Single-Walled Carbon Nanotubes. *Nano Letters*, 9(2):800–805, 2009. ISSN 1530-6984. doi: 10.1021/nl803496s.

[16] B Q Wei, R Vajtai, and P M Ajayan. Reliability and current carrying capacity of carbon nanotubes. *Applied Physics Letters*, 79(8):1172–1174, 2001. doi: 10.1063/1.1396632. URL https://doi.org/10.1063/1.1396632.

[17] Jean-Christophe Charlier, Xavier Blase, and Stephan Roche. Electronic and transport properties of nanotubes. *Rev. Mod. Phys.*, 79(2):677–732, 5 2007. doi: 10.1103/RevModPhys.79.677. URL https://link.aps.org/doi/10.1103/RevModPhys.79.677.

[18] P Kim, L Shi, A Majumdar, and P L McEuen. Thermal Transport Measurements of Individual Multiwalled Nanotubes. *Phys. Rev. Lett.*, 87(21):215502, 10 2001. doi: 10.1103/PhysRevLett.87.215502. URL https://link.aps.org/doi/10.1103/PhysRevLett.87.215502.

[19] Eric Pop, David Mann, Qian Wang, Kenneth Goodson, and Hongjie Dai. Thermal conductance of an individual single-wall carbon nanotube above room temperature. *Nano Letters*, 6(1):96–100, 2006. ISSN 15306984. doi: 10.1021/nl052145f.

[20] Wen-Tai Hong and Nyan-Hwa Tai. Investigations on the thermal conductivity of composites reinforced with carbon nanotubes. *Diamond and Related Materials*, 17(7):1577–1581, 2008. ISSN 0925-9635. doi: https://doi.org/10.1016/j.diamond.2008.03.037. URL http://www.sciencedirect.com/science/article/pii/S0925963508002550.

[21] Saion Sinha, Saimir Barjami, Germano Iannacchione, Alexander Schwab, and George Muench. Off-axis thermal properties of carbon nanotube films. *Journal of Nanoparticle Research*, 7(6):651–657, 2005. ISSN 13880764. doi: 10.1007/s11051-005-8382-9.

[22] T Ozaki, Y Iwasa, and T Mitani. Stiffness of single-walled carbon nanotubes under large strain. *Physical review letters*, 84(8):1712–1715, 2 2000. ISSN 1079-7114 (Electronic). doi: 10.1103/PhysRevLett.84.1712.

[23] Shigenobu Ogata and Yoji Shibutani. Ideal tensile strength and band gap of single-walled carbon nanotubes. *Physical Review B - Condensed Matter and Materials Physics*, 68(16), 2003. ISSN 1550235X. doi: 10.1103/PhysRevB.68.165409.

[24] Bei Peng, Mark Locascio, Peter Zapol, Shuyou Li, Steven L. Mielke, George C. Schatz, and Horacio D. Espinosa. Measurements of near-ultimate strength for multiwalled carbon nanotubes and irradiation-induced crosslinking improvements. *Nature Nanotechnology*, 3(10):626–631, 2008. ISSN 17483395. doi: 10.1038/nnano.2008.211.

[25] Steven L Mielke, Diego Troya, Sulin Zhang, Je-Luen Li, Shaoping Xiao, Roberto Car, Rodney S Ruoff, George C Schatz, and Ted Belytschko. The role of vacancy defects and holes in the fracture of carbon nanotubes. *Chemical Physics Letters*, 390(4): 413–420, 2004. ISSN 0009-2614. doi: https://doi.org/10.1016/j.cplett.2004.04.054. URL http://www.sciencedirect.com/science/article/pii/S0009261404005998.

[26] Akira Takakura, Ko Beppu, Taishi Nishihara, Akihito Fukui, Takahiro Kozeki, Takahiro Namazu, Yuhei Miyauchi, and Kenichiro Itami. Strength of carbon nanotubes depends on their chemical structures. *Nature Communications*, 10(1): 1–7, 2019. ISSN 20411723. doi: 10.1038/s41467-019-10959-7. URL http://dx.doi.org/10.1038/s41467-019-10959-7.

[27] Michele Meo and Marco Rossi. Prediction of Young's modulus of single wall carbon nanotubes by molecular-mechanics based finite element modelling. *Composites Science and Technology*, 66(11):1597–1605, 2006. ISSN 0266-3538. doi: https://doi.org/10.1016/j.compscitech.2005.11.015. URL http://www.sciencedirect.com/science/article/pii/S0266353805004367.

[28] Erik T Thostenson, Zhifeng Ren, and Tsu-Wei Chou. Advances in the science and technology of carbon nanotubes and their composites: a review. *Composites Science and Technology*, 61(13):1899–1912, 2001. ISSN 0266-3538. doi: https://doi.org/10.1016/S0266-3538(01)00094-X. URL http://www.sciencedirect.com/science/article/pii/S026635380100094X.

[29] Ray H Baughman, Anvar A Zakhidov, and Walt A de Heer. Carbon Nanotubes–the Route Toward Applications. *Science*, 297(5582):787–792, 2002. ISSN 0036-8075. doi: 10.1126/science.1060928. URL https://science.sciencemag.org/content/297/5582/787.

[30] Grzegorz Lota, Krzysztof Fic, and Elzbieta Frackowiak. Carbon nanotubes and their composites in electrochemical applications. *Energy Environ. Sci.*, 4(5):1592–1605, 2011. doi: 10.1039/C0EE00470G. URL http://dx.doi.org/10.1039/C0EE00470G.

[31] Chunmei Ban, Zhuangchun Wu, Dane T Gillaspie, Le Chen, Yanfa Yan, Jeffrey L Blackburn, and Anne C Dillon. Nanostructured Fe3O4/SWNT Electrode: Binder-Free and High-Rate Li-Ion Anode. *Advanced Materials*, 22(20):E145–E149, 2010. doi: https://doi.org/10.1002/adma.200904285. URL https://onlinelibrary.wiley.com/doi/abs/10.1002/adma.200904285.

[32] Andreas R Köhler, Claudia Som, Aasgeir Helland, and Fadri Gottschalk. Studying the potential release of carbon nanotubes throughout the application life cycle. *Journal of Cleaner Production*, 16(8):927–937, 2008. ISSN 0959-6526. doi: https://doi.org/10.1016/j.jclepro.2007.04.007. URL http://www.sciencedirect.com/science/article/pii/S0959652607001126.

[33] Liming Dai, Dong Wook Chang, Jong-Beom Baek, and Wen Lu. Carbon Nanomaterials for Advanced Energy Conversion and Storage. *Small*, 8(8):1130–1166, 2012. doi: https://doi.org/10.1002/smll.201101594. URL https://onlinelibrary.wiley.com/doi/abs/10.1002/smll.201101594.

[34] Elzbieta Frackowiak and François Béguin. Electrochemical storage of energy in carbon nanotubes and nanostructured carbons. *Carbon*, 40(10):1775–1787, 2002. ISSN 0008-6223. doi: https://doi.org/10.1016/S0008-6223(02)00045-3. URL http://www.sciencedirect.com/science/article/pii/S0008622302000453.

[35] Jonghwan Suhr, Nikhil Koratkar, Pawel Keblinski, and Pulickel Ajayan. Viscoelasticity in carbon nanotube composites. *Nature Materials*, 4(2):134–137, 2005. ISSN 14761122. doi: 10.1038/nmat1293.

[36] Zhuangchun Wu, Zhihong Chen, Xu Du, Jonathan M Logan, Jennifer Sippel, Maria Nikolou, Katalin Kamaras, John R Reynolds, David B Tanner, Arthur F Hebard, and Andrew G Rinzler. Transparent, Conductive Carbon Nanotube Films. *Science*, 305 (5688):1273–1276, 2004. ISSN 0036-8075. doi: 10.1126/science.1101243. URL https://science.sciencemag.org/content/305/5688/1273.

[37] C. Journet, W. K. Maser, P. Bernier, A. Loiseau, M. Lamy de la Chapelle, S. Lefrant, P. Deniard, R. Lee, and J. E. Fischer. Large-scale production of single-walled carbon nanotubes by the electric-arc technique. *Nature*, 388:756–758, 1997.

[38] A. M. Cassell, J. A. Raymakers, J. Kong, and H. Dai. Large Scale CVD Synthesis of Single-Walled Carbon Nanotubes. 1999.

[39] Yoshinori Ando, Xinluo Zhao, and Masato Ohkohchi. Sponge of Purified Carbon Nanotubes. *Japanese Journal of Applied Physics*, 37(Part 2, No. 1A/B):L61–L63, 1 1998. doi: 10.1143/jjap.37.l61. URL https://doi.org/10.1143/jjap.37.l61.

[40] Yoshinori Ando. The Preparation of Carbon Nanotubes. *Fullerene Science and Technology*, 2(2):173–180, 1994. doi: 10.1080/15363839408009542. URL https://doi.org/10.1080/15363839408009542.

[41] Yoshinori Ando, Xinluo Zhao, Toshiki Sugai, and Mukul Kumar. Growing carbon nanotubes. *Materials Today*, 7(10):22–29, 2004. ISSN 1369-7021. doi: https://doi.org/10.1016/S1369-7021(04)00446-8. URL http://www.sciencedirect.com/science/article/pii/S1369702104004468.

[42] T Guo, P Nikolaev, A Thess, D T Colbert, and R E Smalley. Catalytic growth of single-walled manotubes by laser vaporization. *Chemical Physics Letters*, 243(1): 49–54, 1995. ISSN 0009-2614. doi: https://doi.org/10.1016/0009-2614(95)00825-O. URL http://www.sciencedirect.com/science/article/pii/000926149500825O.

[43] H Kataura, Y Kumazawa, Y Maniwa, Y Ohtsuka, R Sen, S Suzuki, and Y Achiba. Diameter control of single-walled carbon nanotubes. *Carbon*, 38(11):1691–1697, 2000. ISSN 0008-6223. doi: https://doi.org/10.1016/S0008-6223(00)00090-7. URL http://www.sciencedirect.com/science/article/pii/S0008622300000907.

[44] Shunji Bandow, S Asaka, Y Saito, A M Rao, L Grigorian, E Richter, and P C Eklund. Effect of the Growth Temperature on the Diameter Distribution and Chirality of Single-Wall Carbon Nanotubes. *Phys. Rev. Lett.*, 80(17):3779–3782, 4 1998. doi: 10.1103/PhysRevLett.80.3779. URL https://link.aps.org/doi/10.1103/PhysRevLett.80.3779.

[45] Rahul Sen, Y Ohtsuka, T Ishigaki, D Kasuya, S Suzuki, H Kataura, and Y Achiba. Time period for the growth of single-wall carbon nanotubes in the laser ablation process: evidence from gas dynamic studies and time resolved imaging. *Chemical Physics Letters*, 332(5):467–473, 2000. ISSN 0009-2614. doi: https://doi.org/10.1016/S0009-2614(00)01320-8. URL http://www.sciencedirect.com/science/article/pii/S0009261400013208.

[46] Andreas Thess, Roland Lee, Pavel Nikolaev, Hongjie Dai, Pierre Petit, Jerome Robert, Chunhui Xu, Young Hee Lee, Seong Gon Kim, Andrew G Rinzler, Daniel T Colbert, Gustavo E Scuseria, David Tománek, John E Fischer, and Richard E Smalley. Crystalline Ropes of Metallic Carbon Nanotubes. *Science*, 273(5274):483–487, 1996. ISSN 0036-8075. doi: 10.1126/science.273.5274.483. URL https://science.sciencemag.org/content/273/5274/483.

[47] J Howard, K Chowdhury, and J Sande. Carbon shells in flames. *Nature*, 370:603, 1994.

[48] Shuiqing Li, Yihua Ren, Pratim Biswas, and Stephen D Tse. Flame aerosol synthesis of nanostructured materials and functional devices: Processing, modeling, and diagnostics. *Progress in Energy and Combustion Science*, 55:1–59, 2016. ISSN 0360-1285. doi: https://doi.org/10.1016/j.pecs.2016.04.002. URL http://www.sciencedirect.com/science/article/pii/S0360128515300393.

[49] Wilson Merchan-Merchan, Alexei Saveliev, Lawrence Kennedy, and Walmy Jimenez. Combustion synthesis of carbon nanotubes and related nanostructures. *Progress in Energy and Combustion Science - PROG ENERG COMBUST SCI*, 36:696–727, 2010. doi: 10.1016/j.pecs.2010.02.005.

[50] Randall L Vander Wal, Lee J Hall, and Gordon M Berger. The chemistry of premixed flame synthesis of carbon nanotubes using supported catalysts. *Proceedings of the Combustion Institute*, 29(1):1079–1085, 2002. ISSN 1540-7489. doi: https://doi.org/10.1016/S1540-7489(02)80136-5. URL http://www.sciencedirect.com/science/article/pii/S1540748902801365.

[51] Murray J Height, Jack B Howard, Jefferson W Tester, and John B Vander Sande. Flame synthesis of single-walled carbon nanotubes. *Carbon*, 42(11):2295–2307, 2004. ISSN 0008-6223. doi: https://doi.org/10.1016/j.carbon.2004.05.010. URL http://www.sciencedirect.com/science/article/pii/S0008622304003276.

[52] Randall L Vander Wal. Fe-catalyzed single-walled carbon nanotube synthesis within a flame environment. *Combustion and Flame*, 130(1):37–47, 2002. ISSN 0010-2180.

doi: https://doi.org/10.1016/S0010-2180(02)00360-7. URL http://www.sciencedirect.com/science/article/pii/S0010218002003607.

[53] Ya-Li Li, Ian A Kinloch, and Alan H Windle. Direct Spinning of Carbon Nanotube Fibers from Chemical Vapor Deposition Synthesis. *Science*, 304(5668):276–278, 2004. ISSN 0036-8075. doi: 10.1126/science.1094982. URL https://science.sciencemag.org/content/304/5668/276.

[54] J.-F Colomer, C Stephan, S Lefrant, G Van Tendeloo, I Willems, Z Kónya, A Fonseca, Ch Laurent, and J B Nagy. Large-scale synthesis of single-wall carbon nanotubes by catalytic chemical vapor deposition (CCVD) method. *Chemical Physics Letters*, 317(1):83–89, 2000. ISSN 0009-2614. doi: https://doi.org/10.1016/S0009-2614(99)01338-X. URL http://www.sciencedirect.com/science/article/pii/S000926149901338X.

[55] Firoozeh Danafar, A Fakhru'l-Razi, Mohd Amran Mohd Salleh, and Dayang Radiah Awang Biak. Fluidized bed catalytic chemical vapor deposition synthesis of carbon nanotubes—A review. *Chemical Engineering Journal*, 155(1):37–48, 2009. ISSN 1385-8947. doi: https://doi.org/10.1016/j.cej.2009.07.052. URL http://www.sciencedirect.com/science/article/pii/S1385894709005373.

[56] K B K Teo, S-B Lee, M Chhowalla, V Semet, Vu Thien Binh, O Groening, M Castignolles, A Loiseau, G Pirio, P Legagneux, D Pribat, D G Hasko, H Ahmed, G A J Amaratunga, and W I Milne. Plasma enhanced chemical vapour deposition carbon nanotubes/nanofibres˜how uniform do they grow? *Nanotechnology*, 14(2):204–211, 1 2003. doi: 10.1088/0957-4484/14/2/321. URL https://doi.org/10.1088/0957-4484/14/2/321.

[57] P Chen, H.-B. Zhang, G.-D. Lin, Q Hong, and K R Tsai. Growth of carbon nanotubes by catalytic decomposition of CH4 or CO on a NiMgO catalyst. *Carbon*, 35(10):1495–1501, 1997. ISSN 0008-6223. doi: https://doi.org/10.1016/S0008-6223(97)00100-0. URL http://www.sciencedirect.com/science/article/pii/S0008622397001000.

[58] Morinobu Endo, Takuya Hayashi, and Yoong-Ahm Kim. Large-scale production of carbon nanotubes and their applications. *Pure and Applied Chemistry*, 78(9):1703–1713, 2006. doi: https://doi.org/10.1351/pac200678091703. URL https://www.degruyter.com/view/journals/pac/78/9/article-p1703.xml.

[59] Christian Hoecker, Fiona Smail, Mark Bajada, Martin Pick, and Adam Boies. Catalyst nanoparticle growth dynamics and their influence on product morphology in a CVD process for continuous carbon nanotube synthesis. *Carbon*, 96:116–124, 2016. ISSN 00086223. doi: 10.1016/j.carbon.2015.09.050. URL http://dx.doi.org/10.1016/j.carbon.2015.09.050.

[60] Ya-Li Li, Ian A Kinloch, and Alan H Windle. Direct Spinning of Carbon Nanotube Fibers from Chemical Vapor Deposition Synthesis. *Science (Washington, DC, United States)*, 304(5668):276–278, 2004. ISSN 0036-8075. doi: 10.1126/science.1094982. URL http://reichling.physik.uos.de/download_paper.php?paper=Science304p276(2004)_Li.pdf.

[61] Anna Moisala, Albert G. Nasibulin, David P. Brown, Hua Jiang, Leonid Khriachtchev, and Esko I. Kauppinen. Single-walled carbon nanotube synthesis using ferrocene and iron pentacarbonyl in a laminar flow reactor. *Chemical Engineering Science*, 61(13): 4393–4402, 2006. ISSN 00092509. doi: 10.1016/j.ces.2006.02.020.

[62] Marcelo Motta, Ya Li Li, Ian Kinloch, and Alan Windle. Mechanical properties of continuously spun fibers of carbon nanotubes. *Nano Letters*, 5(8):1529–1533, 2005. ISSN 15306984. doi: 10.1021/nl050634+.

[63] Ya-Li Li, Liang-Hong Zhang, Xiao-Hua Zhong, and Alan H Windle. Synthesis of high purity single-walled carbon nanotubes from ethanol by catalytic gas flow CVD reactions. *Nanotechnology*, 18(22):225604, 2007. ISSN 0957-4484. doi: 10.1088/0957-4484/18/22/225604. URL http://stacks.iop.org/0957-4484/18/i=22/a=225604?key=crossref.1111dabb906394bbef2c68bad4a5abc0.

[64] J N Wang, X G Luo, T Wu, and Y Chen. High-strength carbon nanotube fibre-like ribbon with high ductility and high electrical conductivity. *Nature communications*, 5: 3848, 2014. ISSN 2041-1723. doi: 10.1038/ncomms4848. URL http://www.ncbi.nlm.nih.gov/pubmed/24964266.

[65] Wei Xu, Yun Chen, Hang Zhan, and Jian Nong Wang. High-Strength Carbon Nanotube Film from Improving Alignment and Densification. *Nano Letters*, 16(2):946–952, 2016. ISSN 15306992. doi: 10.1021/acs.nanolett.5b03863.

[66] Is'haq A Mohammed, Mercy T Bankole, Ambali S Abdulkareem, Stephen S Ochigbo, Ayo S Afolabi, and Oladiran K Abubakre. Full factorial design approach to carbon nanotubes synthesis by CVD method in argon environment. *South African Journal of Chemical Engineering*, 24:17–42, 2017. ISSN 1026-9185. doi: https://doi.org/10.1016/j.sajce.2017.06.001. URL http://www.sciencedirect.com/science/article/pii/S1026918516300427.

[67] Hongjie Dai. Carbon nanotubes: opportunities and challenges. *Surface Science*, 500 (1):218–241, 2002. ISSN 0039-6028. doi: https://doi.org/10.1016/S0039-6028(01)01558-8. URL http://www.sciencedirect.com/science/article/pii/S0039602801015588.

[68] Devin Conroy, Anna Moisala, Silvana Cardoso, Alan Windle, and John Davidson. Carbon nanotube reactor: Ferrocene decomposition, iron particle growth, nanotube aggregation and scale-up. *Chemical Engineering Science*, 65(10):2965–2977, 2010. ISSN 00092509. doi: 10.1016/j.ces.2010.01.019. URL http://dx.doi.org/10.1016/j.ces.2010.01.019.

[69] Lee Weller, Fiona R. Smail, James A. Elliott, Alan H. Windle, Adam M. Boies, and Simone Hochgreb. Mapping the parameter space for direct-spun carbon nanotube aerogels. *Carbon*, 146:789–812, 2019. ISSN 00086223. doi: 10.1016/j.carbon.2019.01.091. URL https://doi.org/10.1016/j.carbon.2019.01.091.

[70] Q. Jiang, M.Z. Qu, G. M. Zhou, B. L. Zhang, and Z.L Yu. A study of activated carbon nanotubes as electrochemical super capacitors electrode materials. *Materials Letters*, 57:988–991, 2002.

[71] Kevin Wepasnick, Billy Smith, Julie Bitter, and D Fairbrother. Chemical and structural characterization of carbon nanotube surfaces. *Analytical and bioanalytical chemistry*, 396:1003–1014, 2010. doi: 10.1007/s00216-009-3332-5.

[72] T S Gspann, F R Smail, and A H Windle. Spinning of carbon nanotube fibres using the floating catalyst high temperature route: purity issues and the critical role of sulphur. *Faraday Discuss.*, 173(0):47–65, 2014. doi: 10.1039/C4FD00066H. URL http://dx.doi.org/10.1039/C4FD00066H.

[73] Sung-Hyun Lee, Junbeom Park, Hye-Rim Kim, Taeseon Lee, Jaegeun Lee, Yong-O. Im, Cheol-Hun Lee, Hyunjung Cho, Hyeseon Lee, Chi-Hyuck Jun, Yu-Chan Ahn, In-Beum Lee, and Kun-Hong Lee. Synthesis of carbon nanotube fibers using the direct spinning process based on Design of Experiment (DOE). *Carbon*, 100:647–655, 2016. ISSN 0008-6223. doi: https://doi.org/10.1016/j.carbon.2016.01.034. URL http://www.sciencedirect.com/science/article/pii/S0008622316300343.

[74] Víctor Reguero, Belén Alemán, Bartolomé Mas, and Juan José Vilatela. Controlling carbon nanotube type in macroscopic fibers synthesized by the direct spinning process. *Chemistry of Materials*, 26(11):3550–3557, 2014. ISSN 15205002. doi: 10.1021/cm501187x.

[75] John S Bulmer, Adarsh Kaniyoor, Thurid Gspann, Jenifer Mizen, James Ryley, Patrick Kiley, Gijs Ratering, Wouter Sparreboom, Gerhard Bauhuis, Troy Stehr, Dion Oudejans, Martin Sparkes, Bill O'Neill, and James A Elliott. Forecasting continuous carbon nanotube production in the floating catalyst environment. *Chemical Engineering Journal*, 390:124497, 2020. ISSN 1385-8947. doi: https://doi.org/10.1016/j.cej.2020.124497. URL http://www.sciencedirect.com/science/article/pii/S1385894720304885.

[76] Christian Hoecker, Fiona Smail, Martin Pick, and Adam Boies. The influence of carbon source and catalyst nanoparticles on CVD synthesis of CNT aerogel. *Chemical Engineering Journal*, 314:388–395, 2017. ISSN 1385-8947. doi: https://doi.org/10.1016/j.cej.2016.11.157. URL http://www.sciencedirect.com/science/article/pii/S1385894716317454.

[77] Jay B. Jeffries, George A. Raiche, and Michael S. Brown. Optical diagnostics of diamond CVD plasmas. *Laser Techniques for State-Selected and State-to-State Chemistry II*, 2124(June 1994):270–277, 1994. doi: 10.1117/12.178101.

[78] Roberto Muñoz and Cristina Gómez-Aleixandre. Review of CVD Synthesis of Graphene. *Chemical Vapor Deposition*, 19(10-11-12):297–322, 2013. doi: https://doi.org/10.1002/cvde.201300051. URL https://onlinelibrary.wiley.com/doi/abs/10.1002/cvde.201300051.

[79] Jaeho Jeon, Sung Kyu Jang, Su Min Jeon, Gwangwe Yoo, Yun Hee Jang, Jin Hong Park, and Sungjoo Lee. Layer-controlled CVD growth of large-area two-dimensional MoS2 films. *Nanoscale*, 7(5):1688–1695, 2015. ISSN 20403372. doi: 10.1039/c4nr04532g.

[80] Sreekar Bhaviripudi, Ervin Mile, Stephen A. Steiner, Aurea T. Zare, Mildred S. Dresselhaus, Angela M. Belcher, and Jing Kong. CVD synthesis of single-walled

carbon nanotubes from gold nanoparticle catalysts. *Journal of the American Chemical Society*, 129(6):1516–1517, 2007. ISSN 00027863. doi: 10.1021/ja0673332.

[81] Alan M. Cassell, Jeffrey A. Raymakers, Jing Kong, and Hongjie Dai. Large Scale CVD Synthesis of Single-Walled Carbon Nanotubes. *Journal of Physical Chemistry B*, 103(31):6484–6492, 1999. ISSN 15206106. doi: 10.1021/jp990957s.

[82] Avetik R. Harutyunyan, Bhabendra K. Pradhan, U. J. Kim, Gugang Chen, and P. C. Eklund. CVD Synthesis of Single Wall Carbon Nanotubes under "Soft" Conditions. *Nano Letters*, 2(5):525–530, 2002. ISSN 15306984. doi: 10.1021/nl0255101.

[83] Cecilia Mattevi, Christoph Tobias Wirth, Stephan Hofmann, Raoul Blume, Mirco Cantoro, Caterina Ducati, Cinzia Cepek, Axel Knop-Gericke, Stuart Milne, Carla Castellarin-Cudia, Sheema Dolafi, Andrea Goldoni, Robert Schloegl, and John Robertson. In-situ X-ray photoelectron spectroscopy study of catalyst-support interactions and growth of carbon nanotube forests. *Journal of Physical Chemistry C*, 112(32): 12207–12213, 2008. ISSN 19327447. doi: 10.1021/jp802474g.

[84] David Edmond Motaung, Mathew Kisten Moodley, E. Manikandan, and Neil J. Coville. In situ optical emission study on the role of C2 in the synthesis of single-walled carbon nanotubes. *Journal of Applied Physics*, 107(4), 2010. ISSN 00218979. doi: 10.1063/1.3311563.

[85] Qingfeng Liu, Wencai Ren, Zhi-Gang Chen, Da-Wei Wang, Bilu Liu, Bing Yu, Feng Li, Hongtao Cong, and Hui-Ming Cheng. Diameter-selective growth of single-walled carbon nanotubes with high quality by floating catalyst method. *ACS nano*, 2(8): 1722–8, 2008. ISSN 1936-086X. doi: 10.1021/nn8003394. URL http://www.ncbi.nlm.nih.gov/pubmed/19206377.

[86] Shigeo Maruyama, Erik Einarsson, Yoichi Murakami, and Tadao Edamura. Growth process of vertically aligned single-walled carbon nanotubes. *Chemical Physics Letters*, 403(4-6):320–323, 2005. ISSN 00092614. doi: 10.1016/j.cplett.2005.01.031.

[87] Erik Einarsson, Yoichi Murakami, Masayuki Kadowaki, and Shigeo Maruyama. Growth dynamics of vertically aligned single-walled carbon nanotubes from in situ measurements. *Carbon*, 46(6):923–930, 2008. ISSN 00086223. doi: 10.1016/j.carbon.2008.02.021.

[88] Itaru Gunjishima, Takashi Inoue, and Atsuto Okamoto. In situ optical imaging of carbon nanotube growth. *Japanese Journal of Applied Physics, Part 1: Regular Papers and Short Notes and Review Papers*, 46(5 A):3149–3151, 2007. ISSN 00214922. doi: 10.1143/JJAP.46.3149.

[89] Anastasios John Hart, Lucas Van Laake, and Alexander H. Slocum. Desktop growth of carbon-nanotube monoliths with in situ optical imaging. *Small*, 3(5):772–777, 2007. ISSN 16136810. doi: 10.1002/smll.200600716.

[90] Karla Reinhold-López, Andreas Braeuer, Bettina Romann, Nadejda Popovska-Leipertz, and Alfred Leipertz. Simultaneous in situ Raman monitoring of the solid and gas phases during the formation and growth of carbon nanostructures inside a cold wall CCVD reactor. *Carbon*, 78:164–180, 2014. ISSN 00086223. doi: 10.1016/j.carbon.2014.06.064.

[91] Shohei Chiashi, Yoichi Murakami, Yuhei Miyauchi, and Shigeo Maruyama. Cold wall CVD generation of single-walled carbon nanotubes and in situ Raman scattering measurements of the growth stage. *Chemical Physics Letters*, 386(1-3):89–94, 2004. ISSN 00092614. doi: 10.1016/j.cplett.2003.12.126.

[92] R. Salter, J. Chu, and M. Hippler. Cavity-enhanced Raman spectroscopy with optical feedback cw diode lasers for gas phase analysis and spectroscopy. *Analyst*, 137: https://www.overleaf.com/project/597f62717467430e5c464c9c4621–4868, 2012.

[93] H A Michelsen. Probing soot formation , chemical and physical evolution , and oxidation : A review of in situ diagnostic techniques and needs. *Proceedings of the Combustion Institute*, 36(1):717–735, 2017. ISSN 1540-7489. doi: 10.1016/j.proci.2016.08.027. URL http://dx.doi.org/10.1016/j.proci.2016.08.027.

[94] J Kiefer, T Seeger, S Steuer, S Schorsch, M C Weikl, and a Leipertz. Design and characterization of a Raman-scattering-based sensor system for temporally resolved gas analysis and its application in a gas turbine power plant. *Measurement Science and Technology*, 19(8):085408, 2008. ISSN 0957-0233. doi: 10.1088/0957-0233/19/8/085408.

[95] G. Bulat, E. Fedina, C. Fureby, W. Meier, and U. Stopper. Reacting flow in an industrial gas turbine combustor: Les and experimental analysis. *Proceedings of the Combustion Institute*, 35(3):3175–3183, 2015. ISSN 15407489. doi: 10.1016/j.proci.2014.05.015. URL http://dx.doi.org/10.1016/j.proci.2014.05.015.

[96] U. Stopper, M. Aigner, H. Ax, W. Meier, R. Sadanandan, M. Stöhr, and A. Bonaldo. PIV, 2D-LIF and 1D-Raman measurements of flow field, composition and temperature in premixed gas turbine flames. *Experimental Thermal and Fluid Science*, 34(3):396–403, 2010. ISSN 08941777. doi: 10.1016/j.expthermflusci.2009.10.012. URL http://dx.doi.org/10.1016/j.expthermflusci.2009.10.012.

[97] Guillaume Cléon, Denis Stepowski, and Armelle Cessou. Long-cavity Nd:YAG laser used in single-shot spontaneous Raman scattering measurements. *Optics Letters*, 32 (22):3290, 2007. ISSN 0146-9592. doi: 10.1364/ol.32.003290.

[98] Hassan Ajrouche, Amath Lo, Pierre Vervisch, and Armellle Cessou. 1D single-shot thermometry in flames by Spontaneous Raman Scattering through a fast electro-optical shutter. *17th International Symposium on Applications of Laser Techniques to Fluid Mechanics Lisbon, Portugal,*, (July):1–17, 2014. doi: 978-989-98777-8-8.

[99] K. Müller-Dethlefs, M. Pealat, and J.-P. E. Taran. Temperature and Hydrogen Concentration Measurements by CARS in an Ethylene-Air Bunsen Flame. *Berichte der Bunsengesellschaft für physikalische Chemie*, 85(8):803–807, 1981. ISSN 0005-9021. doi: 10.1002/bbpc.19810850813.

[100] Frédéric Grisch, Paul Bouchardy, and Walter Clauss. CARS thermometry in high pressure rocket combustors. *Aerospace Science and Technology*, 7(4):317–330, 2003. ISSN 12709638. doi: 10.1016/S1270-9638(03)00017-8.

[101] Mathew P Thariyan, Aizaz H Bhuiyan, Scott E Meyer, Sameer V Naik, Jay P Gore, and Robert P Lucht. Dual-pump coherent anti-Stokes Raman scattering system for temperature and species measurements in an optically accessible high-pressure gas turbine combustor facility. *Measurement Science and Technology*, 22(1):15301, 12 2010. doi: 10.1088/0957-0233/22/1/015301. URL https://doi.org/10.1088/0957-0233/22/1/015301.

[102] C. V. Raman and K. S. Krishnan. A new type of secondary radiation. *Nature*, 121: 501–502, 1928.

[103] Dr. Derek, J. Gardiner, Dr. Pierre, and R. Graves. *Practical Raman Spectroscopy*. Springer - Vierlag, 1989.

[104] B. Schrader. *Infrared and Raman Spectroscopy Methods*, page 24. Weinheim, 1995.

[105] Antonija Oklopčić, Christopher M. Hirata, and Kevin Heng. Raman Scattering By Molecular Hydrogen and Nitrogen in Exoplanetary Atmospheres. *The Astrophysical Journal*, 832(1):30, 2016. ISSN 0004-637X. doi: 10.3847/0004-637x/832/1/30.

[106] B. Lavorel, G. Millot, M. Rotger, G. Rouille, H. berger, and H. W. Schrotter. Non-linear Raman spectroscopy in gases. *Journal of Molecular Structure*, 273:49–59, 1992.

[107] G. A West, J. J. Barrett, D. R. Siebert, and K. V Reddy. Photoacoustic spectroscopy. *Review of Scientific Instruments*, 54:797–817, 1983.

[108] D. J. Gardiner and P. R. Graves. *Practical Raman Spectroscopy*. Springer-Verlag, 1989.

[109] Michael Hercher, William Mueller, Stanley Klainer, Robert F Adamowicz, Ronald E Meyers, and Stephen E Schwartz. An Efficient Intracavity Laser Raman Spectrometer. *Applied Spectroscopy*, 32(3):298–302, 1978. doi: 10.1366/000370278774331260. URL https://doi.org/10.1366/000370278774331260.

[110] D. L. A de Faria, S. V. Silva, and M. T. de Oliveira. Raman Microspectroscopy of Some Iron Oxides and Oxyhydroxies. *Journal of Raman Spectroscopy*, 28:873–878, 1997.

[111] Jun Kojima and Quang-Viet Nguyen. Laser pulse-stretching with multiple optical ring cavities. *Appl. Opt.*, 41(30):6360–6370, 10 2002. doi: 10.1364/AO.41.006360. URL http://ao.osa.org/abstract.cfm?URI=ao-41-30-6360.

[112] A. N. Malov and S. Yu Fedorov. XeCl and KrF excimer lasers for diagnostics of flames by spontaneous Raman scattering. *Combustion, Explosion, and Shock Waves*, 24(4):431–434, 1988. ISSN 15738345. doi: 10.1007/BF00750014.

[113] W Meier and O Keck. Laser Raman scattering in fuel-rich flames: background levels at different excitation wavelengths. *Measurement Science and Technology*, 13(5): 741–749, 4 2002. doi: 10.1088/0957-0233/13/5/312. URL https://doi.org/10.1088%2F0957-0233%2F13%2F5%2F312.

[114] A G Gaydon. *The spectroscopy of flames*. Chapman and Hall, London, 1974. ISBN 0412128705 9780412128707.

[115] Alan C. Eckbreth, Paul A. Bonczyk, and James F. Verdieck. Combustion diagnostics by laser Raman and fluorescence techniques. *Progress in Energy and Combustion Science*, 5(4):253–322, 1979. ISSN 03601285. doi: 10.1016/0360-1285(79)90011-X.

[116] G Magnotti, D Geyer, and R S Barlow. Interference free spontaneous Raman spectroscopy for measurements in rich hydrocarbon flames. *Proceedings of the Combustion Institute*, 35(3):3765–3772, 2015. doi: 10.1016/j.proci.2014.05.076.

[117] C Dreyer, T Parker, and M A Linne. Raman scattering at 532 and 355 nm in atmospheric pressure propane/air flames, with and without liquid fuels. *Applied Physics B*, 79(1):121–130, 2004.

[118] Amnon Yariv. Quantum electronics, 3rd. *Edn.(John WieLy & Sons, New York, 1988) p*, 389, 1989.

[119] Benjamin James Petrak. *Microcavity Enhanced Raman Scattering*. PhD thesis, 2016.

[120] T Niioka, M Kono, and J Sato. Fundamentals of combustion phenomena. *Ohmsha Publi-cation Ltd., Tokyo*, 2001.

[121] Kevin L McNesby and Jeffrey B Morris. Fourier transform raman spectroscopy of nitrogen at high pressures. *Journal of Raman Spectroscopy*, 26(6):487–490, 1995.

[122] LA Rahn and Rt E Palmer. Studies of nitrogen self-broadening at high temperature with inverse raman spectroscopy. *JOSA B*, 3(9):1164–1169, 1986.

[123] Alan Corney. *Atomic and laser spectroscopy*. Clarendon Press Oxford, 1978.

[124] E. Riedle and H. J. Neusser. Homogeneous linewidths of single rotational lines in the "channel three" region of C6H6. *The Journal of CHemical Physics*, 80, 1984.

[125] G. J. Dixon, C. E. Tanner, and Carl E. Wieman. 432-nm source based on efficient second-harmonic generation of GaAlAs diode-laser radiation in a self-locking external resonant cavity . *Optics Letters*, 14:731–733, 1989.

[126] M. de Labachelerie, K. Nakagawa, and M. Ohtsu. Ultranarrow 13C2H2 saturated-absorption lines at 1.5 m . *Optics Letters*, 19:840–842, 1994.

[127] J. A. Barnesand T. E. Gough and M. Stoer. Laser power build-up cavity for high-resolution laser spectroscopy . *Review of Scientific Instruments*, 70, 1999.

[128] D. A. King, W. F. Carlsen, D. F. Gray, and R. J. Pittaro. *Diode-pumped power build-up cavity for chemical sensing*. US Patent. US5432610 A, 1995.

[129] D. A. King and R. J. Pittaro. Simple diode pumping of a power-buildup cavity. *Optics Letters*, 23:774–776, 1998.

[130] D. J. Taylor, M. Glugla, and R. Penzhorn. Enhanced Raman sensitivity using an actively stabilized external resonator . *Review of Scientific Instruments*, 72, 1970.

[131] S. Ohara, S.Yamaguchi, M. Endo, K. Nanri, and T. Fujioka. Performance Characteristics of Power Build-Up Cavity for Raman Spectroscopic Measurement. *Quantum optics and spectroscopy*, 10:342–345, 2003.

[132] X. Li, Y. Xia, L. Zhan, and J. Huang. Near-confocal cavity-enhanced Raman spectroscopy for multitrace-gas detection . *Optics Letters*, 33:2143–2145, 2008.

[133] J. Throstensen, K. Haugholt, A. Ferber, K. Bakke, and J. Tschudi. Low-cost resonant cavity Raman gas probe for multi-gas detection. *Journal of European Optical Society*, 9, 2014.

[134] Adam J. Friss, Christopher M. Limbach, and Azer P. Yalin. Cavity-enhanced rotational Raman scattering in gases using a 20 mW near-infrared fiber laser. *Optics Letters*, 41 (14):3193, 2016. ISSN 15394794. doi: 10.1364/OL.41.003193.

[135] A. Siegman. *Lasers*, page 433. University Science Books, 1986.

[136] O. Svelto. *Principles of Lasers*, pages 298–304. Plenum Press, 1982.

[137] C. C. Davis. *Lasers and Electro-Optics: fundamentals and engineering*, pages 348–354. Cambridge University Press, 1996.

[138] M. Young. *Optics and Lasers*, page 161. Springer-Verlag, 1986.

[139] D. C. O'Shea, W.R. Callen, and W. T. Rhodes. *Introduction to Lasers and Their Applications*, pages 89–97. Addison-Wesley, Reading, MA, 1978.

[140] H. Kogelnik and T. Li. Laser Beams and Resonators. *Applied Optics*, 5:1550–1567, 1966.

[141] Wikipedia. Gaussian beam. Accessed on 30/08/2017. Available: https://en.wikipedia.org/wiki/Gaussian_beam#/media/File:Hermite-gaussian.png.

[142] H. Kogelnik. Imaging of optical mode - Resonators with internal lenses. *Bell System Technical Journal*, 44:455–494, 1965.

[143] A. Siegman. *Lasers*, page 436. University Science Books, 1986.

[144] J. Barnes, T. Gough, and M. Stoer. Laser power build-up cavity for high-resolution laser spectroscopy. *Review of Scientific Instruments*, 70:3515, 1999.

[145] E Riedle and H J Neusser. Homogeneous linewidths of single rotational lines in the "channel three" region of C6H6. *The Journal of Chemical Physics*, 80(10):4686–4693, 1984. doi: 10.1063/1.446533. URL https://doi.org/10.1063/1.446533.

[146] Wan-Ü L Brillet and A Gallagher. Inert-gas collisional broadening and shifts of Rb Rydberg states. *Phys. Rev. A*, 22(3):1012–1017, 9 1980. doi: 10.1103/PhysRevA.22.1012. URL https://link.aps.org/doi/10.1103/PhysRevA.22.1012.

[147] Alessandro Rossi, Roberto Buffa, Mario Scotoni, Davide Bassi, Salvatore Iannotta, and Andrea Boschetti. Optical enhancement of diode laser-photoacoustic trace gas detection by means of external Fabry-Perot cavity. *Applied Physics Letters*, 87(4): 41110, 2005. doi: 10.1063/1.2000341. URL https://doi.org/10.1063/1.2000341.

[148] Michael Hercher. The spherical mirror fabry-perot interferometer. *Applied Optics*, 7 (5):951–966, 1968.

[149] Richard W. Fox, Chris W. Oates, and Leo W. Hollberg. Stabilizing Diode Lasers to High-Finesse Cavities. *Experimental Methods in the Physical Sciences*, 40:1–46, 2003.

[150] Charlotte Bond, Daniel Brown, Andreas Freise, and Kenneth A Strain. Interferometer techniques for gravitational-wave detection. *Living Reviews in Relativity*, 19(1):3, 2016.

[151] David S Rabeling, Jong H Chow, Malcolm B Gray, and David E McClelland. Experimental demonstration of impedance match locking and control for coupled resonators. *Optics Express*, 18(9):9314–9323, 2010.

[152] E. M. Purcell. Spontaneous emission probabilities at radio frequencies. *Phys. Rev*, 69: 681–681, 1946.

[153] K. J. Vahala. Optical microcavities. *Nature*, 424:839, 2003.

[154] T. Hümmer, J. Noe, M. S. Hofmann, T. W. Hänsch, A. Högele, and D. Hunger. Cavity-enhanced Raman microscopy of individual carbon nanotubes. *Nature communications*, 7, 2016.

[155] A. Aufféves, D. Gerace, J.M. Gérard, M. Franca Santos, L.C. Andreani, and J.P. Poizat. Controlling the dynamics of a coupled atom-cavity system by pure dephasing : basics and potential applications in nanophotonics. *Physical Review B*, 81, 2010.

[156] Thomas W Smith and Michael Hippler. Cavity-enhanced raman spectroscopy in the biosciences: In situ, multicomponent, and isotope selective gas measurements to study hydrogen production and consumption by escherichia coli. *Analytical chemistry*, 89 (3):2147–2154, 2017.

[157] S. K. Sengupta, J. M. Farnham, and J. E. Whitten. "A Simple Low-Cost Lock-In Amplifier for the Laboratory. *J. Chem. Educ.*, 82:1399, 2005.

[158] R. W. P. Drever, J. L Hall, F. V. Kowalski, J. Hough, G. M. Ford A. J. Munley, and H. Ward. Laser phase and frequency stabilisation using an optical resonator. *Applied Physics B*, 31:97–105, 1983.

[159] X Checoury, Z Han, M El Kurdi, and P Boucaud. Deterministic measurement of the purcell factor in microcavities through raman emission. *Physical Review A*, 81(3): 033832, 2010.

[160] https://www.layertec.de/en/shop/datasheet-110650/, 2019. URL https://www.layertec.de/en/shop/datasheet-110650/.

[161] https://www.layertec.de/en/shop/datasheet-109446/, 2019. URL https://www.layertec.de/en/shop/datasheet-109446/.

[162] Kam Kong Chow, Michael Short, Stephen Lam, Annette McWilliams, and Haishan Zeng. A Raman cell based on hollow core photonic crystal fiber for human breath analysis. *Medical physics*, 41(9):92701, 2014.

[163] Yasushi Numata, Yuta Shinohara, Tomoya Kitayama, and Hiroyuki Tanaka. Rapid and accurate quantitative analysis of fermentation gases by Raman spectroscopy. *Process Biochemistry*, 48(4):569–574, 2013.

[164] Vincenz Sandfort, Jens Goldschmidt, Jürgen Wöllenstein, and Stefan Palzer. Cavity-enhanced Raman spectroscopy for food chain management. *Sensors*, 18(3):709, 2018.

[165] Dewang Yang, Jinjia Guo, Qingsheng Liu, Zhao Luo, Jingwen Yan, and Ronger Zheng. Highly sensitive Raman system for dissolved gas analysis in water. *Applied optics*, 55 (27):7744–7748, 2016.

[166] R.s Barlow. Laser diagnostics and their interplay with computations to understand turbulent combustion. *Proceedings of the Combustion Institute*, 31:49–75, 2007. doi: 10.1016/j.proci.2006.08.122.

[167] Alan C. Eckbreth. Averaging considerations for pulsed, laser Raman signals from turbulent combustion media. *Combustion and Flame*, 31(C):231–237, 1978. ISSN 00102180. doi: 10.1016/0010-2180(78)90134-7.

[168] Anna Lombardi, Mikołaj K. Schmidt, Lee Weller, William M. Deacon, Felix Benz, Bart De Nijs, Javier Aizpurua, and Jeremy J. Baumberg. Pulsed Molecular Optomechanics in Plasmonic Nanocavities: From Nonlinear Vibrational Instabilities to Bond-Breaking. *Physical Review X*, 8(1):1–17, 2018. ISSN 21603308. doi: 10.1103/PhysRevX.8.011016.

[169] Baokun Huang, Yanjie Tian, Zuowei Li, Shuquin Gao, and Zhaokai Li. Temperature measurement from the intensity ratio of the Raman-scattering lines in carbon tetrachloride constituting the liquid core of an optical fiber. *Instruments and Experimental Techniques*, 50(2):282–285, 2007. ISSN 00204412. doi: 10.1134/S0020441207020200.

[170] Teobald Kupka, Roman Wrzalik, Grazyna Pasterna, and Karol Pasterny. Theoretical DFT and experimental Raman and NMR studies on thiophene, 3-methylthiophene and selenophene. *Journal of Molecular Structure*, 616(1-3):17–32, 2002. ISSN 00222860. doi: 10.1016/S0022-2860(02)00177-1.

[171] Bálint Somogyi, Emilie Bruyer, and Adam Gali. Photoluminescence, infrared, and Raman spectra of co-doped Si nanoparticles from first principles. *Journal of Chemical Physics*, 149(15), 2018. ISSN 00219606. doi: 10.1063/1.5053100. URL http://dx.doi.org/10.1063/1.5053100.

[172] Soonil Lee, Jaehyun Ahn, Leo Mathew, Rajesh Rao, Zhongjian Zhang, Jae Hyun Kim, Sanjay K. Banerjee, and Edward T. Yu. Highly improved passivation of c-Si surfaces using a gradient i a-Si:H layer. *Journal of Applied Physics*, 123(16), 2018. ISSN 10897550. doi: 10.1063/1.5023000. URL http://dx.doi.org/10.1063/1.5023000.

[173] A. Slenczka, G. Marowsky, and M. Vodegel. H2 vibrational CARS thermometry. *Applied Physics B Photophysics and Laser Chemistry*, 47(1):41–46, 1988. ISSN 07217269. doi: 10.1007/BF00696207.

[174] Eric Jourdanneau, Frederic Chaussard, Robert Saint-Loup, Tony Gabard, and Hubert Berger. The methane Raman spectrum from 1200 to 5500 cm-1: A first step toward temperature diagnostic using methane as a probe molecule in combustion systems. *Journal of Molecular Spectroscopy*, 233(2):219–230, 2005. ISSN 00222852. doi: 10.1016/j.jms.2005.07.004.

[175] Chamseddine Guizani, Francisco Javier Escudero Sanz, and Sylvain Salvador. The nature of the deposited carbon at methane cracking over a nickel loaded wood-char. *Comptes Rendus Chimie*, 19(4):423–432, 2016. ISSN 1631-0748. doi: https://doi.org/10.1016/j.crci.2015.10.009. URL http://www.sciencedirect.com/science/article/pii/S163107481500332X.

[176] Adil Emin, Anwar Hushur, and Tursunay Mamtimin. Raman study of mixed solutions of methanol and ethanol. *AIP Advances*, 10(6), 2020. ISSN 21583226. doi: 10.1063/1.5140722. URL https://doi.org/10.1063/1.5140722.

[177] Peter Francis Bernath. Spectra of Atoms and Molecules, 2005. ISSN 00029505. URL http://eprints.whiterose.ac.uk/72681/.

[178] S Iordanova. Spectroscopic temperature measurements in hydrogen inductively-driven plasmas at low pressures. In *Journal of Physics: Conference Series*, volume 113, page 12005. IOP Publishing, 2008.

[179] Bingjia Xiao, Shinichiro Kado, Shin Kajita, and Daisuke Yamasaki. Rovibrational distribution determination of H2 in low temperature plasmas by Fulcher-α band spectroscopy. *Plasma physics and controlled fusion*, 46(4):653, 2004.

[180] Stefan Briefi, David Rauner, and Ursel Fantz. Determination of the rotational population of H2 and D2 including high-N states in low temperature plasmas via the Fulcher-α transition. *Journal of Quantitative Spectroscopy and Radiative Transfer*, 187:135–144, 2017.

[181] V N Ochkin, Y S Savinov, and N N Sovolev. Electron Excited Molecules in Nonequilibrium Plasma. *NY Niva Publ., Proc. Lebedev Phys. Inst*, 179(suppl V):2, 1989.

[182] M Pealat, J P E Taran, J Taillet, M Bacal, and A M Bruneteau. Measurement of vibrational populations in low-pressure hydrogen plasma by coherent anti-Stokes Raman scattering. *Journal of Applied Physics*, 52(4):2687–2691, 1981.

[183] A. V. Sepman, V. V. Toro, A. V. Mokhov, and H. B. Levinsky. Determination of temperature and concentrations of main components in flames by fitting measured Raman spectra. *Applied Physics B: Lasers and Optics*, 112(1):35–47, 2013. ISSN 09462171. doi: 10.1007/s00340-013-5389-2.

[184] Jun Kojima and Quang Viet Nguyen. Measurement and simulation of spontaneous Raman scattering in high-pressure fuel-rich H2-air flames. *Measurement Science and Technology*, 15(3):565–580, 2004. ISSN 09570233. doi: 10.1088/0957-0233/15/3/009.

[185] V. Bergmann and W. Stricker. H2 CARS thermometry in a fuel-rich, premixed, laminar CH4/air flame in the pressure range between 5 and 40 bar. *Applied Physics B Laser and Optics*, 61(1):49–57, 1995. ISSN 09462171. doi: 10.1007/BF01090971.

[186] S. A. Astashkevich, M. Käning, E. Käning, N. V. Kokina, B. P. Lavrov, A. Ohl, and J. Röpcke. Radiative characteristics of 3p Σ, Π; 3d Π-, Δ- states of H2 and determination of gas temperature of low pressure hydrogen containing Plasmas. *Journal of Quantitative Spectroscopy and Radiative Transfer*, 56(5):725–751, 1996. ISSN 00224073. doi: 10.1016/S0022-4073(96)00103-3.

[187] S A Astashkevich, M Käning, E Käning, N V Kokina, B P Lavrov, A Ohl, and J Röpcke. Radiative characteristics of 3p $Σ$, $Π$; 3d $Π$-, $Δ$- states of H2 and determination of gas temperature of low pressure hydrogen containing plasmas. *Journal of Quantitative Spectroscopy and Radiative Transfer*, 56(5):725–751, 1996.

[188] Gerhard Heinrich Dieke. *The hydrogen molecule wavelength tables of Gerhard Heinrich Dieke.* Wiley-Interscience, New York, 1972. ISBN 0471188905 9780471188902.

[189] S A Alexander and R L Coldwell. Spectroscopic constants of H2 using Monte Carlo methods. *International Journal of Quantum Chemistry*, 100(6):851–857, 2004. doi: https://doi.org/10.1002/qua.20148. URL https://onlinelibrary.wiley.com/doi/abs/10.1002/qua.20148.

[190] I Dabrowski. The Lyman and Werner bands of H2. *Canadian Journal of Physics*, 62: 1639–1664, 2011. doi: 10.1139/p84-210.

[191] Charles D. Hurd, Robert V. Levetan, and A. R. Macon. Pyrolytic Formation of Arenes. II. Benzene and Other Arenes from Thiophene, 2-Methylthiophene and 2-(Methyl-14C)-Thiophene. *Journal of the American Chemical Society*, 84(23):4515–4519, 1962. ISSN 15205126. doi: 10.1021/ja00882a029.

[192] Hans Wynberg and A. Bantjes. Pyrolysis of Thiophene. *Journal of Organic Chemistry*, 24(10):1421–1423, 1959. ISSN 15206904. doi: 10.1021/jo01092a008.

[193] C. F. Cullis and A. C. Norris. The pyrolysis of organic compounds under conditions of carbon formation. *Carbon*, 10(5):525–537, 1972. ISSN 00086223. doi: 10.1016/0008-6223(72)90092-9.

[194] Nathan R. Hore and Douglas K. Russell. The thermal decomposition of 5-membered rings: A laser pyrolysis study. *New Journal of Chemistry*, 28(5):606–613, 2004. ISSN 11440546. doi: 10.1039/b315093c.

[195] Hafeez Ur Rahman Memon, Alan Williams, and Paul T Williams. Shock tube pyrolysis of thiophene. *International Journal of Energy Research*, 27(3):225–239, 2003. doi: https://doi.org/10.1002/er.870. URL https://onlinelibrary.wiley.com/doi/abs/10.1002/er.870.

[196] Fiona Smail, Adam Boies, and Alan Windle. Direct spinning of CNT fibres: Past, present and future scale up. *Carbon*, 152:218–232, 2019. ISSN 00086223. doi: 10.1016/j.carbon.2019.05.024. URL https://doi.org/10.1016/j.carbon.2019.05.024.

[197] Cen Zhang. *An Investigation of Carbon Nanotube Synthesis: Modeling and Experiments*. PhD thesis, 2018.

[198] David G. Goodwin, Raymond L. Speth, Harry K. Moffat, and Bryan W. Weber. Cantera: An object-oriented software toolkit for chemical kinetics, thermodynamics, and transport processes. https://www.cantera.org, 2021. Version 2.5.1.

[199] Michael Hippler. Cavity-Enhanced Raman Spectroscopy of Natural Gas with Optical Feedback cw-Diode Lasers. *Analytical Chemistry*, 87(15):7803–7809, 2015. ISSN 15206882. doi: 10.1021/acs.analchem.5b01462.

[200] Frederik Fuest, Robert S. Barlow, Gaetano Magnotti, Andreas Dreizler, Isaac W. Ekoto, and Jeffrey A. Sutton. Quantitative acetylene measurements in laminar and turbulent flames using 1D Raman/Rayleigh scattering. *Combustion and Flame*, 162 (5):2248–2255, 2015. ISSN 15562921. doi: 10.1016/j.combustflame.2015.01.021. URL http://dx.doi.org/10.1016/j.combustflame.2015.01.021.

[201] Jiang Shimei and Wang Yue. Vibrational spectra of an open ferrocene and a half-open ferrocene. *Spectrochimica Acta - Part A: Molecular and Biomolecular Spectroscopy*, 55(5):1025–1033, 1999. ISSN 13861425. doi: 10.1016/S1386-1425(98)00246-7.

[202] Amelia Barreiro, Silke Hampel, Mark H Rümmeli, Christian Kramberger, Alexander Grüneis, Kati Biedermann, Albrecht Leonhardt, Thomas Gemming, Bernd Büchner, Adrian Bachtold, and Thomas Pichler. Thermal Decomposition of Ferrocene as a Method for Production of Single-Walled Carbon Nanotubes without Additional Carbon Sources. *The Journal of Physical Chemistry B*, 110(42):20973–20977, 2006. doi: 10.1021/jp0636571. URL https://doi.org/10.1021/jp0636571.

[203] Karine Elihn. *Synthesis of carbon-covered iron nanoparticles by photolysis of ferrocene*. PhD thesis, Acta Universitatis Upsaliensis, 2002.

[204] Durham University. Gaussian Beams and the Knife-Edge Measurement. Accessed on 23/08/2017. Available: http://massey.dur.ac.uk/resources/grad_skills/KnifeEdge.pdf.

[205] Michal Fulem, Luis M N B F Santos, and Robert F. Berg. Recommended vapor pressure and thermophysical data for ferrocene. *Journal of Chemical Thermodynamics*, 57:530–540, 2013. ISSN 00219614. doi: 10.1016/j.jct.2012.07.023.

[206] Guy Waddington, J. W. Knowlton, D. W. Scott, W. N. Hubbard, J. C. Smith, Hugh M. Huffman, G. D. Oliver, and S. S. Todd. Thermodynamic Properties of Thiophene. *Journal of the American Chemical Society*, 71(3):797–808, 1949. ISSN 15205126. doi: 10.1021/ja01171a010.

[207] D. Ambrose and C. H.S. Sprake. Thermodynamic properties of organic oxygen compounds XXV. Vapour pressures and normal boiling temperatures of aliphatic alcohols. *The Journal of Chemical Thermodynamics*, 2(5):631–645, 1970. ISSN 10963626. doi: 10.1016/0021-9614(70)90038-8.

Appendix A

Appendix A - Knife Edge

Knife edge is a commonly used technique to work out the beam waist of an unknown Laser beam. It consists of placing a knife edge, such as a razor plade, mounted on a micrometer translational platform, perpendicular to the axis propagation of the beam at some point away from its origin. The knife edge is then translated and the total power in the beam is recorded by a detector. The detector records the integral of the Gaussian beam between $-\infty$ and the position of the knife.

The measured power can be expressed by the follows [204]:

$$P_{measured} = \frac{P1}{2}\left[1 \pm erf\left(\frac{\sqrt{2}(X-P2)}{P3}\right)\right] \tag{A.1}$$

Where $P1$ corresponds to the maximum power, $P2$ is the size of the beamwaist, $P3$ corresponds to the $1/e^2$ radius of the Gaussian beam and the $+$ or $-$ are chosen depending on the translation direction of the knife edge.

By fitting the curve in Matlab using EzFit tool, and providing some initial coefficients the beam waist was calculated at two different positions from the diode, allowing to acquire the beam divergence

Appendix B

Rate of evaporation by Antoine equation

The mass flow rate, $\dot{m}$ (g s^{-1}), of any molecule can be calculated by using the Antoine equation and partial pressures. The vapour pressure, P_v, for any molecule can be calculated by the Antoine equation.

$$\log P_v = A - \frac{B}{C+T} \ , \tag{B.1}$$

where *A, B* and *C* are the molecule specific constants and *T* is the absolute temperature of the environment in Kelvin. Taking thiophene as a molecule of interest, one can expect thiophene vapour pressure of $\approx$ 2850 Pa, using values provided in B.1. This calculated pressure divided by the standard pressure, P_0 (101325 Pa) is equivalent to the partial pressure.

The volume of 1 mole of gas under standard conditions is given by the ideal gas law.

Thiophene molar fraction in the bubbler flow is then given by vapour pressure divided by the atmospheric pressure, resulting in $X_{thio} = 0.028137$.

To precisely control the amount of thiophene delivered into the system the thiophene pot was kept at 0°C. Number of moles in the reactor is then equal to the flow rate of carrier gas through the pot divided by thiophene gas volume at 0 °C, times the molar fraction.

$$n_t = \dot{Q} \times X_{thio}/V_{thio} \tag{B.2}$$

Table B.1 Antione equation parameters and range of temperatures for the molecules of interest.

Molecule	T_{min} (K)	T_{min} (K)	*A*	*B*	*C*	Reference
Ferrocene	288.16	452.09	6.43321	2982.168	-38.258	[205]
Thiophene	312.21	392.94	4.07358	1239.578	-52.585	[206]
Ethanol	292.77	366.63	5.24677	1598.673	-46.424	[207]

The number of molecules in the reactor is equal to the number of moles times Avogadro's number

$$M_n = n_t \times N_a \tag{B.3}$$

and the mass rate of thiophene is equal to molar mass divided by the molar rate.

$$\dot{m} = M_t / \dot{n}_{thio} \tag{B.4}$$

which was 8.81e-7 kgs^{-1} or 52.9 mg/min for 0.5 SLPM of H_2 carrier gas. This is equal to 0.0529 g/min.

Appendix C

Oxygen and Water content inside of the reactor

The peak magnitude of oxygen mode was monitored across all of the calibration conditions listed in Table 7.1, with corresponding raw Raman spectra shown in Fig.C.1a corresponding to X_{H_2} = 1 as a function of temperature. As can be seen, the magnitude of oxygen does not change by more than 10% percent as a function of temperature highlighting that no oxygen got into the reactor and the Raman signatures arise from the ambient air. Magnitude fluctuations can be due to the laser energy fluctuations or changes of the lab temperature, which were not controlled.

Water is another molecule that is present in ambient air and therefore can also serve as an indicator for leaks. Akin to oxygen, its peak magnitude was monitored across all of the experimental calibration conditions with the raw Raman spectra of X_{H_2} = 1.0 as a function of temperature shown in Fig.C.1b. It can be seen that the magnitude of the water Raman mode diminishes as a function of temperature. This is confirmed by plotting the peak values as a function of furnace set-temperature in Fig.C.1c. As water has a boiling point of 100 °C with the increase of furnace temperature the water in the ambient air close to the furnace starts to evaporate, reducing its molar fraction in the beam path. This instead would increase the molar fraction of other gases present in the ambient air such as nitrogen and oxygen. However, water making up 1% of ambient air the change in molar fraction of the gases outside of the reactor is negligible.

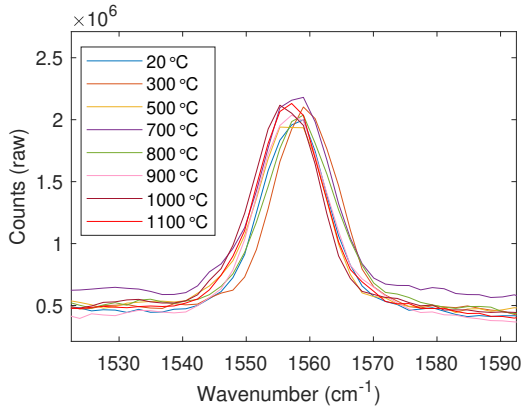

(a) Raw Raman spectra of oxygen mode at X_{H_2} = 1.0 as a function of temperature.

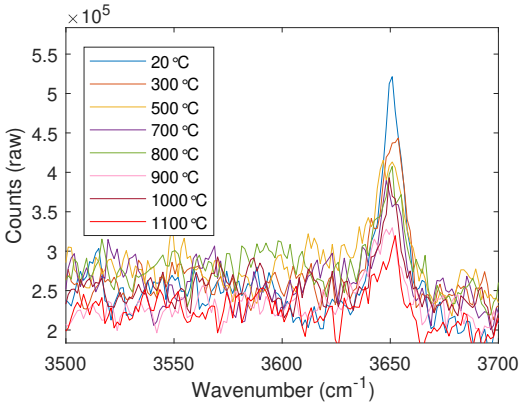

(b) Raw Raman spectra of water mode at X_{H_2} = 1.0 as a function of temperature.

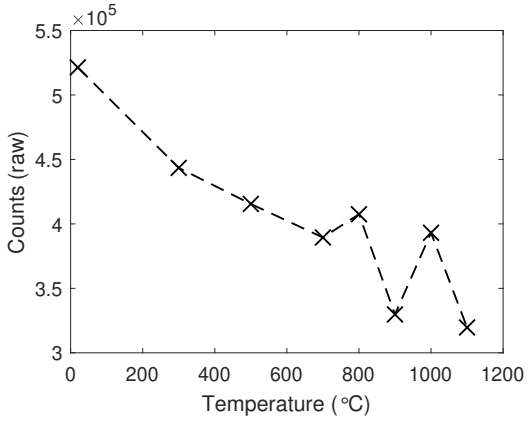

(c) The O-H (water) mode peak magnitudes as function of temperature.

Fig. C.1 Shows the water Raman peaks and their magnitudes as a function of temperature.